



CZECH TECHNICAL UNIVERSITY IN PRAGUE
Faculty of Civil Engineering

Ing. Jan Sýkora, Ph.D.

Transport Processes and Related Inverse Problems

Transportní procesy a přidružené inverzní problémy

November, 2019

ACKNOWLEDGMENTS

Most importantly, I would like to thank my family – Anna, Anna Berenika, Marie Noemi and Antonie Lea, parents, brother and friends for their never ending encouragement and support that help me to attain the goals I have ever set for myself.

I wish also to thank other colleagues who have given me valuable comments and advices. Especially, I would like to express my deepest gratitude to Prof. Michal Šejnoha, Prof. Petr Kabele, Prof. Jiří Šejnoha, Doc. Jan Vorel, and Prof. Jan Zeman for their support.

Last but not least, the financial support provided by the GAČR Grant No. 18-04262S is also gratefully acknowledged.

TABLE OF CONTENTS

Abstract (english)	ii
Abstrakt (czech)	iii
Chapter 1: Introduction	1
1.1 Convection models	3
1.2 Diffusion models	4
1.3 Advanced models	7
1.3.1 Modeling of transport processes in wood structures	7
1.3.2 Modeling of impact of fire on concrete	9
1.3.3 Modeling of damage caused by ice crystallization process	10
1.4 Inverse problems	11
1.4.1 Bayesian updating of uncertainties	12
References	17
Chapter 2: Modeling of transport processes in wood structures	26
List of selected journal papers and book chapters	26
Chapter 3: Modeling of impact of fire on concrete	60
List of selected journal papers and book chapters	60
Chapter 4: Modeling of damage caused by ice crystallization process	90
List of selected journal papers and book chapters	90
Chapter 5: Probabilistic identification methods	110
List of selected journal papers and book chapters	110
List of author's publications	131

Czech Technical University in Prague

Abstract

Transport Processes and Related Inverse Problems

Jan Sýkora

Understanding the heat and moisture damage mechanisms has a significant impact on the design and life cycle of all building materials and structures. Such a task should be accomplished with the help of advanced coupled transport models representing one of the prime objectives of this work. The group of advanced models in the realm of civil engineering can be considered as a special type of coupled heat and moisture transport models extended by another physical and/or chemical phenomena. These multiphysics/multidisciplinary models symbolize nowadays a large and diverse cluster. Therefore, in the present work we limit our attention to the following three modeling strategies: (i) modeling of transport processes in wood structures, (ii) modeling of impact of fire on concrete, and (iii) modeling of damage caused by ice crystallization process in the porous medium. Last chapter outlines, in addition, some identification techniques exploited for the estimation of transport parameters. A novel probabilistic parameter identification technique based on non-invasive experimental measurements is introduced. The idea is to obtain crucial information about the material properties inside the domain under consideration while keeping the test sample intact.

Keywords: Coupled heat and moisture transport; Fire induced spalling; Ice crystallization process; Bayesian inference; Calderón's inverse problem

České vysoké učení technické v Praze

Abstrakt

Transportní procesy a přidružené inverzní problémy

Jan Sýkora

Pochopení mechanismu poškození vlivem tepla a vlhkosti má zásadní dopad na navrhování a životní cyklus budov a stavebních materiálů. Řešení tohoto problému lze dosáhnout pomocí pokročilých sdružených transportních modelů, které představují jeden z hlavních cílů této práce. Na skupinu pokročilých transportních modelů používaných ve stavebním inženýrství lze nahlížet jako na sdružené modely přenosu tepla a vlhkosti, které jsou rozšířeny o další fyzikální anebo chemický jev. Tyto multifyzikální/multidisplinární modely představují v dnešní době velmi rozmanitou a značně početnou skupinu a proto se v předložené práci omezíme na následující tři modelová schémata: (i) modelování transportních procesů ve dřevu, (ii) modelování vlivu požáru na strukturu betonu a (iii) modelování poškození vlivem krystalizace ledu v porézní struktuře. V poslední kapitole jsou navíc diskutovány identifikační techniky potřebné pro odhad transportních materiálových parametrů. Nová pravděpodobnostní identifikace parametrů založená na neinvazivních experimentálních měření je uvedena s cílem získat klíčové informace o materiálových vlastnostech uvnitř zkoumaného vzorku, aniž bychom narušili jeho strukturu.

Klíčová slova: Sdružený přenos tepla a vlhkosti; Odprýskávání materiálu vlivem požáru; Proces krystalizace ledu; Bayesovská inference; Calderónův inverzní problém

Chapter 1

INTRODUCTION

Accurate determination of the temperature and moisture fields is needed to mitigate moisture-induced degradation processes inside materials (see Fig. 1.1 and (Nunes et al., 2012)) and structures, resulting in the shortening of the service life, decrease of energy efficiency, as well as the deterioration of health and safety conditions in buildings¹. Modeling of transport phenomena in the porous media has been studied for decades and two main modeling strategies models can be distinguished, see (Schrefler, 2002): (i) phenomenological

¹ For example, according to (Yverás, 2009), 9 billion euros was spent on repair of moisture-related damages in the European Union in 2009.

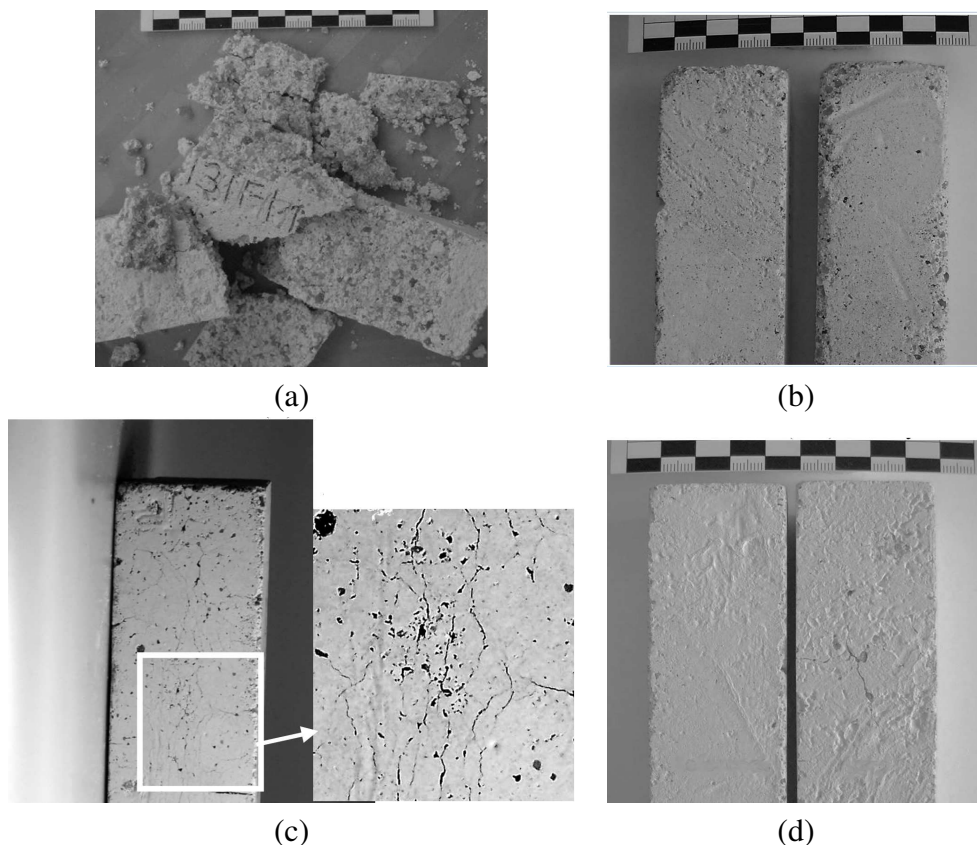


Figure 1.1: Mortar specimens subjected to the different number of freeze-thaw cycles: (a) Lime mortar, 1 cycle; (b) Lime mortar with linseed oil additive, 10 cycles; (c) Lime-metakaolin mortar, 10 cycle; (d) Lime-metakaolin mortar with linseed oil additive, 20 cycles. From Nunes, C., Slížková, Z., and Křivánková, D. (2012). Frost resistance of lime-based mortars with linseed oil. In *XIII Bilateral Czech/German Symposium*

approaches and mixture theories, and (ii) averaging theories. In the averaging theories, thermodynamic equilibrium equations are formulated on the microscopic level which brings the possibility of a better description of microscopic problems and their relations to the macroscopic one. The principles formulated firstly in (Hassanizadeh and Gray, 1979a,b) were summarized in a well-arranged and comprehensible form in (Schrefler and Lewis, 1998). A serious weakness of phenomenological approaches is that balance equations modeling moisture transport have been obtained purely intuitively (de Boer, 2000). Heuristic laws need to be introduced for relations of thermodynamic forces and fluxes through transport coefficients depending on moisture and temperature potentials. However, the phenomenological models are still preferred to the averaging ones, namely when calculating the heat and moisture transport in building materials. Here, we start with the overview of phenomenological based coupled heat and moisture models which are categorized according to the main transport mechanisms of water and water vapor, see Tab. 1.1 summarizing the basic causes and potentials of the transport mechanism. Three basic groups of models can be introduced,

	Transport mechanism	Cause and potential of transport
heat transport	heat conduction	temperature
	heat radiation	temperature
	enthalpy flows through moisture movement	vapor diffusion with phase change and liquid transport flows in the temperature field
	air flow	total pressure, density differentials
vapor transport	gas diffusion	vapor pressure (temperature, total pressure)
	molecular transport (effusion)	vapor pressure
	solution diffusion	vapor pressure
	convection	total pressure gradient
liquid transport	capillary conduction	capillary suction stress
	surface diffusion	relative humidity
	seepage flow	gravitation
	hydraulic flow	total pressure differentials
	electrokinesis	electrical fields
	osmosis	ion concentration

Table 1.1: Heat and moisture transport mechanisms according to (Künzel, 1995)

namely convection–driven, diffusion–driven and hybrid models, see (Schrefler and Lewis, 1998; Černý and Rovnaníková, 2002). The latter one combining moisture diffusion with convective moisture movement into one material model strategy. This model synthesis is

fully described in (Černý and Rovnaníková, 2002) and we focus our attention on the first two mentioned categories representing most widely applied and used in the literature.

1.1 Convection models

The empirical linear relationship describing the liquid flow in saturated porous media was firstly derived by Darcy (Darcy, 1856). He interpreted his experimental data modeling water saturated flow in soils induced by gravity force in common known Darcy's law. This transport schema was further elaborated by Buckingham (Buckingham, 1907) deriving the relations for unsaturated flow and by Richards (Richards, 1931) introducing the Richards equation modeling the water in unsaturated soils. The modeling under non-isothermal conditions was the next logical step in convective moisture analysis. Following promising coupled heat and moisture transport based on Darcy's law were established during the last decades:

- Model of Philip and de Vries, see (Philip and De Vries, 1957) - This convection model of coupled heat and moisture transport was developed on a theory of non-isothermal moisture flow in the liquid and vapor phases. Utilizing Fick's and Darcy's laws the authors formulated the total moisture flux as a sum of vapor and liquid water flux

$$\mathbf{q}_m = \mathbf{q}_w + \mathbf{q}_v, \quad (1.1)$$

where the liquid water flux \mathbf{q}_w is expressed as

$$\mathbf{q}_w = -D_{ww}\nabla w - D_{\theta w}\nabla\theta - K, \quad (1.2)$$

where D_{ww} is the isothermal liquid diffusivity, $D_{\theta w}$ is the thermal liquid diffusivity, K is the unsaturated hydraulic conductivity. In the same sense, vapor flux is expressed by isothermal part driven by the moisture content gradient (∇w) and a thermal part driven by the temperature gradient ($\nabla\theta$) as

$$\mathbf{q}_v = -D_{wv}\nabla w - D_{\theta v}\nabla\theta, \quad (1.3)$$

where D_{wv} and $D_{\theta v}$ are the appropriate diffusivities.

The final balance equations of the Philip and de Vries model for two unknown variables – moisture content w and temperature θ – have the following form:

$$\frac{dw}{dt} = \nabla \cdot [(D_{ww} + D_{wv})\nabla w] + \nabla \cdot [(D_{\theta w} + D_{\theta v})\nabla\theta] + \frac{dK}{dz}, \quad (1.4)$$

$$\rho c \frac{d\theta}{dt} = \nabla \cdot [\lambda \nabla\theta] + h_v \nabla \cdot [D_{wv}\nabla w]. \quad (1.5)$$

- Model of Milly, see (Milly, 1982) - Based on the theory of Philip and de Vries, Milly reformulated the original coupled heat and moisture transport model in a more general way. Instead of moisture content w , matric head is employed as a new variable. According to (Milly, 1982), it brings several advantages such as an incorporation of moisture retention hysteresis and inhomogeneities in the porous structure.

1.2 Diffusion models

The concept of moisture transfer in porous materials based on the diffusion theory started with the derivation of Fick's law by (Fick, 1855). The proposed relation is analogous to Darcy's law and/or Fourier's law and was inspired by the experimental measurements observing the concentrations and fluxes of salt diffusing between two reservoirs through waters tubes. Coupled heat and moisture transport based on the diffusion theory was introduced simultaneously by Krischer (Krischer, 1963) and Luikov (Luikov, 1975). Both works were initially motivated by the modeling of industrial drying processes, and on their basis, many researchers defined own coupled models differing mostly in the description of moisture potential.

- Model of Krischer, see (Krischer, 1963) - Krischer proposed two transport mechanisms for moisture transport, the gradient of partial pressure in the air has been introduced as the driving force for the water vapor transport and the gradient of liquid moisture content as the driving force for the water transport.
- Model of Luikov, see (Luikov, 1975) - Luikov developed an unique model for the simultaneous heat and moisture transfer on the basis of thermodynamics of irreversible processes. His methodology utilized the gradient of total moisture content as the driving force for both transport phenomena. This fact stems from his experimental and theoretical explanation of moisture migration based on the temperature gradient.

$$\rho c \frac{\partial \theta}{\partial t} = \nabla \cdot \left[\left(\lambda + \frac{\varepsilon h_v k_g \zeta}{c_g} \right) \nabla \theta \right] + \nabla \cdot [\varepsilon h_v k_g \zeta \nabla u], \quad (1.6)$$

$$\rho c_g \frac{\partial u}{\partial t} = \nabla \cdot [k_g \nabla u] + \nabla \cdot \left[\left(\frac{k_g \zeta}{c_g} \right) \nabla \theta \right], \quad (1.7)$$

where c is the heat capacity, ε is the ratio of vapor diffusion coefficient to coefficient of total moisture diffusion, k_g is the moisture conductivity, ζ is the thermal gradient coefficient, c_g is the moisture capacity and u is the moisture potential.

- Model of Kiessl, see (Kießl, 1983) - Kiessl developed own version of the diffusion model as an extension of Krischer's model. The proposed modification is based on the introduction of moisture potential Φ as a driving force for moisture movement. This state variable unifies the description of moisture transport in the hygroscopic $\varphi \leq 0.9$ and overhygroscopic $\varphi > 0.9$ intervals. The moisture potential Φ is given by the following formulas

$$\Phi = 1.7 + 0.1 \log r, \quad \varphi > 0.9, \quad (1.8)$$

$$\Phi = \varphi, \quad \varphi \leq 0.9, \quad (1.9)$$

where r is the equivalent radius of pores in material which means that Kiessl's model takes into account shapes and sizes of pore structure. Nevertheless, the definition of moisture potential in the overhygroscopic interval has been established artificially and without any theoretical background, see (Černý and Rovnaníková, 2002).

- Model of Künzle - In view of the fact that we successfully applied this model in the field of multi-scale simulations (Sýkora et al., 2012, 2013), uncertainty propagation (Kučerová et al., 2012; Kučerová and Sýkora, 2013), and modeling of degradation

processes (Sýkora, 2014), we describe in more detail basic assumptions and derivation of model equations. Künzel proposed balance equations based on concepts of Krischer and Kiessl, see (Künzel and Kiessl, 1996). He neglected the liquid water and water vapor convection driven by gravity and total pressure as well as enthalpy changes due to liquid flow and choose relative humidity φ as the only moisture potential. The water vapor diffusion is then described by Fick's law written as

$$\mathbf{g}_v = -\delta_p \nabla (\varphi p_{\text{sat}}), \quad (1.10)$$

where \mathbf{g}_v is the water vapor flux, δ_p is the water vapor permeability of a porous material and $p_{\text{sat}} = p_{\text{sat}}(\theta)$ is the saturation water vapor pressure being exponentially dependent on temperature. The transport of liquid water is assumed in the form of surface diffusion in an absorbed layer and capillary flow typically represented by Kelvin's law

$$\mathbf{g}_w = -D_\varphi \nabla \varphi, \quad (1.11)$$

where \mathbf{g}_w is the flux of liquid water, $D_\varphi = D_w (dw/d\varphi)$ is the liquid conductivity, $D_w = D_w (w/w_f)$ is the liquid diffusivity, $dw/d\varphi$ is the derivative of water retention function and w/w_f is the water content related to the capillary saturation with w_f being the free water saturation. The Fourier law is then used to express the heat flux \mathbf{q} as

$$\mathbf{q} = -\lambda \nabla \theta, \quad (1.12)$$

where λ is the thermal conductivity and θ is the local temperature. Introducing the above constitutive equations into energy and mass conservation equations we finally get

- The energy balance equation

$$\frac{dH}{d\theta} \frac{d\theta}{dt} = \nabla \cdot [\lambda \nabla \theta] + h_v \nabla \cdot [\delta_p \nabla (\varphi p_{\text{sat}})], \quad (1.13)$$

- The conservation of mass equation

$$\frac{dw}{d\varphi} \frac{d\varphi}{dt} = \nabla \cdot [D_\varphi \nabla \varphi] + \nabla \cdot [\delta_p \nabla (\varphi p_{\text{sat}})], \quad (1.14)$$

where H is the enthalpy of moist building material and h_v is the evaporation enthalpy of water. The second term on the right hand side of Eq. (1.13) represents the change of enthalpy due to phase transition being considered the only heat source or sink. The applicability of Künzel's model is demonstrated in the following case study depicted in Fig. 1.2. This figure displays temperature and moisture profiles and also evolutions of temperature and relative humidity in a particular point of the structural domain obtained from different experimental measurements. It can be seen relatively good correspondence with results calculated with the help of Künzel's equations. The description of this comparison and other details related to the geometrical and material inputs are published in (Sýkora et al., 2013).

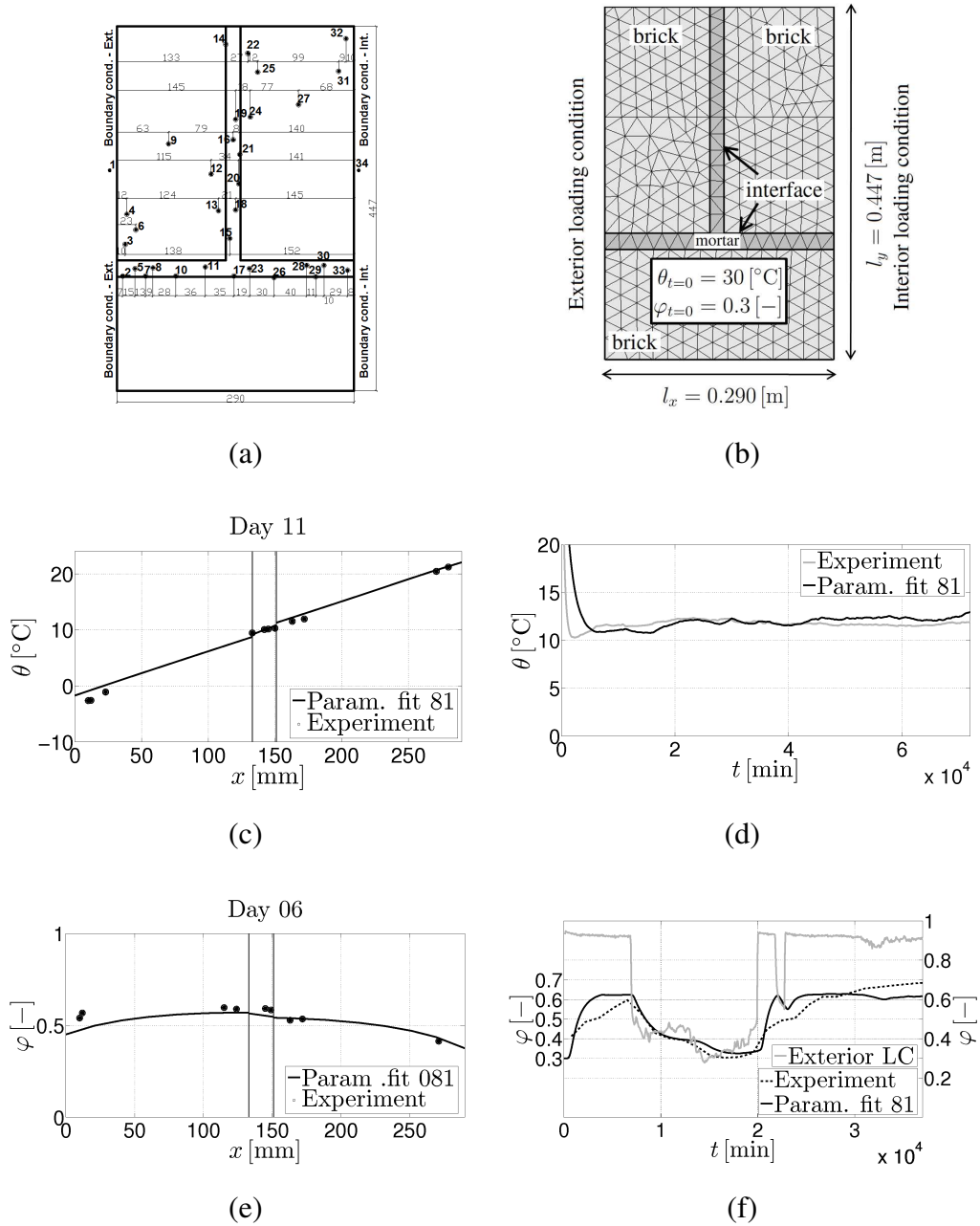


Figure 1.2: (a) Geometry of the masonry block with positions of sensors; (b) Finite element mesh with applied loading; (c) Calculated and measured temperature profile in chosen sensors corresponding to 11th day; (d) Evolution of temperature obtained numerically for optimal data and from experiment in sensor No. 12; (e) Calculated and measured relative humidity profile in chosen sensors corresponding to 6th day; (f) Evolution of relative humidity obtained numerically for optimal data and from experiment in sensor No. 14

1.3 Advanced models

The group of advanced models in the realm of civil engineering is the special type of coupled heat and moisture transport models² extended by another physical and/or chemical phenomena. These multi-model strategies expanded to many fields ranging from salt crystallization (Koniarczyk and Gawin, 2011; Castellazzi et al., 2013; Derluyn et al., 2014; Koniarczyk et al., 2018), fire-induced spalling (Tenchev et al., 2001a; Davie et al., 2006; Gawin et al., 2011a; Dauti et al., 2018), hygroexpansion in wooden structures (Konopka and Kaliske, 2018; Huč et al., 2018; Fortino et al., 2019), pyrolysis (Janssens, 2004; Lautenberger and Fernandez-Pello, 2009; Moghtaderi, 2006; Shi and Chew, 2013), stone decay caused by air pollution (Saba et al., 2018; Ali et al., 2007; Giavarini et al., 2008), degradation processes in concrete – carbonation process (Isgor and Razaqpur, 2004; Song et al., 2006; Talukdar et al., 2012) – chloride diffusion (Saetta et al., 1993; Shafikhani and Chidiac, 2019; Fenaux et al., 2019) – decalcification (Glasser et al., 2008), and many others, see (Choo and Sun, 2018; Huang et al., 2018; Yin et al., 2018). Of course, such problems in their full generality are far too complex to be solved completely within this work. Therefore, the emphasis is given to the physical problems related to our work done during the past ten years. In the following sections, we present modeling strategies focusing on (i) modeling of transport processes in wood structures, (ii) modeling of the impact of fire on concrete, and (iii) modeling of damage caused by ice crystallization process.

1.3.1 Modeling of transport processes in wood structures

Structures made of wood - termed the light weight constructions - are a promising alternative to traditional concrete/masonry constructions approaches. On the other hand, the service life of structures made of wood is strongly affected by moisture content inside the material. Changes in moisture content induce dimensional changes like shrinkage and swelling. Furthermore, biological pathogenic degradation depends on the presence of water, reduced thermal performance of building components and other undesired processes. Numerical models have been developed to simulate hygrothermal behavior of building envelopes. These simulation tools take into account fundamental transport phenomena of heat, air and moisture, two-dimensional and three-dimensional aspects and different moisture sources, such as wind-driven rain, rising damp, etc., see (Desta et al., 2011; Langmans et al., 2012b,a; Remki et al., 2012; Thoemen et al., 2008; Younsi and Kocafe, 2006).

Moisture transport in wood structures is a diffusion process, see (Eitelberger and Hofstetter, 2011b). Three phases of water as diffusing substances can be distinguished in wood: free water and water vapor in the lumens, as well as bound water in the cell walls (Eitelberger et al., 2011). The standard formulation of moisture transport in wood structures grounds on the work presented in (Frandsen et al., 2007) and further extended in (Eitelberger and Hofstetter, 2011b) to account for thermal effects. The stepping stone is the condition below the fiber saturation point³. In such a case the moisture transport in wood structures exposed to air is a diffusion process described mainly by three phenomena, see Fig. 1.3: (i)

² It has to be pointed out that a large majority of utilized transport models is based on the phenomenological description of moisture movement.

³ Fiber saturation point corresponds to moisture content at which the cell walls are saturated with bound water with no free water in the lumens.

transport of water vapor in lumens, (ii) transport of bound water in cell walls and (iii) the balance between two water phases introduced as a sorption rate. The phase changes between these two states of water generate energy changes which need to be taken into account. All these phenomena are combined in (Eitelberger and Hofstetter, 2011b) in the coupled heat and moisture transport in wood.

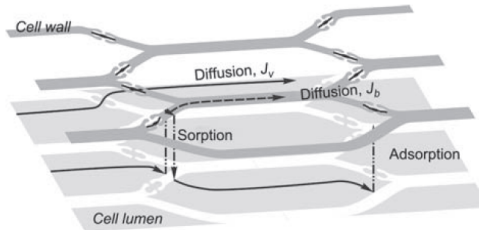


Figure 1.3: Various time-dependent processes responsible for moisture transport in the cellular structure of wood. From Frandsen, H. L., Damkilde, L., and Svensson, S. (2007). A revised multi-Fickian moisture transport model to describe non-Fickian effects in wood. *Holzforschung*, 61(5):563–572

Due to more suitable physical description of moisture transport in wood and hierarchical structure, the multiscale framework has become a preferred technique in the modeling of moisture transport in wood structures, see. (Eitelberger and Hofstetter, 2011b,a; Eitelberger et al., 2011). The macroscopic mathematical description of transport processes involves effective material properties derived from multiscale homogenization approach. Currently, two main approaches are available: (i) computational homogenization, (Šýkora et al., 2012, 2013), and (ii) effective media theories, (Vorel and Šejnoha, 2009; Zeman and Šejnoha, 2001, 2007). While the first class of methods studies the distribution of local fields within a typical heterogeneity pattern using a numerical method, the second group estimates the response analytically on the basis of limited geometrical information (e.g. the volume fractions of constituents) of the analyzed medium. The practical applicability of both approaches to a number of real engineering problems showing both their advantages and drawbacks is available in (Šejnoha and Zeman, 2013).

As an illustration, the presented example, see (Šejnoha et al., 2019) for more details, is devoted to the matching the moisture uptake in the cup experiments carried out for different directions and thicknesses of wood specimens. Four loading scenarios representing the steps in relative humidities ((i) $\varphi : 0 \rightarrow 0.2$, (ii) $\varphi : 0.2 \rightarrow 0.4$, (iii) $\varphi : 0.4 \rightarrow 0.6$ and (iv) $\varphi : 0.6 \rightarrow 0.8$) were examined for each thickness of wood sample and for two different principal material direction, namely longitudinal and tangential. The Fig. 1.4 depicts the comparisons carried out for the longitudinal principal direction with thicknesses 10 mm and 4 mm of wood specimens and the tangential principal direction with thickness 6 mm, respectively. It is apparent from this figure that computed moisture contents match the experimentally obtained moisture uptakes relatively accurately. Such good agreement can be found in all computed results.

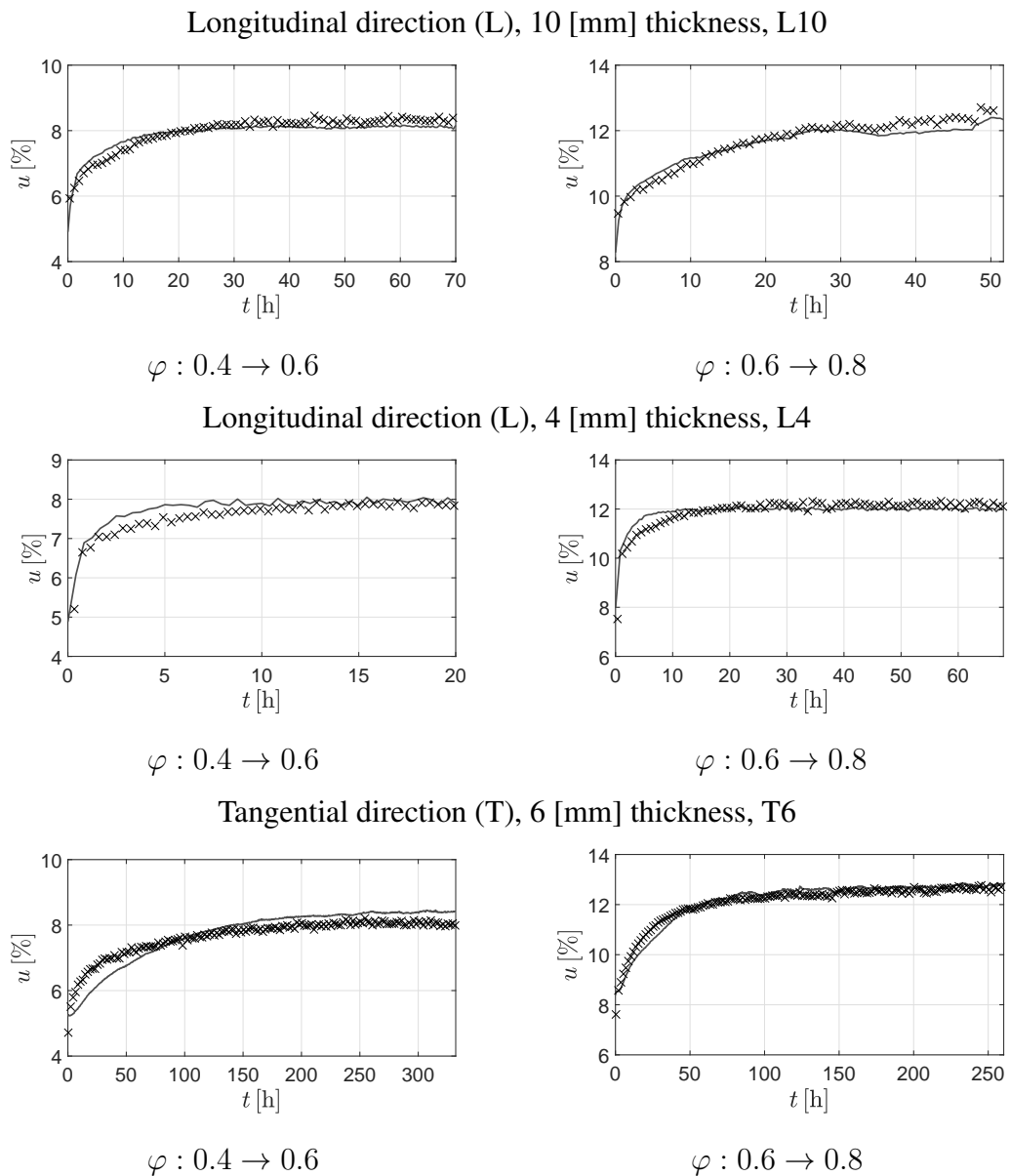


Figure 1.4: Simulated moisture uptake (dotted line) compared to experimental observation (solid line)

1.3.2 Modeling of impact of fire on concrete

Again, there is a variety of elaborate papers on this topic, e.g. (Tenchev et al., 2001b; Davie et al., 2006; Dwaikat and Kodur, 2009; Davie et al., 2012, 2014; Majorana et al., 2015). In the first part of the paper by Gawin et al., see (Gawin et al., 2011a), the physical phenomena, and the heat and mass flux and sources in a concrete element were studied. Then, the mathematical model of concrete was presented and all constitutive relations of the model were summarized and discussed. In part 2, see (Gawin et al., 2011b), a literature review of the existing models of concrete at high temperatures and a summary of their main features were presented. To evaluate the difference between the results obtained with simplified models

and the very complex one proposed in Part 1, an extensive numerical study was performed. In quest for a cogent yet effective model which would be less demanding for computer time, with regard to probabilistic calculations, a special combination of models originally proposed by Bažant–Thonguthai (Bažant and Thonguthai, 1979) and Künzel and Kiessl (Künzel and Kiessl, 1996) is presented in (Sýkora et al., 2018). The mathematical aspects of a coupled model based on similar assumptions in (Sýkora et al., 2018) were discussed in (Beneš et al., 2013). It is relatively simple, and despite the fact that cross-effects between heat and mass fluxes are missing, it describes all substantial phenomena and its results comply well with experimentally obtained data. The only exception is a certain discrepancy in the prediction of temperature distribution after long-range fire exposure (over 3 hours). It is assumed to be the consequence of the model simplification, neglecting the effect of the dry air pressure which dominates the water vapor pressure after the maximum of the gas pressure has been overstepped. When calibrating the model against the experiments carried out in the furnace, the findings of Davie et al. (Davie et al., 2012) have to be taken into consideration. It was proved that the most significant of all were the relationships chosen to define the relative permeabilities. These were shown to strongly control the results of analyses of both low and high temperature problems and to potentially imply apparently different permeability values for the same concrete.

Due to the lack of information on the prediction of fire-induced spalling for reasons described in (Dwaikat and Kodur, 2009), the conservative engineering approach is currently used methodology, see (Beneš et al., 2013). It defines the occurrence of fire-induced spalling as a certain threshold when the pore pressure weighted by porosity exceeds the temperature-dependent tensile strength, $f_t(\theta)$ [Pa]:

$$\phi p \geq f_t(\theta), \quad (1.15)$$

where $\phi [-]$ is the porosity. When fire-induced spalling, governed here solely by Eq. (1.15), occurs in a certain part of the investigated domain, this part is removed from the analysis and boundary conditions are applied to a new free boundary surface,

1.3.3 Modeling of damage caused by ice crystallization process

High moisture content in building material and its phase changes are often a cause of internal damage. Understanding the hydro-thermo-mechanical behavior of building materials exposed to weather conditions is the first step toward avoiding deterioration of historical monuments and/or buildings. Because of variable climatic conditions, moisture gradients induce mechanical stresses in the porous material. These stresses mostly develop due to the growth of ice crystals through the pore structure; therefore, there is a strong need for investigating the influence of moisture on the mechanical material behavior, which leads to a numerical and experimental coupling of mechanical and heat and moisture transport phenomena.

In the literature, above-mentioned problem has been addressed from several perspectives. Analysis of coupled heat and moisture transport reflecting the moisture migration under the conditions of the ice crystal formation in the pore structure was published for example in (Kong and Wang, 2011; Künzel and Kiessl, 1996; Tan et al., 2011). While models for transport processes have been developed during several decades (see Sec. 1.1 and 1.2), the theory of ice crystallization in the pores has emerged only recently, (Coussy and Monteiro, 2007, 2008; Fagerlund, 1973; Matala, 1995; Scherer, 1993, 1999; Sun and Scherer,

2010; Wardeh and Perrin, 2008; Zuber and Marchand, 2000). The authors established relations between physical state of porous system and pore pressures. An ice formation process was introduced as a thermodynamic balance equation between ice, liquid water, and a solid matrix. To be more specific, let us consider spherical liquid-ice interface at the entrance of the pore and cylindrical shape of the pore. Two interface equilibrium conditions are assumed to describe the interaction between ice crystals and pore walls. The Laplace relation is applicable to control the interface between the ice crystal and the liquid water:

$$p_i - p_l = \frac{2\gamma_{li}}{r_{ir}(\theta)}, \quad (1.16)$$

where p_l [Pa] is the liquid pressure, p_i [Pa] is the pressure in the ice crystal and r_{ir} [m] is the curvature radius of ice crystal (liquid-ice interface) formed at a given temperature. The second interface relation is expressed in the form of mechanical equilibrium between the ice crystal and the pore pressure exerted by the ice crystal, p_p [Pa], as

$$p_i - p_p = \frac{\gamma_{li}}{r - r_{ar}(\theta)}, \quad (1.17)$$

where r_{ar} [m] is the layer of adsorbed water which cannot freeze during crystallization process. Finally, combining Eq. (1.16) and Eq. (1.17), we can write

$$p_p = p_l + \chi(r, \theta), \quad (1.18)$$

where $\chi(r, \theta)$ [Pa] is the local pressure on the frozen pore walls due to the ice formation and it is characterized by following relation, see Multon et al. (2012); Zuber and Marchand (2000),

$$\chi(r, \theta) = \gamma_{li} \left(\frac{2}{r_{ir}(\theta)} - \frac{1}{r - r_{ar}(\theta)} \right). \quad (1.19)$$

Mechanical response of porous media subjected to the frost action has been studied by several authors (Coussy and Monteiro, 2008; Wardeh and Perrin, 2008; Zuber and Marchand, 2000). Biot's continuum model adopted in the poroelasticity formulation representing an efficient method for elastic modeling of a porous system subjected to the pressure of the fluid. Moreover, a novel micromechanics approach was introduced to analyze the creation of microcracks in the microstructure during freezing process (Koster, 2010; Liu et al., 2011). These results predict effective mechanical and transport properties at microscopic level and can be utilized as an input for multi-scale analysis of porous media.

1.4 Inverse problems

In computational mechanics one tries to model a real *system* A , where system *parameters* q , a *loading* f and a system *response* u are related as

$$A(u; q) = f. \quad (1.20)$$

The goal here is to obtain the response of the system for given parameters and loading conditions. In the field of inverse analysis, the goal is to find the values of system parameters q corresponding to given loading conditions f and experimental observations z . Therefore,

one uses the numerical model of the system A and derives a so-called *observation operator* Y mapping the response u given parameters q and loading f to observed quantities z

$$Y(q, f) = z. \quad (1.21)$$

The subject of this work is primarily concerned with the description of coupled heat and moisture transport in porous materials and the system parameters q are related here to the material behavior. Material parameters are usually determined in the context of a chosen experimental setup, where the loading conditions are fixed, hence, the loading f is assumed to be constant in the following text. When simulating some real experiment, the model response is usually not equal to measured data because of experimental errors or imperfection of the numerical model itself. It is often difficult to distinguish these sources of errors and they are described together in error vector ϵ , so Eq. (1.21) becomes

$$Y(q) + \epsilon = z. \quad (1.22)$$

In general, the estimation of material properties from experimental measurements is an ill-posed problem because of issues related to the existence of a solution and uniqueness. Small variations in measured data can also result in large changes in a solution and this affects the stability of a problem, see (Marzouk and Najm, 2009). Traditional approaches have used regularization methods to impose well-posedness and to search for deterministic solutions, mostly by employing optimization techniques, see (Havelka and Sýkora, 2018). It can be further divided into linearisation based methods, e.g. back-projection (Santosa and Vogelius, 1990; Berenstein and Casadio, 1991), Calderón's approach (Blue et al., 2000), moment methods (Allers and Santosa, 1991) and Newton family methods (Blue, 1997; Mueller et al., 2001; Cheney et al., 1990), which all are based on the assumption of small perturbations of the parameter field and non-iterative fully non-linear methods, e.g. layer stripping (Somersalo et al., 1991), scattering transform, i.e. D-Bar or $\bar{\partial}$ methods (Siltanen et al., 2000; Knudsen et al., 2009; Bikowski et al., 2010). Besides, a variety of techniques is available to identify material parameters via soft-computing methods, see e.g. (Mahnken, 2004). According to (Kučerová et al., 2009), the gradient-based methods are usually considered to be the most computationally efficient soft-computing algorithms and have been successfully used in a variety of identification problems, e.g. (Iacono et al., 2006; Mahnken and Stein, 1996). For a comprehensive overview, we refer an interested reader to highly cited reference (Tarantola, 2005).

1.4.1 Bayesian updating of uncertainties

Another possibility is casting the inverse problem in a probabilistic setting, see (Rosić et al., 2013). Bayesian inference is the statistical inference in which the experimental observations are not used as the only source of information, but they are used to update the preliminary probabilistic description of system - the so-called prior information - to give the posterior distribution Kennedy and O'Hagan (2001). Recall that in realistic applications, observations are noisy, uncertain and limited in number relative to the dimension or complexity of the model space. Also, the model of a system may have limitations on its predictive value because of its imprecision, filtering or smoothing effects. Taking into account all pertinent uncertainties, the process of material properties estimation cannot lead to a single 'optimal'

parameter set, but one has to find a probability distribution of parameters that represents the knowledge about parameter values. The Bayesian setting for the inverse problems offers a rigorous foundation for inference from noisy data and uncertain forward models, a natural mechanism for incorporating prior information, and a quantitative assessment of uncertainty in the inferred results summarizing all available information about the unknown quantity Tarantola (2005). Besides, unlike other techniques that aim to regularize the ill-posed inverse problem to achieve a point estimate, the Bayesian method treats the inverse problem as a well-posed problem in an expanded stochastic space.

The Bayesian approaches to inverse problems have received much recent interest since increasing performance of modern computers and clusters enables exhaustive Monte Carlo computations. Among recent applications one can cite applications in computational mechanics (Rosić and Matthies, 2013; Adeli et al., 2019), environmental modeling (Yee et al., 2008; Humphries et al., 2012; Jing et al., 2018), hydrology (Fu and Gómez-Hernández, 2009; Chen et al., 2018; Moreira et al., 2016) or heat transfer (Parthasarathy and Balaji, 2008; Kučerová and Sýkora, 2013; Kučerová et al., 2012; Rosić et al., 2013). We review this approach below; for more extensive introductions, see (Tarantola, 2005; Gelman et al., 2013).

In the probabilistic setting, material parameters \mathbf{q} as well as observations \mathbf{z} and also the response of forward operator $Y(\cdot)$ are considered as random variables and/or random fields. Therefore, we introduce the following notation. We consider a set Ω of random elementary events ω together with σ -algebra \mathcal{S} to which a real number in the interval $[0, 1]$ may be assigned, the probability of occurrence - mathematically a measure \mathbb{P} . In the Bayesian setting, we assume three sources of information and uncertainties, which should be taken into account. The first one is our prior knowledge about the model/material parameters $\mathbf{q}(\omega)$, which is represented by defining the prior density function $p_{\mathbf{q}}(\mathbf{q})$. Prior models may embody simple constraints on \mathbf{q} , such as a range of feasible values, or may reflect more detailed knowledge about the parameters, such as correlations or smoothness. Another source of information comes from measurements, which are violated by uncertain experimental errors $\epsilon(\bar{\omega})$. Last uncertainty arises from imperfection of the numerical model included in the observation operator $Y(\cdot)$, when for example our description of the real system A does not include all important phenomena and therefore the forward operator response $Y(\cdot, \bar{\omega})$ can be assumed as uncertain. The probabilistic formulation of Eq. (1.22) now becomes

$$\mathbf{z} = Y(\mathbf{q}(\omega), \bar{\omega}) + \epsilon(\bar{\omega}). \quad (1.23)$$

If modeling uncertainties $\bar{\omega}$ cannot be neglected, they can be described by conditional probability density $p(\mathbf{z}|\mathbf{q})$ for predicted data \mathbf{z} and given model parameters \mathbf{q} . If these uncertainties can be neglected, only model parameters $\mathbf{q}(\omega)$ and observations $\mathbf{z}(\bar{\omega})$ remain uncertain. In practise, it is sometimes difficult to distinguish the imperfection of the system description A from measurement error ϵ . Hence modeling uncertainties $\bar{\omega}$ can be hidden in measuring error $\epsilon(\bar{\omega})$. Finally, for noisy measurements we define the last probability density $p_{\mathbf{z}}(\mathbf{z})$.

To update our prior knowledge about model parameters we must include measurements with our theoretical knowledge. The Bayesian update is based on the idea of Bayes' rule defined for probabilities. Definition of Bayes' rule for continuous distribution is, however, more problematic and hence (Tarantola, 2005, Chapter 1.5) derived the posterior state of information $\pi(\mathbf{q}, \mathbf{z})$ as a conjunction of all information at hand

$$\pi(\mathbf{q}, \mathbf{z}) = \kappa p_{\mathbf{q}}(\mathbf{q}) p_{\mathbf{z}}(\mathbf{z}) p(\mathbf{z}|\mathbf{q}), \quad (1.24)$$

where κ is a normalization constant.

The posterior state of information defined in the space of model parameters \mathbf{q} is given by the marginal probability density

$$\pi_{\mathbf{q}}(\mathbf{q}) = \mathbb{E}_{\bar{\omega}} [\pi(\mathbf{q}, \mathbf{z})] = \kappa p_{\mathbf{q}}(\mathbf{q}) \int_{\bar{\Omega}} p(\mathbf{z}|\mathbf{q}) p_{\mathbf{z}}(\mathbf{z}) \mathbb{P}(d\bar{\omega}) = \kappa p_{\mathbf{q}}(\mathbf{q}) L(\mathbf{q}), \quad (1.25)$$

where $\bar{\Omega}$ is a set of random elementary events $\bar{\omega}$ and measured data \mathbf{z} enters through the *likelihood function* $L(\mathbf{q})$, which gives a measure of how good a forward operator $\mathbf{Y}(\mathbf{q})$ is in explaining the data \mathbf{z} . Here, $\mathbb{E}_{\bar{\omega}}$ is the expectation operator averaging over $\bar{\Omega}$.

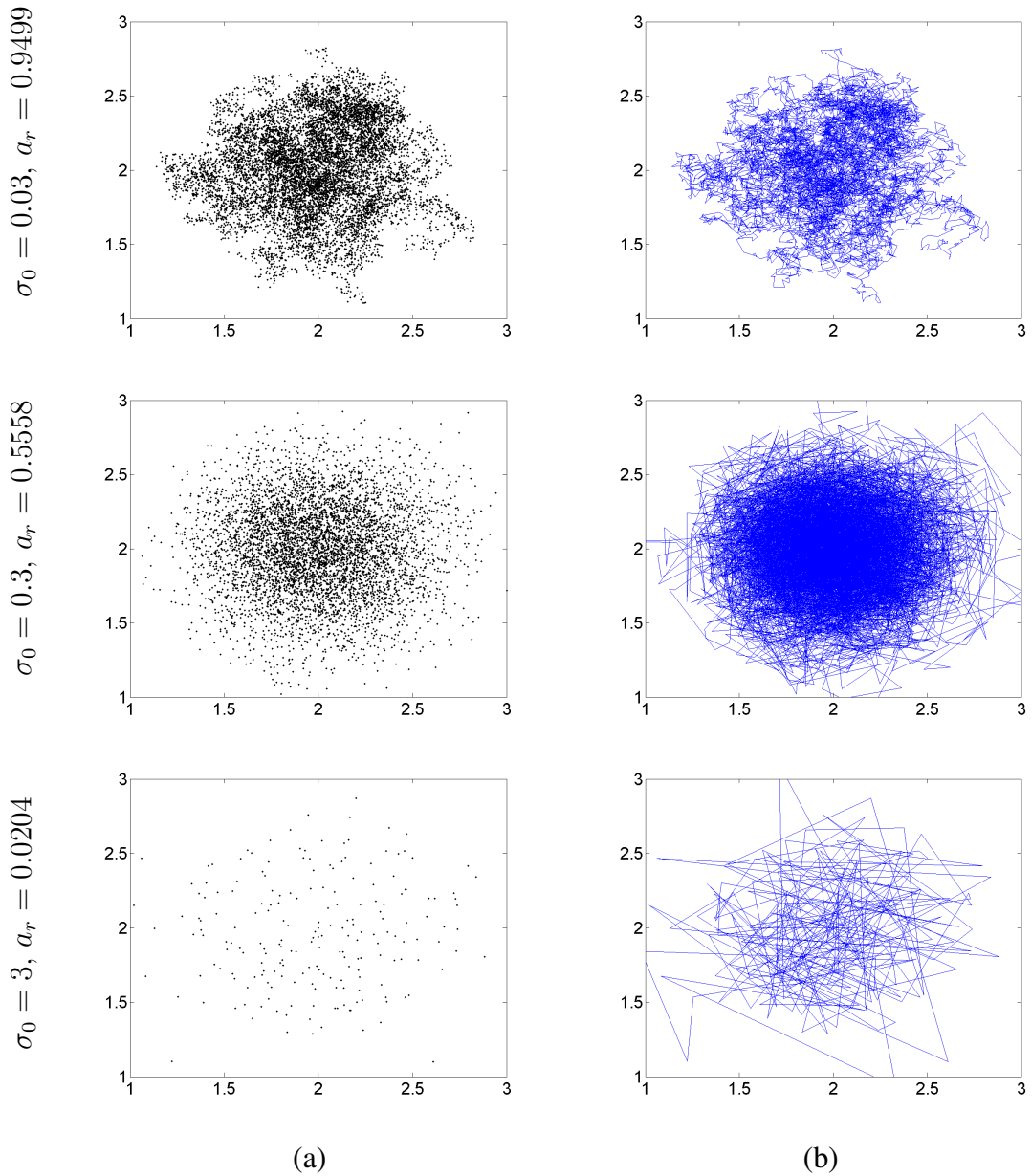


Figure 1.5: Random walker sampling: (a) Set of samples; (b) Sequence of walks

To keep the presentation of different numerical aspects of particular methods clear and transparent, we focus here on a quite common and simple case, where modeling-uncertainties

are neglected and measurement errors are assumed to be Gaussian. Then the likelihood function takes the form

$$L(\mathbf{q}) = \kappa \exp \left(-\frac{1}{2} (\mathbf{Y}(\mathbf{q}) - \mathbf{z})^T C_{\text{obs}}^{-1} (\mathbf{Y}(\mathbf{q}) - \mathbf{z}) \right), \quad (1.26)$$

where C_{obs} is a covariance among measurements \mathbf{z} .

The primary computational challenge in Bayesian inference is based on extracting information from the posterior density. Most estimates take the form of expectations w.r.t. the posterior. These expectations, mathematically integrals, may be numerically evaluated via asymptotic, deterministic, or sampling methods. Nowadays, Markov chain Monte Carlo (MCMC) methods remain the most general, flexible, and wide-spread techniques employed. To be more specific, the Metropolis-Hastings algorithm is the most common method for obtaining a sequence of random samples from a probability distribution, see Gelman et al. (2013). The basic principle relies on performing a random walk to sample the prior probability distribution and then apply an appropriate probabilistic rule to accept or reject samples for obtaining the resulting set of accepted walks sampling the posterior distribution, see Kučerová et al. (2012). To demonstrate the effect of proposal standard deviation, Fig. 1.5 shows the resulting sets of samples and the sequence of random walks for three different values of σ_0 – standard deviation of proposal distribution. To make it clearly visible, the two-dimensional distribution was chosen as the desired prior distribution with the same mean value $\mu_m = 2$ and standard deviation $\sigma_m = 0.3$ for both dimensions. The figure includes also the information about the acceptance rate a_r . It is visible that the acceptance rate for a high value of proposal standard deviation is very low. As a consequence, a lot of proposed walks are rejected and the last position of the random walker is copied into the set instead. Therefore it seems that the final number of samples is smaller than in other cases, because a lot of samples are multiple. Therefore, also the correlation among the samples start to increase for very high values of proposal standard deviation.

The illustrative example presents a Bayesian identification of a homogeneous material property - thermal conductivity, which is considered as uncertain. Since the Bayesian inference consists of a posterior distribution sampling, it is profitable to replace the expensive simulation of a forward model (finite element model) by its cheaper approximation (surrogate model). Polynomial chaos approximation is used here as an appropriate tool to overcome this problem. The whole concept is demonstrated on a very simple example of stationary heat conduction, where interesting phenomena can be clearly understood, see Fig. 1.6. The detailed description and other information about numerical and sampling procedures are published in (Kučerová and Matthies, 2010). From the figure, we can conclude that polynomial chaos expansion is a powerful approximation tool. In the presented application, fifth-degree polynomial is sufficient to describe the nonlinear relation of model response with good precision. Furthermore, polynomial chaos approximation enables more efficient Bayesian identification of model parameters. Savings in the computational time increases with the complexity of the model or especially with finer finite element discretization.

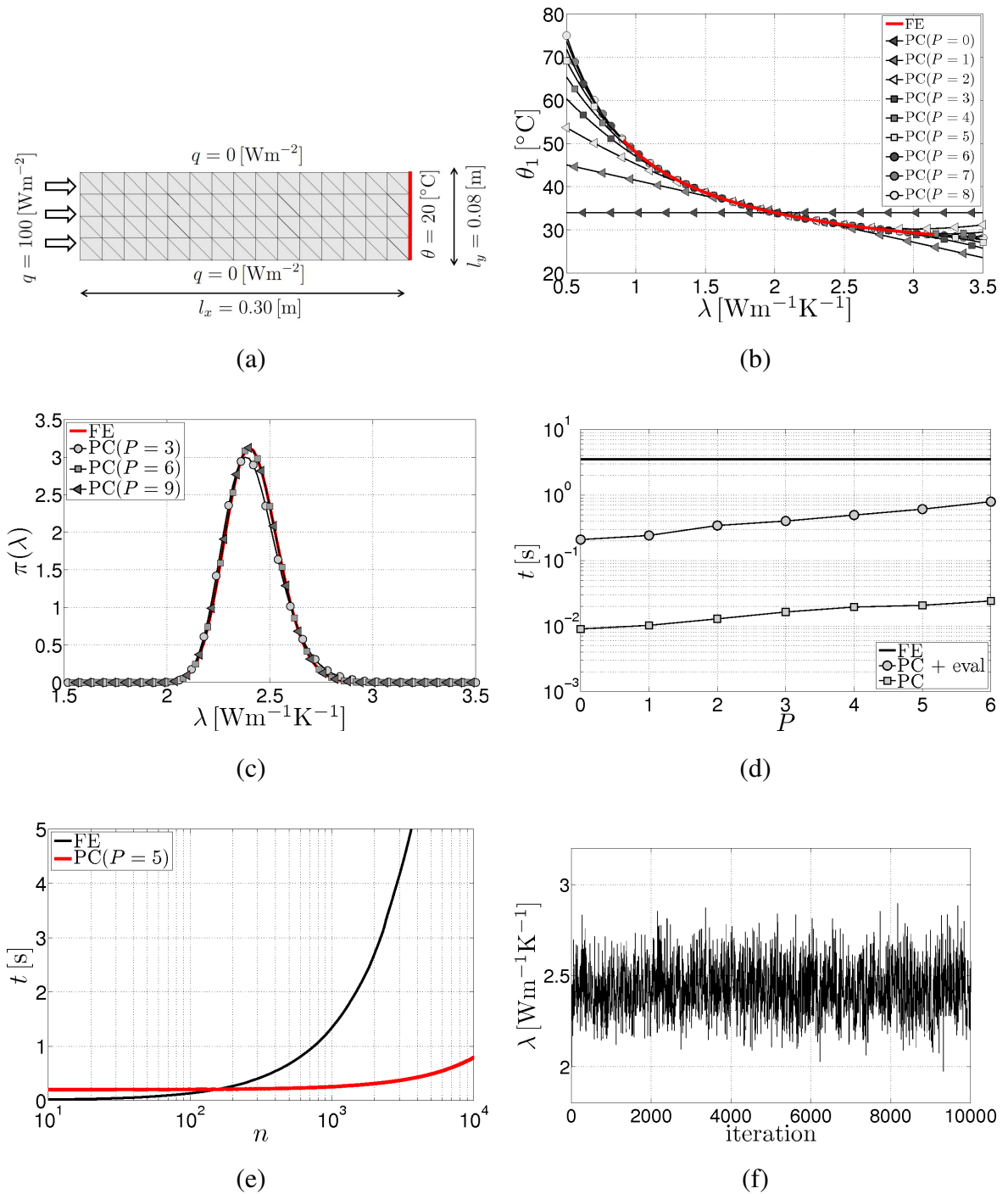


Figure 1.6: (a) Domain setup; (b) Polynomial chaos approximation of temperature θ_1 , $\theta_1(x = 0.02 \text{ m}, y = 0.06 \text{ m})$; (c) Posterior probability density functions calculated for different surrogate models and finite element model; (d) Comparison of time requirements for 1000 computations of system response; (e) Time requirements for n evaluations of system response computed by direct finite element simulation and polynomial chaos with order $P = 5$; (f) Markov chain over 10000 iterations

References

- Adeli, E., Matthies, H. G., Reinstädler, S., and Dinkler, D. (2019). Comparison of bayesian methods on parameter identification for a viscoplastic model with damage. *Journal of Computational Mechanics*.
- Alì, G., Furuholt, V., Natalini, R., and Torricollo, I. (2007). A mathematical model of sulphite chemical aggression of limestones with high permeability. part i. modeling and qualitative analysis. *Transport in Porous Media*, 69(1):109–122.
- Allers, A. and Santosa, F. (1991). Stability and resolution analysis of a linearized problem in electrical impedance tomography. *Inverse problems*, 7(4):515.
- Bažant, Z. P. and Thonguthai, W. (1979). Pore pressure in heated concrete walls: theoretical prediction. *Magazine of Concrete Research*, 31(107):67–76.
- Beneš, M., Štefan, R., and Zeman, J. (2013). Analysis of coupled transport phenomena in concrete at elevated temperatures. *Applied Mathematics and Computation*, 239:7262–7274.
- Berenstein, C. A. and Casadio, T. E. (1991). Inversion formulas for the k -dimensional radon transform in real hyperbolic spaces. *Duke Mathematical Journal*, 62(3):613–631.
- Bikowski, J., Knudsen, K., and Mueller, J. L. (2010). Direct numerical reconstruction of conductivities in three dimensions using scattering transforms. *Inverse Problems*, 27(1):015002.
- Blue, R. (1997). *Real-time three-dimensional electrical impedance tomography*. Phd thesis, R.P.I, Troy.
- Blue, R. S., Isaacson, D., and Newell, J. C. (2000). Real-time three-dimensional electrical impedance imaging. *Physiological measurement*, 21(1):15.
- Buckingham, E. (1907). Studies on the movement of soil moisture. *US Dept. Agric. Bur. Soils Bull.*, 38.
- Castellazzi, G., Colla, C., De Miranda, S., Formica, G., Gabrielli, E., Molari, L., and Ubertini, F. (2013). A coupled multiphase model for hygrothermal analysis of masonry structures and prediction of stress induced by salt crystallization. *Construction and Building Materials*, 41:717–731.
- Chen, M., Izady, A., Abdalla, O., and Amerjeed, M. (2018). A surrogate-based sensitivity quantification and bayesian inversion of a regional groundwater flow model. *Journal of Hydrology*, 557:826–837. cited By 5.
- Cheney, M., Isaacson, D., Newell, J. C., Simske, S., and Goble, J. (1990). NOSER: An algorithm for solving the inverse conductivity problem. *International Journal of Imaging Systems and Technology*, 2(2):66–75.

- Choo, J. and Sun, W. (2018). Cracking and damage from crystallization in pores: Coupled chemo-hydro-mechanics and phase-field modeling. *Computer Methods in Applied Mechanics and Engineering*, 335:347–379.
- Coussy, O. and Monteiro, P. (2007). Unsaturated poroelasticity for crystallization in pores. *Computers and Geotechnics*, 34(4):279–290.
- Coussy, O. and Monteiro, P. (2008). Poroelastic model for concrete exposed to freezing temperatures. *Cement and Concrete Research*, 38(1):40–48.
- Černý, R. and Rovnaníková, P. (2002). *Transport Processes in Concrete*. London: Spon Press.
- Darcy, H. P. G. (1856). *Les Fontaines publiques de la ville de Dijon. Exposition et application des principes à suivre et des formules à employer dans les questions de distribution d'eau, etc.* V. Dalmont.
- Dauti, D., Dal Pont, S., Weber, B., Briffaut, M., Toropovs, N., Wyrzykowski, M., and Sciumé, G. (2018). Modeling concrete exposed to high temperature: Impact of dehydration and retention curves on moisture migration. *International Journal for Numerical and Analytical Methods in Geomechanics*, 42(13):1516–1530.
- Davie, C. T., Pearce, C. J., and Bićanić, N. (2006). Coupled heat and moisture transport in concrete at elevated temperatures—effects of capillary pressure and adsorbed water. *Numerical Heat Transfer Part A: Applications*, 49(8):733–763.
- Davie, C. T., Pearce, C. J., and Bićanić, N. (2012). Aspects of permeability in modelling of concrete exposed to high temperatures. *Transport in Porous Media*, 95(3):627–646.
- Davie, C. T., Pearce, C. J., and Bićanić, N. (2014). Fully coupled, hygro-thermo-mechanical sensitivity analysis of a pre-stressed concrete pressure vessel. *Engineering Structures*, 59:536–551.
- de Boer, R. (2000). Contemporary progress in porous media theory. *Applied Mechanics Reviews*, 53(12):323–370.
- Derluyn, H., Moonen, P., and Carmeliet, J. (2014). Deformation and damage due to drying-induced salt crystallization in porous limestone. *Journal of the Mechanics and Physics of Solids*, 63:242–255.
- Desta, T. Z., Langmans, J., and Roels, S. (2011). Experimental data set for validation of heat, air and moisture transport models of building envelopes. *Building and Environment*, 46:1038–1046.
- Dwaikat, M. B. and Kodur, V. K. R. (2009). Hydrothermal model for predicting fire-induced spalling in concrete structural systems. *Fire Safety Journal*, 44:425–434.
- Eitelberger, J., Hofstetter, H., and Dvinskikh, S. V. (2011). A multi-scale approach for simulation of transient moisture transport processes in wood below the fiber saturation point. *Composites Science and Technology*, 71:1727–1738.

- Eitelberger, J. and Hofstetter, K. (2011a). A comprehensive model for transient moisture transport in wood below the fiber saturation point: Physical background, implementation and experimental validation. *International Journal of Thermal Sciences*, 50:1861–1866.
- Eitelberger, J. and Hofstetter, K. (2011b). Prediction of transport properties of wood below the fiber saturation point – A multiscale homogenization approach and its experimental validation. Part ii: Steady state moisture diffusion coefficient. *Composites Science and Technology*, 71:145–151.
- Fagerlund, G. (1973). Determination of pore-size distribution from freezing-point depression. *Materials and Structures*, 6(3):215–225.
- Fenaux, M., Reyes, E., Gálvez, J., and Moragues, A. (2019). Modelling the transport of chloride and other ions in cement-based materials. *Cement and Concrete Composites*, 97:33–42.
- Fick, A. (1855). Ueber diffusion. *Annalen der Physik*, 170(1):59–86.
- Fortino, S., Hradil, P., and Metelli, G. (2019). Moisture-induced stresses in large glulam beams. case study: Vihantasalmi bridge. *Wood Material Science & Engineering*, 14(5):366–380.
- Frandsen, H. L., Damkilde, L., and Svensson, S. (2007). A revised multi-Fickian moisture transport model to describe non-Fickian effects in wood. *Holzforschung*, 61(5):563–572.
- Fu, J. and Gómez-Hernández, J. J. (2009). Uncertainty assessment and data worth in groundwater flow and mass transport modeling using a blocking Markov chain Monte Carlo method. *Journal of Hydrology*, 364(3–4):328–341.
- Gawin, D., Pesavento, F., and Schrefler, B. A. (2011a). What physical phenomena can be neglected when modelling concrete at high temperature? A comparative study. Part 1: Physical phenomena and mathematical model. *International Journal of Solids and Structures*, 48:1927–1944.
- Gawin, D., Pesavento, F., and Schrefler, B. A. (2011b). What physical phenomena can be neglected when modelling concrete at high temperature? A comparative study. Part 2: Comparison between models. *International Journal of Solids and Structures*, 48:1945–1961.
- Gelman, A., Carlin, J., Stern, H. S., Dunson, D., Vehtari, A., and Rubin, D. (2013). *Bayesian data analysis*. Chapman and Hall/CRC.
- Giavarini, C., Santarelli, M., Natalini, R., and Freddi, F. (2008). A non-linear model of sulphation of porous stones: Numerical simulations and preliminary laboratory assessments. *Journal of Cultural Heritage*, 9(1):14–22.
- Glasser, F. P., Marchand, J., and Samson, E. (2008). Durability of concrete—degradation phenomena involving detrimental chemical reactions. *Cement and Concrete Research*, 38(2):226–246.

- Hassanizadeh, M. and Gray, W. G. (1979a). General conservation equations for multi-phase systems: 1. averaging procedure. *Advances in Water Resources*, 2:131–144.
- Hassanizadeh, M. and Gray, W. G. (1979b). General conservation equations for multi-phase systems: 2. mass, momenta, energy, and entropy equations. *Advances in Water Resources*, 2(4):191–203.
- Havelka, J. and Sýkora, J. (2018). Application of Calderón’s inverse problem in civil engineering. *Applications of Mathematics*, 63(6):687–712.
- Huang, S., Liu, Q., Cheng, A., Liu, Y., and Liu, G. (2018). A fully coupled thermo-hydro-mechanical model including the determination of coupling parameters for freezing rock. *International Journal of Rock Mechanics and Mining Sciences*, 103:205–214.
- Huč, S., Svensson, S., and Hozjan, T. (2018). Hygro-mechanical analysis of wood subjected to constant mechanical load and varying relative humidity. *Holzforschung*, 72(10):863–870.
- Humphries, R., Jenkins, C., Leuning, R., Zegelin, S., Griffith, D., Caldow, C., Berko, H., and Feitz, A. (2012). Atmospheric tomography: A bayesian inversion technique for determining the rate and location of fugitive emissions. *Environmental Science and Technology*, 46(3):1739–1746. cited By 27.
- Iacono, C., Sluys, L., and Van Mier, J. (2006). Estimation of model parameters in nonlocal damage theories by inverse analysis techniques. *Computer Methods in Applied Mechanics and Engineering*, 195(52):7211–7222.
- Isgor, O. B. and Razaqpur, A. G. (2004). Finite element modeling of coupled heat transfer, moisture transport and carbonation processes in concrete structures. *Cement and Concrete Composites*, 26(1):57–73.
- Janssens, M. L. (2004). Modeling of the thermal degradation of structural wood members exposed to fire. *Fire and Materials*, 28(2-4):199–207.
- Jing, L., Chen, R., Bai, X., Meng, F., Yao, Z., Teng, Y., and Chen, H. (2018). Utilization of a bayesian probabilistic inferential framework for contamination source identification in river environment. volume 246. cited By 0.
- Kennedy, M. C. and O’Hagan, A. (2001). Bayesian calibration of computer models. *Journal of the Royal Statistical Society: Series B (Statistical Methodology)*, 63(3):425–464.
- Kießl, K. (1983). *Kapillarer und dampfförmiger Feuchtetransport in mehrschichtigen Bauteilen: Rechnerische Erfassung und bauphysikalische Anwendung*. PhD thesis, Universität-Gesamthochschule Essen.
- Knudsen, K., Lassas, M., Mueller, J. L., and Siltanen, S. (2009). Regularized D-bar method for the inverse conductivity problem. *Inverse Problems and Imaging*, 3(4):599–624.
- Kong, F. and Wang, H. (2011). Heat and mass coupled transfer combined with freezing process in building materials: Modeling and experimental verification. *Energy and Building*, 43(10):2850–2859.

- Koniorczyk, M. and Gawin, D. (2011). Numerical modeling of salt transport and precipitation in non-isothermal partially saturated porous media considering kinetics of salt phase changes. *Transport in Porous Media*, 87(1):57–76.
- Koniorczyk, M., Gawin, D., and Schrefler, B. A. (2018). Multiphysics model for spalling prediction of brick due to in-pore salt crystallization. *Computers & Structures*, 196:233–245.
- Konopka, D. and Kaliske, M. (2018). Transient multi-fickian hygro-mechanical analysis of wood. *Computers & Structures*, 197:12–27.
- Koster, M. (2010). 3D multi-scale model of moisture transport in cement-based materials. In Brameshuber, W., editor, *International RILEM Conference on Material Science*, pages 165–176.
- Krischer, O. (1963). *Trocknungstechnik: Die wissenschaftlichen Grundlagen der Trocknungstechnik*. Springer.
- Künzel, H. M. (1995). Simultaneous heat and moisture transport in building components. *One-and two-dimensional calculation using simple parameters*. IRB-Verlag Stuttgart.
- Künzel, H. M. and Kiessl, K. (1996). Calculation of heat and moisture transfer in exposed building components. *International Journal of Heat and Mass Transfer*, 40(1):159–167.
- Kučerová, A., Brancherie, D., Ibrahimbegović, A., Zeman, J., and Bittnar, Z. (2009). Novel anisotropic continuum-discrete damage model capable of representing localized failure of massive structures. Part II: identification from tests under heterogeneous stress field. *Engineering Computations*, 26(1/2):128–144.
- Kučerová, A. and Matthies, H. G. (2010). Uncertainty updating in the description of heterogeneous materials. *Technische Mechanik*, 30(1–3):211–226.
- Kučerová, A., Sýkora, J., Rosić, B., and Matthies, H. G. (2012). Acceleration of uncertainty updating in the description of transport processes in heterogeneous materials. *Journal of Computational and Applied Mathematics*, 236(18):4862–4872.
- Kučerová, A. and Sýkora, J. (2013). Uncertainty updating in the description of coupled heat and moisture transport in heterogeneous materials. *Applied Mathematics and Computation*, 219(13):7252—7261.
- Langmans, J., Klein, R., and Roels, S. (2012a). Hygrothermal risks of using exterior air barrier systems for highly insulated light weight walls: A laboratory investigation. *Building and Environment*, 56:192–202.
- Langmans, J., Nicolai, A., Klein, R., , and Roels, S. (2012b). A quasi-steady state implementation of air convection in a transient heat and moisture building component model. *Building and Environment*, 58:208–218.
- Lautenberger, C. and Fernandez-Pello, C. (2009). Generalized pyrolysis model for combustible solids. *Fire Safety Journal*, 44(6):819–839.

- Liu, L., Ye, G., Schlagen, E., Chen, H., Qian, Z., Sun, W., and van Breugel, K. (2011). Modeling of the internal damage of saturated cement paste due to ice crystallization pressure during freezing. *Cement and Concrete Research*, 33(5):562–571.
- Luikov, A. V. (1975). Systems of differential equations of heat and mass transfer in capillary-porous bodies. *International Journal of Heat and mass transfer*, 18(1):1–14.
- Mahnken, R. (2004). Identification of material parameters for constitutive equations. *Encyclopedia of computational mechanics*.
- Mahnken, R. and Stein, E. (1996). Parameter identification for viscoplastic models based on analytical derivatives of a least-squares functional and stability investigations. *International Journal of Plasticity*, 12(4):451–479.
- Majorana, C. E., Salomoni, V. A., Xotta, G., Pomaro, B., and Mazzucco, G. (2015). Computational issue in multifield, multiscale and three-dimensional structural engineering. In *Computational Techniques for Civil and Structural Engineering*.
- Marzouk, Y. M. and Najm, H. N. (2009). Dimensionality reduction and polynomial chaos acceleration of bayesian inference in inverse problems. *Journal of Computational Physics*, 228(6):1862–1902.
- Matala, S. (1995). *Effects of carbonation on the pore structure of granulated blast furnace slag concrete*. PhD thesis, Helsinki University of Technology.
- Milly, P. C. D. (1982). Moisture and heat transport in hysteretic, inhomogeneous porous media: A matrix head-based formulation and a numerical model. *Water Resources Research*, 18(3):489–498.
- Moghtaderi, B. (2006). The state-of-the-art in pyrolysis modelling of lignocellulosic solid fuels. *Fire and Materials*, 30(1):1–34.
- Moreira, P., Van Genuchten, M., Orlande, H., and Cotta, R. (2016). Bayesian estimation of the hydraulic and solute transport properties of a small-scale unsaturated soil column. *Journal of Hydrology and Hydromechanics*, 64(1):30–44. cited By 9.
- Mueller, J. L., Isaacson, D., and Newell, J. C. (2001). Reconstruction of conductivity changes due to ventilation and perfusion from EIT data collected on a rectangular electrode array. *Physiological Measurement*, 22(1):97.
- Multon, S., Sellier, A., and Perrin, B. (2012). Numerical analysis of frost effects in porous media. Benefits and limits of the finite element poroelasticity formulation. *International Journal for Numerical and Analytical Methods in Geomechanics*, 36(4):438–458.
- Nunes, C., Slížková, Z., and Křivánková, D. (2012). Frost resistance of lime-based mortars with linseed oil. In *XIII Bilateral Czech/German Symposium*.
- Parthasarathy, S. and Balaji, C. (2008). Estimation of parameters in multi-mode heat transfer problems using Bayesian inference – effect of noise and a priori. *International Journal of Heat and Mass Transfer*, 51(9–10):2313–2334.

- Philip, J. and De Vries, D. (1957). Moisture movement in porous materials under temperature gradients. *Eos, Transactions American Geophysical Union*, 38(2):222–232.
- Remki, B., Abahri, K., Tahlaiti, M., and Belarbi, R. (2012). Hygrothermal transfer in wood drying under the atmospheric pressure gradient. *International Journal of Thermal Sciences*, 57:135–141.
- Richards, L. A. (1931). Capillary conduction of liquids through porous mediums. *Physics*, 1(5):318–333.
- Rosić, B. V., Kučerová, A., Sýkora, J., Pajonk, O., Litvinenko, A., and Matthies, H. G. (2013). Parameter identification in a probabilistic setting. *Engineering Structures*, 50:179–196.
- Rosić, B. V. and Matthies, H. G. (2013). Identification of properties of stochastic elastoplastic systems. In *Computational methods in stochastic dynamics*, pages 237–253. Springer.
- Saba, M., Quiñones-Bolaños, E., and López, A. L. B. (2018). A review of the mathematical models used for simulation of calcareous stone deterioration in historical buildings. *Atmospheric Environment*, 180:156–166.
- Saetta, A. V., Scotta, R. V., and Vitaliani, R. V. (1993). Analysis of chloride diffusion into partially saturated concrete. *Materials Journal*, 90(5):441–451.
- Santosa, F. and Vogelius, M. (1990). A backprojection algorithm for electrical impedance imaging. *SIAM Journal on Applied Mathematics*, 50(1):216–243.
- Scherer, G. W. (1993). Freezing gels. *Journal of Non-Crystalline Solids*, 155(1):1–25.
- Scherer, G. W. (1999). Crystallization in pores. *Cement and Concrete Research*, 29(8):1347—1358.
- Schrefler, B. (2002). Mechanics and thermodynamics of saturated/unsaturated porous materials and quantitative solutions. *Applied Mechanics Reviews*, 55(4):351–388.
- Schrefler, B. and Lewis, R. (1998). *The finite element method in the deformation and consolidation of porous media*. Chichester: Wiley.
- Shafikhani, M. and Chidiac, S. (2019). Quantification of concrete chloride diffusion coefficient—a critical review. *Cement and Concrete Composites*, 99:225–250.
- Shi, L. and Chew, M. Y. L. (2013). A review of fire processes modeling of combustible materials under external heat flux. *Fuel*, 106:30–50.
- Siltanen, S., Mueller, J., and Isaacson, D. (2000). An implementation of the reconstruction algorithm of A. Nachman for the 2d inverse conductivity problem. *Inverse Problems*, 16(3):681.
- Somersalo, E., Cheney, M., Isaacson, D., and Isaacson, E. (1991). Layer stripping: a direct numerical method for impedance imaging. *Inverse problems*, 7(6):899.

- Song, H.-W., Kwon, S.-J., Byun, K.-J., and Park, C.-K. (2006). Predicting carbonation in early-aged cracked concrete. *Cement and Concrete Research*, 36(5):979–989.
- Sun, Z. and Scherer, G. W. (2010). Effect of air voids on salt scaling and internal freezing. *Cement and Concrete Research*, 40(2):260–270.
- Sýkora, J. (2014). Modeling of degradation processes in historical mortars. *Advances in Engineering Software*, 72:203–212.
- Sýkora, J., Jarušková, D., Šejnoha, M., and Šejnoha, J. (2018). Fire risk analysis focused on damage of the tunnel lining. *Fire Safety Journal*, 95:51–65.
- Sýkora, J., Krejčí, T., Kruis, J., and Šejnoha, M. (2012). Computational homogenization of non-stationary transport processes in masonry structures. *Journal of Computational and Applied Mathematics*, 18:4745—4755.
- Sýkora, J., Šejnoha, M., and Šejnoha, J. (2013). Homogenization of coupled heat and moisture transport in masonry structures including interfaces. *Applied Mathematics and Computation*, 219(13):7275—7285.
- Šejnoha, M. and Zeman, J. (2013). *Micromechanics in Practice*. WIT Press, Southampton.
- Šejnoha, M., Sýkora, J., Vorel, J., Kucíková, L., Antoš, J., Pokorný, J., and Pavlík, Z. (2019). Moisture induced strains in spruce from homogenization and transient moisture transport analysis. *Computers & Structures*, 220:114 – 130.
- Talukdar, S., Banthia, N., and Grace, J. (2012). Carbonation in concrete infrastructure in the context of global climate change—part 1: Experimental results and model development. *Cement and Concrete Composites*, 34(8):924–930.
- Tan, X., Chen, W., Tian, H., and Cao, J. (2011). Water flow and heat transport including ice/water phase change in porous media: Numerical simulation and application. *Cold Regions and Technology*, 68(1–2):74–84.
- Tarantola, A. (2005). *Inverse Problem Theory and Methods for Model Parameter Estimation*. Society for Industrial and Applied Mathematics.
- Tanchev, R. T., Li, L., and Purkiss, J. (2001a). Finite element analysis of coupled heat and moisture transfer in concrete subjected to fire. *Numerical Heat Transfer: Part A: Applications*, 39(7):685–710.
- Tanchev, R. T., Li, L. Y., Purkiss, J. A., and Khalafallah, B. H. (2001b). Finite element analysis of coupled heat and mass transfer in concrete when it is in a fire. *Magazine of Concrete Research*, 53(2):117–125.
- Thoemen, H., Walther, T., and Wiegmann, A. (2008). 3D simulation of macroscopic heat and mass transfer properties from the microstructure of wood fibre networks. *Composites Science and Technology*, 68:608–616.

- Vorel, J. and Šejnoha, M. (2009). Evaluation of homogenized thermal conductivities of imperfect carbon-carbon textile composites using the mori-tanaka method. *Structural Engineering and Mechanics*, 33:429–446.
- Wardeh, G. and Perrin, B. (2008). Numerical modelling of the behaviour of consolidated porous media exposed to frost action. *Construction and Building Materials*, 22(4):600–608.
- Yee, E., Lien, F.-S., Keats, A., and D'Amours, R. (2008). Bayesian inversion of concentration data: Source reconstruction in the adjoint representation of atmospheric diffusion. *Journal of Wind Engineering and Industrial Aerodynamics*, 96(10–11):1805–1816.
- Yin, X., Liu, E., Song, B., and Zhang, D. (2018). Numerical analysis of coupled liquid water, vapor, stress and heat transport in unsaturated freezing soil. *Cold Regions Science and Technology*, 155:20–28.
- Younsi, R. and Kocaefe, D. and Kocaefe, Y. (2006). Three-dimensional simulation of heat and moisture transfer in wood. *Applied Thermal Engineering*, 26:1274–1285.
- Yverås, V. (2009). *A performance prediction method for moisture safety design*. PhD thesis, Chalmers University of Technology.
- Zeman, J. and Šejnoha, M. (2001). Numerical evaluation of effective elastic properties of graphite fibre tow impregnated by polymer matrix. *Journal of the Mechanics and Physics of Solids*, 49:69–90.
- Zeman, J. and Šejnoha, M. (2007). From random microstructures to representative volume elements. *Modelling and Simulation in Materials Science and Engineering*, 15:325–335.
- Zuber, B. and Marchand, J. (2000). Modeling the deterioration of hydrated cement systems exposed to frost action - Part 1: Description of the mathematical model. *Cement and Concrete Research*, 30(12):1929–1939.

Chapter 2

MODELING OF TRANSPORT PROCESSES IN WOOD STRUCTURES

A micromechanics based approach is outlined in this paper to predict evolution of moisture induced strains in spruce wood. Both analytical and numerical homogenization techniques are adopted first to provide estimates of effective coefficients of hygroexpansion to be multiplied by the current change in moisture content. This latter quantity is addressed next within the framework of non-Fickian constitutive model. Experimental measurements of coefficients of hygroexpansion exploiting the digital image correlation as well as determination of moisture transport using the cup model are carried out to support both applicability and numerical implementation of the presented approach.

List of selected journal papers and book chapters

Šejnoha, M., Sýkora, J., Vorel, J., Kucíková, L., Antoš, J., Pokorný, J., and Pavlík, Z. (2019). Moisture induced strains in spruce from homogenization and transient moisture transport analysis. *Computers & Structures*, 220:114–130.

List of related journal papers and book chapters

Šejnoha, M., Kucíková, L., Vorel, J., Sýkora, J., and De Wilde, W. (2019). Effective material properties of wood based on homogenization. *International Journal of Computational Methods and Experimental Measurements*, 7(2):167–180.

Moisture induced strains in spruce from homogenization and transient moisture transport analysis

Michal Šejnoha

Department of Mechanics, Faculty of Civil Engineering, Czech Technical University in Prague, Czech Republic

Jan Vorel

Department of Mechanics, Faculty of Civil Engineering, Czech Technical University in Prague, Czech Republic

Jan Sýkora

Department of Mechanics, Faculty of Civil Engineering, Czech Technical University in Prague, Czech Republic

Lucie Kucíková

Department of Mechanics, Faculty of Civil Engineering, Czech Technical University in Prague, Czech Republic

Jakub Antoš

Department of Mechanics, Faculty of Civil Engineering, Czech Technical University in Prague, Czech Republic

Jaroslav Pokorný

Department of Materials Engineering and Chemistry, Faculty of Civil Engineering, Czech Technical University in Prague, Czech Republic

Zbyšek Pavlík

Department of Materials Engineering and Chemistry, Faculty of Civil Engineering, Czech Technical University in Prague, Czech Republic

Keywords: Moisture induced strains, Homogenization, Effective coefficients of hygroexpansion, Heat and moisture transport, Spruce, Cup model, Digital image correlation

1. Introduction

Wood is a natural building material used in construction for centuries. Its natural origin and renewability are of great advantage, particularly at the present time when environmental

Email addresses: sejnom@fsv.cvut.cz (Michal Šejnoha), jan.vorel@fsv.cvut.cz (Jan Vorel), jan.sykora.1@fsv.cvut.cz (Jan Sýkora), lucie.kucikova@fsv.cvut.cz (Lucie Kucíková), jakub.antos@fsv.cvut.cz (Jakub Antoš), jaroslav.pokorny@fsv.cvut.cz (Jaroslav Pokorný), pavlikz@fsv.cvut.cz (Zbyšek Pavlík)

issues are at the forefront of the global interest. A reliable computational analysis especially at the initial stages of structural design thus plays an important role. Therein, the variability of material properties with ambient conditions, i.e. humidity and temperature, must be taken into account. Realizing also a complicated internal structure of wood can make the structural analysis quite complex. A suitable method of attack that balances computational efficiency and accuracy of numerical predictions typically relies on uncoupled multi-scale analysis combining analytical micromechanical models, computational homogenization and fitted parametric models [1, 2, 3]. In this contribution, such an approach will be adopted to revisit an important topic in the field of wood analysis associated with damage caused, apart from mechanical loading, by moisture induced strains [4, 5, 6]. Such eigenstrains when developed in constrained material may generate stresses that exceed the material strength [7, 8, 9]. A suitable constitutive model describing a wood response beyond elasticity limits reads

$$\sigma = E(\varepsilon - \mu), \quad \mu = \varepsilon_c + \varepsilon_\theta + \varepsilon_h, \quad (1)$$

where the eigenstrain μ is caused by various mechanical and physical sources limiting here attention to the crack strain ε_c , thermal strain ε_θ and hygroexpansion strain ε_h . Further effects such as creep and mechanosorption can also be included [4, 10]. Since often implemented in staggered format the evolution of crack strain and the non-mechanical parts of the eigenstrain μ can be treated separately. The former issue is currently investigated in the framework of smeared crack model [11, 12, 13] using the cohesive zone model [14]. The evaluation of thermal strain is relatively well understood even for generally heterogeneous materials [15, 1]. This is why we focus in this contribution on the hygroscopic strain ε_h with emphases on accuracy and efficiency.

Given a typical format of a hygroscopic strain

$$\varepsilon_h = \alpha_h^{\text{hom}} \Delta u, \quad (2)$$

calls for the solution of two problems. The first one is concerned with the evaluation of the macroscopic coefficient of hygroexpansion α_h^{hom} whereas the second one requires computation of moisture change Δu due to, e.g. variable climatic conditions. Both topics have received considerable attention in the past. In both cases, hierarchical modeling based on homogenization has often been pursued.

The 1st order homogenization exploiting the concept of periodic unit cell was adopted in [16, 3] to provide α_h^{hom} for all principal directions. Herein, we follow the work presented in [16] and combine in Section 3 analytical homogenization and periodic unit cell simulations to get both the effective hygroexpansion coefficients and elastic stiffnesses. We consider the class of softwood with attention accorded to spruce wood. The specifics of its microstructure required in homogenization are addressed in Section 2.4. To support the proposed homogenization strategy we examine in Section 2.3 the swelling behavior of spruce wood also experimentally. To that end, the digital image correlation (DIC) successfully applied in this context, e.g. in [17, 18, to cite a few], was adopted. We would also like to draw the reader's attention to [10] where a similar approach based on the grid method was applied to address the influence of coupling the moisture phenomena with mechanical loading and thermal effects on the resulting local strain profiles given the microstructural details.

From the accuracy point of view the above approach can certainly be justified in connection with the second topic devoted to the simulation of moisture content evolution as

advocated in [2, 19, 20]. However, in this paper we attempt to show in Section 4 that the preceding formulations based on parametric expressions for the macroscopic material parameters are sufficiently accurate and thus certainly more appealing to practical engineers. Nevertheless, regardless of calculation of effective properties all formulations build on application of two Fickian equations modeling the bound-water and water vapor diffusion, which interact through sorption. Such complex moisture transport, referred to as non-Fickian behavior, was firstly observed from the experimental measurements in the 1950s and became subsequently standard approach in wood material modeling in the 2000s known as multi-Fickian moisture transport model, see [21, 22]. It is worth mentioning that no adjustments to relevant data provided by literature were made in this paper when comparing the numerical predictions with experiments. These are discussed in Section 2.2 accompanying an extensive experimental program carried out on the examined type of wood.

Although repeated in relevant sections we mention, for the sake of clarity, the basic assumptions and thus also potential limitations accepted in this study:

- The material phases at cell wall level are limited to lignin, hemicellulose, and cellulose. Their stiffness and hygroexpansion properties including volume fractions pertinent to individual cell wall layers are taken from [16] and are assumed independent of moisture content (Sections 3.1). The thermal and moisture properties at cell wall level are adopted from [23, 24] (Section 4.2).
- Unlike in [23] the volume fractions of lumens identified in Section 2.4 are assumed constant independent of moisture. This is a legitimate assumption as the difference derived either from Eq. (7) or from numerical simulations based on the approach mentioned in Section 3 is negligible.

Unless otherwise stated the vector-matrix notation is used throughout the text. The symbol \mathbf{a} is reserved for a column matrix or a vectorial representation of a symmetric second-order tensor while the notation \mathbf{A} is employed for a matrix or a matrix representation of a fourth-order tensor [25].

2. Experiment

An extensive experimental campaign was carried out to provide sufficient data allowing verification of individual numerical analyses addressed in subsequent sections. The measurements of moisture transport grounded on the cup method are summarized first followed by the measurements of moisture induced strains caused by free swelling. A considerable attention has also been accorded to microstructure quantification. Nevertheless, we begin by briefly summarizing the measurement of sorption isotherm as playing a crucial role in a reliable description of moisture transport numerically.

2.1. Measuring sorption isotherm

Although various analytical models are available in the literature, see e.g. the Nelson model [26], the three parameter Guggenheim - Andersen - de Boer sorption equation [27] or the parametric model proposed in [28] and adopted in numerical simulations in [9], we performed our own experimental investigation to acquire data relevant to the wood samples at hand.

The sorption isotherm was measured using the dynamic vapor sorption device DVS Advantage II, which offers a high temperature stability and humidity performance. Upon drying, the sample of 5×5 mm in in-plane dimensions and 10 mm in thickness measured along the grains was placed into the climatic chamber of the DVS-Advantage instrument and hung on the automatic balances in a special steel tube. The initial (dry) sample mass was less than 1 g. The samples were then exposed to the selected partial pressure profile at 20°C to follow the loading program shown in Fig. 1(a) (solid line)

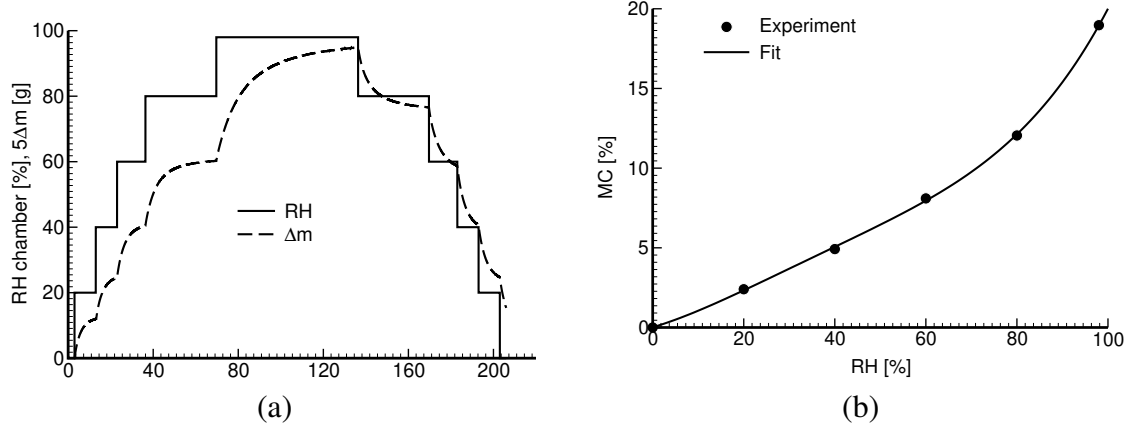


Figure 1: a) Loading program, b) Sorption isotherm

During measurements the instrument run in the dm/dt mode (the mass variation over the time variation) to determine the state of equilibrium. This is clearly seen for the adsorption part of the test in Fig. 1(a) when plotting the gain in mass $\Delta m = m - m_{\text{dry}}$ ($5\times$ magnification) for individual relative humidity steps. When the rate of change of mass fell below the limiting value, the relative humidity set point proceeded to the next programmed level, see e.g. [29] for further details.¹ Since only adsorption experiments were considered in this study, we limited our attention to adsorption branch of the sorption isotherm plotted in Fig. 1(b), see also [30] for the sake of comparison. The moisture content u (define also $MC = u \times 100\%$) was derived in a standard way from

$$u = \frac{m - m_{\text{dry}}}{m_{\text{dry}}}, \quad (3)$$

where m is the sample mass at equilibrium at a given level of relative humidity φ (define also $RH = \varphi \times 100\%$) and m_{dry} is the oven dry mass of a sample. For computational purpose, it is more convenient to fit the measured data to a continuous function. It is clear from Fig. 1(b) that the the 4th order polynomial function

$$MC = 34.8999\varphi^4 - 46.8996\varphi^3 + 23.5060\varphi^2 + 8.4820\varphi + 0.0137, \quad (4)$$

is sufficiently accurate giving an average difference in MC at the measurement points (circles on adsorption curve in Fig. 1(b)) less than 0.09%. Representing desorption would clearly call for a separate fitting equation. As indicated in Fig. 1(a) this would require much longer times

¹In this experiment the running mode of DVS device was optimized in accordance with an adsorption process resulting in non-equilibrium moisture states for almost all desorption steps.

to arrive at equilibrium state in comparison to adsorption in order to acquire relevant data. Since modeling cyclic climatic changes goes beyond the present scope, we did not elaborate this issue any further.

2.2. Measuring moisture transport in cup

To describe the moisture transport in spruce wood experimentally we relied on the classical cup method [31, 32, 30] assuming wet conditions. We focused on the determination of effective coefficient of moisture diffusion and transient evolution of moisture content throughout the sample due to variable climatic conditions. In general, specimens having $100 \times 100 \text{ mm}^2$ in-plane dimensions and variable thickness ranging from 2 to 8 mm were examined. Such a specimen was positioned in a stainless steel cup, sealed on the top of the cup and isolated with epoxy resin on its edges to ensure a one-dimensional water vapor transport. The cup was then placed in a temperature and humidity controlled test chamber set to $23 \pm 1^\circ\text{C}$ and 50% of relative humidity. The resulting pressure gradient caused a one-dimensional vapor flow through the specimen. An experimental setup is plotted in Fig. 2.



Figure 2: Cup method: a) measured sample, b) testing chamber

The measurements of the effective coefficient of moisture diffusion were performed according to the EN ISO 12572 standard [33] in steady state under isothermal conditions. In this particular case, we focused on the moisture transport along the direction of lumens only. A saturated solution of KNO_3 inside the cup maintained a $95 \pm 5\%$ of relative humidity in a thin layer of 10 mm left between the specimen and the solution.

The cups were periodically weighted until the mass loss per time unit was constant. The resulting effective water vapor diffusion coefficient D_L^{exp} [m^2s^{-1}] was computed from the measured data as follows [34]

$$D_L^{\text{exp}} = \frac{R(\theta + 273.15)\Delta m d}{MA\Delta t\Delta p}, \quad (5)$$

where $R = 8.31 \text{ Jmol}^{-1}\text{K}^{-1}$ is the universal gas constant, θ [$^\circ\text{C}$] is the actual temperature, $M = 0.018 \text{ kg mol}^{-1}$ is the molar mass of water, Δt [s] is the duration of the transport of water vapor mass Δm , d [m] is the sample thickness, A [m^2] is the area of the specimen surface, and Δp [Pa] is the difference in partial water vapor pressure above the studied specimen (RH and θ controlled chamber) and under the specimen placed in the cup. The partial water pressure was determined based on RH and θ measurement using miniature humidity and temperature sensor Almemo FHA646-R, Ahlborn (Germany), having diameter 5 mm and length 50 mm. It is a combined temperature NTC and RH capacitive sensor having accuracy of RH measurement $\pm 2\%$ for $\text{RH} < 90\%$ and for temperature monitoring $\pm 0.1^\circ\text{C}$ in

the temperature range 0 – 70°C. The partial water pressures above and under the test specimen were then assessed based on tabular values of the dependence of saturated water vapor pressure upon temperature.

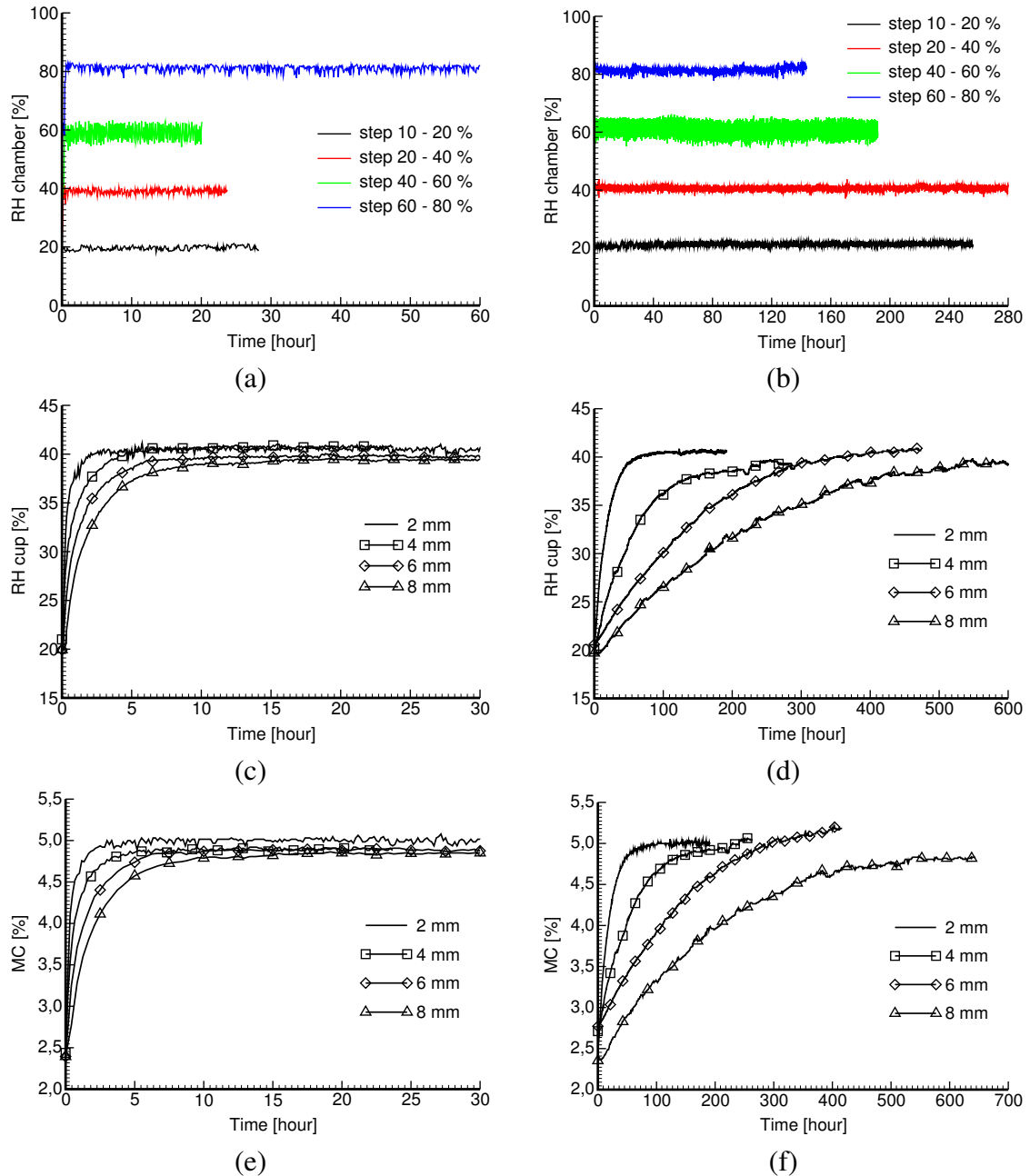


Figure 3: (a-b) Chamber relative humidity in 4 mm thick sample, (c-d) Evolution of cup relative humidity for loading step 20 - 40% RH, (e-f) Evolution of moisture content for loading step 20 - 40% RH; (a,c,e) - longitudinal direction, (b,d,f) - transverse direction

The last set of experiments aimed at generating a set of curves representing a time evolution of moisture content for various sample thicknesses. A one-dimensional moisture transport both along and perpendicular to lumens was examined. While two specimens were tested on each thickness for the lumen direction providing comparable results, only one specimen was considered for perpendicular direction given the test duration. In all cases the

specimens were first equilibrated at 10% of relative humidity attained both in the chamber and the cup. The relative humidity in chamber was then increased to 20% and the evolution of relative humidity in the cup was recorded until arriving at equilibrium. The sample was gradually weighted to obtain a corresponding evolution of the moisture content again with the help of Eq. (3). Afterwards, we continued with three additional steps of 20% of relative humidity increase.

This is apparent from Fig. 3(a) (transport in direction of lumens - longitudinal direction) and Fig. 3(b) (transport in direction perpendicular to lumens - transverse direction). Therein, the variation of relative humidity within the chamber is plotted for illustration for the sample of 4 mm in thickness. The evolution of relative humidity in the cup for specimens of variable thicknesses is displayed in Figs. 3(c,d) for one particular load step from 20 to 40% of chamber relative humidity. It is evident that arriving at equilibrium moisture content takes more than the order of magnitude longer for the transverse direction in comparison to the longitudinal direction. While for this particular step the target value of 40% of relative humidity was maintained for samples of 2 and 4 mm in thickness, compare with Fig. 3(a) for the 4 mm thick sample, the chamber relative humidity was found slightly below the target value for the remaining two samples. This is clearly supported in Fig. 3(c) by the value of cup relative humidity at steady state. The evolution of corresponding moisture contents seen in Figs. 3(e,f) is perfectly consistent with actual loading scenarios.

2.3. Measuring free swelling using digital image correlation

The objective of this study is to provide macroscopic strain averages to enter Eq. (2) in the evaluation of α_h^{hom} from the measurements of free swelling.

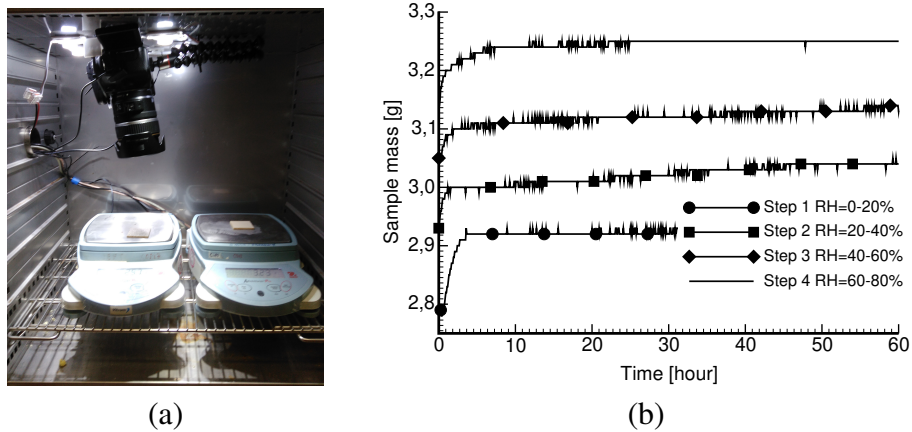


Figure 4: DIC measurements: a) testing chamber, b) evolution of sample mass with RH increments

The experimental setup is plotted in Fig. 4(a). Two specimens having dimensions of $40 \times 40 \times 4 \text{ mm}^3$ were placed in the climatic chamber and gradually weighted every 5 min during moisture uptake to check equilibrated states. Evolution of mass within the sample is plotted for illustration in Fig. 4(b). Note that only one specimen was airbrushed with a random pattern of black dots, while the other one served merely as a reference one to check whether the speckle pattern has any effect on the moisture transport. To avoid errors due to lens distortion [35], the camera Canon EOS 70D equipped with APS-C CMOS sensor with 20.2 Mpx resolution was placed directly into the chamber collecting images every 6 hours to allow for tracking a time evolution of strains within the sample [17, 18, 36, 37]. The actual

experiment proceeded in four consecutive steps equilibrating both specimens (no increase in sample mass) at relative humidities of 20, 40, 60 and 80%. Unlike in [18], this simple experimental setup did not allowed us to measure simultaneously a local (intra-link) variation of moisture content. But because we focus on the homogenized response only, it would be sufficient to derive the moisture content from the results presented in Fig. 4(b) adopting Eq. (3) similarly to Section 2.2. In the present approach, however, the change in moisture content for individual moisture steps was found simply from the sorption isotherm, Eq. (4), for a given value of RH.

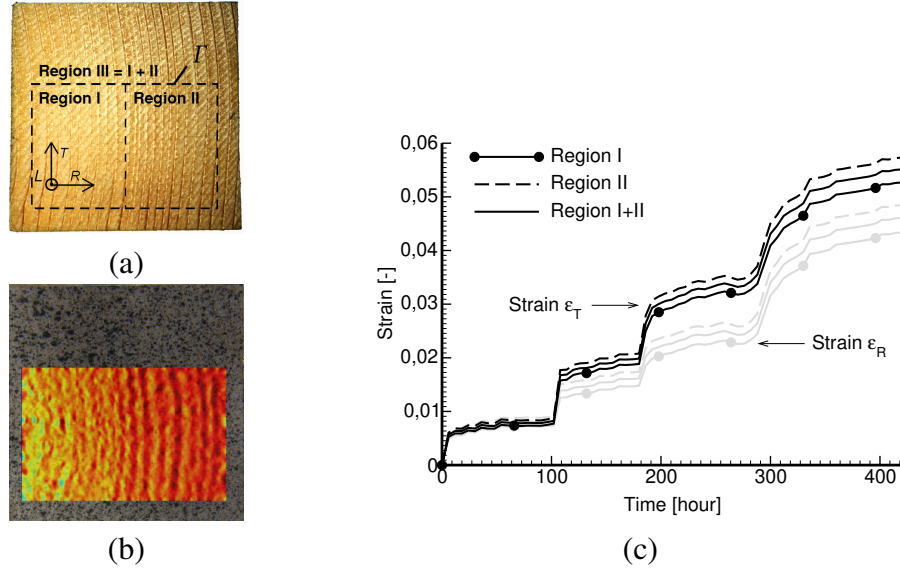


Figure 5: a) Examples of boundary lines to solve Eq.(6), b) Example of distribution of local radial strain at RH=60%, c) Time evolution of average radial strain

The strain averages were calculated at every equilibrium state to examine the assumed linearity of Eq. (2). To minimize the error these averages were found from the displacements measured in the R,T direction, see Fig. 5(a), adopting the following surface integral²

$$\varepsilon_{ij} = \frac{1}{2A} \int_{\Gamma} (u_i n_j + u_j n_i) d\Gamma, \quad (6)$$

where u_i, n_i represent, respectively, the R,T components of the displacement field and unit outward normal to the boundary line Γ identified in Fig. 5(a).

The open-source code Ncorr-Post-CSTool [38, 39] was used to perform this integration³. The resolution of original images subjected to DIC analysis was 3420 px. The pictures did not undergo upscaling or downscaling. The Region of Interest (ROI) window was 2450×2450 px. It was experimentally determined that DIC sensitivity is about 0.02 mm for 1 m long specimen for the adopted camera.

²Point out that Eq. (6) assumes a uniform through-thickness distribution of in-plane strains $\varepsilon_R, \varepsilon_T$. A tensorial notation is used so ε_{ij} , $i, j = 1, 2, 3$, is a second order tensor with, e.g. $2\varepsilon_{12} = \gamma_{12}$, where γ_{ij} are components of an engineering strain introduced in Eq. (13).

³This software package also allows for the determination of detailed distribution of local strains as illustrated in Fig. 5(b) for the radial strain component. This, however, goes beyond the present scope.

Note that a slight deviation of annual rings from the horizontal direction seen in Fig. 5(a) was neglected when evaluating the tangential and radial strain components. Three such boundaries, identifying regions over which the local strains were averaged, are presented. Consistency in the derivation of strain averages from various regions is evident from Fig. 5(c) showing a time evolution of average radial ε_R and tangential ε_T strains.

Thus given the increments of radial and tangential strains $\Delta\varepsilon_R, \Delta\varepsilon_T$ and the increment of moisture content Δu , the corresponding coefficients of hygroexpansion α_T, α_R follow directly from Eq. (2). We observed a good agreement with the assumed linearity of Eq. (2) at low values of relative humidity not exceeding 60%. A notable increase in swelling strains, the radial strain ε_R in particular, for the last loading step from 60 to 80% RH, Fig. 5(c), while still not deviating much from linearity in sorption isotherm, see 1(b), gives values of α_h^{hom} excessively high. On the other hand, such a rapid increase in swelling strain has not been reported in previous studies, see e.g. [3] where the measured radial strain averaged over the range of moisture content MC=0 - 19.24% did not exceed 2.79%. This issue is under current investigation.

Therefore, only the average values of the coefficient of hygroscopic expansion derived from the first three RH steps and two independent measurements are stored in Table 5 to be compared with predictions provided by homogenization.

2.4. Microstructure quantification

It is the principal objective of this paper to provide estimates of effective properties of wood measured in the previous sections computationally via homogenization. A considerable effort has been devoted to this issue in the past with emphases on the microstructure quantification [16, 40, 3, to cite a few closely related to homogenization and the present topic]. Modeling wood as a hierarchical structure, which displays over multiple scales, is now generally accepted. A schematic representation of the hierarchical structure of wood, which we will refer to henceforward, is displayed in Fig. 6⁴.

Apart from intrinsic properties of wood constituents below the cell wall level and their volume fractions particular attention deserve the deviation of wood microfibrils in individual cell wall layers known as the microfibril angle (MFA) [41], the structure of lumens within individual growth rings, and the variation of actual width of growth rings. Some microstructural aspects of cell wall are partially addressed in Section 3. The determination of MFA for the studied material can be found in [42]. In this section we therefore turn our attention to top two levels, the level of tracheids or lumens and the level of growth rings illustrated in Fig. 6. It will be seen that both geometrical details and volume fractions of material phases defined at these two levels will prove useful in constructing an appropriate mesoscopic computational model in Section 3 as well as in application of the non-Fickian moisture model in Section 4.

Because wood is a natural material with properties depending on growth site we do not wish to blindly adopt the results provided in [16] presenting a detailed and comprehensive study on the cellular structure of wood, but rather rely on similar measurements pertinent to the same material as already tested in the previous two sections. Collecting specimens from one particular lamella of a glued laminated timber beam tested in [43], all found in

⁴Notice that the level of rays as introduced in literature [40, 23, 2, to cite a few] was not considered in this study.

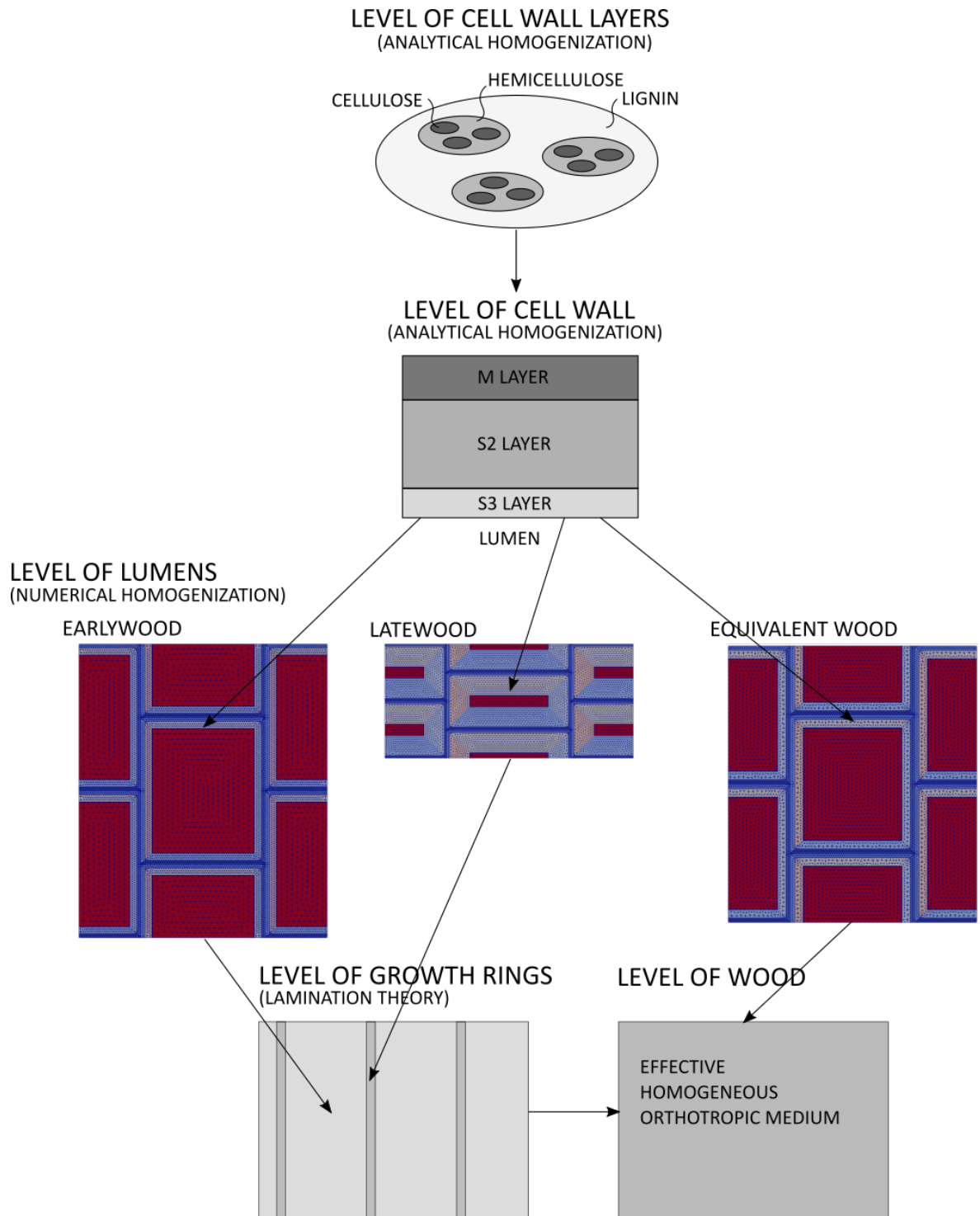


Figure 6: Hierarchical structure of wood identifying individual scales, simplified geometrical and computational models and homogenization methods.

the heartwood region, allowed us to further reduce uncertainties in microstructural details associated with the sample position within a single tree.

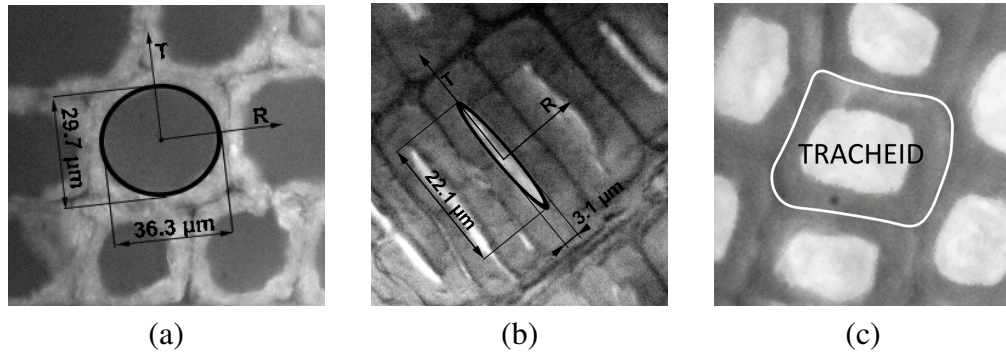


Figure 7: a) Earlywood b) Latewood, c) Transition wood

To open the subject we first recall a typical structure of tracheid [44] often imagined as a long closed tube-like cell with a cavity inside called lumen, see Fig. 7(c). Two types of tracheids can easily be identified with reference to the earlywood and latewood parts of the growth ring. While the earlywood tracheid is characterized by almost square cross-section and thin cell wall, the latewood tracheid is characterized by much thicker cell wall and its cross-section is almost half in width in the radial direction compare to the earlywood tracheid. One particular example is presented in Fig. 7 for illustration. The objective now becomes to construct a tracheid of an equivalent wood (EqW) based on the volume fraction of lumens in both earlywood and latewood, and earlywood and latewood width within a typical growth ring. This step reduces the computational effort as only one computational model at the level of lumens is needed and the level of annual rings does not have to be considered, recall Fig. 6.

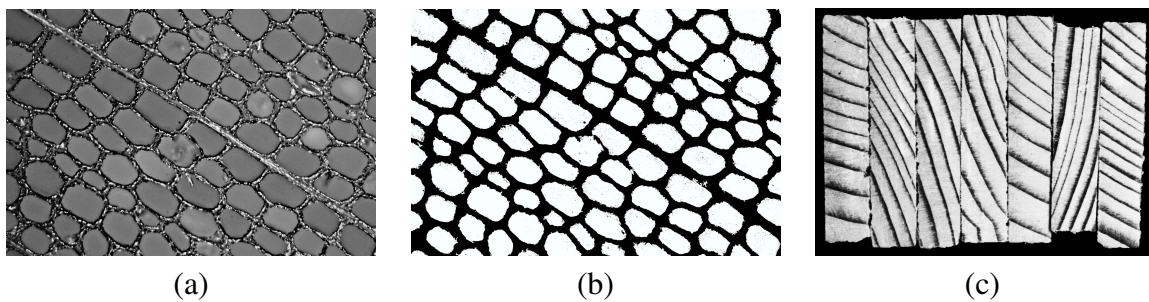


Figure 8: a) Original gray-scale image of earlywood, b) Transformed binary image of earlywood, c) Images of growth rings

A potential approach to derive these quantities employs image analysis. To that end, small clear samples of Norway spruce wood were carefully prepared to get cross-sectional surfaces as smooth as possible. High resolution photographs of the surface were taken and edited by commercial software to obtain high contrast between phases. Their binary counterparts allowed us to estimate the phase volume fractions by evaluating the proportional parts of individual black and white regions in relation to the whole sample area. An illustrative example is presented in Figs. 8(a,b). These images were collected at several locations within several growth rings to increase reliability of the estimated volume fractions by taking into account, at least to some extent, the variability of microstructure over the length of

the growth ring. The transition zone (a gradual change between earlywood and latewood, recall Fig. 7(c)) was, however, neglected. Altogether, 18 images taken from 6 small size specimens subjected to nanoindentation measurements in our accompanied study [42] were examined to acquire volume fractions of lumens. Additional 58 specimens were then used to measure the growth ring width. Herein, only the average value taken over the sample width in Fig. 8(c) was considered for further processing. The same specimens were exploited to provide averages of dry wood density ($\rho_{\text{dry}} \approx 410 \text{ kgm}^{-3}$ - oven dry).

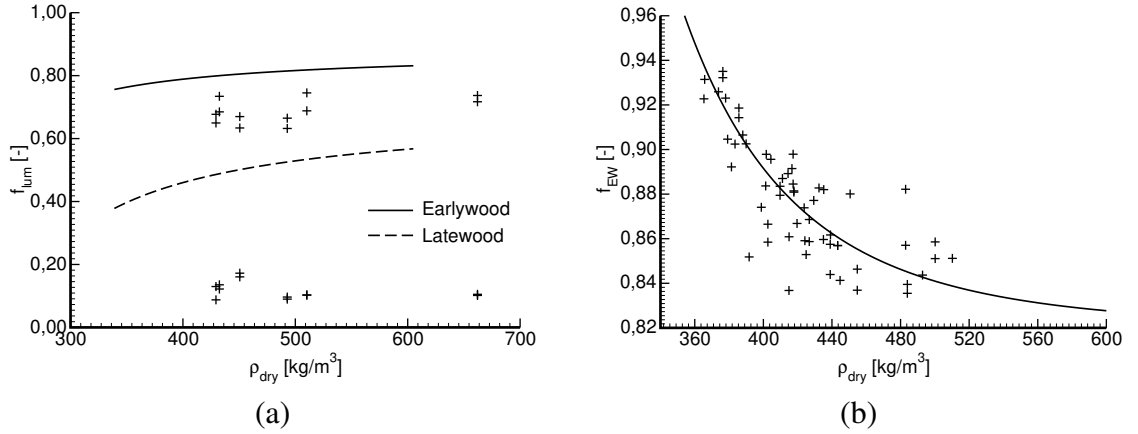


Figure 9: a) Volume fraction of lumens and b) Volume fraction of earlywood as a function of oven dry density

The volume fraction of lumens was determined for earlywood and latewood separately. The resulting values, plotted as a function of the oven dry density in Fig. 9(a), seem to be rather constant. The plus symbols in the upper part correspond to the lumen volume fraction in earlywood, with the average value of 0.69, and the lower ones correspond to latewood, with the average value of 0.12. Note that these values correspond to the moisture content MC around 4.5%. The solid curves were derived from [23]

$$f_{\text{lum,EW}} = 1 - \frac{\rho_{\text{wet,EW}}}{\rho_{\text{wet,CW}}}, \quad f_{\text{lum,LW}} = 1 - \frac{\rho_{\text{wet,LW}}}{\rho_{\text{wet,CW}}}, \quad (7)$$

where the wet densities of the earlywood, latewood and cell wall were obtained from expressions provided in [40] considering the average value of moisture content $\text{MC} = 4.5\%$ found from the ensemble of tested specimens [45] and the three basic cell wall constituents mentioned in Table 1. It is seen that particularly the latewood estimates generated by these relationships are significantly overestimated⁵

The volume fractions of earlywood and latewood at the level of growth rings were derived similarly adopting images such as the one in Fig. 8(c). From an engineering point of view it appears interesting to relate these volume fractions to dry wood density. One may either exploit analytical expressions provided, e.g. in [40] or take the advantage of already measured ring widths as proposed in [16]. In the latter approach it is interesting to begin by plotting the earlywood and latewood widths as a function of the growth ring width seen in Fig. 10. We immediately observe a linear correlation between the growth ring width and the earlywood width whereas no such relation exists for the latewood width. This suggests

⁵It is worth mentioning that Eq. (7) is assumed general and applicable to any type of softwood.

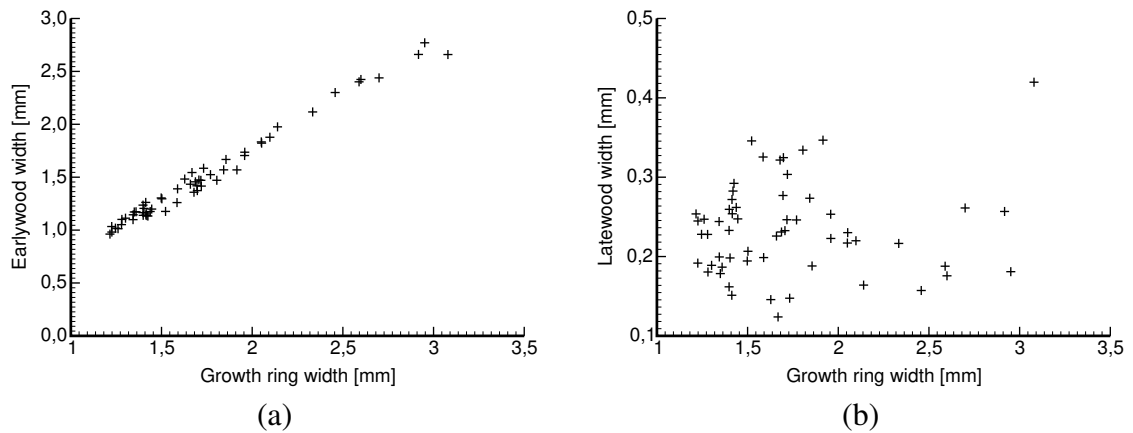


Figure 10: Dependence of earlywood (a) and latewood (b) width on growth ring width

the earlywood width as the only variable, while the latewood width is set constant equal to 0.2 mm. Similar conclusion has been put forward in [16].

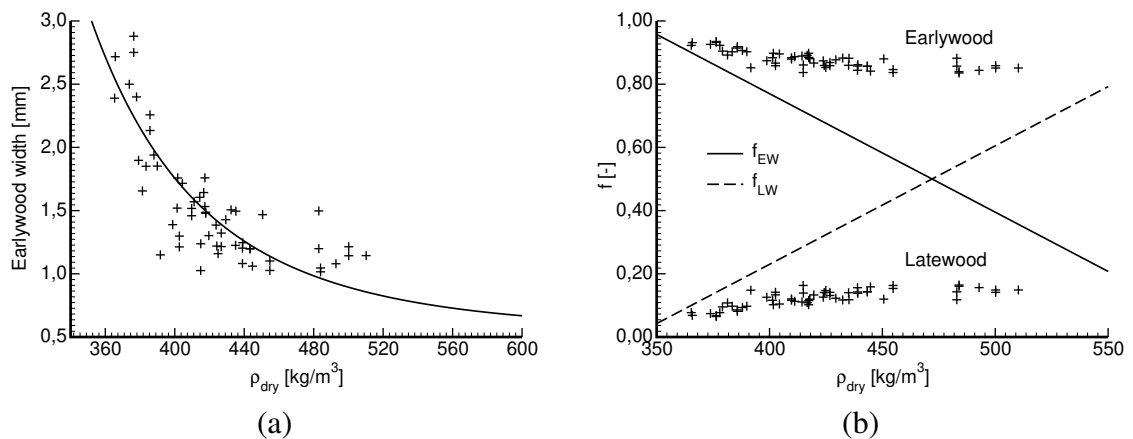


Figure 11: a) Dependence of earlywood width on oven dry density, b) Dependence of earlywood and latewood volume fractions on oven dry density

Grounding on this observation and proceeding further in footsteps of [16], we plotted in Fig. 11(a) the variation of earlywood width as a function of the dry wood density rendering again a clear correlation between these two parameters. Thus keeping in mind the constant width of the latewood within the growth ring it is now easy to relate the volume fraction of earlywood at the level of growth ring to the dry wood density. Such a relationship is plotted in Fig. 9(b) supporting what appears intuitive that higher volume fraction of earlywood leads to lower wood density. For the sake of comparison, this relationship is re-plotted in Fig. 11(b) for both the earlywood and latewood together with already mentioned analytical predictions (solid and dashed lines), recall [40]. It is evident that the measured values represented by plus symbols, where the upper marks correspond to the volume fraction of earlywood and the bottom marks to that of latewood, are mostly too far from the presented lines.

The measured data in Fig. 9(b) can be favorably represented by an approximate formula.

For our studied material it is given by⁶

$$f_{EW} = \left(\frac{250}{\rho_{dry}} \right)^{5.5} + 0.82, \quad (8)$$

where ρ_{dry} [kgm^{-3}] is the dry wood density. The volume fraction of latewood is then simply given by

$$f_{LW} = 1 - f_{EW}. \quad (9)$$

It is now possible to define the equivalent wood as basic weighted average of both the earlywood and latewood. The volume fraction of lumens of equivalent wood $f_{lum,EqW}$ is therefore

$$f_{lum,EqW} = f_{EW} \cdot f_{lum,EW} + f_{LW} \cdot f_{lum,LW}, \quad (10)$$

where $f_{lum,EW}$, $f_{lum,LW}$ are the volume fractions of lumens of earlywood and latewood, respectively. For the material tested in Sections 2.1 - 2.3 the dry wood density $\rho_{dry}=410 \text{ kgm}^{-3}$ was obtained, which gives the volume fraction $f_{lum,EqW} = 0.62$. This value will be used next in Section 3 in the derivation of effective coefficients of hygroexpansion and later also in Section 4 in numerical analyses of moisture transport.

3. Effective coefficients of hygroscopic expansion

With the limit to elastic behavior we write the local constitutive law in the form

$$\boldsymbol{\sigma}(\boldsymbol{x}) = \mathbf{L}(\boldsymbol{x})(\boldsymbol{\varepsilon}(\boldsymbol{x}) - \boldsymbol{\varepsilon}_h(\boldsymbol{x})), \quad \boldsymbol{\varepsilon}_h(\boldsymbol{x}) = \boldsymbol{\alpha}_h(\boldsymbol{x})\Delta u, \quad (11)$$

where Δu is the uniform change in moisture content, \mathbf{L} represents the material stiffness matrix, $\boldsymbol{\varepsilon}_h$ the hygroexpansion strain, and $\boldsymbol{\alpha}_h$ the vector of hygroexpansion coefficients. The macroscopic form of Eq. (11) then reads

$$\boldsymbol{\Sigma} = \mathbf{L}^{\text{hom}}(\mathbf{E} - \boldsymbol{\alpha}_h^{\text{hom}}\Delta u), \quad (12)$$

where $\boldsymbol{\Sigma}$ and \mathbf{E} are the macroscopically uniform stress and strain vectors, \mathbf{L}^{hom} is the effective stiffness matrix and $\boldsymbol{\alpha}_h^{\text{hom}}$ lists the macroscopic coefficients of hygroexpansion. Note that similarly to coefficients of thermal expansion the prediction of $\boldsymbol{\alpha}_h^{\text{hom}}$ requires, apart from knowing the phase coefficients of hygroexpansion, also the knowledge of the phase material stiffnesses. In the present study the derivation of $\boldsymbol{\alpha}_h^{\text{hom}}$ at the level of wood will combine both analytical and numerical homogenization. A quick introduction to both subjects is available in [1].

3.1. Analytical homogenization at cell wall level

To begin we recall a multilayered structure of a cell wall in Fig. 6 often simplified to three layers [16]: M layer (middle lamella, primary wall and outer layer of secondary wall S_1), S_2 layer (middle layer of secondary wall), and S_3 layer (inner layer of secondary wall). Each layer is composed of four basic elements: lignin, hemicellulose, cellulose (crystalline and amorphous) and extractives. Due to their low volume fraction, the extractives are often

⁶This function, applicable for $\rho_{dry} > 340 \text{ kgm}^{-3}$, is bounded from the bottom by the value of $f_{EW} = 0.82$.

neglected, as was also the case in the present study. The cellulose and hemicellulose are in the form of microfibrils, bonded together by lignin [46]. The microfibrils wound helically along the cell and their deviation from a longitudinal axis is called microfibril angle, recall Section 2.4. The microfibril angle generally changes within the cell wall, but for simplicity it is assumed constant in individual layers.

Cell wall constituents are very small particles, whose properties are difficult to measure. This is also the reason for their relatively high variability provided by various literature sources.

Table 1: Phase properties at cell wall level [16].

Local constituents	E_{11} [GPa]	$E_{22,33}$ [GPa]	$G_{12,13}$ [GPa]	$\nu_{21,31}$ [-]	ν_{23} [-]	$\alpha_{h,11}$ [-]	$\alpha_{h,22,33}$ [-]
Cellulose	150.00	17.50	4.50	0.01	0.50	0.000	0.000
Hemicellulose	16.00	3.50	1.50	0.10	0.40	0.000	1.368
Lignin	2.75	2.75	1.03	0.33	0.33	0.351	0.351

Herein, the material data presented in [16, and references therein] were assumed most relevant. The specific values of the three main constituents common to all layers are listed in Table 1⁷. As for the Poisson ratio, the notation used in [16] is followed throughout the paper to give the individual entries in the compliance matrix \mathbf{M} with respect to the components of stress and engineering strain vectors as

$$\begin{Bmatrix} \varepsilon_{11} \\ \varepsilon_{22} \\ \varepsilon_{33} \\ \gamma_{23} \\ \gamma_{31} \\ \gamma_{12} \end{Bmatrix} = \begin{bmatrix} \frac{1}{E_{11}} & -\frac{\nu_{21}}{E_{22}} & -\frac{\nu_{31}}{E_{33}} & 0 & 0 & 0 \\ -\frac{\nu_{12}}{E_{11}} & \frac{1}{E_{22}} & -\frac{\nu_{32}}{E_{33}} & 0 & 0 & 0 \\ -\frac{\nu_{13}}{E_{11}} & -\frac{\nu_{23}}{E_{22}} & \frac{1}{E_{33}} & 0 & 0 & 0 \\ 0 & 0 & 0 & \frac{1}{G_{23}} & 0 & 0 \\ 0 & 0 & 0 & 0 & \frac{1}{G_{13}} & 0 \\ 0 & 0 & 0 & 0 & 0 & \frac{1}{G_{12}} \end{bmatrix} \begin{Bmatrix} \sigma_{11} \\ \sigma_{22} \\ \sigma_{33} \\ \tau_{23} \\ \tau_{31} \\ \tau_{12} \end{Bmatrix}. \quad (13)$$

Owing to a relatively low knowledge of actual distribution of individual phases we shall treat each layer as an ergodic and statistically isotropic heterogeneous medium. The only relevant information needed are the volume fractions of all phases and the shape and orientation of inclusions. The present approach assumes two homogenization steps at the cell wall level. We first consider an infinitely long rod of elliptical cross-section representing cellulose, which is bonded to the matrix of hemicellulose. This step provides the effective properties of microfibrils to be introduced next, again in the form of elliptical rods, into the matrix of lignin. The elliptical shapes of cylindrical inclusions were estimated from the microfibril models proposed in [16]. The volume fractions taken again from [16] together with MFA for M and S_3 layers appear in Table 2. The microfibril angle pertinent to S_2 layer as

⁷Axis-11 denotes the longitudinal (microfibril) direction and axes-22,33 represent the transverse plane.

Table 2: Volume fraction of cell wall constituents and volume fraction and MFA of individual cell wall layers [16].

Layer	M	S ₂	S ₃
$f_{\text{cellulose}}$	0.20	0.49	0.49
$f_{\text{hemicellulose}}$	0.15	0.27	0.27
f_{lignin}	0.65	0.24	0.24
$f_{M,S_2,S_3}(\text{EW})$	0.352	0.609	0.039
$f_{M,S_2,S_3}(\text{LW})$	0.117	0.870	0.013
MFA [°]	45	15	75

the principal carrier of cell wall stiffness was adopted from [42]. Because needed later in Section 3.2, the volume fractions of individual layers within the volume of cell wall of both the earlywood and latewood are also provided.

Given the proposed homogenization procedure it is sufficient to consider a two-phase medium only and write the Mori-Tanaka estimate [47, 1, 15] of the effective stiffness matrix \mathbf{L}^{MT} within each layer in the form

$$\mathbf{L}^{\text{MT}} = \mathbf{L}_0 + f_1(\mathbf{L}_1 - \mathbf{L}_0)\mathbf{A}_1^{\text{dil}}(f_0\mathbf{I} + f_1\mathbf{A}_1^{\text{dil}})^{-1}, \quad (14)$$

where \mathbf{L}_0 and \mathbf{L}_1 are the stiffness matrices of the matrix phase (hemicellulose, lignin) and inclusions (cellulose, microfibril), \mathbf{I} is the second order identity tensor, f_0 and f_1 are the volume fractions of corresponding phases, and $\mathbf{A}_1^{\text{dil}}$ is the partial strain concentration factor of the inclusion defined as

$$\mathbf{A}_1^{\text{dil}} = (\mathbf{I} + \mathbf{S}_1\mathbf{L}_0^{-1}(\mathbf{L}_1 - \mathbf{L}_0))^{-1}, \quad (15)$$

where \mathbf{S}_1 is the Eshelby tensor depending on the inclusion shape. The effective hygroexpansion coefficients are best found by employing the Levin formula as [15]

$$\alpha_h^{\text{hom}} = f_0(\mathbf{B}_0^{\text{MT}})^{\text{T}}\alpha_0 + f_1(\mathbf{B}_1^{\text{MT}})^{\text{T}}\alpha_1 \quad (16)$$

where α_r ($r \in \{0, 1\}$) denotes the vector of hygroexpansion coefficients of individual phases, \mathbf{B}_r^{MT} is the stress concentration factor derived again from the Mori-Tanaka method. For individual phases we get

$$\begin{aligned} \mathbf{B}_0^{\text{MT}} &= (f_0\mathbf{I} + f_1\mathbf{B}_1^{\text{dil}})^{-1}, & \mathbf{B}_1^{\text{MT}} &= \mathbf{B}_1^{\text{dil}}\mathbf{B}_0^{\text{MT}}, \\ \mathbf{B}_1^{\text{dil}} &= (\mathbf{I} + \mathbf{L}_0(\mathbf{I} - \mathbf{S}_1)(\mathbf{L}_1^{-1} - \mathbf{L}_0^{-1}))^{-1}. \end{aligned} \quad (17)$$

The homogenized properties resulting from the application of Eqs. (14) and (16) are provided for all layers and MFA=0° in Tables 3 and 4.

3.2. Numerical homogenization at level of equivalent wood

Accepting more or less periodic distribution of tracheids within the earlywood and latewood promotes application of the 1st order homogenization. Such an approach builds upon the formulation of a certain periodic unit cell (PUC). The geometry of the unit cell should reflect the actual microstructure as close as possible. To that end, a reasonable point of departure in constructing the PUC model would be to treat the cell wall thickness, shape and

Table 3: Effective elastic properties from analytical homogenization

	E_{11}	E_{22}	E_{33}	G_{23}	G_{13}	G_{12}	ν_{21}	ν_{31}	ν_{32}
	[GPa]	[GPa]	[GPa]	[GPa]	[GPa]	[GPa]	[-]	[-]	[-]
M layer	34.24	4.62	3.96	1.32	1.32	1.60	0.03	0.04	0.41
S _{2,3} layer	78.72	7.15	6.01	2.05	2.05	2.46	0.02	0.02	0.41

Table 4: Effective coefficients of hygroexpansion from analytical homogenization

	α_{11}	α_{22}	α_{33}
	[-]	[-]	[-]
M layer	0.025	0.392	0.541
S _{2,3} layer	0.008	0.325	0.509

area of lumens, and their arrangement within both earlywood and latewood as random. A series of Monte Carlo simulations could be then carried out to address a potential influence of variability of the selected geometrical parameters on the estimates of effective properties [48, 49]. Alternatively, images of real microstructure could be used directly [50] to derive, by matching material statistics of real microstructure and PUC, the so called statistically equivalent periodic unit cell (SEPUC) [51, 1]. However, these steps go beyond the present scope and we settle for a simple model assuming a regular arrangement of tracheids.

While for the earlywood a hexagonal shape of PUC seems more appropriate, recall Figs. 8(a,b), the latewood microstructure in Fig. 7(b) suggests a rectangular arrangement of tracheids within PUC. Because we expect the annual ring be well represented by an equivalent wood, the hexagonal arrangement of tracheids will be adopted. Further simplification is concerned with a rectangular shape of the tracheid. A schematic representation of the relevant PUCs is plotted in Fig. 12.

When deriving the geometry of a single tracheid we assumed first the inner dimensions of the lumen be equal to major and minor semi-axes of the ellipse approximating the real shape of lumens as proposed in [44], see also Fig. 7. Considering the volume fractions of lumens as $f_{\text{lum,EW}} = 0.69$ for the earlywood, $f_{\text{lum,LW}} = 0.12$ for the latewood, recall Section 2.4, and dry wood density $\rho_{\text{dry}} = 410 \text{ kgm}^{-3}$ allowed us to calculate the cell wall thickness. The volume fractions of individual layers in the cell wall, recall Table 2, then provided its final subdivision distinguishing again M layer (blue, b), S₂ layer (red, r), and S₃ layer (green, g). The thicknesses of individual layers are listed in the right bottom corner of the picture (Fig. 12(a)) for the sake of completeness. The dimensions of the equivalent wood were finally derived in analogy with Eq. (10) as the weighted average of the dimensions of earlywood and latewood. The resulting PUC of equivalent wood is shown in Fig. 12(b). The colors identify individual homogeneous material systems from Tables 3 and 4 properly adjusted for specific MFA in Table 2 and orientation of a given layer with respect to the selected global coordinate system⁸. Note that \pm value of MFA was considered for layers on opposite sides of the lumen to account for microfibril wounding.

Next, suppose that the periodic unit cell is loaded either by a uniform macroscopic strain \mathbf{E} or stress $\mathbf{\Sigma}$ and a macroscopic uniform moisture change Δu . The macroscopic constitutive

⁸Horizontal layers are aligned with the global L (longitudinal (lumen) direction), T (tangential (circumferential) direction) and R (radial direction) coordinate system.

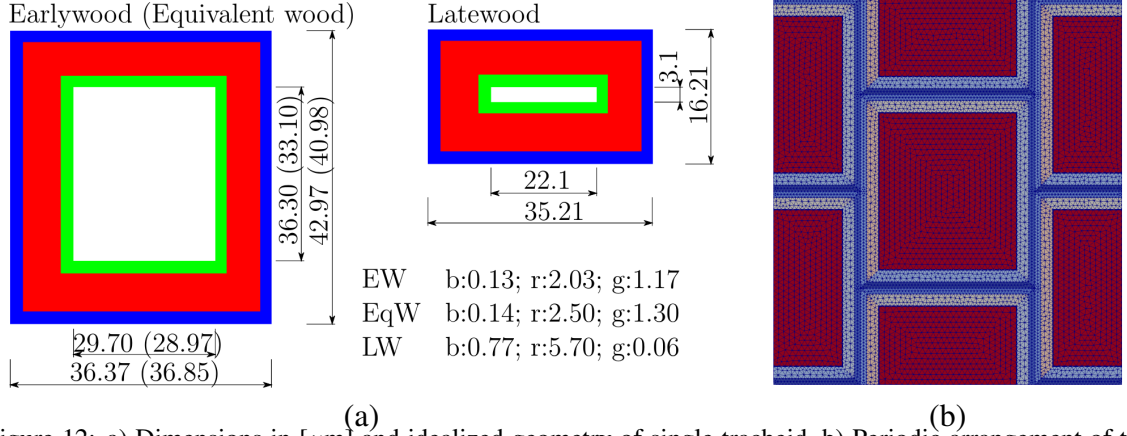


Figure 12: a) Dimensions in [μm] and idealized geometry of single tracheid, b) Periodic arrangement of tracheids within PUC of EqW

relations, corresponding to the *homogenized medium*, is then provided by

$$\begin{aligned} \langle \boldsymbol{\sigma}(\mathbf{x}) \rangle &= \langle \mathbf{L}(\mathbf{x})(\boldsymbol{\varepsilon}(\mathbf{x}) - \boldsymbol{\alpha}(\mathbf{x})\Delta u) \rangle = \mathbf{L}^{\text{hom}}(\mathbf{E} - \boldsymbol{\alpha}_h^{\text{hom}}\Delta u), \\ \langle \boldsymbol{\varepsilon}(\mathbf{x}) \rangle &= \langle \mathbf{M}(\mathbf{x})\boldsymbol{\sigma}(\mathbf{x}) + \boldsymbol{\alpha}(\mathbf{x})\Delta u \rangle = \mathbf{M}^{\text{hom}}\boldsymbol{\Sigma} + \boldsymbol{\alpha}_h^{\text{hom}}\Delta u, \end{aligned} \quad (18)$$

where $\mathbf{M} = \mathbf{L}^{-1}$ is the compliance matrix and $\langle \cdot \rangle$ stands for the spatial average of a given field. Equations (18) follow directly from Hill's lemma [52]. He proved that for the assumed loading conditions the following relation holds

$$\langle \delta \boldsymbol{\varepsilon}(\mathbf{x})^\top \boldsymbol{\sigma}(\mathbf{x}) \rangle = \delta \mathbf{E}^\top \boldsymbol{\Sigma}. \quad (19)$$

The above relations provide the stepping stone for the numerical derivation of effective properties of composite materials via finite element schemes. To do so we proceed in the footsteps of [53] and decompose the local displacements $\mathbf{u}(\mathbf{x})$ and associated strains $\boldsymbol{\varepsilon}(\mathbf{x})$ as

$$\mathbf{u}(\mathbf{x}) = \mathbf{E} \cdot \mathbf{x} + \mathbf{u}^*(\mathbf{x}), \quad \boldsymbol{\varepsilon}(\mathbf{x}) = \mathbf{E} + \boldsymbol{\varepsilon}^*(\mathbf{x}), \quad (20)$$

where the macroscopic strain \mathbf{E} is constant over the PUC and $\mathbf{u}^*(\mathbf{x})$ and $\boldsymbol{\varepsilon}^*(\mathbf{x})$ are local displacement and strain fluctuations, respectively. Because $\langle \boldsymbol{\varepsilon}(\mathbf{x}) \rangle = \mathbf{E}$ it becomes clear that $\boldsymbol{\varepsilon}^*(\mathbf{x})$ has to disappear upon volume averaging. This can be achieved, e.g. through the application of periodic boundary conditions⁹ in the solution of the discretized system of governing equations (22). Further details can be found, e.g. in [1]. The FEM discretization provides the local fluctuation displacements and consequently the local strain in the form

$$\mathbf{u}^*(\mathbf{x}) = \mathbf{N}(\mathbf{x})\mathbf{r}, \quad \boldsymbol{\varepsilon}(\mathbf{x}) = \mathbf{E} + \mathbf{B}(\mathbf{x})\mathbf{r}, \quad (21)$$

where \mathbf{r} represents the nodal displacements of the fluctuation displacement field \mathbf{u}^* and $\mathbf{B}(\mathbf{x})$ is the geometrical matrix obtained by differentiating the shape functions $\mathbf{N}(\mathbf{x})$ with respect to \mathbf{x} . In case of rectangular PUCs the periodicity is achieved by simply forcing the components of \mathbf{r} be the same on opposite edges of PUC [1]. For the application with commercial codes we refer the interested reader to [54].

⁹In the present formulation the periodic boundary conditions assume the same fluctuation displacements on the opposite sides of PUC. Given Eq. (6) it now becomes clear that under such conditions $\langle \boldsymbol{\varepsilon}^*(\mathbf{x}) \rangle = \mathbf{0}$.

If interested in coefficients of α_h^{hom} we must continue with so called stress loading regime [53, 1] by prescribing Σ and Δu . The macroscopic strain \mathbf{E} is then unknown and will become part of the solution. To see this, we substitute Eq. (21) combined with Eq. (11) back into Eq. (19) and collect terms associated with $\delta \mathbf{r}$ and $\delta \mathbf{E}$ to finally get the discretized system of algebraic equations in the form

$$\begin{bmatrix} \int_{\Omega} \mathbf{L} \, d\Omega & \int_{\Omega} \mathbf{L} \mathbf{B} \, d\Omega \\ \int_{\Omega} \mathbf{B}^T \mathbf{L} \, d\Omega & \int_{\Omega} \mathbf{B}^T \mathbf{L} \mathbf{B} \, d\Omega \end{bmatrix} \begin{Bmatrix} \mathbf{E} \\ \mathbf{r} \end{Bmatrix} = \begin{Bmatrix} \Omega \Sigma + \int_{\Omega} \mathbf{L} \alpha_h \Delta u \, d\Omega \\ \int_{\Omega} \mathbf{B}^T \mathbf{L} \alpha_h \Delta u \, d\Omega \end{Bmatrix}, \quad (22)$$

where Ω represents the domain of PUC.

Solving the system (22), while setting the macroscopic stress $\Sigma = \mathbf{0}$ and the moisture change $\Delta u = 1$, provides the effective hygroexpansion coefficients α_h^{hom} as components of the macroscopic strain \mathbf{E} . If using the PUC corresponding to equivalent wood we get the effective coefficients of hygroexpansion directly at the level of the solid wood as already suggested in Fig. 6. The result of this computational step appears in the second row of Table 5. Given the epistemic uncertainty, or in other words an unknown experimental error, the results provided by homogenization are reasonably close to those derived experimentally in our present study reported in Section 2.3.

Table 5: Effective coefficients of hygroexpansion of wood from experimental measurements, homogenization, and other literature sources

Method	$\alpha_{h,L}$	$\alpha_{h,T}$	$\alpha_{h,R}$
Experiment	-	0.35	0.22
Homogenization	0.001	0.339	0.231
Rafsanjani et al. [3]	-	0.30	0.14
Lanvermann et al. [36]	-	0.33	0.14
Persson [16]	0.001 - 0.006	0.25 - 0.41	0.13 - 0.25

4. Evolution of moisture content

Predicting the evolution of moisture content in wood is the second necessary step in the calculation of moisture induced strains. As intimated in the introductory part the modeling strategy based on the non-Fickian constitutive model is now widely accepted. This part thus merely supports the original formulation initiated, e.g. in [21] and further elaborated in [22]. Although the progress in microstructure identification certainly promotes the use of complex and rigorous homogenization techniques [23, 24, 20, 2] in the derivation of macroscopic thermal and diffusion properties, it is seen in this paper that the original approach based on empirical expressions is, at least from engineering prospective, sufficient. We thus limit our attention to most essential aspects of the formulation, remain as brief as possible, and refer to the above cited sources and references therein for further details.

4.1. Theoretical formulation

The theoretical formulation grounds on the work presented in [22] and further extended in [2] to account for thermal effects. The stepping stone is the condition below the fiber saturation point (FSP)¹⁰. In such a case the moisture transport in wood structures exposed

¹⁰FSP corresponds to moisture content at which the cell walls are saturated with bound water with no free water in the lumens.

to air is a diffusion process described mainly by three phenomena: (i) transport of water vapor in lumens, (ii) transport of bound water in cell walls and (iii) the balance between two water phases introduced as a sorption rate. The phase changes between these two states of water generate energy changes which need to be taken into account. All these phenomena are combined in [2] in the coupled heat and moisture transport in wood.

To proceed, consider first the following primary physical variables: (i) the concentration of bound water - ρ_b [kgm^{-3}], i.e. mass of water per dry total volume of wood, (ii) the concentration of water vapor - ρ_v [kgm^{-3}], i.e. mass of water vapor per dry total volume of wood, and (iii) the temperature - θ [$^{\circ}\text{C}$]. The resulting set of macroscopic differential equations then reads:

- Bound water balance equation

$$\frac{\partial \rho_b}{\partial t} = \nabla \cdot (\mathbf{D}_b \nabla \rho_b) + \dot{\rho}. \quad (23)$$

- Water vapor balance equation

$$\frac{\partial \rho_v}{\partial t} = \nabla \cdot (\mathbf{D}_v \nabla \rho_v) - \dot{\rho} \quad (24)$$

- Heat balance equation

$$\rho_{\text{wood}} c_h \frac{\partial \theta}{\partial t} = \nabla \cdot (\lambda \nabla \theta) + \nabla \cdot (\mathbf{D}_b \nabla \rho_b) h_b + \nabla \cdot (\mathbf{D}_v \nabla \rho_v) h_v + \dot{\rho} \Delta h_{bv}, \quad (25)$$

where t [s] is the time, $\dot{\rho}$ [$\text{kgm}^{-3}\text{s}^{-1}$] is the sorption rate taken per the total volume of wood, the 3×3 macroscopically homogeneous diagonal matrices \mathbf{D}_b and \mathbf{D}_v [m^2s^{-1}] store the bound water and water vapor diffusion coefficients, respectively, and λ [$\text{Wm}^{-1}\text{K}^{-1}$] is the 3×3 diagonal macroscopic thermal conductivity matrix. The diagonal terms of these matrices reflect the principal material directions, recall Section 3. A short note on their determination including the sorption rate is presented in Section 4.2. It is worth noting that the concentration of water vapor ρ_v is related to the relative humidity φ through the equation of state as

$$\rho_v = f_{\text{lum,EqW}} \frac{M_w}{R(\theta + 273.15)} p_v = f_{\text{lum,EqW}} \frac{M_w}{R(\theta + 273.15)} p_{\text{sat}} \varphi, \quad (26)$$

where p_v [Pa] is the pressure of water vapor, p_{sat} [Pa] is the saturation pressure of water vapor expressed as a function of temperature [55], M_w [kgmol^{-1}] is the molar mass of water, R [$\text{Jmol}^{-1}\text{K}^{-1}$] is the gas constant and $f_{\text{lum,EqW}}$ [-] is the volume fraction of lumens of equivalent wood, recall Eq. (10), assumed constant independent of moisture. The remaining symbols in Eq. (25) were adopted from [56, 57, 2] and have the following meaning:

- ρ_{wood} [kgm^{-3}] is the macroscopic density of wood given by [58]

$$\rho_{\text{wood}} = \rho_{\text{dry}} \frac{1 + u}{1 + 0.84 \rho_{\text{dry}} u}. \quad (27)$$

- c_h [$\text{Jkg}^{-1}\text{K}^{-1}$] is the specific heat capacity of wood, [57], written as

$$c_h = \frac{c_{h,\text{dry}} + c_{h,w}u}{(1 + u)} + c_{h,\text{adj}}, \quad (28)$$

where $c_{h,\text{dry}}$ [$\text{Jkg}^{-1}\text{K}^{-1}$] is the specific heat capacity of dry wood, $c_{h,w}$ [$\text{Jkg}^{-1}\text{K}^{-1}$] is the specific heat capacity of water and $c_{h,\text{adj}}$ [$\text{Jkg}^{-1}\text{K}^{-1}$] is the additional adjustment factor given by [57]

$$c_{h,\text{adj}} = u(-6191 + 23.6(\theta + 273.15) - 1330 u).$$

- Δh_{bv} [Jkg^{-1}] is the specific enthalpy of the phase transition of water from the bound state to the vapor state, [2], expressed as

$$\Delta h_{\text{bv}} = h_v - h_b, \quad (29)$$

where h_b [Jkg^{-1}] is the specific enthalpy of bound water, h_v [Jkg^{-1}] is the specific enthalpy of water vapor. The latter two quantities are provided by

$$\begin{aligned} h_v &= 1840\theta + 2.5008 \cdot 10^6, \\ h_b &= c_{h,w}\theta - 8.368 \cdot 10^5 \exp(-14 u). \end{aligned}$$

The material/computational model is completed by introducing the initial and boundary conditions (BC) defined commonly in terms of the Dirichlet, Neumann, and Robin BC together with initial values of primary physical variables at time $t = 0$, see e.g. [55]. Herein, the Robin BC were adopted in the form

$$\mathbf{n} \cdot \mathbf{J}_h = k_h(\theta - \theta_\infty), \quad (30)$$

$$\mathbf{n} \cdot \mathbf{J}_v = k_v(\rho_v - \rho_{v,\infty}), \quad (31)$$

where \mathbf{n} [–] is the unit normal vector, k_h [$\text{Wm}^{-2}\text{K}^{-1}$] is the heat transfer coefficient, k_v [ms^{-1}] is the film boundary coefficient for the water vapor transfer, θ_∞ and $\rho_{v,\infty}$ are the ambient temperature and concentration of water vapor obtained from Eq. (26), respectively.

The system of differential equations (23) – (25) was discretized in space using standard finite element formulation. As for time discretization, the Crank-Nicolson scheme assuming the mid-point integration rule was employed. The discretized model was implemented into our in-house Matlab finite element code and solved with the help of Newton-Raphson iterative procedure.

4.2. Short note on homogenization

Special attention deserves evaluation of the material data at the level of wood. Certainly, an interesting option offers again the theory of homogenization. With regard to the present topic this path has successfully been proceeded in [23] and [24] where the analytical homogenization described in Section 3.1 was exercised in the framework of multi-scale homogenization all the way up to the level of wood. Therefore, unlike in Section 3.2, the analytical micromechanical models of the type of Eq. (14) were employed also at the level of earlywood and latewood. In this case the 6×6 phase stiffness matrices are replaced by the 3×3 phase thermal conductivity and moisture diffusivity equivalents. This applies also to

the Eshelby tensor having much simpler format in comparison to the elasticity problem [1]. If avoiding the FEM simulations, the lamination theory is needed both at the level of cell wall and the level of annual rings.

A rather engineering approach, on the other hand, relies on the application of closed form expressions pertinent already to the level of wood. For individual principal directions they assume the following forms:

- λ [$\text{Wm}^{-1}\text{K}^{-1}$] - the thermal conductivity matrix is taken from [57]

$$\begin{aligned} \lambda_i &= \xi_i (G_{\text{wood}}(0.1941 + 0.4064u) + 0.01864), \quad i \in \{\text{L}, \text{T}, \text{R}\}, \\ \xi_{\text{L}} &= 2.0, \quad \xi_{\text{T}} = 1.0, \quad \xi_{\text{R}} = 1.0, \end{aligned} \quad (32)$$

where $G_{\text{wood}}[-]$ is the specific gravity. The empirical reduction factors $\xi_i[-]$ account for differences in the moisture transport in L, T, R principal directions due to inherent wood anisotropy.

- D_v [m^2s^{-1}] - the water vapor diffusion matrix is derived from semi-empirical expression for the diffusion coefficient in air [59] adjusted again with specific reduction factors ξ_i to describe the water vapor diffusion at the level of wood while accounting again for wood anisotropy [22, 2]

$$\begin{aligned} D_{v,i} &= \xi_i \left(2.31 \cdot 10^{-5} \frac{p_{\text{at}}}{p_{\text{at}} + p_{\text{sat}}\varphi} \left(\frac{\theta + 273.15}{273.15} \right)^{1.81} \right), \\ i \in \{\text{L}, \text{T}, \text{R}\}, \quad \xi_{\text{L}} &= 0.98, \quad \xi_{\text{T}} = 0.05, \quad \xi_{\text{R}} = 0.07, \end{aligned} \quad (33)$$

where p_{at} [Pa] is the atmospheric pressure ($p_{\text{at}} = 101325$ [Pa]).

- D_b [m^2s^{-1}] - the bound water diffusion matrix is derived from the expression provided for the transverse direction in [60] and further adjusted for the longitudinal direction in [61, 62]

$$\begin{aligned} D_{b,i} &= D_{0,i} \exp \left(-\frac{38500 - 29000u}{R(\theta + 273.15)} \right), \quad i \in \{\text{L}, \text{T}, \text{R}\} \\ D_{0,\text{L}} &= 17 \cdot 10^{-6}, \quad D_{0,\text{T}} = 7 \cdot 10^{-6}, \quad D_{0,\text{R}} = 7 \cdot 10^{-6}. \end{aligned} \quad (34)$$

Equations (32) and (34) are plotted in Fig. 13. The results provided by analytical homogenization for the moisture content $\text{MC} = 4.5\%$, adopting material data of cell wall constituents from [23, 24], are also shown. These were found by combining the Mori-Tanaka method and lamination theory. Clearly, the homogenized effective thermal conductivities are reasonably close to those provided by Eq. (32). The homogenized bound water diffusivities deviate seemingly more from predictions given by Eq. (34) but they are still found within the same order of magnitude. This supports the use of these parametric expressions in Eqs. (23) and (25).

In [2] the authors present a homogenization model to predict the evolution of sorption rate $\dot{\rho}$. However, to keep similarity with the adopted empirical expressions (32) - (34) we follow the work in [21, 22], where experimentally determined relation describing the balance

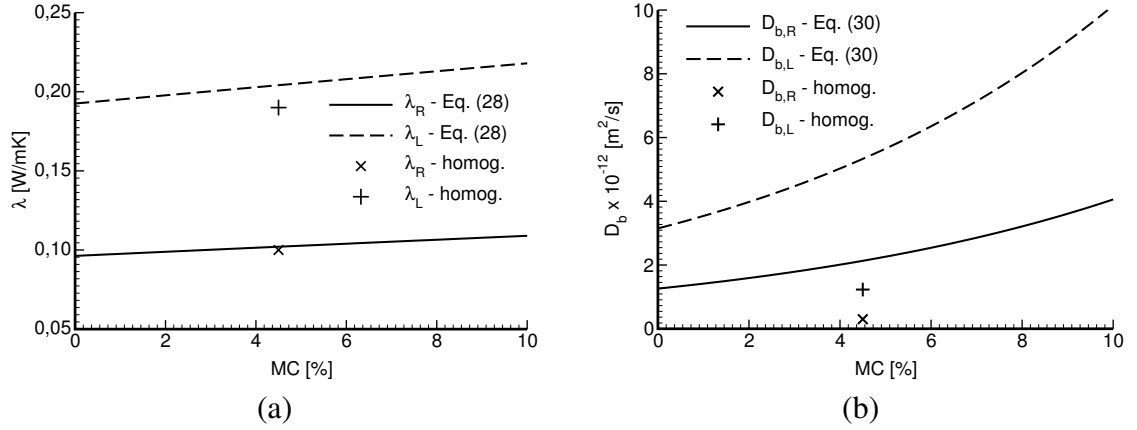


Figure 13: Evolution of effective transport coefficients as a function of moisture content: a) coefficient of thermal conductivity λ_i , b) coefficient of bound water diffusion $D_{b,i}$

between the water vapor pressure p_v [Pa] and bound water concentration ρ_b recalculated with the help of sorption isotherm into the wood vapor pressure p_b [Pa] was presented as

$$\dot{\rho} = f(p_v, p_b)(p_v - p_b), \quad (35)$$

where $f(p_v, p_b)$ [kgm⁻³Pa⁻¹s⁻¹] is the moisture-reaction rate function defined as

$$f(p_v, p_b) = \left\{ \begin{array}{ll} C_1 \exp\left(-C_2 \left(\frac{p_b}{p_v}\right)^{C_3}\right) + C_4 & p_b \leq p_v \\ C_1 \exp\left(-C_2 \left(2 - \frac{p_b}{p_v}\right)^{C_3}\right) + C_4 & p_b > p_v \end{array} \right\}. \quad (36)$$

For adsorption ($p_b \leq p_v$) and desorption ($p_b > p_v$) the moisture-reaction rate function $f(p_v, p_b)$ attains relatively high values of the order of 10^6 . When approaching equilibrium between the two concentrations, i.e. $\rho_v \simeq \rho_b$, this function slows down significantly ($f(p_v, p_b) \rightarrow 1$). The corresponding coefficients C_i in Eq. (36) were taken from literature [22, 63] and are summarized in Table 6.

C_1 [kgm ⁻³ Pa ⁻¹ s ⁻¹]	C_2 [-]	C_3 [-]	C_4 [kgm ⁻³ Pa ⁻¹ s ⁻¹]
$2.6 \cdot 10^{-6}$	$5.22 \cdot 10^{-6} \exp(19 \varphi)$	50	$8.0 \cdot 10^{-8}$

4.3. Numerical simulation of cup experiment

Two experiments presented in Section. 2.2 are numerically investigated here not only to promote the outlined methodology for the simulation of moisture transport processes in wood, but also to support the results provided by experiments computationally. While the latter issue is not typically addressed, it helps to disclose potential experimental errors. First we consider the evaluation of effective coefficient of moisture diffusion whereas in the second step we recalculate numerically the moisture uptake in the cup experiments again for several thicknesses of wood specimens and two principal directions of moisture transport.

To this purpose, geometrical domains in Fig. 14 representing the cuts along the longitudinal or transverse directions were discretized with four-node quadrilateral elements assuming an average element edge length of 0.05 mm. Because of the assumed one-dimensional transport, only one element over the domain width was considered. To support this assumption the results of one-dimensional transport were compared with those obtained from a two-dimensional analysis for 8 mm thick sample and the width equal to the sample size of 10 cm to see no significant differences.

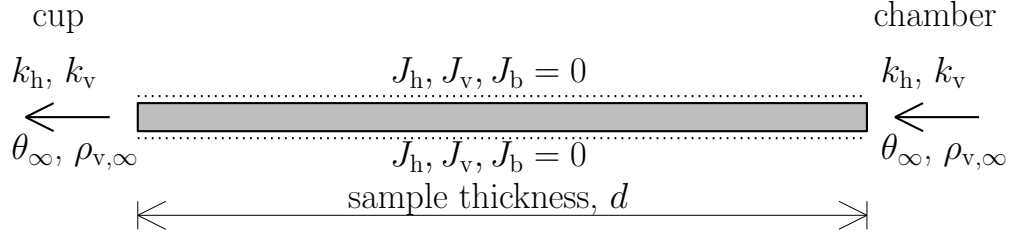


Figure 14: Geometrical domain with prescribed boundary conditions

To revisit the experimental measurements of the effective coefficient of moisture diffusion D_L numerically we considered a one-dimensional moisture transport in the direction of lumens through a 8 mm thick sample to comply with the experimental arrangement. Similarly we adopted the initial and boundary conditions. In accord with the actual experiment the moisture and heat exchange between ambient air and wood samples was prescribed on both sides of the model boundaries utilizing the values of relative humidity and temperature collected during the experiment, see Fig. 14. To comply with the assumed formulation of moisture transport, Eq. (24) in particular, we employed Eq. (26) to convert the measured relative humidity to the calculated variable, i.e. the water vapor concentration ρ_v . In numerical simulations the prescribed quantities were introduced with the help of transfer coefficients of water vapor and temperature, which were set according to recommendations in [2] to $k_h = 5.18 \text{ W m}^{-2} \text{ K}^{-1}$ and $k_v = 8.55 \cdot 10^{-4} \text{ ms}^{-1}$.

Table 7: Effective coefficients of moisture diffusion

Method	$D_L [\text{m}^2 \text{s}^{-1}]$	$D_R [\text{m}^2 \text{s}^{-1}]$	$D_T [\text{m}^2 \text{s}^{-1}]$
Experiment (D^{exp})	$5.1 \cdot 10^{-6}$	—	—
Numerical analysis (D^{num})	$4.6 \cdot 10^{-6}$	$2.3 \cdot 10^{-10}$	$2.3 \cdot 10^{-10}$
Homogenization (D^{hom}) - 2 steps	$16.7 \cdot 10^{-6}$	$5.4 \cdot 10^{-12}$	$5.9 \cdot 10^{-12}$
Homogenization (D^{hom}) - 1 step	$16.7 \cdot 10^{-6}$	$5.2 \cdot 10^{-12}$	$6.2 \cdot 10^{-12}$

The effective moisture diffusivities were then computed from averaging the local diffusion fluxes, i.e. the flux of bound water and the flux of water vapor, divided by the macroscopic gradient of bound water at the end of numerical analysis when arriving at the stationary state of moisture

$$D_L^{\text{num}} = \frac{\langle J_L(\mathbf{x}) \rangle}{\langle \nabla_L \rho_b(\mathbf{x}) \rangle}. \quad (37)$$

Although not measured, the moisture transport in the transverse direction was also examined. The results appear in Table 7. The predictions provided by analytical homogenization

briefly mentioned in Section 4.2 are also presented. Both 2-step homogenization considering earlywood, latewood and growth rings separately and 1 step homogenization adopting the equivalent wood at the level of lumens are compared. We see that predictions along the longitudinal directions are found within the same order of magnitude, while the results of numerical calculations and homogenization corresponding to R,T directions differ significantly. Note that the former one relies on the application of Eq. (34), recall the results plotted in Fig. 13(b). This can be attributed to the fact that in plane normal to lumens the cell wall provides a strong barrier for the water vapor transport as there is no interconnection of lumens. Such obstacle could be overcome by examining the real microstructure with the help of X-ray microtomography combined with numerical homogenization based, e.g. on Extended Finite Element Method. Some initiatives can be found in [64]. The application of Eq. (34) thus seems from the engineering point of view appropriate.

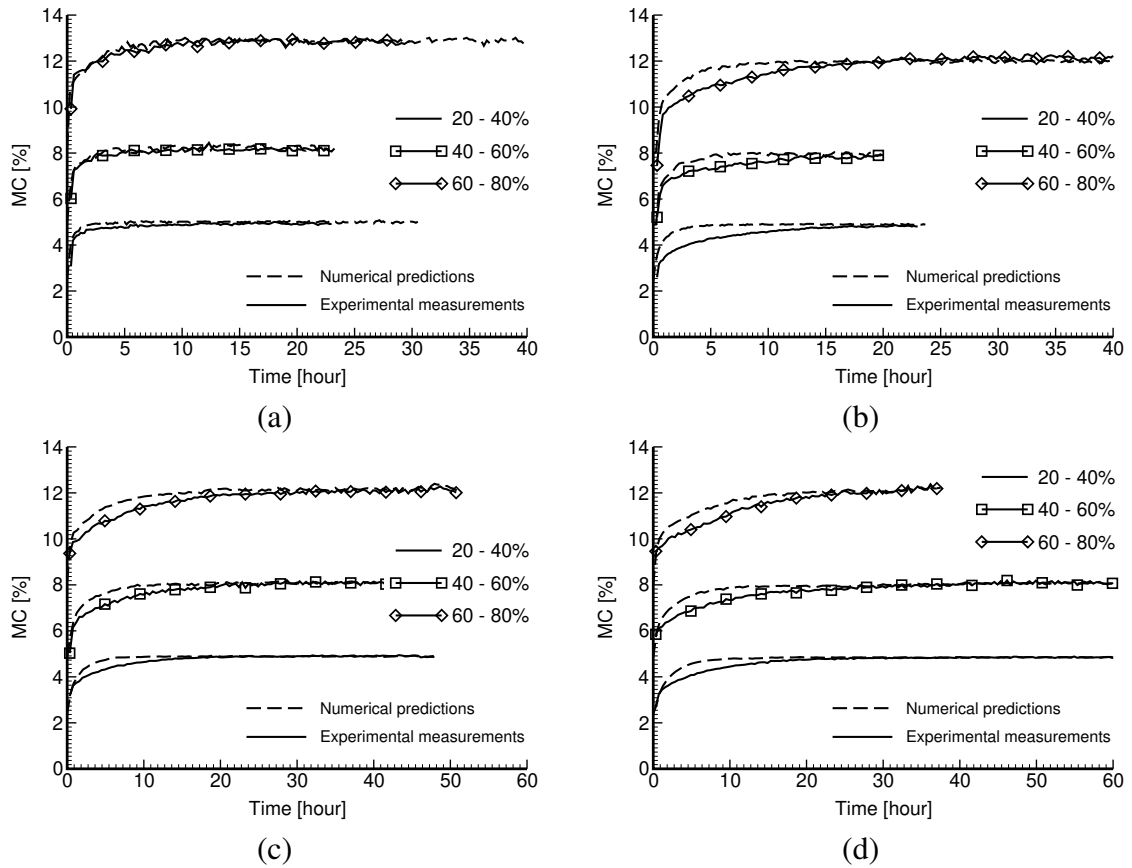


Figure 15: Moisture uptake in longitudinal (L) direction comparing numerical simulations and experimental observations for various specimen thicknesses d : a) $d = 2$ mm, b) $d = 4$ mm, c) $d = 6$ mm, d) $d = 8$ mm

When simulating the non-stationary moisture transport in the cup the same computational model as used previously was exploited. The boundary conditions were also prescribed analogously reflecting the actual measurements, recall again Section 2.2, taking into account the time evolution of relative humidities in the chamber and the cup as displayed in Fig. 3. These were introduced through the Robin BC [55]. As for the bound water the natural or Neumann BC were considered [22]. The results are plotted in Figs. 15 and 16 for the longitudinal (along lumens) and transverse (perpendicular to lumens) directions, respectively, for all examined thicknesses and three loading steps of relative humidity. Clearly,

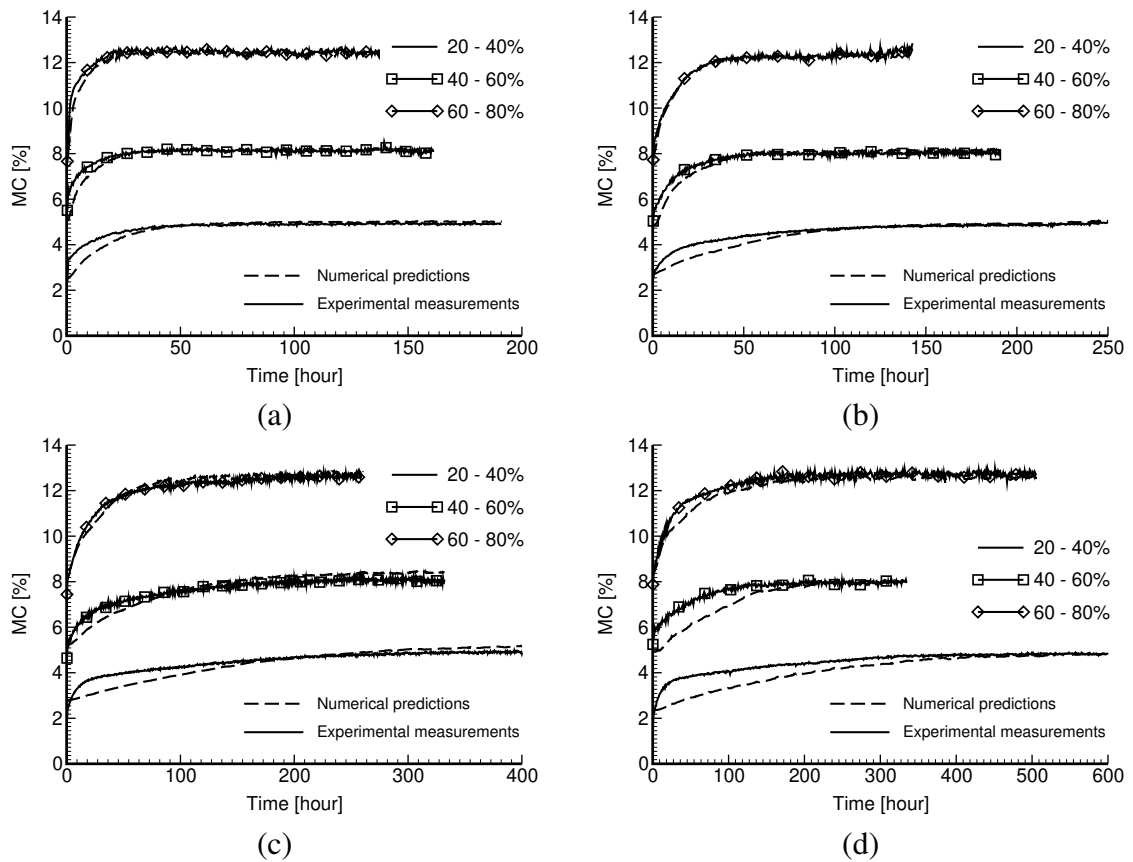


Figure 16: Moisture uptake in transverse (T) direction comparing numerical simulations and experimental observations for various specimen thicknesses d : a) $d = 2$ mm, b) $d = 4$ mm, c) $d = 6$ mm, d) $d = 8$ mm

the numerical simulations tend to approach the measurements at steady state conditions for all sample thicknesses and all loading steps. The major deviation can be observed at initial stages of transport process for both directions, particularly for lower moisture contents and larger thicknesses. This can be attributed to the fact that the assumption of one dimensional moisture transport is no longer valid. From the engineering point of view the agreement seems therefore satisfactory. Recall that, apart from the estimated volume fraction of lumens and the measured sorption isotherm, no particular adjustments to the model parameters were made thus further promoting the adopted empirical relations for ρ , λ , D_v , D_b presented in Section 4.2.

5. Conclusions

Two specific areas in wood engineering concerned with response of wood exposed to moisture were reviewed. Emphasis was placed on close interaction between computational and experimental aspects of research. In this regard it is worth mentioning that all specimens used in the present as well as in the accompanied experimental campaign in [42] were collected from one particular lamella of a glued laminated timber beam tested in [43]. Therefore, the microstructural details needed in computational part were extracted from the same piece of wood as used in determining its bulk response experimentally. This allowed us to validate the theoretical assumptions, stated in Section 1, in connection to experimental investigation more reliably.

In the analysis of heterogeneous materials the number of assumptions supplanting the lack of information can be reduced through a hierarchical modeling. This approach was adopted when predicting the macroscopic coefficients of hygroexpansion computationally. Therein, we settled for literature data pertinent to the cell wall level only while adopting further information needed in homogenization steps on individual scales from detailed inspection of wood microstructure. Then, combining the Mori-Tanaka micromechanical model at the cell wall level and PUC at the level of equivalent wood provided the bulk coefficients of hygroexpansion well supported by experimental measurements. Since experiencing some inconsistencies when comparing the present results with those available in literature, recall Table 5 and the discussion in Section 2.3, the experimental program continues aiming also at the identification of experimental error with the help of Bayesian inference [43, 42].

However, the detailed information are often not available which precludes advanced analyses and calls for purely phenomenological modeling. In many applications such an approach is sufficiently accurate, generally much more efficient and thus appealing to practical engineers. This is demonstrated in the second part of this contribution devoted to the analysis of transient moisture transport. Therein, the non-Fickian model combined with energy balance equation was implemented in the form proposed in [22]. Apart from the measured sorption isotherm, all material data and relations were taken from literature with no additional adjustments. Comparing experimental measurements with numerical simulation of cup experiment clearly promotes applicability of such an approach further supported by close match of the effective coefficients of thermal conductivity and moisture diffusivity provided by both phenomenological expressions and homogenization.

Successfully completing the above mentioned tasks makes possible to determine the moisture induced strains in continuously evolving environment. Their introduction in the mechanical part of a general hygro-thermo-mechanical analysis in the form of staggered solution now opens the way to damage analysis of wood caused by moisture swelling in constrained material or structural systems.

Acknowledgment

We are thankful for financial support provided by the Czech Grant Agency, project No. 18-05791S.

- [1] M. Šejnoha, J. Zeman, *Micromechanics in Practice*, WIT Press, Southampton, Boston, 2013.
- [2] J. Eitelberger, K. Hofstetter, S. V. Dvinskikh, A multi-scale approach for simulation of transient moisture transport processes in wood below the fiber saturation point, *Composites Science and Technology* 71 (15) (2011) 1727–1738.
- [3] A. Rafsanjani, C. Lanvermann, P. Niemz, J. Carmeliet, D. Derome, Multiscale analysis of free swelling of Norway spruce, *Composites: Part A* 54 (2013) 70–78.
- [4] S. Fortino, F. Mirianon, T. Toratti, A 3D moisture-stress FEM analysis for time dependent problems in timber structures, *Mechanics of Time-Dependent Materials* 13 (2009) 333–356.

- [5] M. Häglund, Parameter influence on moisture induced eigen-stresses in timber, *European Journal of Wood and Wood Products* 68 (2010) 397–406.
- [6] S. Ormarsson, O. Dahlblom, Finite element modelling of moisture related and visco-elastic deformations in inhomogeneous timber beams, *Engineering Structures* 49 (2013) 182–189.
- [7] T. Gereke, P. Hass, P. Niemz, Moisture-induced stresses and distortions in spruce cross-laminates and composite laminates, *Holzforschung* 64 (2010) 127–133.
- [8] M. Fragiaco, S. Fortino, D. Tononi, I. Usardi, T. Toratti, Moisture-induced stresses perpendicular to grain in cross-sections of timber members exposed to different climates, *Engineering Structures* 33 (2011) 3071–3078.
- [9] D. Konopka, M. Kaliske, Transient multi-fickian hygro-mechanical analysis of wood, *Computers & Structures* 197 (2018) 12–27.
- [10] D. Dang, R. Moutou Pitti, E. Toussaint, M. Grédiac, Investigating wood under thermo-hydrmechanical loading at the ring scale using full-field measurements, *Wood Science and Technology* 52 (2018) 1473–1493.
- [11] E. Bartůňková, Constitutive model of timber, Master's thesis, Czech Technical University in Prague, Faculty of Civil Engineering (2012).
- [12] E. Šmídová, P. Kabele, Constitutive model for timber fracture under tensile and shear loads, *Applied Mechanics and Materials* 784 (2015) 137–144.
- [13] E. Šmídová, P. Kabele, Constitutive model for timber fracture used for FE simulation of VLF arch, *Acta Polytechnica CTU Proceedings* 15 (2018) 109–113.
- [14] J. Vorel, P. Kabele, Inverse analysis of traction-separation relationship based on sequentially linear approach, *Computers and Structures*, <https://doi.org/10.1016/j.compstruc.2018.10.005>.
- [15] J. Dvorak, *Micromechanics of composite materials*, Dordrecht : Springer, 2013.
- [16] K. Persson, *Micromechanical modelling of wood and fibre properties*, Ph.D. thesis, Lund University (2000).
- [17] D. Keunecke, K. Novosseletz, C. Lanvermann, D. Mannes, P. Niemz, Combination of X-ray and digital image correlation for the analysis of moisture-induced strain in wood: opportunities and challenges, *European Journal of Wood and Wood Products* 70 (2012) 407–413.
- [18] C. Lanvermann, S. Sanabria, D. Mannes, P. Niemz, Combination of neutron imaging (NI) and digital image correlation (DIC) to determine intra-ring moisture variation in Norway spruce, *Holzforschung* 68 (2014) 113–122.
- [19] J. Eitelberger, K. Hofstetter, A comprehensive model for transient moisture transport in wood below the fiber saturation point: Physical background, implementation and experimental validation, *International Journal of Thermal Science* 50 (2011) 1861–1866.

- [20] J. Eitelberger, S. Svensson, K. Hofstetter, Theory of transport processes in wood below the fiber saturation point. Physical background on the microscale and its macroscopic description, *Holzforschung* 65 (3) (2011) 337–342.
- [21] K. Krabbenhoft, L. Damkilde, A model for non-fickian moisture transfer in wood, *Materials and Structures* 37 (9) (2004) 615–622.
- [22] H. L. Frandsen, L. Damkilde, S. Svensson, A revised multi-Fickian moisture transport model to describe non-Fickian effects in wood, *Holzforschung* 61 (5) (2007) 563–572.
- [23] J. Eitelberger, K. Hofstetter, Prediction of transport properties of wood below the fiber saturation point—A multiscale homogenization approach and its experimental validation: Part I: Thermal conductivity, *Composites Science and Technology* 71 (2) (2011) 134–144.
- [24] J. Eitelberger, K. Hofstetter, Prediction of transport properties of wood below the fiber saturation point A multiscale homogenization approach and its experimental validation. Part II: Steady state moisture diffusion coefficient, *Composites Science and Technology* 71 (2) (2011) 145–151.
- [25] Z. Bittnar, J. Šejnoha, *Numerical methods in structural engineering*, ASCE Press, 1996.
- [26] R. M. Nelson, A model for sorption of water vapor by cellulosic materials, *Wood Fiber Science* 15 (1) (1983) 8–22.
- [27] E. Timmermann, Multilayer sorption parameters: BET or GAB values?, *Colloids and Surfaces A: Physicochemical and Engineering Aspects* 220 (2003) 235–260.
- [28] C. Zuritz, R. Singh, S. Moini, H. S.M., Desorption isotherms of rough rice from 10 degree to 40 degree C, *Transactions of the American Society of Agricultural Engineer* 22 (1979) 433–440.
- [29] Z. Pavlík, I. Žumár, J. ans Medved, R. Černý, Water vapor adsorption in porous building materials: Experimental measurement and theoretical analysis, *Transport in Porous Media* 91 (2012) 939–954.
- [30] O. Vololonirina, M. Coutand, B. Perrin, Characterization of hygrothermal properties of wood-based products - impact of moisture content and temperature, *Construction and Building Materials* 63 (2014) 223–233.
- [31] R. Černý, P. Rovnaníková, *Transport properties in concrete*, Spon Press, 2002.
- [32] J. Eitelberger, S. Svensson, The sorption behavior of wood studied by means of an improved cup method, *Transport in Porous Media* 92 (2) (2012) 321–335.
- [33] EN ISO 12572, *Hygrothermal performance of building materials and products - Determination of water vapour transmission properties - Cup method*, 2011.
- [34] Z. Pavlík, J. Fořt, M. Pavlíková, J. Pokorný, A. Trník, R. Černý, Modified lime-cement plasters with enhanced thermal and hygric storage capacity for moderation of interior climate, *Energy and Buildings* 126 (2016) 113–127.

- [35] B. Pan, D. Yu, L. Wu, L. Tang, Systematic errors in two-dimensional digital image correlation due to lens distortion, *Optics and Lasers in Engineering* 51 (2013) 140–147.
- [36] C. Lanvermann, F. K. Wittel, P. Niemz, Full-field moisture induced deformation in norway spruce: intra-ring variation of transverse swelling, *European Journal of Wood and Wood Products* 72 (2014) 43–52.
- [37] J. Mallet, S. Kalyanasundaram, P. D. Evans, Digital image correlation of strains at profiled wood surfaces exposed to wetting and drying, *Journal of Imaging* 4 (2018) 38.
- [38] V. Nežerka, Ncorr-post: DIC Post-Processing Tool, Tech. rep., CTU in Prague, Czech Republic (2014).
- [39] V. Nežerka, Ncorr-post-CSTool: ...DIC Post-Processing Tool to Display Strains along Cross-Section, Tech. rep., CTU in Prague, Czech Republic (2015).
- [40] K. Hofstetter, C. Hellmich, J. Eberhardsteiner, Development and experimental validation of a continuum micromechanics model for the elasticity of wood, *European Journal of Mechanics - A/Solids* 24 (6) (2005) 1030–1053.
- [41] L. Donaldson, Microfibril angle: measurement, variation and relationships – a review, *Iawa Journal* 29 (4) (2008) 345–386.
- [42] M. Šejnoha, T. Janda, J. Vorel, L. Kucíková, P. Padevět, V. Hrbek, Bayesian inference as a tool for improving predictions of effective elastic properties of wood, *Computers and Structures* 0 (2018) 0–0, accepted.
- [43] M. Šejnoha, T. Janda, L. Melzerová, V. Nežerka, J. Šejnoha, Modeling glulams in linear range with parameters updated using Bayesian inference, *Engineering Structures* 138 (2017) 293–307.
- [44] P. O. Kettunen, *Wood: Structure and Properties*, Material Science Foundation, Trans Tech Publications Limited, 2006.
- [45] L. Kucíková, Micromechanical study of spruce wood, Master’s thesis, Czech Technical University in Prague (2018).
- [46] H. E. Desch, J. M. Dinwoodie, *Timber: Structure, Properties, Conversion and Use*, 7th edition, Macmillan Press, Hampshire, 1996.
- [47] Y. Benveniste, A new approach to the application of Mori-Tanaka theory in composite materials, *Mechanics of Materials* 6 (1987) 147–157.
- [48] G. Milani, P. Lourenco, Monte Carlo homogenized limit analysis model for randomly assembled blocks in-plane loaded, *Computational Mechanics* 46 (6) (2010) 827–849.
- [49] G. Milani, P. Lourenco, A simplified homogenized limit analysis model for randomly assembled blocks out-of-plane loaded, *Computers & Structures* 88 (2010) 690717.

- [50] S. Tiberti, G. Milani, L. Macorini, A novel pixel limit analysis homogenization model for random masonry, in: P. T. E. Simos (Ed.), ICNAAM 2017, XV International Conference on Numerical Analysis and Applied Mathematics, Thessaloniki, Greece, 25-30 September, AIP Conference Proceedings 1978, 2018.
- [51] J. Zeman, M. Šejnoha, From random microstructures to representative volume elements, *Modelling and Simulation in Materials Science and Engineering* 15 (4) (2007) S325–S335.
- [52] R. Hill, Elastic properties of reinforced solids - Some theoretical principles, *Journal of the Mechanics and Physics of Solids* 11 (1963) 357–372.
- [53] J. C. Michel, H. Moulinec, P. Suquet, Effective properties of composite materials with periodic microstructure: A computational approach, *Computer Methods in Applied Mechanics and Engineering* 172 (1999) 109–143.
- [54] S. Urbanová, J. Vorel, M. Šejnoha, The influence of different implementation of periodic boundary conditions into FEM software, in: V. Fuis (Ed.), 20th International Conference Engineering Mechanics 2014, Brno University of Technology Institute of Solid Mechanics, Mechatronics and Biomechanics, 2014, pp. 672–675.
- [55] J. Sýkora, Modeling of degradation processes in historical mortars, *Advances in Engineering Software* 72 (2014) 203–212.
- [56] G. Tsoumis, *Science and technology of wood: Structure, properties, utilization*, Chapman & Hall, NY, 1991.
- [57] Forest Products Laboratory, *Wood Handbook: Wood as an Engineering Material*, United States Department of Agriculture Forest Service, Madison, Wisconsin, 2010.
- [58] F. Kollmann, *Technologie des Holzes und der Holzwerkstoffe*, Berlin: Springer-Verlag, 1982.
- [59] R. Schirmer, *Die diffusionszahl von wasserdampf-luft-gemischen und die verdampfungsgeschwindigkeit*, Ph.D. thesis, Technische Hochschule München (1938).
- [60] C. Skaar, J. F. Siau, Thermal diffusion of bound water in wood, *Wood Science and Technology* 15 (1981) 105–112.
- [61] J. F. Siau, *Transport Processes in Wood*, Springer-Verlag, 1984.
- [62] J. F. Siau, Influence of moisture on physical properties, Tech. rep., Department of Wood Science and Forest Products, Virginia Polytechnic Institute and State University (1995).
- [63] L. Wadsö, Unsteady-state water vapor adsorption in wood: An experimental study, *Wood and Fiber Science* 26 (1) (2007) 36–50.
- [64] M. Šejnoha, L. Kucíková, J. Vorel, J. Sýkora, W. De Wilde, Effective material properties of wood based on homogenization, *International Journal of Computational Methods and Experimental Measurements* 7 (2) (2019) 167–180.

List of symbols

A	Area, [m ²]
α	Hygroexpansion coefficient, [–]
c	Specific heat capacity, [Jkg ⁻¹ K ⁻¹]
d	Thickness, [mm], [m]
D	Diffusion coefficient, [ms ⁻²]
Δh	Specific enthalpy of the phase transition, [Jkg ⁻¹]
E	Young's modulus, [Pa]
ε	Strain, [–]
σ	Stress, [Pa]
f	Volume fraction, [–]
G	Shear modulus, [Pa]
h	Specific enthalpy, [Jkg ⁻¹]
φ	Relative humidity, [–]
J	Flux, [Wm ⁻²], [kgm ⁻² s ⁻¹]
k	Transfer coefficient, [Wm ⁻² K ⁻¹], [ms ⁻¹]
λ	Thermal conductivity, [Wm ⁻¹ K ⁻¹]
M	Molar mass, [kgmol ⁻¹]
m	Mass, [kg]
ν	Poisson's ratio, [–]
p	Pressure, [Pa]
R	Gas constant, [Jmol ⁻¹ K ⁻¹]
ρ	Density of wood, concentration, [kgm ⁻³]
ρ_b	Concentration of bound water, [kgm ⁻³]
ρ_v	Concentration of water vapor, [kgm ⁻³]
$\dot{\rho}$	Sorption rate, [kgm ⁻³ s ⁻¹]
σ	Stress, [Pa]
t	Time, [s]
θ	Temperature, [°C]
u	Moisture content, [–]
ξ	Reduction factor, [–]

Subscripts

CW	Cell wall
at	Atmospheric
b	Bound water
dry	Dry sample
EW	Earlywood
EqW	Equivalent wood
h	Hygroscopic, heat
lum	Lumen
LW	Latewood
sat	Saturation level
v	Water vapor
w	Water
wet	Wet sample

Abbreviations

BC	Boundary condition
DIC	Digital image correlation
FSP	Fiber saturation point
L	Longitudinal direction
MFA	microfibril angle
MC	Moisture content, [%]
PUC	Periodic unit cell
R	Radial direction
RH	Relative humidity, [%]
T	Tangential direction

Chapter 3

MODELING OF IMPACT OF FIRE ON CONCRETE

In this chapter, risk is calculated as the probable damage caused by a fire in the tunnel lining. The model is intended to be as simple as possible and still able to reflect the reality. In the first part, focused on probabilistic modeling, the traffic flow is described as a stationary Markov chain of joint states consisting of a combination of trucks/buses (TB) and personal cars (PC) from adjoining lanes. The heat release rate is then taken for a measure of the fire power and two probability mass functions of this variable are suggested for one TB and two TBs, respectively. The intensity λ_f reflecting the frequency of fires was assessed based on extensive studies carried out in Austria and Italy. Eventually, the traffic density AADT, the length of the tunnel L , the percentage of TBs, and the number of lanes are the remaining parameters characterizing the traffic flow. In the second part, a special combination of models originally proposed by Bažant and Thonguthai, and Künzel & Kiessl for the description of transport processes in concrete at very high temperatures creates a basis for the prediction of the thickness of the spalling zone and the volume of concrete degraded by temperatures that exceeded a certain temperature level. The model was calibrated by fitting its parameters against a macroscopic test on concrete samples placed into the furnace. Though effective and easy to apply, there is room for the model as a whole to be gradually improved. These possibilities are outlined in conclusions.

List of selected journal papers and book chapters

Sýkora, J., Jarušková, D., Šejnoha, M., and Šejnoha, J. (2018). Fire risk analysis focused on damage of the tunnel lining. *Fire Safety Journal*, 95:51–65.

List of related journal papers and book chapters

Šejnoha, J., Sýkora, J., Jarušková, D., Novotná, E., and Šejnoha, M. (2015). Analýza rizika požáru v silničních tunelech. *BETON-technologie*, 15(6):68–72.

Fire risk analysis focused on damage of the tunnel lining

Jan Sýkora

Faculty of Civil Engineering, Czech Technical University in Prague, Thákurova 7, 166 29 Prague 6, Czech Republic

Daniela Jarušková

Faculty of Civil Engineering, Czech Technical University in Prague, Thákurova 7, 166 29 Prague 6, Czech Republic

Michal Šejnoha

Faculty of Civil Engineering, Czech Technical University in Prague, Thákurova 7, 166 29 Prague 6, Czech Republic

Jiří Šejnoha

Faculty of Civil Engineering, Czech Technical University in Prague, Thákurova 7, 166 29 Prague 6, Czech Republic

Keywords: Risk, Traffic flow, Fire-induced spalling, Concrete, Tunnel lining, Damage

1. Introduction

The aim of this paper is to propose a methodology for fire risk analysis focused downright on damage of the tunnel lining. This allows the designer estimating the probable damage to the lining and, in the end, making use of this prediction when deciding on Fire Safety Strategy. Throughout the paper, we therefore rely on a standard definition of risk as the the product of the probability of a fire incident and damage, i.e. the probable amount of money to be spent to eliminate the consequences of the fire incident. Such an approach can be extended considering a group of incident scenarios, which could affect a defined area. In fire risk-informed evaluations one is concerned with how the performance of fire protection systems (FPS) mitigates an existing risk level. According to [1, Chap. 88], the following three factors play a decisive role: (i) frequency of the initiating event, (ii) probability of the failure of FPS performance, (iii) expected consequences (damage). Apart from the installation of automatic FPS in tunnels, the following loss prevention and mitigation measures are recommended, see. e.g. [1, Chap. 88], [11]: (i) use of non-combustible and non-toxic construction materials for the tunnel structure and pavement, (ii) provision of emergency ventilation and the smoke control system to maximize the exhaust rate in the ventilation zone that contains the fire and to minimize the amount of outside air that is introduced, (iii) establishment of adequate emergency response planning.

Email addresses: jan.sykora.1@fsv.cvut.cz (Jan Sýkora), Daniela.Jaruskova@cvut.cz (Daniela Jarušková), sejnom@fsv.cvut.cz (Michal Šejnoha), sejnoha@fsv.cvut.cz (Jiří Šejnoha)

Thus, the risk analysis monitors both probabilistic and economic viewpoints and interacts with the risk management and live safety. A large number of papers have been published on this topic. Handbooks [1, 2] represent a rich seam of knowledge and experience. The probability of a fire is related either to the frequency of a traffic accident (a collision of two or more vehicles) or of any event causing the vehicles' inflammation (overheating of the engine, brakes, leakage of fuel, etc.).

In order to address the fire risk assessment as a whole, the paper is composed of two parts. In the first part, the probabilistic concept of the fire appearance in a road tunnel will be outlined. The second part then concentrates on the prediction of the amount of material degraded during a fire.

Probabilistic analysis of tunnels has been studied for many years in Japan (see e.g. [3, 5]). A summary of the Japanese approach to the road tunnel safety is contained in [6, 9]. The data concerning the USA can be found in e.g. [2, Chap. 1], [4, 7, 8], and/or Australia (see e.g. [2]). In this paper, to demonstrate that our methodology is viable, we focus our attention on the findings of two extensive studies carried out in Austria [15] and Italy [16, 17], which will be now briefly commented on and exploited. According to the ASFiNAG report [15], a spontaneous ignition prevails against the fire as an after effect of the collision, namely as for passenger cars (PC) in the ratio of 86 [%] : 14 [%] and 97 [%] : 3 [%] in the case of trucks and buses (TB). The Austrian study carried out in 2006-2012 keeps a record of 67 fires per $10.3 \cdot 10^9$ vehicle-kilometers [veh. km] traveled in tunnels. The results are put clearly in Tab. 1¹.

Type of vehicle	Number of fires	10^9 [veh. km] traveled in tunnels (2006-2012)	Number of fires per 10^9 [veh. km]
all	67	10.3	6.5
PC	38	9.1	4.5
TB	30	1.2	25.0

Table 1: Frequency of fires in Austrian tunnels, see [15]

The results of an analogous study carried out in Italy within the period of 2006-2009 have been summarized in [16]. The study covers 195 one-way tunnels, from which 172 have two lanes and 23 three lanes, and records 762 serious accidents (662 in two-lane and 94 in three-lane tunnels). During the study period, the fire was recorded in 45 tunnels out of all investigated (35 in two-lane and 10 in three-lane tunnels).

Both studies serve as a source of information on the traffic intensity, which is of paramount importance when estimating the probability of extraordinary events. It ensues from the available data (see, e.g. [16]) that the severe accident rates in the investigated tunnels due to traffic are in general higher than those on free stretches of corresponding motorways. Moreover, it has been suggested in [16] that severe accident cost rates of road tunnels are higher than those on the respective motorways in about four-fifths of the monitored tunnels. However, this piece of knowledge should not be overestimated and even go as far as to claim that the safety in tunnels is always lower than on motorways. And besides, this finding contra-

¹Tab. 1 implies that in one case two cars were involved in the fire as a consequence of the collision of PC and TB.

dicts that in [9]. Apart from the behavior of drivers and visibility, the frequency of severe accidents is affected by the geometric and traffic characteristics of the tunnel (ascending, descending, curvature, etc.). Combining these attributes may yield higher or lower safety in tunnels compared to free stretches. Another statistical analysis of traffic accidents and interesting complementary data can be found, e.g. in [18] and [19]. With reference to fire accidents, a comparison between fire accident rates and traffic accident rates in tunnels was made in [16] without distinguishing between two-lane and three-lane tunnels. More especially fire accident rate was found to be between one half and one fourth of that due to traffic.

From the probabilistic point of view the fire occurrence is regarded as part of the Poisson process characterized by its intensity (see the last column in Tab. 1), which is equal to both the mean value and the variance of the process. In many situations, however, incident counts appear to be "overdispersed" with respect to the prediction based on the Poisson model. To overcome this discrepancy, Caliendo et al. [17] recommended utilizing the negative binomial model. Exploiting the generalized linear model of regression analysis, the following variables were detected as most affecting the process: (i) the traffic density AADTL (annual average daily traffic per lane), (ii) the length of the tunnel L [m], (iii) the percentage of trucks and (iv) the number of lanes.

The second factor affecting the extent of damage due to a fire in a tunnel and corresponding financial costs is, barring the probability of fire occurrence, the evolution of the fire. In this regard the ASFiNAG report draws attention to these two parameters:

- The first one is the evolution rate (Entwicklungsgeschwindigkeit in the original report). The statistics of ASFiNAG distinguishes between the slow rate of fire after a smoke (langsam nach Rauch) and explosion. The latter one, however, is not considered in this paper.
- The second parameter accentuated in [15] is the peak of the heat release rate (HRR).

As stressed in [1, Chap. 26], the HRR is the essential characteristic that describes quantitatively "How big is fire?" It has been described in [10] as the single most important variable in fire hazard. Undoubtedly, explosions and fires are different phenomena which need to be treated as such. Similarly, the HRR is a complex and transient phenomenon that is strongly affected by ventilation and vice versa². These problems are discussed in detail elsewhere (see, e.g. [1, 2]). With regard to the risk analysis it should be emphasized that there are a number of scenarios affecting both the maximum value of the HRR and its evolution in time. The problem lies not only in the configuration of vehicles involved in a fire or in the fire-wall linings interaction, but also in selecting the models considering certain dangerous goods, see e.g. [12]. While studies of a fire can be carried out either numerically using e.g. the CFD code, or experimentally on macro-scale or in a 1/3 scale tunnel [13] (differences between numerical and experimental data being around 19 [%]), the probabilities of individual scenarios are not known and need to be estimated - based on expert judgment and experience, e.g. using FMA.

²In relatively old tunnels the main purpose of ventilation was to evacuate toxic flames released from vehicles only. In more recent tunnels, in all cases the use of existing emergency ventilation systems, intended to remove smoke and heated gases has resulted in aggravated damage to tunnel's concrete structure and to whatever was inside them (see [11]).

A prevailing portion of fires with a known cause (60 events, i.e. 92 [%] reported in [15]) originates from self-ignition (Selbstentzündung in the original paper), i.e. with no foregoing accident. The remaining 5 events, i.e. 8 [%], may be split in around two halves - accidents of single cars and the collision with other vehicles. Two causes were unknown. The spontaneous ignition of PCs was mostly followed by a slow evolution of the fire (92 [%]) while explosion arrived in 8 [%]. On the other hand, as an aftereffect of the accident the slow evolution of the fire and the explosion of PCs were equally probable. The fire evolution of TBs is different. The spontaneous ignition was followed by a slow evolution (80 [%]) and the explosion was triggered out in 20 [%] of cases. Just one explosion after the collision of two cars (1 TB and 1 PC) was reported in [15]. These data come from fire incidents reported in Austria. In other countries they could be different, which must be taken into consideration in particular risk analyses. It follows that there are uncertainties on both parts of the model and both the assessment of the event's probability and consequences should be balanced out. As to the fire of PCs, fully developed and undeveloped (doused) fires are distinguished. In the case of TB, the fire of the cab must be differentiated from the fully developed fire of the whole vehicle. Due to insufficient data, HRR and the frequency of the fire occurrence have been predicted in an expert way by means of event tree analysis [15]. More details about the traffic flow and the fire itself are summarized in Sec. 2.

Based on the data about the traffic flow and fire characteristics, a simple probabilistic model is proposed in Sec. 3. The traffic flow in multiple lanes is described as the stationary Markov process with a given number of states. The data on fires will be exploited in the second part of this paper to analyze the degree of degradation afflicting the tunnel lining. This includes the total volume of material loss and the volume of material exhibiting a strength reduction due to exposure of concrete to high temperatures. Both outcomes are affected by spalling. A number of popular fire spalling theories are available in literature. Their summary can be found, e.g. in [47]. In the present study, when making reference to this phenomenon, we consider its direct consequence, i.e. the reduction of thickness of structural members. The volume of material loss will be thought to be caused by the buildup of pore pressure, see Sec. 4. Other mechanisms such as restrained thermodilation may indirectly affect the pore pressure buildup and temperature dependent tensile strength of concrete [22]. Thus those mechanisms are included in the model.

Since it is difficult to monitor spalling in the fire test we combine the loss of material during early stages of heat exposure ("spalling as an explosive failure") and the subsequent concrete fall-off due to prolonged heat exposure into a common volume of material loss. This is also the key assumption when calibrating the material model on the basis of a macroscopic fire test.

Again, modeling of impact of fire on concrete has received a considerable attention in literature, see e.g. [20] ÷ [25]. In part 1 of the paper by Gawin et al., see [26], the physical phenomena, and the heat and mass flux and sources in a concrete element were studied. Then, the mathematical model of concrete was presented and all constitutive relations of the model were summarized and discussed. In part 2, see [27], a literature review of the existing models of concrete at high temperatures and a summary of their main features were presented. To evaluate the difference between the results obtained with simplified models and the very complex one proposed in Part 1, an extensive numerical study was performed. In quest for a cogent yet effective model which would be less demanding for computer time, with regard to probabilistic calculations, a special combination of models originally proposed by Bažant–

Thonguthai [28] and Künzel and Kiessl [29] is presented in this paper. The mathematical aspects of a coupled model based on similar assumptions to our approach were discussed in [34]. It is relatively simple, and despite the fact that cross-effects between heat and mass fluxes are missing, it describes all substantial phenomena and its results comply well with experimentally obtained data (see Sec. 4). The only exception is a certain discrepancy in the prediction of temperature distribution after a long-range fire exposure (over 3 hours). It is assumed to be the consequence of the model simplification, neglecting the effect of the dry air pressure which dominates the water vapor pressure after the maximum of the gas pressure has been overstepped. When calibrating the model against the experiments carried out in the furnace, the findings of Davie et al. [23] were taken into consideration. It was proved that the most significant of all were the relationships chosen to define the relative permeabilities. These were shown to strongly control the results of analyses of both low and high temperature problems and to potentially imply apparently different permeability values for the same concrete.

In the present context the model allows us not only to identify the volume of material loss but also, as a consequence of a subsequent heat penetration to the material, the potential reduction of temperature dependent tensile strength of concrete [32, 33]. It is worth mentioning that both scenarios contribute to the total volume of material indicated here as damaged (both removed and degraded) and considered in the calculation of risk.

To reliably predict the volume of damaged material requires a proper definition of heat load. The report [35] as well as [2, Chap 13], set forth simple yet reliable formulas, adopted also in the present study, for the description of the phenomena accompanying a fire. The ones of the utmost importance are: (i) the heat release rate, Q [MW], (ii) the peak of the heat release rate, (iii) the fire growth rate, dQ/dt [kW s^{-1}], (iv) the gas temperature beneath the tunnel ceiling. Ingason et al. presented the results from a series of tests in a model tunnel (1 : 23) in [36, 37]. The tests were carried out with longitudinal ventilation under different fire conditions thus providing new data to investigate the effects of longitudinal ventilation on the fire growth rates and backlayering length in tunnels. A review of the other large vehicle fire tests carried out in full-scale tunnels can be found in [1, Chap. 88], and [11]. Dangerous heavy goods transportation is one of the decisive factors when estimating the fire risk in road tunnels.

The details of the hygro-thermo-mechanical model for the prediction of damage due to a fire are addressed in Sec. 4. In Sec. 5, the model parameters will be identified from the experimentally obtained data in the furnace. The theoretical grounds developed in Sec. 3 and 4 are then combined in Sec. 6 to demonstrate the prediction of risk of a fire in a road tunnel through a numerical example under certain simplified assumptions. Conclusions and possibilities of further work on on this topic are outlined in Sec. 7.

2. Available statistical data as a basis of a probabilistic model

In this section, the results already presented in [15, 16, 17, 35] will be addressed and data on the most important statistical characteristics, as a stepping stone of the probabilistic model of a fire in a road tunnel to be developed, will be dealt with in the following order: (i) the frequency of fires, (ii) the fire power expressed via the maxima of the heat release rate Q , and (iii) the probability mass function of Q_{\max} .

2.1. Frequency of accidents and fire occurrence

To begin with, the statistics on the characteristics of traffic in tunnels and corresponding motorways presented in [16] are briefly summarized, see Tab. 2 and Tab. 3

Characteristics	Type of tunnel	Mean	Mode	Standard deviation	Minimum	Maximum
Length [km]	2 lanes	1.16	0.53	0.54	0.49	3.25
	3 lanes	0.81	0.89	0.14	0.52	0.98
AADT per direction in tunnels [veh. day ⁻¹]	2 lanes	17273	6126	8449	4500	40761
	3 lanes	23416	25533	4857	11439	32260
Percentage of trucks [%]	2 lanes	21	16	4	14	31
	3 lanes	22	23	2	17	24

Table 2: Summary statistics of the characteristics of tunnel studied in [16]

Characteristics	Mean	Mode	Standard deviation	Minimum	Maximum
Length [km]	178	131	220	24	804
AADT [veh. day ⁻¹] both directions on motorways	33121	32268	14194	8786	59090
Percentage of trucks [%]	22	22	4	14	31

Table 3: Summary statistics of the characteristics with a reference to the length of motorways containing the tunnels investigated in [16]

Recall that these characteristics most affect the plausibility of the Poisson model as well as the negative binomial model while describing the sequence of fires as a random process [17]. Before addressing the fire occurrence, it is worth mentioning the data on the rate of severe traffic accidents in Italian tunnels and corresponding motorways [16]. Based on the four year monitoring (2006-2009), a reliable assessment gives $91 \div 205$ accidents per 10^9 [veh. km] in tunnels and $80 \div 101$ accidents per 10^9 [veh. km] travelled on corresponding motorways.

Both models mentioned above are useful to estimate the model parameters needed for the prediction of the probability of fire occurrence. Report [15] serves as a guideline for such a prediction providing the data that allow us to assess the rate of fires as the number of fires per 10^9 [km] travelled in tunnels. The results are summarized in Tab. 4. In this table, the total number of fires is classified into two categories, namely fires brought about by (i) self-ignition, and (ii) subsequent fires after a collision. Alpine tunnels are held responsible for a distinctly higher number of TB fires for which self-ignition is the prevailing cause of the fire. These values are seven times higher in mountains than in the flat country, where, however, the subsequent fire mostly emerges after a collision.

The fire frequency data are issued in [16] without compartmentalizing the fires according to the type of vehicles, so the fires are treated as a whole. On the other hand, they are distinguished with respect to the number of lanes (see Tab. 5). The results in Tab. 5 were

Type of vehicle	Number of fires per 10 ⁹ [veh. km]	Self-ignition [%]	Subsequent fire [%]
PC	4.2	3.6	0.6
TB	25.0	24.3	0.7

Table 4: Frequency of fire occurrence (the number of fires per 10⁹ [veh. km] in Austria), source [15]

Type of vehicle	Type of tunnel	Frequency of fire occurrence
All types of vehicles	2 lanes	33.3
	3 lanes	40.8

Table 5: Frequency of the fire occurrence λ_f [fires (veh.km)⁻¹] (the number of fires per 10⁹ [veh. km] in Italy, source [16])

calculated from the following formula

$$\lambda_f \text{ [fires (veh.km)}^{-1}] = \frac{N_f}{365 \{AADT\} L_{ref}}, \tag{1}$$

where N_f [fires year⁻¹] is the average annual number of fires monitored in tunnels with their total length L_{ref} [km] and the average annual daily traffic AADT [veh. day⁻¹] (see Tab 6).

Type of tunnel	N_f	$L_{ref} = \sum L_i$ [km]	AADT [veh. day ⁻¹]
2 lanes	9.5	46.2	16931
3 lanes	5.0	8.3	24247

Table 6: Summary statistics of the characteristics of tunnels with recorded fire occurrence, source [16]

In fire risk analysis, the parameter λ_f will serve as the intensity of the Poisson model (Sec. 3.2).

2.2. Heat release rate and interconnected variables

As was suggested by many authors, see e.g. [1], Babrauskas in Chap. 26, Carvel and Ingason in Chap. 88, a good measure of the severity of a fire is the HRR. For a given scenario it is characterized by the actual fire growth and the maximum value of HRR. This value for different vehicle types can be estimated either based on tabulated data by technical committees such as NFPA or PIARC (using the largest test results) or on engineering methods of calculation. It was observed (see [1, Chap. 88] that the HRR per square meter of exposed fuel is generally found for most vehicles to be in a very narrow range (0.27 [MWm⁻²]-0.4 [MWm⁻²]). In HGV cargo this value ranges from 0.1 [MWm⁻²] (cellulosic materials) to 0.5 [MWm⁻²] (plastics). In the majority of cases the period of burning was relatively short (10 ÷ 20 [min]), followed by a decay which was almost as fast as the rapid growth phase.

A design fire should be at the upper bound of fire scenarios deemed likely to happen within a specified time-scale and characterized by a maximum HRR plateau, the duration of which depends on the maximum number of vehicles deemed likely to be involved in a fire. Peak fire size is influenced by longitudinal ventilation velocity and by the geometry of

the tunnel [13, 14]. The longitudinal ventilation also has a significant effect on fire growth rates [37]. In this connection the effect of water spray systems on fire needs to be briefly discussed. Even though the behavior of the fire itself might not be greatly impacted by the activation of certain types of FFFS, in some situations, such systems may have a large effect by mitigating the consequences of the fire on the structure. Water sprays have excellent thermal radiation blocking properties which serve to protect the structure, to allow the fire brigade to approach the fire to fight it, and also to prevent fire spread to other vehicles in conditions where there is no direct flame impingement, see [1, Chap. 88] and [11].

2.3. Probability mass function of Q_{\max}

According to [12], an operating method to follow in the design of fire safety can be to identify the critical scenarios that give the most significant contribution to the overall risk and then to simulate those scenarios in detail in order to define the risk reduction measures. The next step is to assign the frequency/probability of occurrence of each scenario represented by a given Q_{\max} [MW]. To this end, e.g. the authors of [12] used the well-established Europe PIARC-OECD Quantitative Risk Assessment Model (QRAM). The set of scenarios must be carefully selected for each particular tunnel considering the intention of risk analysis (the requirements to protect the structural components can be different from those for evacuation and rescue). The risk analysis as a starting point for the risk management must be able to pass judgment on alternatives and, therefore, to assess the effectiveness of both prevention measures (elimination of hazards, ignition source controls, combustible control measure) and mitigation measures (passive protection systems, detection systems and active engineering controls, active suppression systems and procedural systems). Detailed reviews of these systems are published elsewhere (see, e.g. [1, 2, 11]) and do not need repeating here. In this paper, we used as an illustrative example the Austrian model which considers three representative scenarios of fires (5 [MW], 30 [MW], 100 [MW]) with the estimated probability of their occurrence.

The distribution of Q_{\max} [MW] was obtained in [15] for trucks and buses (TB) as a combination of databases and the expert assessment exploiting event tree analysis (ETA)³, see Fig. A.14 in Appendix A. The cases when a vehicle engulfed by a fire has been pulled up before entering the tunnel are distinguished from fires developed (either fully or partly) inside the tunnel. Moreover, ETA differentiates fire situations characterized by a mere driver's cab and the fully developed fire of the vehicle as a whole.

ETA implies that just 38 [%] of all ignited vehicles will be engulfed by a partly and/or fully developed fire. Furthermore, it follows that the predicted maxima of Q [MW] are nothing like as high as the maximum, Q_{\max} [MW], attained, e.g. in the course of the first out of four fire tests in the Runehamar tunnel. The point is that ETA predicts a discrete distribution of Q_1 (index 1 indicates that just one vehicle is involved in the fire incident) with a set of outcomes $q_{1,1} = 5$ [MW] (23 [%]), $q_{1,2} = 30$ [MW] (14 [%]), and $q_{1,3} = 100$ [MW] (1 [%]). Yet it does not mean that, depending on the fire load in heavy goods (HGV) trailers, the maximum excess gas temperatures beneath the ceiling would be substantially lower than about 1350 [°C]. The power of fire manifests itself by the temperature development in time

³Extraordinary events such as violent fires in the Mont Blanc tunnel (1999), Tauern tunnel (1999) and Saint Gotthard tunnel (2001) with overall 62 casualties must be analyzed ad hoc.

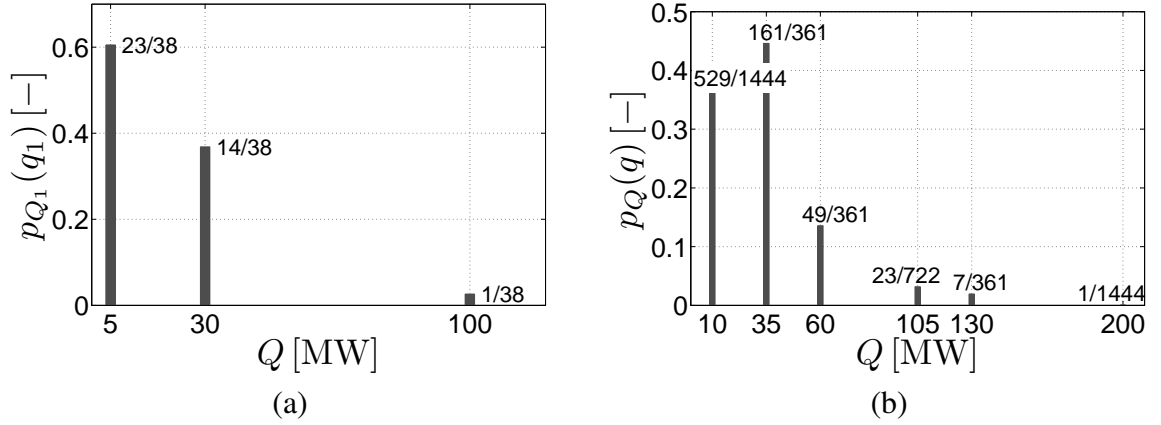


Figure 1: (a) Probability mass function of Q_{\max} [MW] (one truck/bus), (b) probability mass function of Q_{\max} [MW] (two trucks/buses)

and other characteristics along the tunnel. These factors must be taken into account when analyzing the impact of a fire on the damage of the tunnel lining (Sec. 4).

2.4. Distribution of heat during a fire

The results of ETA are a suitable point of departure when estimating the probability mass function of Q_{\max} [MW] conditional on the fire developed on one truck/bus, $p_{Q_1}(q_1)$. This function is displayed in Fig. 1(a). If two trucks/buses are involved in the accident giving rise to a fire, the resulting HRR will be estimated here as a composition of both HRRs, i.e. $Q = Q_1 + Q_2$. Assuming independent sources of the heat characterized by the same $p_{Q_i}(q_i)$, $i = 1, 2$, then using a standard procedure yields, see Fig. 1(b),

$$p_Q(q) = \sum_{(q_2)} p_{Q_1}(q - q_2) p_{Q_2}(q_2). \quad (2)$$

The distributions of any combination of heat sources, e.g. PC and TB, could be obtained accordingly. Undoubtedly, if data of better quality were at disposal in a particular case, the distributions in Fig. 1 could be duly improved.

3. Probabilistic model for the prediction of fire risk in road tunnels

In this section a pragmatic probability-based model will be proposed. In doing this, the following factors will play a decisive role in the model: (i) the probability of a certain configuration of vehicles involved in the fire incident, (ii) the probability that the subsequent fire will ensue a traffic incident (see Tab. 4), (iii) the distribution of heat developed in a given configuration of vehicles engulfed by the fire (Sec. 2.3 and Figs. 1(a) and (b)), and (iv) the damage of the tunnel lining as a result of a fire with a known HRR. Factors (ii) and (iii) have already been discussed in the previous section. The damage of the tunnel lining requires that a suitable hygro-thermo-mechanical model be at hand (see Sec. 4). There is no simple alternative left but analyzing the traffic flow of vehicles as a Markov process to predict the probability of vehicles involved in the accident (fire either due to self-ignition or a subsequent one), i.e. to analyze factor (i) in detail.

3.1. Traffic flow as a Markov process

To begin with, let us consider a one-lane traffic of personal cars (PCs), and trucks and/or buses (TBs) randomly lined up in the Markov chain composed of three states ($0 \equiv$ void (V), $1 \equiv$ PC, $2 \equiv$ TB) as shown in Fig. 2. Assume that the transition probabilities of the

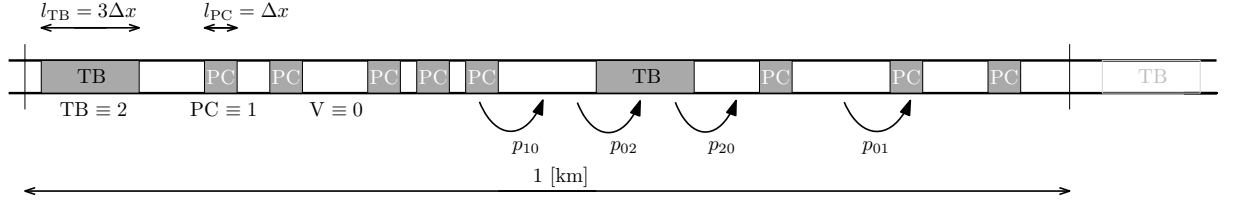


Figure 2: One-lane traffic flow

Markov chain, p_{ij} , $i, j = 0, 1, 2$, are known. They may be regarded as the average number of transitions $V \rightarrow PC$, in the case of p_{01} , and $V \rightarrow TB$, in the case of p_{02} , etc. (see Fig. 2). The direct calculation of p_{ij} is based on the maximum likelihood estimate taking the length of vehicles into account. The chain in Fig. 2 consists of $n_1 = 8$ PCs (elementary states), further of $n_2 = 2 \times 3 = 6$ elementary TB states, and $n_0 = 200 - 14 = 186$ elementary V states, respectively. Each elementary state is characterized by $\Delta x = 0.005$ [km] ($200 \times \Delta x = 1$ [km]).

Obviously, the probabilities of individual states in a stationary process are equal to the percentage of the respective lengths of vehicles identified in the traffic flow. Hence,

$$\begin{aligned}
 P_0 &= \frac{1}{\left(1 + \frac{n_1}{n_0} + \frac{n_2}{n_0}\right)} = \frac{n_0}{n_0 + n_1 + n_2}, \\
 P_1 &= \frac{1}{\left(\frac{n_0}{n_1} + 1 + \frac{n_2}{n_1}\right)} = \frac{n_1}{n_0 + n_1 + n_2}, \\
 P_2 &= \frac{1}{\left(\frac{n_0}{n_2} + \frac{n_1}{n_2} + 1\right)} = \frac{n_2}{n_0 + n_1 + n_2}.
 \end{aligned} \tag{3}$$

where n_0 , n_1 and n_2 are the numbers of sections Δx pertaining to V, PC and TB, respectively, on a one kilometer long stretch of the tunnel.

Lane 1	V	V	PC	PC	V	TB	PC	TB	TB
Lane 2	V	PC	V	PC	TB	V	TB	PC	TB
State	0	1	2	3	4	5	6	7	8

PC = personal car TB = truck/bus V = void

Figure 3: Two-lane traffic flow

The probable configurations of vehicles potentially involved in a fire incident in the traffic flow with two lanes are analyzed accordingly. If the switching of vehicles over lanes is

prohibited then there are two independent traffic flows. The Markov chain of configurations (joint states) relevant to this assumption is displayed in Fig. 3. It is worth noting that a parallel joint state [TB, TB] sets in if at least any two of the parallel parts of the lengths Δx overlap. For two stationary and independent parallel traffic flows, the probabilities of joint states in Fig. 3 can be simply calculated as the product of the probabilities of individual states in adjoining lanes (recall Eq. (3)). Hence

$$P_l = P_i^1 P_j^2, \quad i, j = V \equiv 0, PC \equiv 1, TB \equiv 2, \quad l = 0, 1, \dots, 9. \quad (4)$$

In general, apart from parallel configurations, a series couple of vehicles may appear if an ensuing vehicle (PC and/or TB) either catches up with the preceding one in the same lane or switches over from the adjoining lane⁴.

3.2. Pragmatic model for the prediction of fire risk in road tunnels

We start by recapitulating the set of variables already introduced in the previous sections. The probabilities of the nine configurations of vehicles and voids involved in the fire incident (Fig. 3) form the first set of variables. If all statistical data are available, these probabilities emerge from the solution of equations representing the Markov chain model. Since such an optimistic assumption reminds of a dream rather than reality we have to resort, in most cases, to the assessment of these probabilities using engineering judgment. In the sequel, the fire power expressed by the HRR of PCs will be neglected. Therefore, just five out of the nine original configurations, numbered 4 ÷ 8 (Fig. 3), will play a substantial role and their probabilities will be calculated on the condition that at least one TB is involved in the fire incident. The fire incidents will be regarded as the components of the Poisson process with the intensity λ_f forming the second variable of the risk model. As by far the biggest number of fires are attributed to self-ignition, the rate of fires per 10^9 [veh. km], see Eq. (1), will be taken for the intensity of the process. For a more detailed risk analysis, the total counts should be split at least into two sub-categories involving one TB (original states 4 ÷ 7) and/or two TBs (original state 8). In more detailed modeling, series configurations may be allowed for as well. Denote the probabilities of the states conditional on the fire incident as $P_f^{[i]}$, $[i] = 1, 2$, and express the respective fire intensities as

$$\lambda_f^{[i]} = \kappa^{[i]} \lambda_f, \quad \sum_{i=1}^2 \kappa^{[i]} = 1. \quad (5)$$

Again, if the data are not available for such a specification engineering judgment is called to estimate the set of coefficients $\kappa^{[i]}$. The probability mass function of heat, Q , developed during a fire, $p_Q(q)$, has been discussed in Sec. 2.3. In the optimal case, functions $p_Q^{[i]}(q)$ would be desirable for all possible configurations of vehicles. However, the reduction of these configurations into two sets of the utmost importance seems to be acceptable in this pragmatic model, so only the two functions displayed in Figs. 1(a) and (b) will be adequate.

On the other hand, we should not disregard the fact that, in general, the parameters $P_f^{[i]}$, $\kappa^{[i]}$, λ_f may vary along the length of the tunnel, see Fig. 4. Anyway, when bearing in mind this variability, one could encounter difficulties with insufficient data.

⁴Of course, there is a variety of other intermediate states which could be considered. For further discussion see Conclusions.

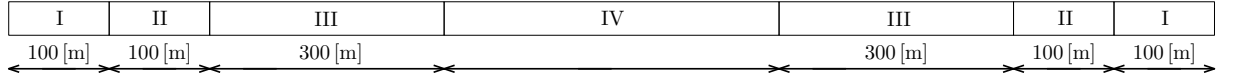


Figure 4: The zones in the tunnel affecting fire incidents, source [19]

In view of the fact that risk is the probable damage and with regard to the chain rule of conditional probabilities, a general formula allowing us to predict the average risk of a fire in road tunnels takes this lucid form

$$\text{RISK} = T\{\text{AADT}\} \sum_{[i]} \sum_{(q)} p_Q^{[i]}(q) \int_L C^{[i]}(q, x) P_f^{[i]}(x) \kappa^{[i]}(x) \lambda_f(x) dx, \quad (6)$$

where T [day] is the period of time for which the risk is calculated, L [km] is the length of the tunnel, $C^{[i]}$ [€] is the cost that must be expended to eliminate the damage inflicted by a fire. It should be pointed out that $C^{[i]}$ is a non-linear function of q and, therefore, any simplifications of Eq. (6), no matter how tempting, cannot be recommended. This variable is also a function of x due to the varying effect of a fire along the tunnel. Putting the accent on the technological aspects of damage, the cost $C^{[i]}$ in Eq. (6) may be alternatively substituted by the volume of the damaged concrete lining to be restored (see Sec. 6). We should remember that AADT is the annual average daily traffic per direction [veh. day⁻¹] and as such it is held constant in Eq. (6).

The structure of this equation deserves a comment. Recall that joint states of TBs involved in a fire incident include either one TB ($i = 1$) or two TBs ($i = 2$). Hence the term $T\{\text{AADT}\} \kappa^{[i]}(x) \lambda_f(x) dx$ expresses the average number of fires in the i -th joint state ($i = 1, 2$) which coincides with the elementary length dx of the tunnel (see Eqs. (1) and (5)). Each joint state represents three (for $i = 1$) or six (for $i = 2$) scenarios of different severity Q [MW] with a probability $p_Q^{[i]}(q)$. The joint state occurs with a probability $P_f^{[i]}$. The calculation will be exemplified in Sec. 6 (Eq. (21)).

4. Material model

As already mentioned in the introduction to this paper, the material model is a special combination of those presented in [28] and [29]. The mathematical formulation consists of two governing equations representing the conservation laws of mass and energy defined as

$$\frac{\partial w}{\partial t} = \nabla \cdot \left(\frac{\kappa}{g} \nabla p \right) + \frac{\partial w_d}{\partial t}, \quad (7)$$

$$\rho c \frac{\partial \theta}{\partial t} - h_v \frac{\partial w}{\partial t} = \nabla \cdot (\lambda \nabla \theta) - c_w \frac{\kappa}{g} \nabla p \cdot \nabla \theta + h_d \frac{\partial w_d}{\partial t}. \quad (8)$$

The set of primary unknown variables includes the temperature θ [°C] and the pore pressure p [Pa]; w [kgm⁻³] is the mass of evaporable water, κ [ms⁻¹] is the permeability, g [ms⁻²] is the gravity acceleration, w_d [kgm⁻³] is the mass of dehydrated water, ρ [kgm⁻³] is the volumetric mass density, c [Jkg⁻¹K⁻¹] is the specific heat capacity, h_v [Jkg⁻¹] is the evaporation enthalpy, h_d [Jkg⁻¹] is the enthalpy of dehydration, c_w [Jkg⁻¹K⁻¹] is the specific heat capac-

ity of water, and λ [$\text{Wm}^{-1}\text{K}^{-1}$] is the thermal conductivity⁵. The nonlinear dependencies of all transport coefficients on the temperature or pore pressure are fully described in Appendix B.

In the formulation of the above balance equations, the following assumptions are made, see [22]:

- The transport of liquid water and dry air is neglected.
- Investigated material is a continuum medium.
- The solid matrix is assumed to be undeformable.
- Water is an incompressible liquid.
- Water vapor is an ideal gas.

Due to the lack of information on the prediction of fire-induced spalling for reasons described in [22], we further pursue the conservative engineering approach, see [34]. It defines the occurrence of fire-induced spalling⁶ as a certain threshold when the pore pressure weighted by porosity exceeds the temperature-dependent tensile strength, $f_t(\theta)$ [Pa]:

$$\phi p \geq f_t(\theta), \quad (9)$$

where ϕ [–] is the porosity.

When fire-induced spalling, governed here solely by Eq. (9), occurs in a certain part of the investigated domain, this part is removed from the analysis and boundary conditions are applied to a new free boundary surface, see [22]. This promotes faster penetration of heat into the material and consequently reduction of strength due to high temperature exposure. Both the decreasing compressive strength, f_c [Pa], and tensile strength, f_t [Pa], are shown as functions of the temperature θ [$^{\circ}\text{C}$] in Appendix B, see Figs. B.15(b),(c).

Point out that the present approach builds upon the application of the Dirichlet boundary condition, which in turn calls for some simplifications, see Sec. 6.2.

4.1. Finite element implementation

The analytical solution of Bažant–Thonguthai’s equations is feasible only for some simple examples, and thus approximation techniques are needed for analyzing more realistic problems. For the spatial discretization of partial differential equations (7) and (8), a finite element method is preferred here to the finite volume technique, see [31]. The discretized form of transport equations then reads

$$\underbrace{\begin{bmatrix} \mathbf{C}_{pp} & \mathbf{C}_{p\theta} \\ \mathbf{C}_{\theta p} & \mathbf{C}_{\theta\theta} \end{bmatrix}}_{\mathbf{C}} \underbrace{\begin{Bmatrix} \dot{\mathbf{r}}_p \\ \dot{\mathbf{r}}_\theta \end{Bmatrix}}_{\dot{\mathbf{r}}} + \underbrace{\begin{bmatrix} \mathbf{K}_{pp} & 0 \\ 0 & \mathbf{K}_{\theta\theta} \end{bmatrix}}_{\mathbf{K}} \underbrace{\begin{Bmatrix} \mathbf{r}_p \\ \mathbf{r}_\theta \end{Bmatrix}}_{\mathbf{r}} = \underbrace{\begin{Bmatrix} \mathbf{F}_p \\ \mathbf{F}_\theta \end{Bmatrix}}_{\mathbf{F}}. \quad (10)$$

⁵This symbol should not be mixed up with a similar symbol used in the preceding section for the fire intensity, λ_f , as it is distinguishable through its index.

⁶Sudden exposure to very high temperatures can result in explosive spalling of the concrete [11]. Spalling decreases the thickness of the lining (see Fig. 6) and consequently promotes degradation of the concrete and decrease of its strength due to the dehydration of the material. Both phenomena are considered when modeling the damage of tunnel lining.

The numerical solution of system (10) is based on a simple temporal finite difference discretization. If we use time steps Δt and denote the quantities at a time step i with a corresponding superscript, the time-stepping equation becomes

$$\mathbf{r}^{i+1} = \mathbf{r}^i + \Delta t[(1 - \gamma)\dot{\mathbf{r}}^i + \gamma\dot{\mathbf{r}}^{i+1}], \quad (11)$$

where γ is a generalized midpoint integration rule parameter. In the results presented in this paper the Crank-Nicolson (trapezoidal rule) integration scheme with $\gamma = 0.5$ was used. Expressing $\dot{\mathbf{r}}^{i+1}$ from Eq. (11) and substituting it into Eq. (10), one obtains a system of non-linear equations

$$(\mathbf{C} + \xi\Delta\tau\mathbf{K})\mathbf{r}^{i+1} = \xi\Delta\tau\mathbf{F} + \mathbf{C}[\mathbf{r}^i + \Delta\tau(1 - \xi)\dot{\mathbf{r}}^i], \quad (12)$$

which can be solved by a suitable iterative method such as Newton-Raphson's.

4.2. Boundary and initial conditions

To complete the material model, the initial conditions are introduced in the whole analyzed domain Ω , and boundary conditions are assigned to its boundary Γ , ($\Gamma = \Gamma_{\text{idx}}^I \cup \Gamma_{\text{idx}}^{II} \cup \Gamma_{\text{idx}}^{III}$, $\text{idx} = \theta, p$). The initial and boundary conditions are set as follows:

- The Dirichlet boundary conditions

$$\begin{aligned} \theta &= \hat{\theta}(t) \quad \text{on} \quad \Gamma_{\theta}^I, \\ p &= \hat{p}(t) \quad \text{on} \quad \Gamma_p^I. \end{aligned} \quad (13)$$

- The Neumann boundary conditions

$$\begin{aligned} -\lambda\nabla\theta \cdot \mathbf{n} &= \hat{q}_{\theta}(t) \quad \text{on} \quad \Gamma_{\theta}^{II}, \\ -\frac{\kappa}{g}\nabla p \cdot \mathbf{n} &= \hat{q}_p(t) \quad \text{on} \quad \Gamma_p^{II}. \end{aligned} \quad (14)$$

- The Robin boundary conditions

$$\begin{aligned} -\lambda\nabla\theta \cdot \mathbf{n} &= \alpha_{\theta}[\theta - \theta_{\infty}(t)] + e\sigma[|\theta|^3\theta - \theta_{\infty}^4(t)] \quad \text{on} \quad \Gamma_{\theta}^{III}, \\ -\frac{\kappa}{g}\nabla p \cdot \mathbf{n} &= \beta_p[p - p_{\infty}(t)] \quad \text{on} \quad \Gamma_p^{III}. \end{aligned} \quad (15)$$

- Initial conditions

$$\theta(0) = \theta_{\text{in}} \quad p(0) = p_{\text{in}} \quad \text{on} \quad (\Omega \cup \Gamma), \quad (16)$$

where the symbol $(\hat{\cdot})$ denotes the prescribed value, $\mathbf{n} [-]$ is the outward unit normal vector, $\alpha_{\theta} [\text{Wm}^{-2}\text{K}^{-1}]$ is the heat transfer coefficient, $\beta_p [\text{kgm}^{-2}\text{s}^{-1}]$ is the water vapor transfer coefficient, $e [-]$ is the emissivity of the surface, $\sigma [\text{Wm}^{-2}\text{K}^{-4}]$ is the Stefan-Boltzmann constant, θ_{∞} and p_{∞} are the ambient temperature and the pressure of water vapor, respectively.

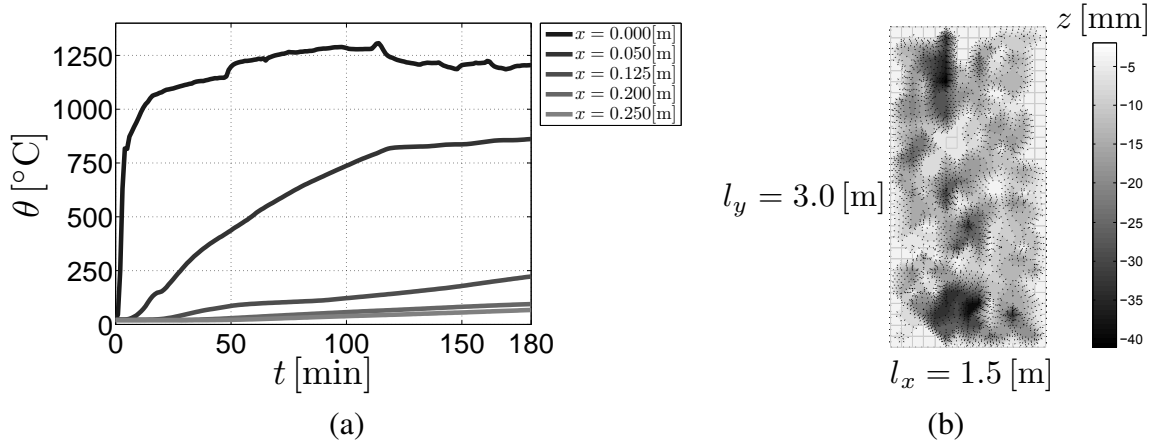


Figure 5: (a) Evolution of temperatures for the FiFAC5 specimen, (b) corresponding spalling zone

5. Identification of material parameters

In this section, we discuss the identification of material parameters exploiting the laboratory tests described in [38]. The extensive experimental program implemented by Šejnoha et al. was focused on large scale experiments carried out on concrete panels $3.0 \times 1.5 \times 0.25$ [m] to test the possible application of fly ash concrete in the production of a precast segmental lining for road tunnels.

From the enormous amount of experimental data, see also [47] for further reference, the FiFAC2⁷ specimen loaded in accordance with the Rijkswaterstaat (RWS) fire curve was chosen as an example of laboratory tests. For illustration, the evolutions of temperatures subsequently measured at depths $z = 0, 0.05, 0.125, 0.20$ and 0.25 [m] are shown in Fig. 5(a) and the corresponding spalling zone⁸ is then displayed in Fig. 5(b). A detailed description of all enhanced concrete mixtures, experimental setups and conclusions can be found in [38, 39]. It is worth mentioning that these results will only be applicable for the same type of concrete.

The geometrical model used in the identification example consists of 60 one-dimensional finite elements with the following boundary conditions: On the heated up (exterior) side of the one-dimensional domain, a varying temperature matching up the RWS curve and, on the interior side, a room temperature were maintained. The overall duration of the experimental measurement was 180 [min].

The following material properties, namely the thermal conductivity of the solid matrix at room temperature, $\lambda_{s,0}$, the specific heat capacity of the solid matrix at room temperature, $c_{s,0}$, the mass of cement per unit volume, m_c , the permeability at room temperature, κ_0 , the mass density, ρ_s , the total porosity, ϕ , and the tensile strength at room temperature, $f_{t,0}$, were found by matching the numerical and experimental temperatures and the depths of the

⁷Amounts of materials used for the FiFAC2 specimen: Cement CEM I 52.5 R = 320 [kgm⁻³], grain fraction 0/4 = 705 [kgm⁻³], grain fraction 4/8 = 130 [kgm⁻³], grain fraction 8/16 = 865 [kgm⁻³], fly ash = 276 [kgm⁻³], water = 187 [kgm⁻³], limestone powder = 40 [kgm⁻³], Gleanium ACE 40 = 4.2 [kgm⁻³] and FORTA-FERRO fibers = 4.5 [kgm⁻³].

⁸As indicated in the introductory part, the “spalling zone” is understood as the region affected by the loss of material regardless of its cause. In the present model the total loss of material measured at the end of experiment is in the identification procedure attributed to the activation of Eq. (9) only.

fire-induced spalling zones. Moreover, the same strategy was utilized to identify the surface parameters, i.e. emissivity, e and the heat transfer coefficient, α_θ , for the limited time upon which no damage due to spalling has been expected.

A variety of identification procedures can be used to find an optimal solution to the identification problem, each has its advantages and drawbacks. A full discussion of such problems lies beyond the scope of this paper. Therefore, we utilized the in-house GRADE algorithm, which is a real-coded stochastic optimization algorithm combining the principles of genetic algorithms and differential evolution, see [40, 41]. The resulting set of material parameters and surface parameters after the identification procedure then becomes $\{\lambda_{s,0}, c_{s,0}, m_c, \kappa_0, \rho_s, \phi, f_{t,0}\} = \{2.85, 700, 320, 4.3 \cdot 10^{-13}, 0.18, 1.5 \cdot 10^6\}$ and $\{\alpha_\theta, e\} = \{25, 0.95\}$, respectively.

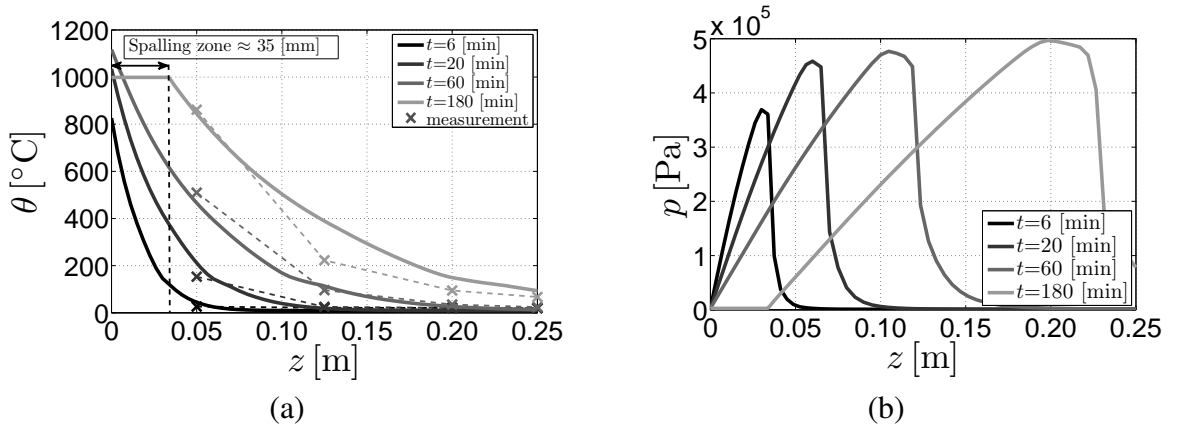


Figure 6: Numerical result for an optimized set of material parameters in different time steps: (a) Evolution of temperature, (b) evolution of pore pressure

Fig. 6(a) displays the evolution of temperature compared to experimental measurements for the optimally fitted set of material parameters. The resulting pore pressure for the same set of input material properties is presented in Fig. 6(b). As evident from Fig. 6(a), the predictions of the temperature field and the depth of the spalling zone correspond with the measured data quite well. The calculated results promote the capability of governing equations to simulate the heat and moisture transport in building materials exposed to fire.

6. Risk assessment of a fire in a road tunnel, case study

In this section, we employ the proposed techniques combining probabilistic (Sec.3) and multi-physics models (Sec.4) to predict the fire risk in road tunnels.

6.1. Fire loading functions

Before proceeding to the complex risk assessment, it is necessary to introduce several mathematical relations defining the fire load in the road tunnel as a function of time and location. In this section we adopt formulas presented in [35] and references therein. They are based on a series of large scale experiments including the Runehamar Tunnel Fire Tests which brought valuable findings briefly commented on in Sec. 2.2. Due to practical constraints, only a few chosen functions and conclusions are utilized in this case study.

The maximum ceiling temperature $\theta_{\text{ceiling,max}} [^{\circ}\text{C}]$ in a specific region⁹ is expressed as

$$\theta_{\text{ceiling,max}} = \begin{cases} \theta_{\text{reg},1} & \theta_{\text{reg},1} < 1350 [^{\circ}\text{C}], \\ 1350 & \theta_{\text{reg},1} \geq 1350 [^{\circ}\text{C}], \end{cases} \quad \theta_{\text{reg},1} = 17.5 Q^{\frac{2}{3}} H_{\text{eff}}^{-\frac{5}{3}}, \quad (17)$$

where $H_{\text{eff}} [\text{m}]$ is the effective height of the tunnel and $Q [\text{MW}]$ is the heat release rate. This term is then used in the definition of the ceiling temperature $\theta_{\text{ceiling}}(t, x) [^{\circ}\text{C}]$, which is a function of location and time as:

$$\theta_{\text{ceiling}}(t, x) = c_{\text{time}}(t) c_{\text{loc}}(x) \theta_{\text{ceiling,max}}. \quad (18)$$

The dimensionless coefficients $c_{\text{time}} [-]$ and $c_{\text{loc}} [-]$ are introduced to reduce the maximum ceiling temperature in dependence on the distance from the location of a fire incident and the time duration from the beginning of the fire appearance, respectively. According to [35], $c_{\text{loc}} [-]$ is described as

$$\text{downstream : } c_{\text{loc}}(x) = 0.57 \exp\left(-0.13 \frac{x}{H}\right) + 0.43 \exp\left(-0.021 \frac{x}{H}\right), \quad (19)$$

$$\text{upstream : } c_{\text{loc}}(x) = \exp\left(-0.183 \frac{|x|}{H}\right), \quad (20)$$

where downstream and upstream are the rear and front areas of the tunnel with regard to the direction of the air flow and the fire incident; $x = 0 [\text{m}]$ is the location of the fire and $H [\text{m}]$ is the height of the tunnel. The definition of $c_{\text{time}} [-]$ is not so straightforward as $c_{\text{loc}} [-]$. Keeping in mind the principal objective of the paper, the risk calculation, we accept a certain limitation and derive this coefficient by fitting the experimental data (heat release rate and gas temperature curves) presented in [35]. For scenarios significantly differing from the one used in the adopted experiment a detailed analysis would be necessary. However, this goes beyond the scope of the present paper and we refer the interested reader to [1, 2]. The evolutions of $c_{\text{time}} [-]$ for typical values of $Q [\text{MW}]$ used as an example in this study and $c_{\text{loc}} [-]$ are shown in Fig. 7. The 3D nature of the problem is captured by using a parabolic

⁹See [35], page 26, definition of tunnel regions depending on the dimensionless ventilation velocity

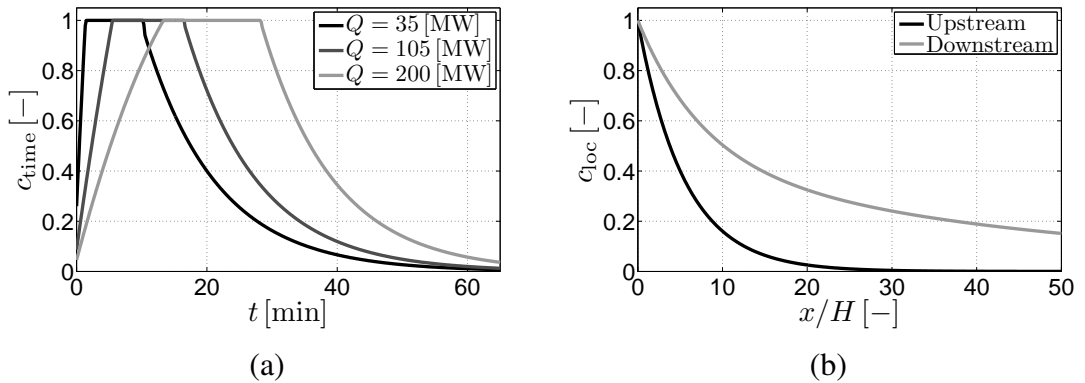


Figure 7: Evolution of dimensionless coefficients: (a) $c_{\text{time}} [-]$, (b) $c_{\text{loc}} [-]$

function of vertical coordinate z to describe the distribution of the gas temperature along the tunnel lining. When comparing experimental and numerical results in a 1/3 scale tunnel [13] it appears that such approximation is satisfactory.

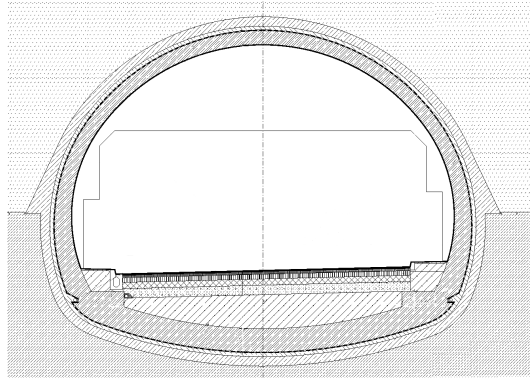


Figure 8: Cross-section of road tunnel

6.2. Numerical example

The present case study is aimed at demonstrating the capability of the proposed methodology to assess the risk of fires in road tunnels. In order to make the example easy to understand, we begin by simulating the damage caused in the lining of a two-lane tunnel due to the fire of a single vehicle (TB). A typical cross-section of the tunnel is shown in Fig. 8.

To this end, we consider the geometric proportions of the concrete lining in the ceiling of the tunnel, together with the initial and loading conditions as displayed in Fig 9. The loading conditions on the exterior surface are driven by Eqs. (17) through (20), and the conclusions written in [35]. To reduce the computational effort required for solving the spalling problem, the surface temperature (the boundary condition of type I⁰) is adopted here in place of the ceiling temperature, where the latter one would have to be modeled as the boundary condition of type III. This strategy involves precalculation of the surface temperature using the emissivity e and the heat transfer coefficient α_θ (type III) on the sub-domain while assuming no fire-induced spalling. Thereafter, the computed surface temperature is applied as the boundary condition of type I to the domain representing the concrete lining. Notwithstanding this restriction, the results reveal no significant differences. For illustration, evolutions of the surface and ceiling temperatures for $Q = 200$ [MW] is shown in Fig. 10(a). Clearly, there is no link between the RWS loading curve exploited in model parameters identification procedure in Sec. 5 and the loading curves assumed to represent real fires when estimating the risk.

The two-dimensional rectangular domain 520×0.3 [m] was discretized by the FE mesh consisting of triangular elements ranging from 0.01 [m] to 0.05 [m]. Input material properties, corresponding to fly ash concrete, were used from Sec. 5. The time duration of the numerical simulation was set to 180 [min]. The uniform time step of 1 [s] was chosen with regard to the convergence criteria of the nonlinear time-dependent solution.

¹⁰see Sec. 4.2

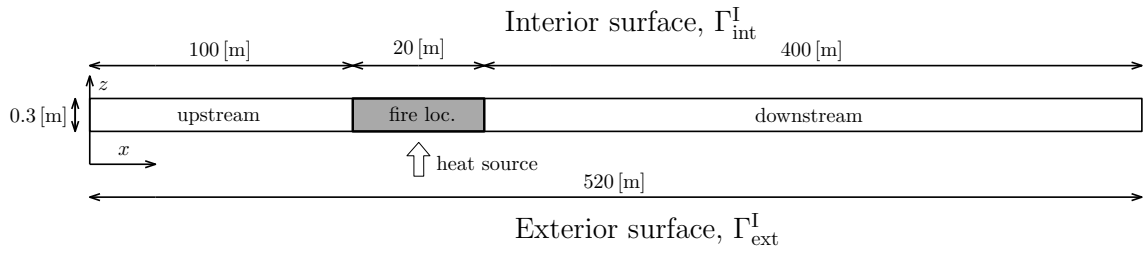


Figure 9: Initial scheme

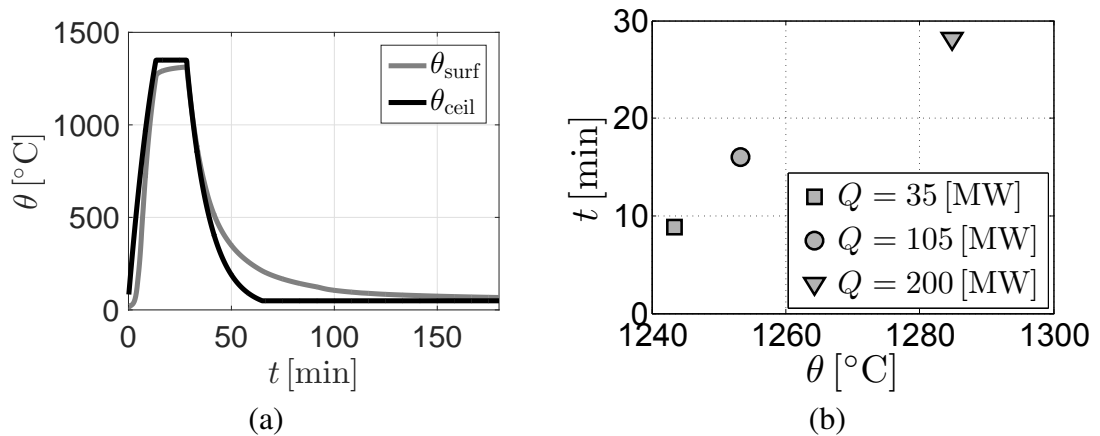


Figure 10: (a) Evolution of the surface and ceiling temperature for $Q = 200$ [MW], (b) duration of spalling event governed by Eq. (9) for individual loading scenarios

The results obtained for $Q = 35$ [MW] are presented in Fig. 11(a)-(d) showing the depth of the spalling zone and the isolines of several physical quantities. These isolines make up the boundary between the sound (above) and damaged (below) concrete and as such they will be further utilized in the risk assessment. The time spent on generating the part of the damaged material associated purely with the material loss governed by Eq. (9) is depicted in Figure 10(b) for illustration. Passed this time the volume of damaged material corresponds to the material suffered from the strength reduction due to a high temperature exposure.

Several interesting results have been derived within the scope of varying levels of the heat release rate. The typical values of Q (5, 10, 30, 35, 60, 100, 105, 130, 200 [MW]) representing the power of fire due to the ignition of one and/or two vehicles, respectively, were considered to take into account the selected scenarios in a two-lane road tunnel. The mitigating effects of FPS are not explicitly expressed in this case study though they can be implicitly covered in these scenarios. The comparison of isolines for the selected values of the heat release rate is shown in Fig. 12.

The damaged volume $V_{\text{dam}} [\text{m}^3]$ of the tunnel lining at the end of simulation (after 3 hours) is displayed in Fig. 13(a). In this study the volume $V_{\text{dam}} [\text{m}^3]$ is limited to the material volume loss when the temperature exceeded a limit value $\bar{\theta}$ given the specified value of Q . It consists of the volume $V_{\text{spal}} [\text{m}^3]$ destroyed by spalling according to Eq. (9), and the volume $V_{\text{deg}} [\text{m}^3]$ degraded through the passage of high temperature. Both volumes constitute a material basis of the risk analysis.

As implied in Eq. (6), a probabilistic basis demands that an appropriate model for the

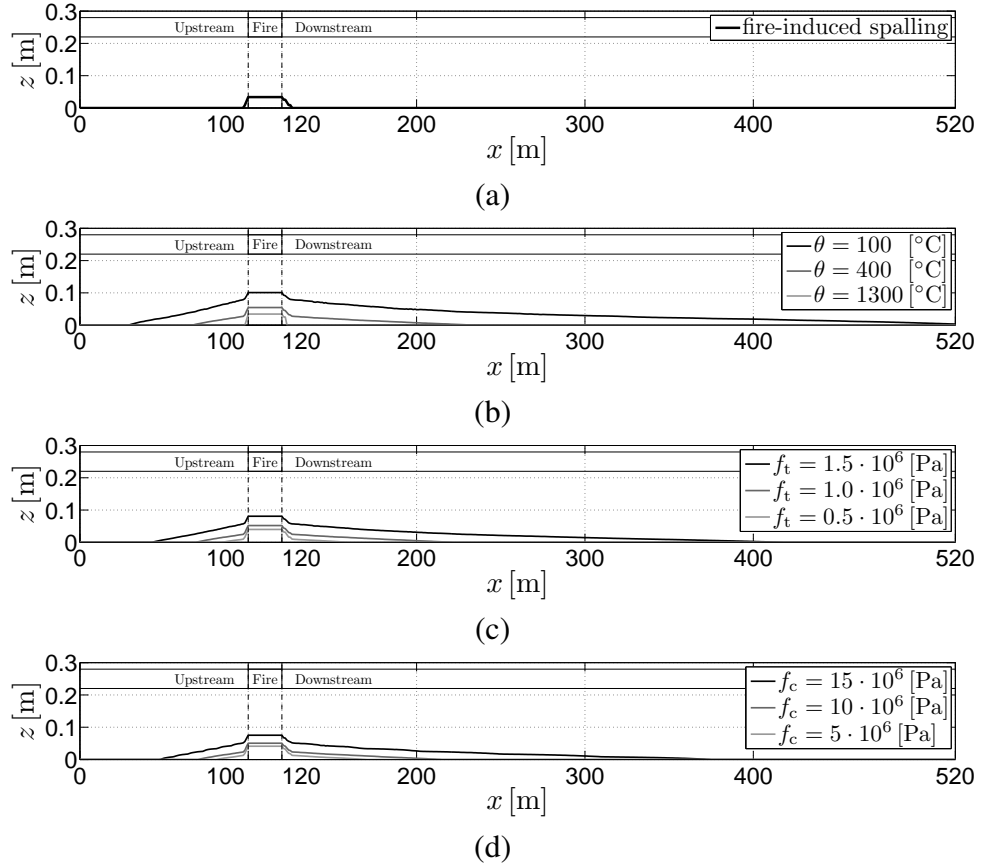


Figure 11: Numerical analysis for $Q = 35$ [MW]: (a) Depth of the spalling zone, (b) isolines of temperature, (c) isolines of temperature dependent tensile strength, (d) isolines of temperature dependent compressive strength

traffic flow be proposed. As a model flow used in the present case study, let us consider a one kilometer long stretch of a two-lane motorway (see Figs. 2 and 3) with 8 PCs and 1 TB in lane 1, and 4 PCs, 1 TB and a series couple of two TBs in lane 2. Combining four individual states of flow, namely, V, PC, TB and a series couple of TBs, we arrive at a set of 16 joint states similar to those displayed in Fig. 3. Since no changes of lanes are allowed in this simple example the probabilities of joint states are calculated as the product of the probabilities of individual states in adjoining lanes (see Eq. (4)). To make this example as simple as possible, the joint state of TB (in lane 1) and a series couple of TBs (in lane 2) was treated as a parallel state [TB,TB], assuming that the first TB from the series couple in lane 2 succeeded in escaping from a potential fire incident. Based on these assumptions, the probability that one TB is involved in the fire incident is $P_f^{[1]} = 0.4518$ and the probability that two TBs are involved (including the series couple of TBs) is $P_f^{[2]} = 0.5482$. Note that $P_f^{[1]} + P_f^{[2]} = 1$. Point out that a series couple of TBs considerably increases the probability of two vehicles involved in a fire incident.

Owing to the limited knowledge of the ratio of the fire intensities pertaining to states $[i]$, $i = 1$ states for 1 TB and $i = 2$ states for 2 TBs (see Eq. (5)), we performed a parametric study by taking into account all the possible combinations of coefficients $\kappa^{[i]}$, $i = 1, 2$.

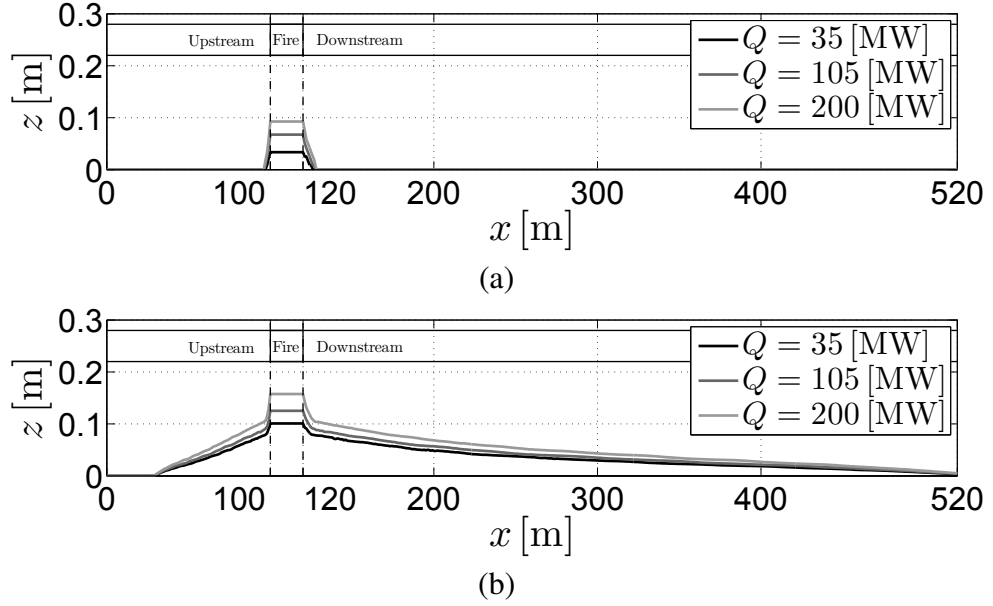


Figure 12: Comparison of isolines for different values of the heat release rate: (a) Depth of the spalling zone , (b) attained temperature equals 100 [°C]

Within the scope of admitted simplifications, formula (6) can be rewritten as

$$\begin{aligned} \text{RISK} = TL\{AADT\}\lambda_f & \left[\left(\sum_{q=5,30,100} V_{\text{dam}}^{[1]}(q)p_{Q_1}(q_1) \right) \kappa^{[1]} P_f^{[1]} \right. \\ & \left. + \left(\sum_{q=10,35,60,105,130,200} V_{\text{dam}}^{[2]}(q)p_{Q_2}(q_2) \right) \kappa^{[2]} P_f^{[2]} \right]. \end{aligned} \quad (21)$$

The right hand side of Eq. (21) is graphically represented in Fig. 13(b) and can be regarded as the damage randomly caused by a single fire incident.

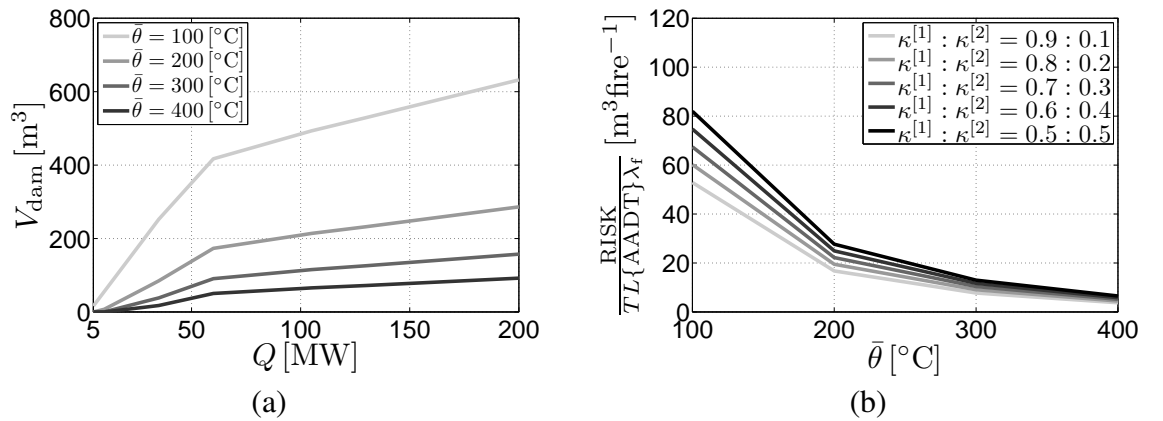


Figure 13: (a) Volumes of the tunnel lining degraded by spalling and high temperatures exceeding a given limiting value $\bar{\theta}$ [°C], $V_{\theta > \bar{\theta}}$ [m³], (b) random damage relative to the number of fire incidents

To be specific let us consider a two-lane road tunnel, 2 [km] long, with AADT= 17000 [veh.day⁻¹], see Tab. 2, and $T = 1$ [year] = 365 [days]. Finally, make a tentative guess of the fire intensity $\lambda_f = 30 \cdot 10^{-9}$ [fires (veh.km)⁻¹], compare Tabs. 4 and 5, and permit $\bar{\theta} = 150$ [°C] as the maximum temperature the tunnel lining is able to sustain without an essential repair.

It follows from Eq. (21) and Fig. 13(b) that RISK ranges from 13 to 20 [m³year⁻¹]. Considering that a total volume of the lining struck by a fire along a 520 [m] long stretch (Figs. 11 and 12) is $V = 3463$ [m³], we arrive at the value of risk relative to this volume $\text{RISK}_{\text{rel}} = (0.38 \div 0.58)$ [%] of damaged concrete per year. The damage due to the fire of a given power Q was taken constant along the tunnel.

Since the risk is defined as the mean value of a certain random variable, recall Eq. (6), and the stretch of the fire effect along the tunnel (see Figs. 11 and 12) tends to shorten when the center of fire approaches the tunnel portals we are justified to intuitively infer that the approximate integration (Eq. (21)) rather overestimates the risk (Eq. (6)). The anticipated reduction could be estimated, e.g. using CFD to grasp at least fire dynamics in the investigated tunnel.

7. Conclusions

In this paper, we proposed a pragmatic model for the risk analysis of road tunnels engulfed by a fire. The model is intended as simple as possible and yet, accounted for its complexity, not substantially diverge from the reality. As such, it has its limitations which concern both the probabilistic and material (damage) aspects.

In the probabilistic modeling of the traffic flow, we restricted ourselves to stationary Markov processes when estimating the probability of joint states of vehicles to be ignited. This assumption seems acceptable for a sufficiently long tunnel. Admitting the possibility of switching lanes increases the number of joint states for which the Markov chain model (non-homogeneous in general) must be developed. Apparently, the probability of changing lanes must be known or reasonably estimated. Our numerical experiments based on the Markov chain model with varying initial conditions imply that the traffic flow becomes homogeneous (stationary) within $300 \div 400$ [m] from the initial position (semaphore). All the same, an in-depth solution demands that more detailed data, especially on switching adjoining lanes, be available.

The probabilistic modeling of the heat release rate, Q , is the second weak point of the present methodology. The respective probability mass function, $p_{Q_1}(q_1)$, was obtained by a team of experts using ETA [15] and it is debatable if an impartial (objective) solution would ever be achieved. Moreover, the probability mass functions of more complex joint states of vehicles (save for two TBs) are still missing.

Last but not least, the fire intensity, λ_f , would not be omitted in this discussion. Insufficient data on the type of vehicle involved in the fire incident does not allow for the fire intensity of joint states to be grasped sufficiently well. Moreover, we have inadequate knowledge of the variability of λ_f along the tunnel, but taking this quantity for a constant seems to be a reasonable compromise. All in all, it is worth noting that the variable probabilities $P_f^{[i]}(x)$ of the joint states of vehicles involved in a non-homogeneous fire process call for the variability of $\lambda_f(x)$ at least in zones I through III, see Eq. (6) and Fig. 4. Due to the lack of data, this difficult task could be solved at the level of engineering judgment based on fault tree analysis (FTA).

The simplifications the damage model relies on should not be belittled in any case. Though the calibrated model for the heat and moisture transport predicts well the experimentally observed spalling zone (see Figs. 5 and 6), some concern arises in particular regarding the permeability κ the theoretical model is very sensitive to. This variable ranges over several orders of magnitude and depends on the material porosity which, on the other hand, varies with damage (see, e.g. [23]). Our model does not take this phenomenon into account. Nevertheless, it is very important and recent works by Majorana et al. [42] represent meaningful progress in this field. The dry air pressure neglected in our model might be one of the sources of inaccuracy when predicting the volume of the deteriorated concrete.

All things considered, the proposed pragmatic model for fire risk analysis is applicable for sufficiently long tunnels. It will be further augmented while estimating damage caused by fire incidents at the proximity of portals. Except for the computational modeling of heat gas using computational fluid dynamics (CFD), see e.g. [43] through [46], the expert approaches based on the prediction of the respective upstream/downstream gas flows seem to be an effective tool to the problem solution.

Acknowledgment

This outcome has been achieved with the financial support from Competence Centres of the Technology Agency of the Czech Republic (TACR) under the project CESTI - Centre for the Effective and Sustainable Transport Infrastructure TE01020168 and the Czech Science Foundation, project No. 15-10354S.

Appendix A.

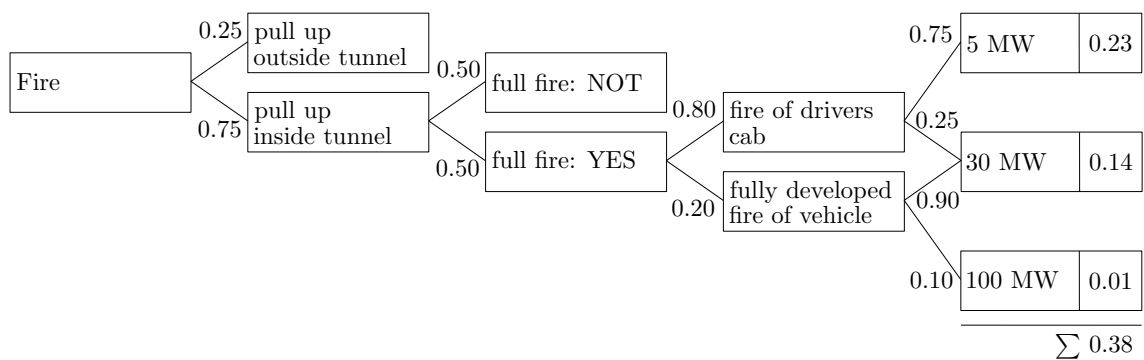


Figure A.14: ETA of fire power, Q_{max} [MW], source [15]¹¹

Appendix B.

The transport coefficients in Eqs. (7) and (8) are provided by the following relations:

¹¹This quantity is known as "maximum fire intensity of trucks" (Maximale Intensität von LKW-Bränden) in [15]

- $w(\theta, p)$ [kgm^{-3}] - sorption isotherm, see [28]

$$w(\theta, p) = \begin{cases} m_c \left(\frac{p}{p_{\text{sat}}} \frac{m_0}{m_c} \right)^{1/m(\theta)} & \frac{p}{p_{\text{sat}}} \leq 0.96 [-], \\ m_{0.96} + \left(\frac{p}{p_{\text{sat}}} - 0.96 \right) \left(\frac{m_{1.04} - m_{0.96}}{0.08} \right) & 0.96 [-] < \frac{p}{p_{\text{sat}}} < 1.04 [-], \\ (m_0 + w_d) \left(1 + 0.12 \left(\frac{p}{p_{\text{sat}}} - 1.04 \right) \right) \left(\frac{\rho_\theta}{\rho_0} \right) & \frac{p}{p_{\text{sat}}} \geq 1.04 [-], \end{cases} \quad (\text{B.1})$$

where m_c [kgm^{-3}] is the mass of cement per unit volume of concrete, m_0 [kgm^{-3}] is the mass of free water at 25 [°C]. The terms $m_{1.04}$ [kgm^{-3}] and $m_{0.96}$ [kgm^{-3}] represent the limit values of water contents at the saturated level and non-saturated level, respectively. Nevertheless, in the transition region ($0.96 < p/p_{\text{sat}} < 1.04$), a smoothed approximation is used to obtain continuous derivatives $\partial w/\partial \theta$ and $\partial w/\partial p$. As an illustrative graph, the sorption isotherm used in the previous numerical analysis is displayed in Fig. B.15(a). According to [28], the remaining terms in Eq. (B.1) are calculated as

$$m(\theta) = 1.04 - \frac{(\theta + 10)^2}{22.3(\theta_0 + 10)^2 + (\theta + 10)^2},$$

$$m_{0.96} = m_c \left(0.96 \frac{m_0}{m_c} \right)^{1/m(\theta)},$$

$$m_{1.04} = (m_0 + w_d) \left(\frac{\rho_\theta}{\rho_0} \right).$$

- $w_d(\theta)$ [kgm^{-3}] - mass of dehydrated water, see [22],

$$w_d(\theta) = \begin{cases} 0 & \theta \leq 100 \text{ [}^\circ\text{C]}, \\ 0.04m_c(\theta - 100)/100 & 100 \text{ [}^\circ\text{C]} < \theta \leq 700 \text{ [}^\circ\text{C]}, \\ 0.24m_c & \theta > 700 \text{ [}^\circ\text{C]}. \end{cases} \quad (\text{B.2})$$

- $p_{\text{sat}}(\theta)$ [Pa] - saturation pressure of water vapor, see [30],

$$p_{\text{sat}}(\theta) = \begin{cases} 611 \exp\left(\frac{22.44\theta}{272.44+\theta}\right) & \theta < 0 \text{ [}^\circ\text{C]}, \\ 611 \exp\left(\frac{17.08\theta}{234.18+\theta}\right) & \theta \geq 0 \text{ [}^\circ\text{C]}. \end{cases} \quad (\text{B.3})$$

- $h_v(\theta)$ [Jkg^{-1}] - evaporation enthalpy, see [20],

$$h_v(\theta) = 2.672 \cdot 10^5 (647.3 - (\theta + 273.15))^{0.38}. \quad (\text{B.4})$$

- h_d [Jkg^{-1}] - enthalpy of dehydration, see [21],

$$h_d = 2.4 \cdot 10^6. \quad (\text{B.5})$$

- $\rho c(\theta, p)$ [$\text{Jm}^{-3}\text{K}^{-1}$] - heat capacity,

$$\rho c = \rho_s c_s + w c_w, \quad (\text{B.6})$$

where $c_s(\theta)$ [$\text{Jkg}^{-1}\text{K}^{-1}$] is the specific heat capacity of the solid matrix, see [34], and it is given as

$$c_s(\theta) = \frac{c_{s,0}}{900} \left(900 + 80 \left(\frac{\theta}{120} \right) - 4 \left(\frac{\theta}{120} \right)^2 \right). \quad (\text{B.7})$$

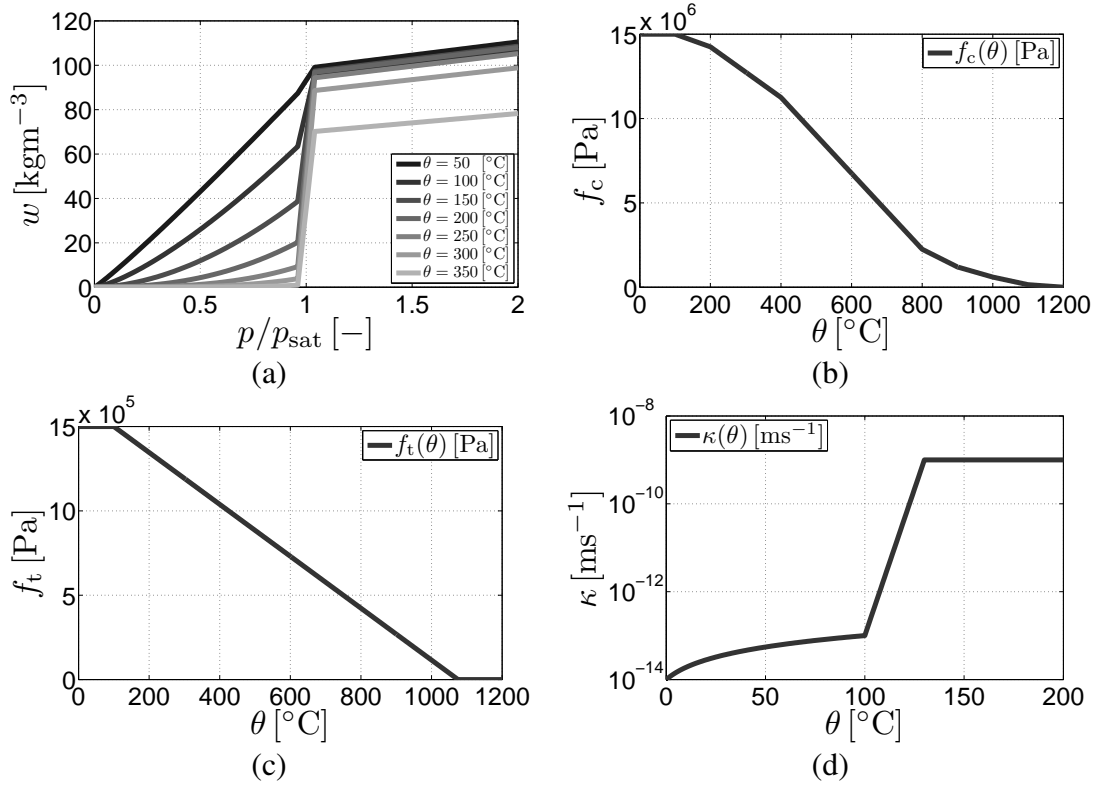


Figure B.15: (a) Sorption isotherm, (b) temperature-dependent compressive strength $f_c(\theta)$, (c) temperature-dependent tensile strength $f_t(\theta)$, (d) permeability $\kappa(\theta)$ as a function of temperature

- $\lambda(\theta, p)$ [Wm⁻¹K⁻¹] - thermal conductivity, see [26],

$$\lambda(\theta, p) = \lambda_s + \phi S_w \lambda_w, \quad (\text{B.8})$$

where $\lambda_w(\theta)$ [Wm⁻¹K⁻¹] is the thermal conductivity of water, S_w [-] is the saturation degree, and $\lambda_s(\theta)$ [Wm⁻¹K⁻¹] is the thermal conductivity of the solid matrix defined as

$$\lambda_s(\theta) = \frac{\lambda_{s,0}}{2.00} \left(2.00 - 0.2451 \left(\frac{\theta}{100} \right) + 0.0107 \left(\frac{\theta}{100} \right)^2 \right). \quad (\text{B.9})$$

- $f_c(\theta)$ [Pa] - compressive strength and $f_t(\theta)$ [Pa] - tensile strength. As specified in [33], both strengths are calculated as the multiplication of the nominal values of compressive and tensile strengths and reduction coefficients decreasingly varying from 1 to 0 as a function of temperature. For illustration, Figs. B.15(b) and (c) display curves for compressive and tensile strengths with values starting from $f_{c,0} = 15 \cdot 10^6$ [Pa] and $f_{t,0} = 1.5 \cdot 10^6$ [Pa].
- $\kappa(\theta)$ [ms⁻¹] - permeability. The determination of permeability in the analysis of a porous system exposed to fire represents the critical aspect for correct predictions of pore pressures and the resulting fire-induced spalling. In 2012, Davie et al. published a paper (see [23]) in which they studied such problem and found that permeability expressed as a function of damage appears to be the most representative and appropriate. As a result of this, Fig. B.15(d) shows such a functional dependence.

References

- [1] M. J. Hurley (editor in chief), SFPE Handbook of fire protection engineering, 5th edition, Springer (2015).
- [2] R. Carvel, A. Beard, The handbook of tunnel fire safety, Thomas Telford (2005).
- [3] I. Nakahori, T. Sakaguchi, B. Kohl, C. Forster, A. Vardy, Risk assessment of zero-flow ventilation strategy for fires in bidirectional tunnels with longitudinal ventilation, 16th International Symposium on Aerodynamics, Ventilation and Fire in Tunnels, Seattle, (2015).
- [4] I. Y. Maevski, Design fires in road tunnels, Transportation Research Board, 415 (2011).
- [5] T. Nakanishi, K. Uamamoto, K. Yokota, Y. Uehara, Risk Assessment Analysis for Water Spray Operation, 5th International Conference on Safety in Road & Rail Tunnels, Marseilles, (2003).
- [6] H. Mashimo, State of Road Tunnel Safety Technology in Japan, Tunnelling & Underground Space Technology 17 (2) (2002) 145–152.
- [7] S. Hostikka, O. Keski-Rahkonen, Probabilistic simulation of fire scenarios, Nuclear Engineering and Design 224 (3) (2003) 301–311.
- [8] National Transit Database, Federal Transit Administration, <https://www.transit.dot.gov/ntd>, accessed: 2016-08.
- [9] A. Beard, D. Cope, Assessment of the Safety of Tunnels, Final Report for the STOA (Science and Technology Options Assessment) Project. European Parliament (2007).
- [10] V. Babrauskas, R. D. Peacock, Heat release rate: the single most important variable in fire hazard, Fire Safety Journal 18 (3) (1992) 255–272.
- [11] D. Schütz, Fire protection in tunnels: Focus on road & train tunnels, Tech. newsl., SCOR Global P&C (2014).
- [12] K. Gkoumas, C. Di Santo, F. Bontempi, Risk analysis for severe traffic accidents in long road tunnels, International Journal of Forensic Engineering 3 (1-2) (2016) 106–126.
- [13] E. Blanchard, P. Boulet, S. Desanghere, E. Cesmat, R. Meyrand, J. P. Garo, J. P. Vantelon, Experimental and numerical study of fire in a midscale test tunnel, Fire Safety Journal 47 (2012) 18–31.
- [14] R. O. Carvel, A. N. Beard, P. W. Jowitt, D. D. Drysdale, The influence of tunnel geometry and ventilation on the heat release rate of a fire, Fire Technology 40 (1) (2004) 5–26.
- [15] ASFiNAG, Wien, Auswertung der ASFINAG-Tunnelbrandstatistik 2006-2012, <https://www.bmvit.gv.at/verkehr/strasse/tunnel/downloads/brandstatistik2012.pdf>, accessed: 2016-08 (2013).

- [16] C. Caliendo, M. L. D. Guglielmo, Evaluation of traffic and fire accidents in road tunnels, and a cost-benefit analysis, *International Journal of Civil Engineering Research* 3 (3) (2012) 201–222.
- [17] C. Caliendo, M. L. D. Guglielmo, M. Guida, A crash-prediction model for road tunnels, *Accident Analysis & Prevention* 55 (2013) 107–115.
- [18] L. Lu, J. Lu, Y. Xing, C. Wang, F. Pan, Statistical analysis of traffic accidents in Shanghai river crossing tunnels and safety countermeasures, *Discrete Dynamics in Nature and Society* 2014.
- [19] Z. Ma, C. Shao, S. Zhang, Characteristics of traffic accidents in Chinese freeway tunnels, *Tunnelling and Underground Space Technology* 24 (3) (2009) 350–355.
- [20] R. T. Tenchev, L. Y. Li, J. A. Purkiss, B. H. Khalafallah, Finite element analysis of coupled heat and mass transfer in concrete when it is in a fire, *Magazine of Concrete Research* 53 (2) (2001) 117–125.
- [21] C. T. Davie, C. J. Pearce, N. Bićanić, Coupled heat and moisture transport in concrete at elevated temperatures—effects of capillary pressure and adsorbed water, *Numerical Heat Transfer Part A: Applications* 49 (8) (2006) 733–763.
- [22] M. B. Dwaikat, V. K. R. Kodur, Hydrothermal model for predicting fire-induced spalling in concrete structural systems, *Fire Safety Journal* 44 (2009) 425–434.
- [23] C. T. Davie, C. J. Pearce, N. Bićanić, Aspects of permeability in modelling of concrete exposed to high temperatures, *Transport in Porous Media* 95 (3) (2012) 627–646.
- [24] C. T. Davie, C. J. Pearce, N. Bićanić, Fully coupled, hygro-thermo-mechanical sensitivity analysis of a pre-stressed concrete pressure vessel, *Engineering Structures* 59 (2014) 536–551.
- [25] C. E. Majorana, V. A. Salomoni, G. Xotta, B. Pomaro, G. Mazzucco, Computational issue in multifield, multiscale and three-dimensional structural engineering, in: *Computational Techniques for Civil and Structural Engineering*, 2015.
- [26] D. Gawin, F. Pesavento, B. A. Schrefler, What physical phenomena can be neglected when modelling concrete at high temperature? A comparative study. Part 1: Physical phenomena and mathematical model, *International Journal of Solids and Structures* 48 (2011) 1927–1944.
- [27] D. Gawin, F. Pesavento, B. A. Schrefler, What physical phenomena can be neglected when modelling concrete at high temperature? A comparative study. Part 2: Comparison between models, *International Journal of Solids and Structures* 48 (2011) 1945–1961.
- [28] Z. P. Bažant, W. Thonguthai, Pore pressure in heated concrete walls: theoretical prediction, *Magazine of Concrete Research* 31 (107) (1979) 67–76.
- [29] H. M. Künzle, K. Kiessl, Calculation of heat and moisture transfer in exposed building components, *International Journal of Heat and Mass Transfer* 40 (1) (1996) 159–167.

- [30] J. Sýkora, T. Krejčí, J. Kruis, M. Šejnoha, Computational homogenization of non-stationary transport processes in masonry structures, *Journal of Computational and Applied Mathematics* 18 (2012) 4745–4755.
- [31] J. Sýkora, M. Šejnoha, J. Šejnoha, Homogenization of coupled heat and moisture transport in masonry structures including interfaces, *Applied Mathematics and Computation* 219 (13) (2013) 7275–7285.
- [32] T. T. Lie, V. R. Kodur, Thermal and mechanical properties of steel-fibre-reinforced concrete at elevated temperatures, *Canadian Journal of Civil Engineering* 23 (4) (1996) 511–517.
- [33] European Committee for Standardization (CEN), Brussels, Eurocode 2: Design of concrete structures - Part 1-2: General rules - Structural fire design (2004).
- [34] M. Beneš, R. Štefan, J. Zeman, Analysis of coupled transport phenomena in concrete at elevated temperatures, *Applied Mathematics and Computation* 239 (2013) 7262–7274.
- [35] H. Ingason, A. Linnermark, Y. Z. Li, Runehamar tunnel fire tests, Tech. rep., SP Technical Research Institute of Sweden (2011).
- [36] H. Ingason, Y. Z. Li, Model scale tunnel fire tests with longitudinal ventilation, *Fire Safety Journal* 45 (2010) 371–384.
- [37] Y. Z. Li, B. Lei, H. Ingason, Study of critical velocity and backlayering length in longitudinally ventilated tunnel fires, *Fire Safety Journal* 45 (2010) 361–370.
- [38] M. Šejnoha, M. Brouček, Fire resistance of concrete with fly ash content - experimental analysis, *Engineering Mechanics* 21 (3) (2014) 159–165.
- [39] M. Šejnoha, M. Brouček, Experimental investigation of the fire resistance of modified concrete, in: *Engineering Mechanics*, 2013.
- [40] A. Ibrahimbegović, C. Knopf-Lenoir, A. Kučerová, P. Villon, Optimal design and optimal control of structures undergoing finite rotations and elastic deformations, *International Journal for Numerical Methods in Engineering* 61 (14) (2004) 2428–2460.
- [41] A. Kučerová, Identification of nonlinear mechanical model parameters based on soft computing methods, Ph.d. thesis, Ecole Normale Supérieure de Cachan, Laboratoire de Mécanique et Technologie (2007).
- [42] G. Mazzucco, C. E. Majorana, V. A. Salomoni, Numerical simulation of polypropylene fibres in concrete materials under fire conditions, *Computers & Structures* 154 (2015) 17–28.
- [43] P. J. Woodburn, R. E. Britter, CFD simulations of a tunnel fire—Part I, *Fire Safety Journal* 26 (1) (1996) 35–62.
- [44] P. J. Woodburn, R. E. Britter, CFD simulations of a tunnel fire—Part II, *Fire Safety Journal* 26 (1) (1996) 63–90.

- [45] L. H. Hu, R. Huo, W. Peng, W. K. Chow, R. X. Yang, On the maximum smoke temperature under the ceiling in tunnel fires, *Tunnelling and Underground Space Technology* 21 (2006) 650–655.
- [46] J. Abanto, M. Reggio, D. Barrero, E. Petro, Prediction of fire and smoke propagation in an underwater tunnel, *Tunnelling and Underground Space Technology* 22 (1) (2007) 90–95.
- [47] R. Jansson, *Fire Spalling of Concrete: Theoretical and Experimental Studies*, Doctoral Thesis in Concrete Structures, KTH Architecture and Built Environment, Stockholm, Sweden (2013).

Chapter 4

MODELING OF DAMAGE CAUSED BY ICE CRYSTALLIZATION PROCESS

The aim of presented chapter is modeling of degradation processes in historical mortars exposed to moisture impact during freezing. Internal damage caused by ice crystallization in pores is one of the most important factors limiting the service life of historical structures. Coupling the transport processes with the mechanical part will allow us to address the impact of moisture on the durability, strength and stiffness of mortars. This should be accomplished with the help of a complex thermo-hygro-mechanical model representing one of the prime objectives of this work. The proposed formulation is based on the extension of the classical poroelasticity models with the damage mechanics. An example of two-dimensional moisture transport in the environment with temperature below freezing point is presented to support the theoretical derivations.

List of selected journal papers and book chapters

Sýkora, J. (2014). Modeling of degradation processes in historical mortars. *Advances in Engineering Software*, 72:203–212.

Modeling of degradation processes in historical mortars

Jan Sýkora

Faculty of Civil Engineering, Czech Technical University in Prague, Thákurova 7, 166 29 Prague 6, Czech Republic

Keywords: Coupled heat and moisture transport, Ice crystallization process, Damage, Mortar

1. Introduction

Understanding the hydro-thermo-mechanical behavior of building materials exposed to weather conditions is the first step toward avoiding deterioration of structures in general and historical ones in particular, as high moisture content in building material and its phase changes are often a cause of internal damage. Because of variable climatic conditions, the moisture gradients induce mechanical stresses in the porous material. These stresses mostly develop due to the growth of ice crystals through the pore structure. Therefore, there is a strong need for investigating the influence of moisture on the mechanical material behavior, which leads to numerical and experimental coupling of mechanical and thermo-hygro phenomena.

In the literature, the above described problem is addressed from several perspectives. The first group of publications is focused on the description of the coupled heat and moisture transport reflecting the moisture migration under the conditions of the ice crystal formation in the pores, 2-D and 3-D aspects and different moisture/heat sources, such as wind driven rain, solar short and long wave radiation etc., see [1, 2, 3]. An extensive overview of various transport models is available in [4, 5]. While models for transport processes have been developed during several decades, the theory of ice crystallization in the pores has emerged only recently, [6, 7, 8]. The authors established relations between physical state of porous system and pore pressures. The physical conditions of ice formation process are described by thermodynamic balance equation between ice, liquid water and solid matrix. Finally, the mechanical response of porous media subjected to the frost action was studied by several authors [9, 10, 11]. On the one hand, the poroelasticity formulation based on Biot's continuum model was adopted. It is an efficient method for elastic modeling of porous system, which is subjected to the pressure of the fluid. On the other hand, a novel micromechanics approach was introduced to analyze the creation of micro-cracks in the microstructure during freezing process [12, 13]. These results predict effective mechanical and transport properties at microscopic level and can be utilized as an input for multi-scale analysis of porous media.

As a preamble, our goal is to quantify the internal damage caused by the ice crystallization pressure in historical mortars. In particular, a critical point in a restoration works is frequent applications of lime mortars for preserving compatibility with the historical materials. However, lime mortars are very porous, their mechanical strength and durability are

Email address: jan.sykora.1@fsv.cvut.cz (Jan Sýkora)

mostly very low [14, 15], thus the development of a lime mortar with improved internal hydrophobicity and associated improved resistance against damage due to the effects of ice crystallization is inevitable. To address this issue with respect to its complexity, an analysis combining both experimental work and numerical simulations has to be done. Nevertheless, the numerical methodology developed within this work can be utilized to simulate the response of any porous material subjected to the frost action.

A theoretical formulation of the problem is presented in Section 2, followed by numerical calculations in Section 3. Section 3.1 then investigates the influence of pore size distribution on the evolution of damage parameter. The essential findings are summarized in Section 4.

2. Material model

The problem of porous system subjected to ice crystallization can be divided into three physical phenomena - heat and moisture transport, ice formation process and evolution of damage caused by pore pressure. Using the thermodynamics, poromechanics and damage mechanics, we propose here the concept of multi-phase constitutive model based on the assumption of the uncoupled system in the sense of numerical analysis, see Fig. 1. These models are characterized by combining different physical or mechanical models (in space and time) in order to accurately describe structural response of deteriorating infrastructure over time. The general framework of the proposed model was primarily inspired by the work published in [16, 17, 9, 18, 2, 6, 10, 11].

In the presented work, the porous material is treated as multi-phase medium consisting of solid matrix, liquid water, water vapor and ice. The mathematical formulation consists of three governing equations representing the conservations of energy Eq. (4), mass Eq. (5) and linear momentum Eq. (36). The chosen primary unknowns are temperature θ [°C], moisture φ [-] and displacement of solid matrix \mathbf{u} [m].

The present section derives the governing equations of the analytical model. After theoretical formulation, a proper numerical time and space integration scheme is introduced to convert the proposed governing equations into a fully discrete form. Some details on the numerical implementation are also available in [19, 20].

2.1. Transport model

We use the diffusion model by Künzle, see [2], which is based on Krischer's concept [5]. Künzle neglected the liquid water and water vapor convection driven by gravity and total pressure as well as enthalpy changes due to liquid flow and choose relative humidity φ as the only moisture driving force. The water vapor diffusion is then described by Fick's law written as

$$\mathbf{q}_v = -\delta_v \nabla (\varphi p_{\text{sat}}), \quad (1)$$

where \mathbf{q}_v [kgm⁻²s⁻¹] is the water vapor flux, δ_v [kgm⁻¹s⁻¹Pa⁻¹] is the water vapor permeability of a porous material and $p_{\text{sat}} = p_{\text{sat}}(\theta)$ [Pa] is the saturation water vapor pressure being exponentially dependent on temperature. The transport of liquid water is assumed in the form of surface diffusion in an absorbed layer and capillary flow typically represented by Kelvin's law

$$\mathbf{q}_l = -D_\varphi \nabla \varphi, \quad (2)$$

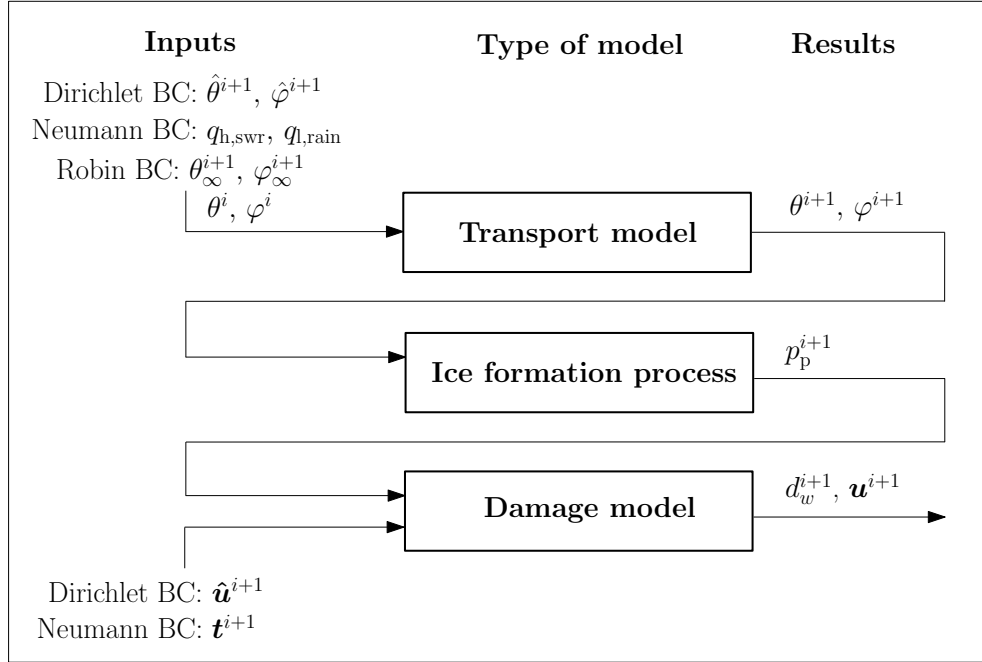


Figure 1: Algorithmic framework of proposed model

where \mathbf{q}_l [$\text{kgm}^{-2}\text{s}^{-1}$] is the flux of liquid water, $D_{\varphi} = D_l (dw/d\varphi)$ [$\text{kgm}^{-1}\text{s}^{-1}$] is the liquid conductivity and D_l [m^2s^{-1}] is the capillary transport coefficient, $dw/d\varphi$ is the derivative of water retention function. The Fourier law is then used to express the heat flux \mathbf{q}_h [Wm^{-2}] as

$$\mathbf{q}_h = -\lambda \nabla \theta, \quad (3)$$

where λ [$\text{Wm}^{-1}\text{K}^{-1}$] is the thermal conductivity and θ [$^{\circ}\text{C}$] is the local temperature. Introducing the above constitutive equations into energy and mass conservation equations we finally get resulting set of differential equations for the description of heat and moisture transfer expressed in terms of temperature and relative humidity as

- the energy balance equation

$$\frac{\partial H}{\partial \theta} \frac{\partial \theta}{\partial t} = \nabla \cdot [\lambda \nabla \theta] + h_v \nabla \cdot [\delta_v \nabla \{\varphi p_{\text{sat}}(\theta)\}], \quad (4)$$

- the conservation of mass equation

$$\frac{dw}{d\varphi} \frac{\partial \varphi}{\partial t} = \nabla \cdot [D_{\varphi} \nabla \varphi] + \nabla \cdot [\delta_v \nabla \{\varphi p_{\text{sat}}(\theta)\}], \quad (5)$$

The transport coefficients defining the material behavior are nonlinear functions of the temperature, moisture and material properties. We briefly recall their particular expressions [2]:

- w - total water content [kgm^{-3}],

$$w = w_f \frac{(b_{\varphi} - 1)\varphi}{b_{\varphi} - \varphi}, \quad (6)$$

where w_f [kgm^{-3}] is the free water saturation and b_φ [-] is the approximation factor, which must always be greater than one. It can be determined from the equilibrium water content (w_{80}) at 0.8 [-] relative humidity by substituting the corresponding numerical values in Eq. (6). Fig. 2(a) shows an example of variation of water content as a function of relative humidity.

- δ_v - water vapor permeability [$\text{kgm}^{-1}\text{s}^{-1}\text{Pa}^{-1}$],

$$\delta_v = \frac{\delta}{\mu}, \quad (7)$$

where μ [-] is the water vapor diffusion resistance factor and δ [$\text{kgm}^{-1}\text{s}^{-1}\text{Pa}^{-1}$] is the vapor diffusion coefficient in air given by

$$\delta = \frac{2.306 \cdot 10^{-5} p_a}{R_v (\theta + 273.15) p} \left(\frac{\theta + 273.15}{273.15} \right)^{1.81}, \quad (8)$$

with p set equal to atmospheric pressure $p_a = 101325$ [Pa] and $R_v = R/M_w = 461.5$ [$\text{Jkg}^{-1}\text{K}^{-1}$]; R is the gas constant (8314.41 [$\text{Jmol}^{-1}\text{K}^{-1}$]) and M_w is the molar mass of water (18.01528 [kgmol^{-1}]). An example of variation of water vapor permeability as a function of temperature is seen in Fig. 2(b).

- D_φ - liquid conduction coefficient [$\text{kgm}^{-1}\text{s}^{-1}$],

$$D_\varphi = D_1 \frac{dw}{d\varphi}, \quad (9)$$

where D_1 [m^2s^{-1}] is the capillary transport coefficient given by

$$D_1 = 3.8 \left(\frac{a}{w_f} \right)^2 \cdot 10^{3w/(w_f-1)}, \quad (10)$$

An example of variation of liquid conductivity D_φ [$\text{kgm}^{-1}\text{s}^{-1}$] as a function of water content is plotted in Fig. 2(c).

- λ - thermal conductivity [$\text{Wm}^{-1}\text{K}^{-1}$],

$$\lambda = \lambda_0 \left(1 + \frac{b_{\text{tcs}} w}{\rho_s} \right), \quad (11)$$

where λ_0 [$\text{Wm}^{-1}\text{K}^{-1}$] is the thermal conductivity of dry building material, ρ_s [kgm^{-3}] is the bulk density and b_{tcs} [-] is the thermal conductivity supplement. An example of variation of thermal conductivity as a function of water content is shown in Fig. 2(d).

- p_{sat} - water vapor saturation pressure [Pa],

$$p_{\text{sat}} = 611 \exp \left(\frac{a \theta}{\theta_0 + \theta} \right), \quad (12)$$

where

$$\begin{aligned} a &= 22.44 & \theta_0 &= 272.44 \text{ [}^\circ\text{C]} & \theta < 0 \text{ [}^\circ\text{C]} \\ a &= 17.08 & \theta_0 &= 234.18 \text{ [}^\circ\text{C]} & \theta \geq 0 \text{ [}^\circ\text{C]} \end{aligned} \quad (13)$$

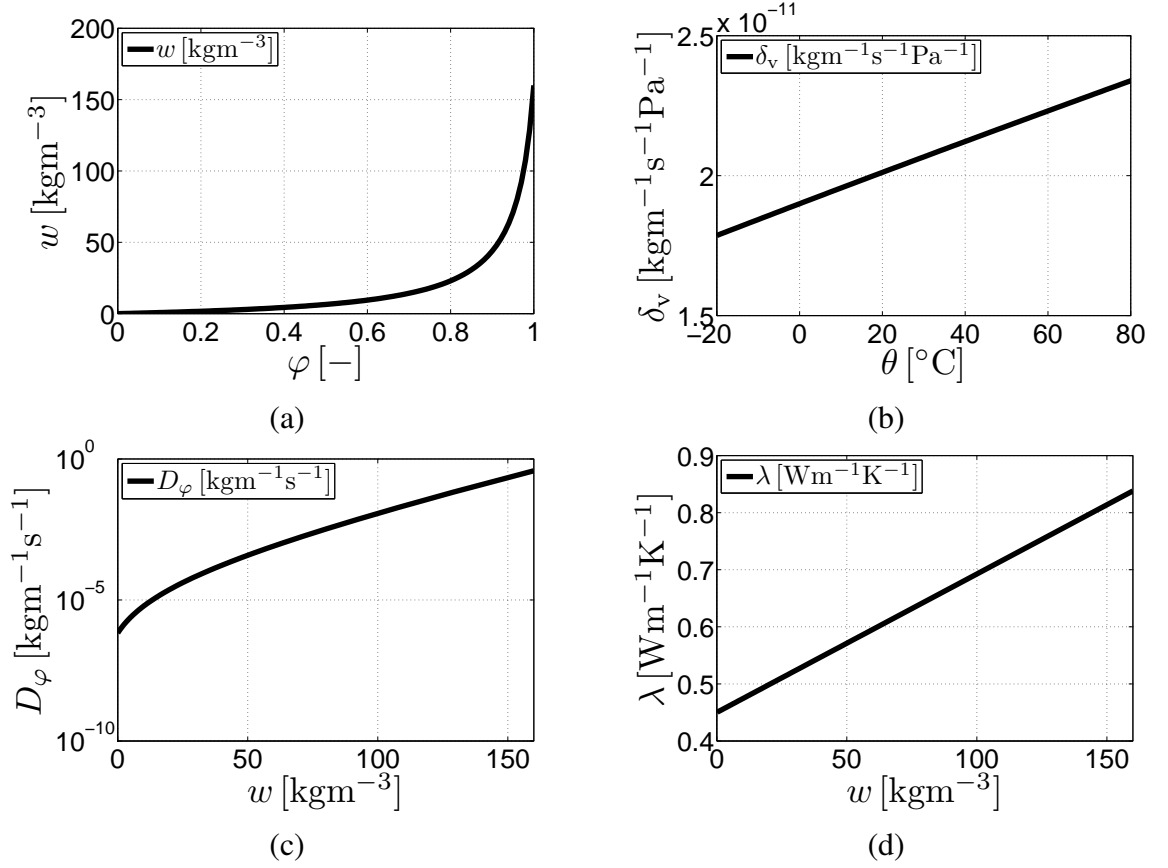


Figure 2: (a) Variation of water content as a function of relative humidity, (b) variation of water vapor permeability as a function temperature, (c) variation of liquid conductivity as a function of water content, (d) variation of thermal conductivity as a function of water content

- h_v - evaporation enthalpy of water [Jkg⁻¹]

$$h_v = 2.5008 \cdot 10^6 \left(\frac{273.15}{\theta} \right)^{(0.167+3.67 \cdot 10^{-4}\theta)}. \quad (14)$$

- H - total enthalpy of porous material [Jm⁻³]

$$H = \rho_s c_s \theta + \left[(w - w_i) c_l + w_i c_i - h_i \frac{dw_i}{d\theta} \right] \theta, \quad (15)$$

where ρ_s [kgm⁻³] is the bulk density, c_i [Jkg⁻¹K⁻¹] is the specific heat capacity of ice, c_s [Jkg⁻¹K⁻¹] is the specific heat capacity of solid matrix, c_l [Jkg⁻¹K⁻¹] is the specific heat capacity of liquid water and h_i [Jkg⁻¹] is the specific melting enthalpy of ice, w_i [kgm⁻³] is the content of ice.

For the spatial discretization of the partial differential equations, a finite element method is preferred here to the finite volume technique. The discretized form of energy and moisture

balance equations then reads

$$\underbrace{\begin{bmatrix} \mathbf{K}_{\theta\theta}(\mathbf{r}_\theta, \mathbf{r}_\varphi) & \mathbf{K}_{\theta\varphi}(\mathbf{r}_\theta, \mathbf{r}_\varphi) \\ \mathbf{K}_{\varphi\theta}(\mathbf{r}_\theta, \mathbf{r}_\varphi) & \mathbf{K}_{\varphi\varphi}(\mathbf{r}_\varphi) \end{bmatrix}}_{\mathbf{K}(\mathbf{r})} \underbrace{\begin{Bmatrix} \mathbf{r}_\theta \\ \mathbf{r}_\varphi \end{Bmatrix}}_{\mathbf{r}} + \underbrace{\begin{bmatrix} \mathbf{C}_{\theta\theta}(\mathbf{r}_\theta, \mathbf{r}_\varphi) & 0 \\ 0 & \mathbf{C}_{\varphi\varphi}(\mathbf{r}_\varphi) \end{bmatrix}}_{\mathbf{C}(\mathbf{r})} \underbrace{\begin{Bmatrix} \frac{d\mathbf{r}_\theta}{dt} \\ \frac{d\mathbf{r}_\varphi}{dt} \end{Bmatrix}}_{\dot{\mathbf{r}}} = \underbrace{\begin{Bmatrix} \mathbf{F}_\theta \\ \mathbf{F}_\varphi \end{Bmatrix}}_{\mathbf{F}}, \quad (16)$$

where \mathbf{K} is the conductivity matrix, \mathbf{C} is the capacity matrix, \mathbf{r} is the vector of nodal values, and \mathbf{F} is the vector of prescribed fluxes transformed into nodes. For a detailed formulation of the matrices \mathbf{K} and \mathbf{C} and the vector \mathbf{F} , we refer the interested reader to [21, 20].

The numerical solution of the system Eq. (16) is based on a simple temporal finite difference discretization. If we use time steps Δt and denote the quantities at time step i with a corresponding superscript, the time-stepping equation is

$$\mathbf{r}^{i+1} = \mathbf{r}^i + \Delta t[(1 - \gamma)\dot{\mathbf{r}}^i + \gamma\dot{\mathbf{r}}^{i+1}], \quad (17)$$

where γ is a generalized midpoint integration rule parameter. In the results presented in this paper the Crank-Nicolson (trapezoidal rule) integration scheme with $\gamma = 0.5$ was used. Expressing $\dot{\mathbf{r}}^{i+1}$ from Eq. (17) and substituting into the Eq. (16), one obtains a system of non-linear equations:

$$[\gamma\Delta t\mathbf{K}^{i+1}(\mathbf{r}^{i+1}) + \mathbf{C}^{i+1}(\mathbf{r}^{i+1})]\mathbf{r}^{i+1} = \gamma\Delta t\mathbf{F}^{i+1} + \mathbf{C}^{i+1}(\mathbf{r}^{i+1})[\mathbf{r}^i + \Delta t\{1 - \gamma\}\dot{\mathbf{r}}^i], \quad (18)$$

which can be solved by some iterative method such as Newton-Raphson.

2.2. Ice formation process

The ice crystallization process in the porous system is described by the penetration of liquid/ice interface from external surfaces or large pores towards the unfrozen zones [6].

The ice formation process is limited by a critical pore radius $r_{\text{cr}}(\theta)$, see Fig. 3(a). It describes the smallest geometrical radius of pore in which ice crystal can form [22, 11],

$$r_{\text{cr}}(\theta) = r_{\text{ir}}(\theta) + r_{\text{ar}}(\theta), \quad (19)$$

where r_{ir} [m] is the curvature radius of ice crystal (liquid-ice interface) formed at a given temperature and r_{ar} [m] is the layer of adsorbed water which cannot freeze during crystallization process. The empirical formula for r_{ar} [m] was proposed by Fagerlund [23] as

$$r_{\text{ar}}(\theta) = 1.97 \cdot 10^{-9} \sqrt[3]{\frac{1}{|\theta|}} \quad \text{for } \theta < 0 \text{ [}^\circ\text{C]} \quad (20)$$

and r_{ir} [m] is introduced through the simplified form of the Gibbs-Duhem equation [10] as

$$r_{\text{ir}}(\theta) = \frac{2\gamma_{\text{li}}}{\Delta s_{\text{m}}|\theta|} \quad \text{for } \theta < 0 \text{ [}^\circ\text{C]}, \quad (21)$$

where γ_{li} [Nm⁻¹] is the liquid/ice surface tension and Δs_{m} [PaK⁻¹] is the melting entropy.

The concept of the pore pressure caused by the ice crystals is well known, see [24, 9, 23, 22, 6, 7, 8, 10, 11]. To be more specific, let us consider spherical liquid-ice interface at the entrance of the pore and cylindrical shape of pores. Two interface equilibrium conditions

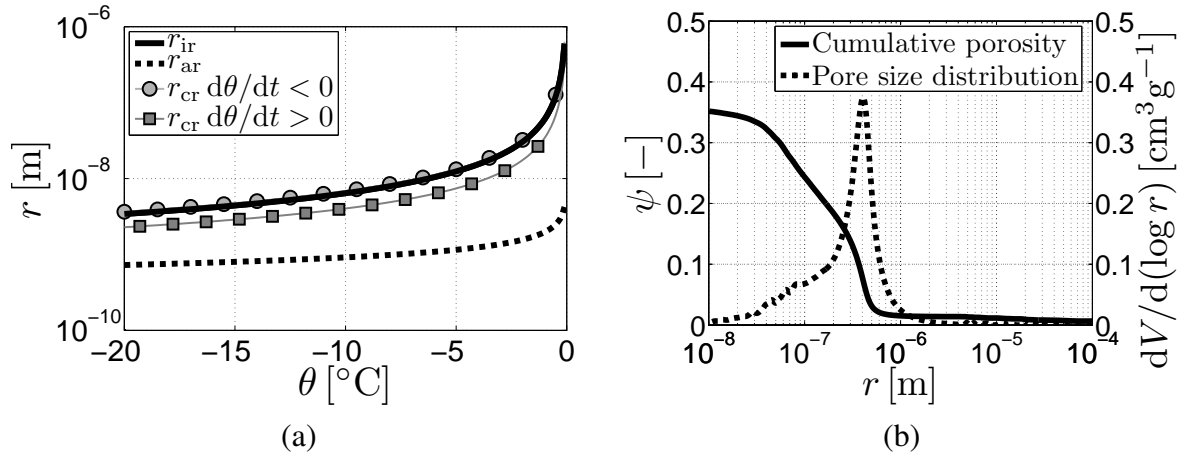


Figure 3: (a) Critical pore radius r_{cr} as a function of temperature, (b) pore size distribution obtained by mercury porosimetry and resulting cumulative porosity

are assumed to describe the interaction between ice crystals and pore walls. The Laplace relation is applicable to control the interface between the ice crystal and the liquid water:

$$p_i - p_l = \frac{2\gamma_{li}}{r_{ir}(\theta)}, \quad (22)$$

where p_l [Pa] is the liquid pressure and p_i [Pa] is the pressure in the ice crystal. The second interface relation is expressed in the form of mechanical equilibrium between the ice crystal and the pore pressure exerted by the ice crystal, p_p [Pa], as

$$p_i - p_p = \frac{\gamma_{li}}{r - r_{ar}(\theta)}. \quad (23)$$

Finally, combining Eq. (22) and Eq. (23), we can write

$$p_p = p_l + \chi(r, \theta), \quad (24)$$

where $\chi(r, \theta)$ [Pa] is the local pressure on the frozen pore walls due to the ice formation and it is characterized by following relation, see [25, 11],

$$\chi(r, \theta) = \gamma_{li} \left(\frac{2}{r_{ir}(\theta)} - \frac{1}{r - r_{ar}(\theta)} \right). \quad (25)$$

It has been advocated in [6] and [11] that the average pore pressure exerted by the ice crystal on the pore walls can be introduced as

$$p_p = p_l + \frac{1}{n} \int_{r_{cr}(\theta)}^{\infty} \chi(r, \theta) \frac{d\psi}{dr} dr, \quad (26)$$

where n [-] is the total porosity and $\psi(r)$ [-] is the cumulative porosity. The cumulative porosity ψ [-] with a pore radius greater than r [m] is defined as, see Fig. 3(b),

$$\psi(r) = \int_r^{\infty} \frac{d\psi}{dr} dr. \quad (27)$$

2.3. Mechanical (damage) model

The description of mechanical behavior of a porous media saturated with a liquid water was firstly proposed by Biot [17] and extended in the more general context of continuum thermodynamics for the ice crystals by Coussy [24, 9]. According to this approach, the formula between the effective stress $\boldsymbol{\sigma}'$ [Pa] and total stress $\boldsymbol{\sigma}$ [Pa] has following form

$$\boldsymbol{\sigma} = \boldsymbol{\sigma}' - bp_p \boldsymbol{i}, \quad (28)$$

where b [–] is Biot's coefficient, p_p [Pa] is the pressure exerted by ice crystal on the pore walls and $\boldsymbol{i} = \{1, 1, 1, 0, 0, 0\}^T$. The standard formulation of Biot's coefficient related to the liquid water is based on introduction of the bulk modulus of porous material K [Pa] and the bulk modulus of solid matrix K_s [Pa]. For our purpose, we utilize more convenient relation for porous system derived in [8].

$$b = \frac{2n}{n+1} \approx 1 - \frac{K}{K_s}, \quad (29)$$

where n [–] is the total porosity. As a further extension, we introduce one parameter isotropic nonlocal damage model given by constitutive law, see [16, 26],

$$\boldsymbol{\sigma}' = (1 - d_w) \mathbf{D}_e \boldsymbol{\varepsilon}, \quad (30)$$

damage law

$$d_w = g(\kappa) \quad (31)$$

and loading-unloading conditions

$$f(\boldsymbol{\varepsilon}, \kappa) = \varepsilon_{\text{eq}}(\boldsymbol{\varepsilon}) - \kappa \leq 0, \quad \dot{\kappa} \geq 0, \quad f(\boldsymbol{\varepsilon}, \kappa) \dot{\kappa} = 0, \quad (32)$$

where \mathbf{D}_e [Pa] is the elastic stiffness matrix, d_w [–] is the damage parameter, κ [–] is the internal variable corresponding to the maximum value of equivalent strain ε_{eq} [–] reached in the loading history. The equivalent strain can be expressed in Mazars's form as

$$\varepsilon_{\text{eq}} = \sqrt{\sum_{I=1}^3 \langle \varepsilon_I \rangle^2}, \quad (33)$$

where ε_I [–] is component of the principal strains and the brackets denote the positive part. According to [16], the local value ε_{eq} [–] is replaced by its nonlocal average defined as

$$\varepsilon_{\text{eq,nonlocal}}(\boldsymbol{x}) = \int_V \phi(\boldsymbol{x}, \boldsymbol{\xi}) \varepsilon_{\text{eq}}(\boldsymbol{\xi}) d\boldsymbol{\xi}, \quad (34)$$

where $\phi(\boldsymbol{x}, \boldsymbol{\xi})$ [–] is the nonlocal weight function representing distance in the domain between the source point $\boldsymbol{\xi}$ [m] and target point \boldsymbol{x} [m]. For more details about nonlocal formulation we refer to [16]. Finally, the damage law $d_w = g(\kappa)$ is provided by following relation

$$g(\kappa) = \begin{cases} 0 & \text{for } 0 \leq \kappa \leq \varepsilon_0, \\ 1 - \frac{\kappa - \varepsilon_0}{\varepsilon_f - \varepsilon_0} & \text{for } \varepsilon_0 \leq \kappa \leq \varepsilon_f, \\ 1 & \text{for } \varepsilon_f \leq \kappa. \end{cases}, \quad (35)$$

where $\varepsilon_f [-]$ is the equivalent strain at critical crack opening and $\varepsilon_0 [-]$ is the strain at the elastic limit.

Considering the stress relation Eq. (28) and Eq. (30), the linear momentum balance equation for the porous system, can be expressed in the following form:

$$\nabla \cdot [\boldsymbol{\sigma}' - bp_p \mathbf{i}] + \mathbf{b} = 0, \quad (36)$$

where $\mathbf{b} [\text{Nm}^{-3}]$ is the body force. The governing equations are discretized in space using the standard finite element approximation. The unknown displacement field $\mathbf{u} [\text{m}]$ is expressed in terms of its nodal values. Details of the formulation may be found in [18].

2.4. Boundary and initial conditions

To complete the proposed material model, the initial and boundary conditions are set as follows:

- The Dirichlet boundary conditions

$$\begin{aligned} \theta &= \hat{\theta}(t) & \text{on } \Gamma_{\theta}^I, \\ \varphi &= \hat{\varphi}(t) & \text{on } \Gamma_{\varphi}^I, \\ \mathbf{u} &= \hat{\mathbf{u}}(t) & \text{on } \Gamma_u^I, \end{aligned} \quad (37)$$

- The Neumann boundary conditions

$$\begin{aligned} [-\lambda \nabla \theta - \delta_v \nabla \{\varphi p_{\text{sat}}(\theta)\}] \cdot \mathbf{n} &= q_h(t) + q_{h,\text{swr}}(t) & \text{on } \Gamma_{\theta}^{\text{II}}, \\ [-D_{\varphi} \nabla \varphi - \delta_v \nabla \{\varphi p_{\text{sat}}(\theta)\}] \cdot \mathbf{n} &= q_v(t) + q_l(t) + q_{l,\text{rain}}(t) & \text{on } \Gamma_{\varphi}^{\text{II}}, \\ \boldsymbol{\sigma}' \cdot \mathbf{n} &= \boldsymbol{\sigma}_t(t) & \text{on } \Gamma_u^{\text{II}}, \end{aligned} \quad (38)$$

- The Robin boundary conditions

$$\begin{aligned} [-\lambda \nabla \theta - \delta_v \nabla \{\varphi p_{\text{sat}}(\theta)\}] \cdot \mathbf{n} &= \alpha_h [\theta - \theta_{\infty}(t)] & \text{on } \Gamma_{\theta}^{\text{III}}, \\ [-D_{\varphi} \nabla \varphi - \delta_v \nabla \{\varphi p_{\text{sat}}(\theta)\}] \cdot \mathbf{n} &= \beta_v [\varphi - \varphi_{\infty}(t)] & \text{on } \Gamma_{\varphi}^{\text{III}}, \end{aligned} \quad (39)$$

- Initial conditions

$$\theta(\mathbf{x}, 0) = \theta_{\text{in}} \quad \varphi(\mathbf{x}, 0) = \varphi_{\text{in}} \quad \mathbf{u}(\mathbf{x}, 0) = \mathbf{u}_{\text{in}} \quad \text{for all } \mathbf{x} \in \Omega, \quad (40)$$

where the symbol $\hat{\cdot}$ denotes prescribed value, $\mathbf{n} [-]$ is the unit normal vector, $q_{h,\text{swr}} [\text{Wm}^{-2}]$ is the solar short-wave radiation flux, $q_{l,\text{rain}} [\text{kgm}^{-2}\text{s}^{-1}]$ is the driving-rain flux, $\boldsymbol{\sigma}_t [\text{Pa}]$ is the imposed traction, $\alpha_h [\text{Wm}^{-2}\text{K}^{-1}]$ is the heat transfer coefficient, $\beta_v [\text{kgm}^{-2}\text{s}^{-1}\text{Pa}^{-1}]$ is the water vapor transfer coefficient, θ_{∞} and φ_{∞} are the ambient temperature and moisture, respectively.

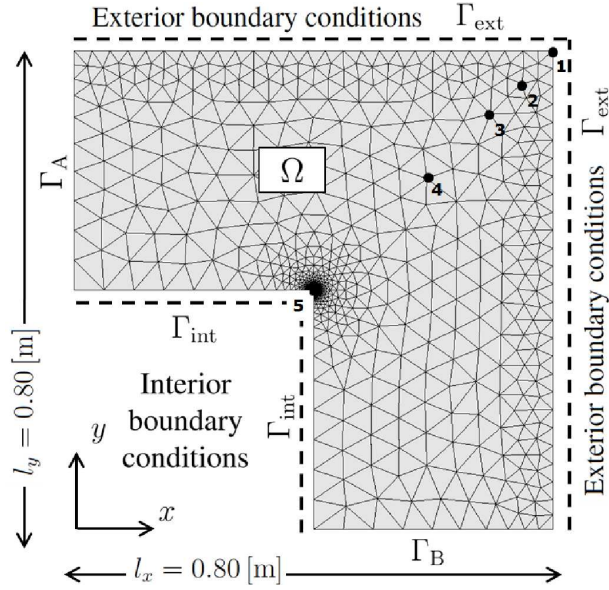


Figure 4: 2-D domain with initial and boundary conditions

3. Numerical example

In this section, we employ the proposed thermo-hygro-mechanical model to perform a numerical simulation of transport processes below freezing point in porous media and their impact on the mechanical properties. In doing so we consider geometry together with the initial and loading conditions displayed in Fig 4. Two-dimensional L-shape domain was discretized by an FE mesh into 741 nodes and 1358 triangular elements. The solution of the time-dependent problem also involves a discretization of the time domain into 744 uniform time steps chosen with regard to the convergence criteria of nonlinear solution.

The measured material parameters, corresponding to a lime mortar, are listed in Tab. 1. Several parameters were obtained from a set of experimental measurements providing mostly the hygric and thermal properties of mortar, see [14]. Unfortunately, no additional experiments were conducted for the mechanical properties, hence we utilize some material parameters of mortars mentioned in the literature, see Tab. 1.

The initial conditions were set equal to $\mathbf{u}_{in} = \mathbf{0}$ [m], $\theta_{in} = 14$ [°C] and $\varphi_{in} = 0.5$ [–] in the whole domain. The following Robin boundary conditions were imposed: on the interior side a constant temperature of 24 [°C] and a constant relative humidity 0.6 [–] were maintained, while on the exterior side the real climatic data representing the winter conditions were prescribed, see Figs. 5(a),(b). Moreover, the exterior side of the domain was loaded by the heat flux from solar short-wave radiation $q_{h,swr}$ [Wm⁻²] and the driving-rain flux $q_{l,rain}$ [kgm⁻²s⁻¹] (the Neumann boundary conditions), see Figs. 5(c),(d) and Tab. 2.

The results are presented in Fig. 6 showing variation of the temperature and moisture at selected nodes labeled in Fig. 4. The obtained results clearly manifesting the influence of exterior boundary conditions on the temperature and moisture fields, especially near the exterior surface of the 2-D domain.

Several interesting results have been derived within the scope of the calculation of internal damage. Figs. 7(a),(b) display the evolution of damage parameter and its dependence on the average pore pressure. Beside the comparison of the evolution of damage parameter in

Symbol	Unit		Value	Ref.
<i>Transport properties of mortar</i>				
w_f	[kgm ⁻³]	free water saturation	160	[21]
w_{80}	[kgm ⁻³]	water content at $\varphi = 0.8$ [-]	23	[21]
λ_0	[Wm ⁻¹ K ⁻¹]	thermal conductivity	0.45	[21]
b_{tcs}	[-]	thermal conductivity supplement	9	[21]
ρ_s	[kgm ⁻³]	bulk density	1670	[21]
μ	[-]	water vapor diffusion resistance factor	9.63	[14, 21]
a	[kgm ⁻² s ^{-0.5}]	water absorption coefficient	0.82	[14, 21]
c_s	[Jkg ⁻¹ K ⁻¹]	specific heat capacity	1000	[14, 21]
<i>Mechanical properties of mortar</i>				
E	[Pa]	Young's modulus	$1 \cdot 10^{10}$	[27, 28]
ν	[-]	Poisson's ratio	0.2	[27, 28]
f_t	[Pa]	tensile strength	$2.5 \cdot 10^6$	[27, 28]
ε_f	[-]	equivalent strain at critical crack opening	$2.5 \cdot 10^{-3}$	[16, 26]
l_{intl}	[m]	internal length	$1 \cdot 10^{-3}$	[16, 26]
α	[K ⁻¹]	thermal expansion coefficient	$1.2 \cdot 10^{-5}$	[27, 28]
<i>Ice formation process</i>				
γ_{li}	[Nm ⁻¹]	liquid/ice surface tension	0.0409	[13]
Δs_m	[PaK ⁻¹]	melting entropy	$1.2 \cdot 10^6$	[13]
n	[-]	total porosity	0.35	[14, 15]
ψ	[-]	cumulative volume of pores	Fig. 3(b)	[14, 15]
<i>Other properties</i>				
α_h	[Wm ⁻² K ⁻¹]	heat transfer coefficient	8	[2]
β_v	[kgm ⁻² s ⁻¹ Pa ⁻¹]	water vapor transfer coefficient	$5.6 \cdot 10^{-8}$	[2]
α_{swr}	[-]	short-wave absorption coefficient	0.6	[2]

Table 1: Input parameters of numerical simulation

the time, we also compare growth of damage parameter in the domain, see Fig. 8. Analysis of these results allows better understanding of physical phenomena in porous media subjected to the frost action. A fast moisture increase in the zone close to the exterior surface (Fig. 6(b)) leads also to the similar trend of the damage parameter, see Fig. 7(a). This can be attributed to the lower exterior temperature and higher moisture content in the surface layer caused by the driving-rain flux. It is evident from the boundary conditions plotted in Figs. 5(a),(c). The calculated results promote the capability of proposed governing equations to simulate a degradation processes in the building materials exposed to real weather conditions.

3.1. Influence of porosity

The formation of ice is mainly controlled by pore size distribution, see [11]. To address this issue we consider the same input data as in the previous numerical example except for the total porosity n [-] and cumulative porosity ψ [-]. Note that the structure of porous system

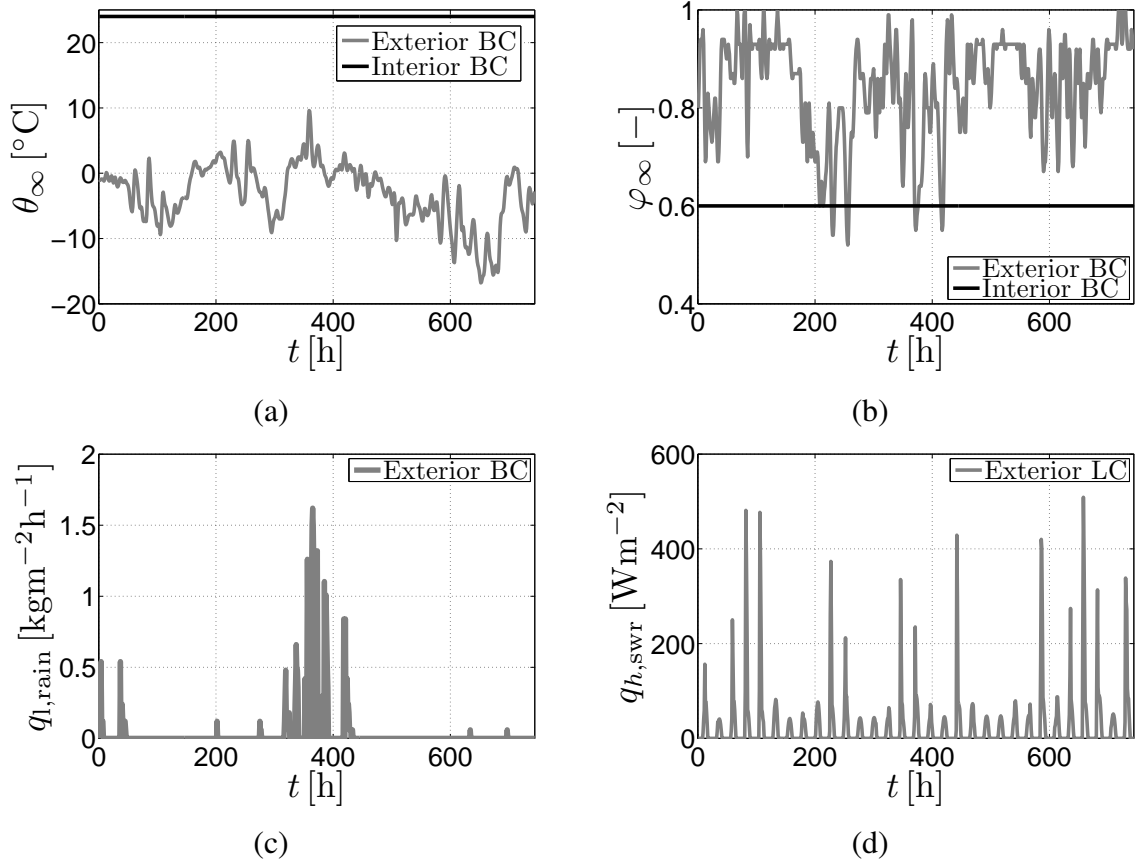


Figure 5: Exterior and interior boundary conditions - (a) temperature, (b) moisture, (c) driving-rain, (d) short-wave radiation

Side	BC type	Description	Fig.
<i>Boundary conditions</i>			
Γ_{ext}	II	$[-\lambda \nabla \theta - \delta_v \nabla \{\varphi p_{\text{sat}}(\theta)\}] \cdot \mathbf{n} = q_{h,\text{swr}}(t)$	5(d)
Γ_{ext}	II	$[-D_\varphi \nabla \varphi - \delta_v \nabla \{\varphi p_{\text{sat}}(\theta)\}] \cdot \mathbf{n} = q_{l,\text{rain}}(t)$	5(c)
Γ_{ext}	III	$[-\lambda \nabla \theta - \delta_v \nabla \{\varphi p_{\text{sat}}(\theta)\}] \cdot \mathbf{n} = 8[\theta - \theta_\infty(t)]$	5(a)
Γ_{ext}	III	$[-D_\varphi \nabla \varphi - \delta_v \nabla \{\varphi p_{\text{sat}}(\theta)\}] \cdot \mathbf{n} = 5.6 \cdot 10^{-8}[\varphi - \varphi_\infty(t)]$	5(b)
Γ_{int}	III	$[-\lambda \nabla \theta - \delta_v \nabla \{\varphi p_{\text{sat}}(\theta)\}] \cdot \mathbf{n} = 8[\theta - 24]$	5(a)
Γ_{int}	III	$[-D_\varphi \nabla \varphi - \delta_v \nabla \{\varphi p_{\text{sat}}(\theta)\}] \cdot \mathbf{n} = 5.6 \cdot 10^{-8}[\varphi - 0.6]$	5(b)
Γ_A	I	$u_x(t) = 0$ [m]	
Γ_B	I	$u_y(t) = 0$ [m]	
<i>Initial conditions</i>			
Ω		$\theta_{\text{in}} = 14$ [°C]	
Ω		$\varphi_{\text{in}} = 0.5$ [-]	
Ω		$\mathbf{u}_{\text{in}} = \mathbf{0}$ [m]	

Table 2: Boundary and initial conditions

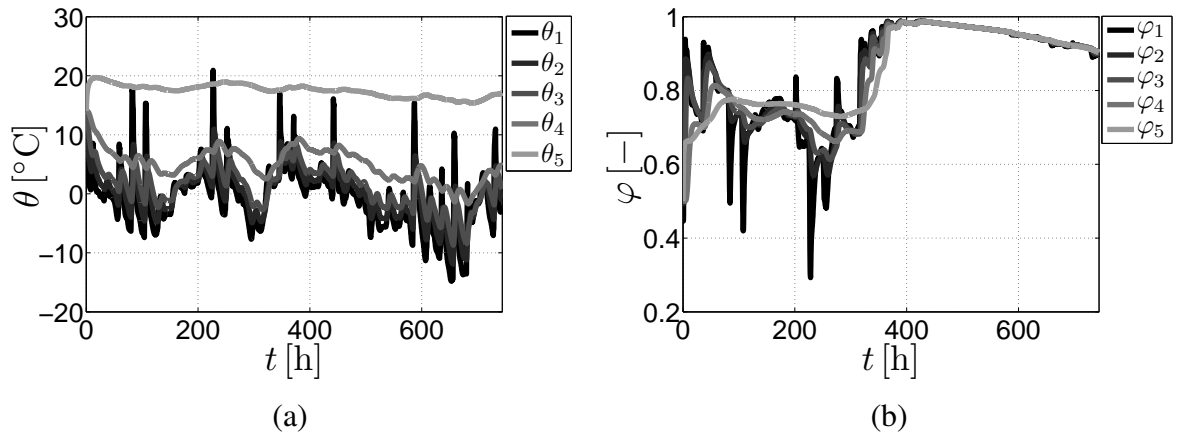


Figure 6: (a) Resulting temperature at selected nodes, (b) resulting moisture at selected nodes

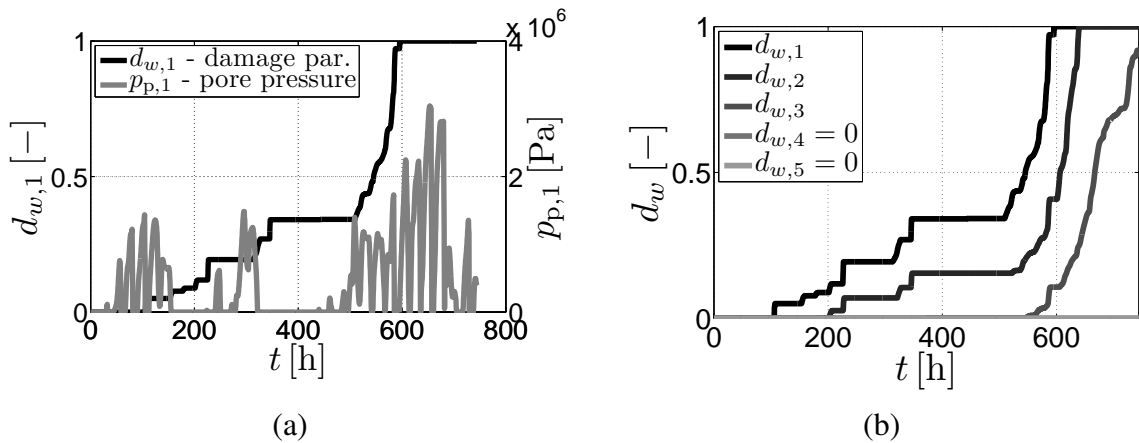


Figure 7: (a) Evolution of damage parameter $d_{w,1}$ [-] and pore pressure $p_{p,1}$ [Pa] at node 1, (b) Evolution of damage parameters d_w [-] at selected nodes

affects surely transport and mechanical properties of mortars, but we focus here only on the influence of different porosity to keep the numerical study clear and transparent, see Eqs. (26) and (36). Therefore, two different pore size distributions were taken into account, see Fig. 9(a). Further we assume in calculations the following values of total porosity $\{n_{\text{spec01}} = 0.35 [-], n_{\text{spec02}} = 0.13 [-]\}$ representing material properties of the lime mortar and the lime mortars with oil additive, respectively.

For a given pore size distributions, Figs. 9(b), (d) shows the evolution of damage parameters in the critical location of the 2-D domain. It is shown that the value of total porosity changes slightly, while the influence on the evolution of damage parameter is significant. This is clearly observed from the comparison of pore pressures displayed in Fig. 7(a) and Fig. 9(c). Combining all the previous results suggests that the structure of porous system plays crucial role in the resulting pore pressure and subsequently calculated internal damage.

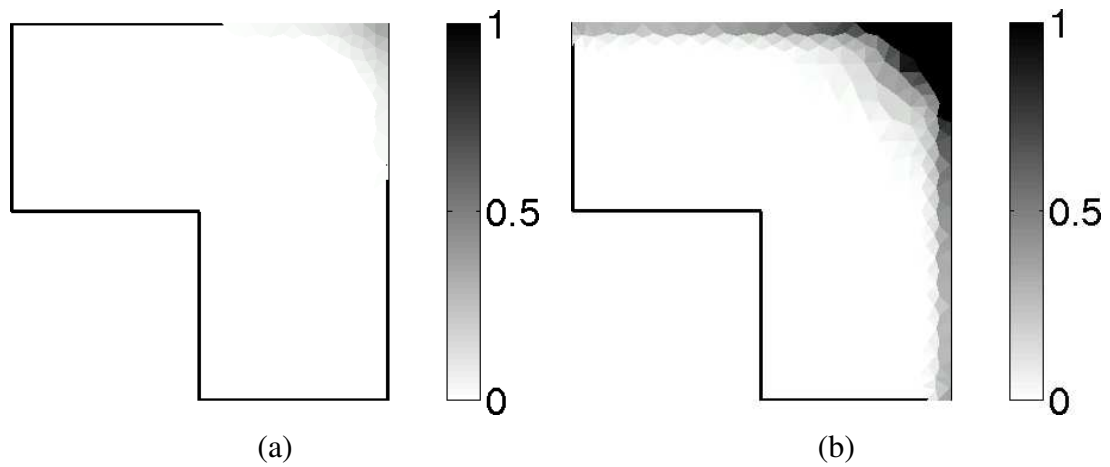


Figure 8: (a) Evolution of damage parameter d_w [-] after $t = 372$ [h], (b) evolution of damage parameter d_w [-] at the end of analyzed time period ($t = 744$ [h])

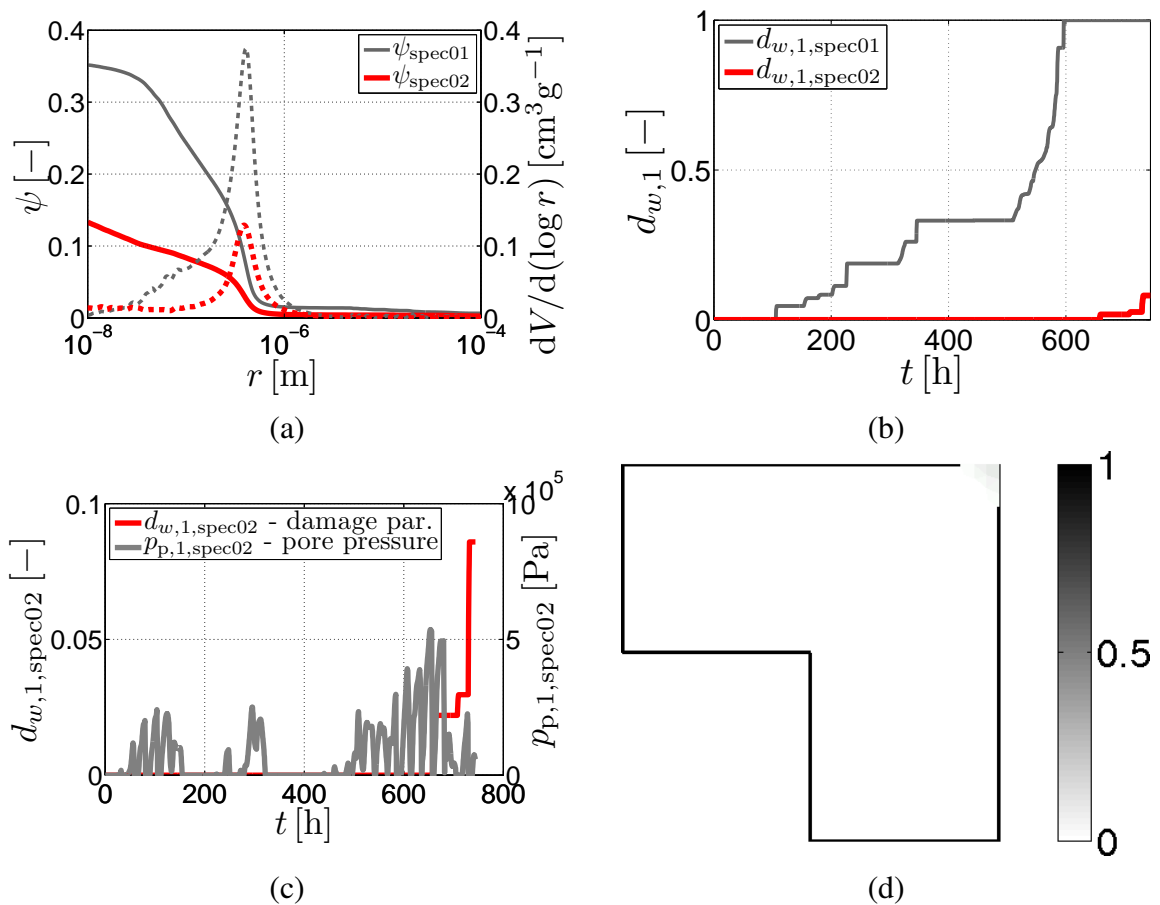


Figure 9: (a) Two different pore size distributions and cumulative porosity functions, (b) comparison of damage evolutions at node 1, (c) evolution of damage parameter $d_{w,1,\text{spec02}}$ [-] and pore pressure $p_{p,1,\text{spec02}}$ [Pa] at node 1 for porosity equal to $n_{\text{spec02}} = 0.13$ [-], (d) evolution of damage parameter $d_{w,\text{spec02}}$ [-] at the end of analyzed time period ($t = 744$ [h])

4. Conclusions

This paper presents the numerical modeling of damage caused by ice crystallization process in mortars. Attention is focused on the thermo-hygro-mechanical model developed here in the framework of uncoupled algorithmic scheme. Two particular issues were addressed: (i) the formulation of material model based on laws of the thermodynamics, poromechanics and damage mechanics, (ii) influence of porosity on the mechanical behavior.

In particular, we employed Künzel's model, which is sufficiently robust to describe real-world materials, but which is also highly nonlinear, time-dependent material model. Supported by several successful applications in civil engineering we adopted Biot's model and the nonlocal isotropic damage model in the framework to simulate the frost action on porous media.

A crucial point in modeling of damage in mortars is the pore size distribution. The obtained results suggest a high importance of porosity on evolution of the damage parameter, at least for the present material parameters and applied range of initial and boundary conditions.

Finally a comparison of the numerical calculations with experimental measurements is under current investigation and will be presented elsewhere.

Acknowledgement

The financial support provided by the NAKI grant No. DF11P01OVV0080 entitled "High-performance and compatible lime mortars for extreme application in restoration, repair and preventive maintenance of architectural heritage" is gratefully acknowledged. The experimental work performed at the Institute of Theoretical and Applied Mechanics AS CR under the leadership of Dr. Zuzana Slížková is also gratefully acknowledged.

Nomenclature

a	water absorption coefficient, [$\text{kgm}^{-2}\text{s}^{-0.5}$]
\mathbf{b}	body force, [Nm^{-3}]
b	Biot's coefficient, $[-]$
b_{tcs}	thermal conductivity supplement, $[-]$
b_{φ}	approximation factor, $[-]$
\mathbf{C}	discretized capacity matrix
c_i	specific heat capacity of ice, [$\text{Jkg}^{-1}\text{K}^{-1}$]
c_s	specific heat capacity of solid matrix, [$\text{Jkg}^{-1}\text{K}^{-1}$]
c_l	specific heat capacity of liquid water, [$\text{Jkg}^{-1}\text{K}^{-1}$]
\mathbf{D}_e	elastic stiffness matrix, [Pa]
D_l	capillary transport coefficient, [m^2s^{-1}]
D_{φ}	liquid conduction coefficient, [$\text{kgm}^{-1}\text{s}^{-1}$]
d_w	damage parameter, $[-]$
E	Young's modulus, [Pa]
\mathbf{F}	prescribed fluxes

f_t	tensile strength, [Pa]
H	total enthalpy of porous material, [Jm^{-3}]
h_i	specific melting enthalpy of ice, [Jkg^{-1}]
h_v	latent heat of phase exchange, [Jkg^{-1}]
\mathbf{K}	discretized conductivity matrix
K	bulk modulus of porous material, [Pa]
K_s	bulk modulus of solid matrix, [Pa]
l_{intl}	internal length, [m]
M_w	molar mass of water, [kgmol^{-1}]
\mathbf{n}	unit normal vector, [–]
n	total porosity, [–]
p_a	atmospheric pressure, [Pa]
p_l	liquid pressure, [Pa]
p_p	average pore pressure, [Pa]
p_{sat}	saturation vapor pressure, [Pa]
\mathbf{q}_h	heat flux, [Wm^{-2}]
\mathbf{q}_l	liquid transport flux, [$\text{kgm}^{-2}\text{s}^{-1}$]
\mathbf{q}_v	water vapor flux, [$\text{kgm}^{-2}\text{s}^{-1}$]
R	gas constant, [$\text{Jmol}^{-1}\text{K}^{-1}$]
r	pore radius, [m]
\mathbf{r}	nodal values
r_{ar}	layer of adsorbed water, [m]
r_{cr}	critical pore radius, [m]
r_{ir}	curvature radius of ice crystal, [m]
S_h	heat source, [Wm^{-3}]
S_w	moisture source, [$\text{kgm}^{-3}\text{s}^{-1}$]
t	time, [s]
\mathbf{u}	displacement vector, [m]
w	total water content, [kgm^{-3}]
w_{80}	water content at 0.8 [–] relative humidity, [kgm^{-3}]
w_i	content of ice, [kgm^{-3}]
w_f	free water saturation, [kgm^{-3}]
α	thermal expansion coefficient, [K^{-1}]
α_h	heat transfer coefficient, [$\text{Wm}^{-2}\text{K}^{-1}$]
α_{swr}	short wave absorption coefficient, [–]
β_v	water vapor transfer coefficient, [$\text{kgm}^{-2}\text{s}^{-1}\text{Pa}^{-1}$]
Γ	boundary
γ	generalized midpoint integration parameter, [–]
γ_{li}	liquid/ice surface tension, [Nm^{-1}]

Δs_m	melting entropy, [PaK ⁻¹]
δ	vapor diffusion coefficient in air, [kgm ⁻¹ s ⁻¹ Pa ⁻¹]
δ_v	water vapor permeability of porous material, [kgm ⁻¹ s ⁻¹ Pa ⁻¹]
ε_0	equivalent strain at elastic limit, [–]
ε_{eq}	equivalent strain, [–]
ε_f	equivalent strain at critical crack opening, [–]
θ	temperature, [°C]
λ	thermal conductivity of moist porous material, [Wm ⁻¹ K ⁻¹]
λ_0	thermal conductivity of dry porous material, [Wm ⁻¹ K ⁻¹]
μ	water vapor diffusion resistance factor, [–]
ν	Poisson's ratio, [–]
ρ_s	bulk density, [kgm ⁻³]
σ	total stress, [Pa]
σ'	effective stress, [Pa]
φ	relative humidity, [–]
χ	local pressure on the frozen pore walls, [Pa]
ψ	cumulative volume of pores, [–]
Ω	domain
Subscripts	
ext	exterior
i	ice
in	initial
int	interior
l	liquid water
p	pore
r	radius
s	solid
v	water vapor

References

- [1] F. Kong, H. Wang, Heat and mass coupled transfer combined with freezing process in building materials: Modeling and experimental verification, *Energy and Building* 43 (10) (2011) 2850–2859.
- [2] H. M. Künzle, K. Kiessl, Calculation of heat and moisture transfer in exposed building components, *International Journal of Heat and Mass Transfer* 40 (1) (1996) 159–167.
- [3] X. Tan, W. Chen, H. Tian, J. Cao, Water flow and heat transport including ice/water phase change in porous media: Numerical simulation and application, *Cold Regions and Technology* 68 (1–2) (2011) 74–84.

- [4] R. W. Lewis, B. A. Schrefler, *The Finite Element Method in the Static and Dynamic Deformation and Consolidation of Porous Media*, John Wiley&Sons, Chichester, England, 2nd edition, 1999.
- [5] R. Černý, P. Rovnaníková, *Transport Processes in Concrete*, London: Spon Press, 2002.
- [6] G. W. Scherer, Freezing gels, *Journal of Non-Crystalline Solids* 155 (1) (1993) 1–25.
- [7] G. W. Scherer, Crystallization in pores, *Cement and Concrete Research* 29 (8) (1999) 1347–1358.
- [8] Z. Sun, G. W. Scherer, Effect of air voids on salt scaling and internal freezing, *Cement and Concrete Research* 40 (2) (2010) 260–270.
- [9] O. Coussy, P. Monteiro, Poroelastic model for concrete exposed to freezing temperatures, *Cement and Concrete Research* 38 (1) (2008) 40–48.
- [10] G. Wardeh, B. Perrin, Numerical modelling of the behaviour of consolidated porous media exposed to frost action, *Construction and Building Materials* 22 (4) (2008) 600–608.
- [11] B. Zuber, J. Marchand, Modeling the deterioration of hydrated cement systems exposed to frost action - Part 1: Description of the mathematical model, *Cement and Concrete Research* 30 (12) (2000) 1929–1939.
- [12] M. Koster, 3D multi-scale model of moisture transport in cement-based materials, in: W. Brameshuber (Ed.), *International RILEM Conference on Material Science*, 2010, pp. 165–176.
- [13] L. Liu, G. Ye, E. Schlagen, H. Chen, Z. Qian, W. Sun, K. van Breugel, Modeling of the internal damage of saturated cement paste due to ice crystallization pressure during freezing, *Cement and Concrete Research* 33 (5) (2011) 562–571.
- [14] C. Nunes, Z. Slížková, D. Kříánková, D. Frankeová, Effect of linseed oil on the mechanical properties of lime mortars, in: *Engineering Mechanics 2012*, 2012.
- [15] Z. Slížková, M. Drdácý, D. Frankeová, L. Nosál, A. Zeman, Study of historic mortars from Charles Bridge, in: *Restaurování a Ochrana Uměleckých děl IV*, 2010, pp. 26–28, in Czech.
- [16] Z. B. Bažant, J. Jirásek, Nonlocal integral formulations of plasticity and damage: Survey of progress, *Journal of Engineering Mechanics* 128 (11) (2002) 1119–1149.
- [17] M. A. Biot, General theory of three-dimensional consolidation, *Journal of Applied Physics* 12 (2) (1941) 155–164.
- [18] D. Gawin, F. Pesavento, B. A. Schrefler, Modelling of hygro-thermal behaviour of concrete at high temperature with thermo-chemical and mechanical material degradation, *Computer Methods in Applied Mechanics and Engineering* 192 (13) (2003) 1731–1771.

- [19] A. Kučerová, J. Sýkora, Uncertainty updating in the description of coupled heat and moisture transport in heterogeneous materials, *Applied Mathematics and Computation* 219 (13) (2013) 7252–7261.
- [20] J. Sýkora, M. Šejnoha, J. Šejnoha, Homogenization of coupled heat and moisture transport in masonry structures including interfaces, *Applied Mathematics and Computation* 219 (13) (2013) 7275–7285.
- [21] J. Sýkora, T. Krejčí, J. Kruis, M. Šejnoha, Computational homogenization of non-stationary transport processes in masonry structures, *Journal of Computational and Applied Mathematics* 18 (2012) 4745–4755.
- [22] S. Matala, Effects of carbonation on the pore structure of granulated blast furnace slag concrete, Ph.D. thesis, Helsinki University of Technology (1995).
- [23] G. Fagerlund, Determination of pore-size distribution from freezing-point depression, *Materials and Structures* 6 (3) (1973) 215–225.
- [24] O. Coussy, P. Monteiro, Unsaturated poroelasticity for crystallization in pores, *Computers and Geotechnics* 34 (4) (2007) 279–290.
- [25] A. S. S. Multon, B. Perrin, Numerical analysis of frost effects in porous media. Benefits and limits of the finite element poroelasticity formulation, *International Journal for Numerical and Analytical Methods in Geomechanics* 36 (4) (2012) 438–458.
- [26] M. Horák, Localization analysis of damage and plasticity models, Master's thesis, CTU in Prague, in Czech (2009).
- [27] G. Milani, A. Tralli, Simple lower bound limit analysis homogenization model for in- and out-of-plane loaded masonry walls, *Construction and Building Materials* 25 (12) (2012) 808–834.
- [28] G. Milani, A. Tralli, A simple meso-macro model based on SQP for the non-linear analysis of masonry double curvature structures, *International Journal of Solids and Structures* 49 (4) (2012) 1999–2011.

Chapter 5

PROBABILISTIC IDENTIFICATION METHODS

Estimation of material parameters plays an important role in many scientific fields ranging from geophysics, medical imaging, archaeology, material science to the preservation of historical structures. This chapter focuses on the civil engineering problem of heat transfer in cases where an intervention into a structure might not be allowed and where estimation of the material parameter can be conducted using only boundary measurements. For two decades, thermal tomography has addressed such scenarios. This study introduces a novel approach for recovering spatially distributed thermal properties based on the random field theory, which efficiently parametrizes the unknown parameter fields. The proposed approach is verified computationally and the results achieved correspond well to those provided by standard thermal tomography procedures.

List of selected journal papers and book chapters

Havelka, J., Kučerová, A., and Sýkora, J. (2019). Dimensionality reduction in thermal tomography. *Computers & Mathematics with Applications*, 78(9):3077–3089.

List of related journal papers and book chapters

Havelka, J. and Sýkora, J. (2018). Application of Calderón’s inverse problem in civil engineering. *Applications of Mathematics*, 63(6):687–712.

Janouchová, E., Sýkora, J., and Kučerová, A. (2018). Polynomial chaos in evaluating failure probability: A comparative study. *Applications of Mathematics*, 63(6):713–737.

Kučerová, A. and Sýkora, J. (2013). Uncertainty updating in the description of coupled heat and moisture transport in heterogeneous materials. *Applied Mathematics and Computation*, 219(13):7252–7261.

Kučerová, A., Sýkora, J., Rosić, B., and Matthies, H. G. (2012). Acceleration of uncertainty updating in the description of transport processes in heterogeneous materials. *Journal of Computational and Applied Mathematics*, 236(18):4862–4872.

Rosić, B., Sýkora, J., Pajonk, O., Kučerová, A., and Matthies, H. G. (2016). Comparison of numerical approaches to bayesian updating. In *Computational Methods for Solids and Fluids*, pages 427–461. Springer.

Rosić, B. V., Kučerová, A., Sýkora, J., Pajonk, O., Litvinenko, A., and Matthies, H. G. (2013). Parameter identification in a probabilistic setting. *Engineering Structures*, 50:179–196.

Dimensionality reduction in thermal tomography

Jan Havelka

Faculty of Civil Engineering, Czech Technical University in Prague, Thákurova 7, 166 29 Prague 6, Czech Republic

Anna Kučerová

Faculty of Civil Engineering, Czech Technical University in Prague, Thákurova 7, 166 29 Prague 6, Czech Republic

Jan Sýkora

Faculty of Civil Engineering, Czech Technical University in Prague, Thákurova 7, 166 29 Prague 6, Czech Republic

Keywords: Bayesian inference, Karhunen-Loève expansion, Heat transport, Random field, Thermal tomography

1. Introduction

Parameter estimation is one of the key procedures in numerical modeling. Having the ability to analyze a given structure without damaging or intervening in opens up new possibilities for saving both time and financial resources in many areas. Application of inverse analysis using only boundary measurements first appeared in the 1930s in geophysics, see [17], and then expanded to many fields such as medicine, see [4, 10, 6, 23]; archaeology, see [5]; and many others, see [3, 2, 11, 12, 28].

In civil engineering problems, thermal tomography approaches have been used, see [3], in order to recover thermal spatially distributed parameters, i.e. thermal conductivity and volumetric heat capacity, from non-destructive imaging surface temperatures. In practice, a domain being analyzed is sequentially subjected to loading states at different source locations and corresponding temperature responses are collected from the boundary layer. Consequently, a true material field is identified based on knowledge of the loading states and the boundary observations.

Thermal tomography has been studied during the past few years from several perspectives. Spatially distributed thermal conductivity for the steady-state heat equation was first estimated from boundary observations in [12]. Defects and inhomogeneities in thermal conductivity fields were presented in [3] and [11]. In [13], the authors demonstrated the feasibility of thermal tomography for the more complex case of a transient problem, i.e. identifying thermal conductivity and also volumetric heat capacity. Furthermore, the methodology has been extended in [27] towards the practical problems encountered when boundary heat flux is unknown, introducing the heat transfer coefficient as an additional field which needs to be

Email addresses: jan.havelka.1@fsv.cvut.cz (Jan Havelka), anna.kucerova@cvut.cz (Anna Kučerová), jan.sykora.1@fsv.cvut.cz (Jan Sýkora)

recovered. The three dimensional aspects of parameter estimation and Bayesian inference for both stationary and non-stationary heat problems were proposed in [28].

In general, the estimation of thermal properties from boundary measurements is an ill-posed problem because of issues related to the existence of a solution and uniqueness. Small variations in measured data can also result in large changes in a solution and this affects the stability of a problem, see [19]. Traditional approaches have used regularization methods to impose well-posedness and to search for deterministic solutions, mostly by employing optimization techniques, see [9]. Another possibility is casting the inverse problem in a probabilistic setting, see [25]. Here, Bayesian inference is addressed as a method, where unknown parameters are modeled as random variables (prior distributions), naturally regularizing the inverse problem. The results obtained from Bayesian updating are probability distributions (posterior distributions) summarizing all available information and any remaining uncertainty in the values of material properties.

The aim of this paper is to provide a novel approach for recovering spatially distributed thermal properties based on the random field theory, which efficiently parametrizes an unknown parameter field of interest, see [1, 29]. Modeling the material properties as random fields has become very popular in the area of spectral stochastic finite element methods, first introduced by Ghanem and Spanos [8] and further elaborated, for instance, in [21, 30, 14]. Here, instead of identifying the unknown parameters for each grid point/element of a geometrical domain, one must only find a few coefficients to the corresponding eigenmodes which form the resulting random field. The spatial variability of the random field is provided by individual basis vectors, i.e. eigenmodes. Moreover, the identification procedure is performed in a Bayesian way. From the results computed here, it can be seen that our proposed approach provides a suitable method for identifying material heterogeneity from boundary measurements.

The fundamental procedures of thermal tomography related to our idea are very briefly presented in three consecutive sections. A physical problem is established using the transient heat balance equation in Section 2; the basic relations of Bayesian inference, such as the likelihood function and/or posterior distribution, are mentioned in the Section 3. Section 4 is devoted to the construction of the random field. In Section 5, the Bayesian updating procedure is examined numerically to support the proposed methodology, presenting a discussion and a comparison of the results obtained by the classical approach with results based on the random field theory together with possible limitations of this study. Finally, the work is summarized in the last section.

2. Forward model

The purpose of this section is to introduce the forward model which is used to predict the temperature u [°C] inside the studied body D . Heat transport in general is described by the transient heat balance equation as

$$\left\{ \begin{array}{ll} \rho_s(\mathbf{x})c_p(\mathbf{x})\frac{\partial u}{\partial t}(\mathbf{x}, t) - \nabla \cdot (\lambda_s(\mathbf{x})\nabla u(\mathbf{x}, t)) = 0, & \mathbf{x}, t \in D \times (0, t_s), \\ \lambda_s(\mathbf{x})\frac{\partial u}{\partial n}(\mathbf{x}, t) = \tilde{f}_N(\mathbf{x}, t), & \mathbf{x} \in \partial D_N, \\ \alpha(u(\mathbf{x}, t) - u_\infty(\mathbf{x}, t)) = \lambda_s(\mathbf{x})\frac{\partial u}{\partial n}(\mathbf{x}, t), & \mathbf{x} \in \partial D_T, \\ \partial D = \partial D_N \cup \partial D_T, \quad u(\mathbf{x}, 0) = 0, & \mathbf{x} \in D. \end{array} \right. \quad (1)$$

where $\rho_s(\mathbf{x})$ [kgm⁻³] is volumetric mass density, $c_p(\mathbf{x})$ [JKg⁻¹K⁻¹] is specific heat capacity, $\lambda_s(\mathbf{x})$ [Wm⁻¹K⁻¹] is thermal conductivity, t_s [s] is the final time of the simulation, $D \subseteq \mathbb{R}^2$ is the open bounded region, and $\partial D_{(N,T)}$ are the non-intersecting subsets of the boundary ∂D with corresponding environmental factors. u_∞ [°C] is the ambient temperature, α [Wm⁻²K⁻¹] is the heat transfer coefficient, and \tilde{f}_N [Wm⁻²] is the prescribed heat flux. For computational purposes, volumetric heat capacity $c_v(\mathbf{x})$ [Jm⁻³K⁻¹] is introduced in the heat balance equation as

$$c_v(\mathbf{x}) = \rho_s(\mathbf{x})c_p(\mathbf{x}). \quad (2)$$

In this paper, a finite element method is preferred for the spatial discretization of the transient heat balance equation. The existence of a solution and uniqueness of the weak form of Eq. (1) is presented by Ladyzhenskaia et al. in [16]. The domain is discretized into N_e triangular elements with N_n nodes; the solution is approximated with $\phi_i(\mathbf{x})$ for $i = 1, \dots, N_n$ linear basis functions. Material parameters $\lambda_s(\mathbf{x})$ and $c_v(\mathbf{x})$ are approximated using element-wise constant functions and can be identified by vectors $\boldsymbol{\lambda}_s, \mathbf{c}_v \in \mathbb{R}^{N_e}$ defining the values in centroids of particular elements. Finally, the forward operator \mathbf{F} is the function of two independent parameters ($\mathbf{q} = [\boldsymbol{\lambda}_s^T, \mathbf{c}_v^T]$) and solves the system for chosen time steps m_t and nodes m_n at once,

$$\mathbf{F}(\mathbf{q}) = \mathbf{u}_r, \quad \mathbf{u}_r \in \mathbb{R}^{m_n \cdot m_t}. \quad (3)$$

The output of the forward operator \mathbf{F} is acquired as a subset ($m_n < N_n$ and $m_t \leq N_t$) of a full solution matrix $\mathbf{u}_{\text{sol}} = [\mathbf{u}_1, \mathbf{u}_2, \dots, \mathbf{u}_{N_t}] \in \mathbb{R}^{N_n \times N_t}$, where N_t is the number of total time steps of the simulation obtained from the following set of linear equations

$$\begin{aligned} \mathbf{K}_C \mathbf{u}_{i+1} &= \left(\mathbf{K}_C - \Delta t \tilde{\mathbf{K}} \right) \mathbf{u}_{i-1} + \dots \\ &\quad \Delta t \left((1 - \tau) \mathbf{f}_{n,i-1} + \tau \mathbf{f}_{n,i} \right) + \dots \\ &\quad \Delta t \left((1 - \tau) \mathbf{f}_{t,i-1} + \tau \mathbf{f}_{t,i} \right), \end{aligned} \quad (4)$$

$$\tilde{\mathbf{K}} = \mathbf{K} + \mathbf{K}_t, \quad (5)$$

$$\mathbf{K}_C = \mathbf{C} + \tau \Delta t \tilde{\mathbf{K}}, \quad (6)$$

where $\Delta t = t_{i+1} - t_i$ is the time step, and $\tau \in \langle 0; 1 \rangle$ is the implicitness parameter. The computations presented here were performed for $\tau = 0.5$, i.e. the implicit Crank-Nicolson scheme. Finally, the system matrices and right hand side vectors are computed in the following way:

$$K_{jk} = \int_{\Omega} \lambda_s \nabla \phi_j \cdot \nabla \phi_k \, dA \quad j, k = 1 \dots N_n, \quad (7)$$

$$C_{jk} = \int_{\Omega} \rho_s c_p \phi_j \phi_k \, dA \quad j, k = 1 \dots N_n, \quad (8)$$

$$K_{t,jk} = \int_{\partial\Omega_T} \alpha \phi_j \phi_k \, dS \quad j, k = 1 \dots N_n, \quad (9)$$

$$f_{t,ji} = \int_{\partial\Omega_T} \alpha u_{0,i} \phi_l \, dS \quad i = 1 \dots N_t, j = 1 \dots N_n, \quad (10)$$

$$f_{n,ji} = - \int_{\partial\Omega_N} f_N(t_i) \phi_j \, dS \quad i = 1 \dots N_t, j = 1 \dots N_n. \quad (11)$$

3. The Bayesian inference

When identifying the thermal properties of a system, one deals with a situation where the observable quantity, i.e. the temperature on the boundary, is measured and the goal is to find the corresponding model parameters $\mathbf{q} = [\boldsymbol{\lambda}_s^T, \mathbf{c}_v^T]$. In the Bayesian setting of parameter identification, the uncertainty in observations is combined together with prior expert knowledge about the parameter values for estimation of the so-called posterior probabilistic description of identified parameters (Gelman et al. [7]; Rosić et al. [25]). To begin with a priori knowledge, both the thermal conductivities $\boldsymbol{\lambda}_s$ and volumetric heat capacities \mathbf{c}_v , cannot be negative in civil engineering problems; hence, lognormal distribution is more suitable for their description. Therefore, q_i is considered to be independent lognormally distributed with the probability density function

$$p_i(q_i) = \frac{1}{q_i \sqrt{2\pi\sigma_g^2}} \exp - \frac{(\ln q_i - \mu_g)^2}{2\sigma_g^2}, \quad (12)$$

where parameters μ_g and σ_g are, respectively, the mean and standard deviation of the variable's natural logarithm. The joint prior density function is then defined as

$$p_q(\mathbf{q}) = \prod_{i=1}^{N_q} p_i(q_i), \quad (13)$$

where N_q is the number of parameters.

The observations \mathbf{z} differ from the modeled values \mathbf{u}_r because of model imperfection and measurement error. Hence, $\mathbf{z} = \mathbf{u}_r + \boldsymbol{\varepsilon}$, where $\boldsymbol{\varepsilon}$ includes both of the aforementioned errors. To keep the presentation of different numerical aspects of particular methods clear and transparent, a quite common and simple case is assumed where modeling imperfections are neglected and measurement errors are modeled as zero-mean Gaussian random variables with the probability density function

$$p_j(\varepsilon_j) = \frac{1}{\sqrt{2\pi\sigma_\varepsilon^2}} \exp - \frac{\varepsilon_j^2}{2\sigma_\varepsilon^2}, \quad (14)$$

where σ_ε^2 is the measurement error variance. Assuming the measurement errors in particular observations to be independent, the likelihood function $L(\mathbf{q})$ is subsequently expressed, see Kučerová et al. [14], as

$$L(\mathbf{q}) = \prod_{j=1}^{N_\varepsilon} p_j(\varepsilon_j) = \prod_{j=1}^{N_\varepsilon} p_j(z_j - F_j(\mathbf{q})). \quad (15)$$

where N_ε is the number of independent observations; in our case, $N_\varepsilon = m_n \cdot m_t$. The result of the probabilistic identification procedure comes with the posterior state of information given by the conjunction of the prior information and the information obtained from measurements, see Tarantola [26], as

$$\pi(\mathbf{q}) = \varpi p_q(\mathbf{q})L(\mathbf{q}), \quad (16)$$

where ϖ is a normalisation constant. The primary computational challenge in Bayesian inference is based on extracting information from the posterior density. Most estimates take the form of expectations w.r.t. the posterior. These expectations, mathematically integrals, may be numerically evaluated via asymptotic, deterministic, or sampling methods. Nowadays, Markov chain Monte Carlo (MCMC) methods remain the most general, flexible, and wide-spread techniques employed. To be more specific, the Metropolis-Hastings algorithm is the most common method for obtaining a sequence of random samples from a probability distribution, see Gelman et al. [7]. The basic principle relies on performing a random walk to sample the prior probability distribution and then apply an appropriate probabilistic rule to accept or reject samples in order to obtain the resulting set of accepted walks sampling the posterior distribution, see Kučerová et al. [14].

4. Random field

In the area of numerical modeling of a heterogeneous material, the random field theory is a widely accepted methodology for describing the spatial variability of material parameters. The definition of lognormal random field $q(\mathbf{x}, \omega)$ starts from the definition of Gaussian random field $g(\mathbf{x}, \omega)$, which is expressed by its mean

$$\mu_g(\mathbf{x}) = \mathbf{E}[g(\mathbf{x}, \omega)] = \int_{\Omega} g(\mathbf{x}, \omega) \mathbf{P}(d\omega) \quad (17)$$

and its covariance

$$\begin{aligned} C_g(\mathbf{x}, \mathbf{x}') &= \mathbf{E}[(g(\mathbf{x}, \omega) - \mu_g(\mathbf{x}))(g(\mathbf{x}', \omega) - \mu_g(\mathbf{x}'))] \\ &= \int_{\Omega} (g(\mathbf{x}, \omega) - \mu_g(\mathbf{x}))(g(\mathbf{x}', \omega) - \mu_g(\mathbf{x}')) \mathbf{P}(d\omega), \end{aligned} \quad (18)$$

where Ω is a set of random elementary events ω together with a σ -algebra \mathcal{S} to which a real number in the interval $[0, 1]$ may be assigned, the probability of occurrence – mathematically a measure \mathbf{P} . Some non-Gaussian fields may be synthesized as nonlinear functions of Gaussian fields (Matthies [20]; Rosić et al. [24]). The lognormal random field $q(\mathbf{x}, \omega)$ is obtained as

$$q(\mathbf{x}, \omega) = \exp(g(\mathbf{x}, \omega)). \quad (19)$$

When the lognormal prior distribution is prescribed in terms of its mean μ_q and variance σ_q^2 instead of the mean μ_g and variance σ_g^2 of the variable's natural logarithm, the latter moments can be then obtained from the former ones according to the following relations, see Rosić et al. [24],

$$\sigma_g^2 = \ln \left(1 + \left(\frac{\sigma_q}{\mu_q} \right)^2 \right), \quad \mu_g = \ln \mu_q - \frac{1}{2} \sigma_g^2. \quad (20)$$

The Karhunen-Loève expansion is an extremely useful tool representing the stochastic process as an infinite linear combination of orthogonal functions. Based on the spectral

decomposition of covariance function $C_g(\mathbf{x}, \mathbf{x}')$ and the orthogonality of eigenfunctions ψ_i , the random field $g(\mathbf{x}, \omega)$ can be written as

$$g(\mathbf{x}, \omega) = \mu_g + \sigma_g \sum_{k=0}^{\infty} \sqrt{\varsigma_k} \xi_k(\omega) \psi_k(\mathbf{x}), \quad (21)$$

where $\xi(\omega)$ is a set of standard i.i.d. random variables. Since the covariance $C_g(\mathbf{x}, \mathbf{x}')$ is symmetric and positive definite, it can be expanded in the series

$$C_g(\mathbf{x}, \mathbf{x}') = \sum_{k=1}^{\infty} \varsigma_k \psi_k(\mathbf{x}) \psi_k(\mathbf{x}'). \quad (22)$$

However, computing the eigenfunctions analytically is usually not feasible. Therefore, one discretizes the covariance spatially according to chosen grid points (usually corresponding to nodes of finite element mesh) and the solution of the problem turns into the series of eigenvalues ς_k and eigenvectors ψ_k . The Karhunen-Loève expansion $\hat{g}(\omega)$ of random field $g(\mathbf{x}, \omega)$ is then expressed as

$$\hat{g}(\omega) = \mu_g + \sigma_g \sum_{k=0}^m \sqrt{\varsigma_k} \xi_k(\omega) \psi_k, \quad (23)$$

where the number m ($m \leq N_n$ in case of nodal discretization) is chosen such that the above equation gives a good approximation, i.e. it captures a high proportion of the total variance. Higher values of m yield better descriptions of a random field; smaller values lead to more significant dimensionality reduction a computation acceleration. Taking into account a lognormal distribution of the parameters, the final formulation of the random field describing the parameter q_i then becomes

$$\hat{q}_i(\omega) = \exp(\mu_g + \sigma_g \sum_{k=0}^m \sqrt{\varsigma_k} \xi_k(\omega) \psi_k). \quad (24)$$

Note that the covariance and eigenvectors discretized to finite element nodes also provide nodal discretization of parameter q_i , which needs to be further mapped into the centroids by means of finite element basis functions before applying Eqs. (7) and (8).

It is obvious that the covariance function plays a key role in the construction of the random field. Therefore, from a group of commonly-used isotropic covariance functions, the Matérn covariance function is introduced for two points separated by the distance $d = \|\mathbf{x} - \mathbf{x}'\|_2$ as

$$C(d) = \frac{2^{1-\nu}}{\Gamma(\nu)} \left(\sqrt{2\nu} \frac{d}{\rho} \right)^\nu K_\nu \left(\sqrt{2\nu} \frac{d}{\rho} \right), \quad (25)$$

where $\Gamma(\nu)$ is the gamma function, K_ν is the modified Bessel function of the second kind, and ρ and ν are non-negative parameters of the covariance. The parameter ρ represents a measure of how the correlation decreases the distance d and ν is the smoothness parameter, see Minasny et al. [22]. As $\nu \rightarrow 1/2$, the Matérn covariance function turns into the exponential covariance function and another limit case is obtained for $\nu \rightarrow \infty$, where the

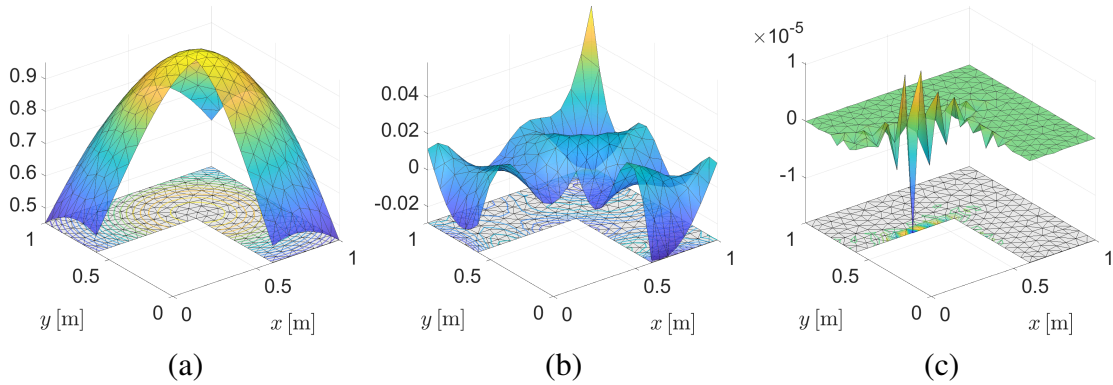


Figure 1: Eigenfunctions of the Matérn covariance function evaluated for $\rho = 0.25$ and $\nu = 5$: (a) $m = 1$; (b) $m = 20$; (c) $m = 216$.

function turns into the Gaussian covariance function. Note that the determination of correlation lengths is generally not obvious. However, in material modeling, one possible way to estimate correlation length is to utilize image analysis as described by Lombardo et al. in [18]. A numerical study for various numbers of eigenmodes m included in the Karhunen-Loève expansion is presented, for example, by Kučerová et al. in [15].

For illustration, several eigemodes computed with the help of Eq. (25) for $\rho = 0.25$ and $\nu = 5$ are depicted in Fig. 1. One can see the low oscillation of the first eigenmode, while the last eigenmode clearly describes higher frequencies. It is worth mentioning that each eigenmode is weighted in the Karhunen-Loève expansion with a different eigenvalue, i.e. the influence of each subsequent eigenmode on a resulting random field has a decreasing tendency. This effect can be also seen in Fig. 2 which shows dimensionless random fields constructed for various numbers of eigenmodes. It is apparent from the reported figures that the last two random fields ($m = 20$ and $m = 216$) are visually similar.

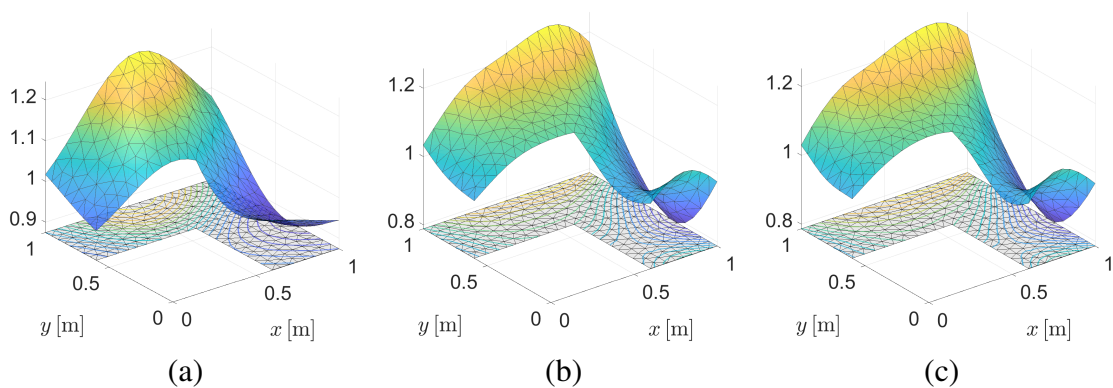


Figure 2: Dimensionless random fields constructed for (a) 5 eigenmodes; (b) 20 eigenmodes; (c) 216 eigenmodes.

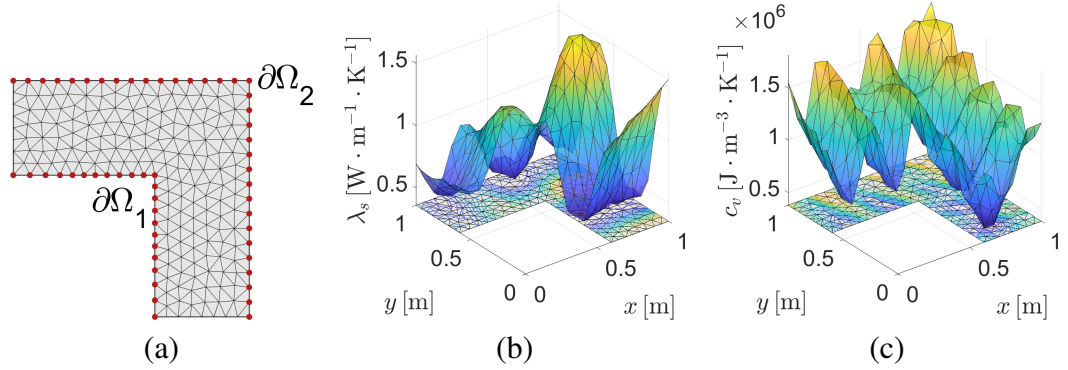


Figure 3: (a) Geometrical l-shaped domain with highlighted boundary conditions; (b) True material field - thermal conductivity; (c) True material field - volumetric heat capacity.

5. Numerical study

This section supports the proposed identification strategy through the numerical study of the transient heat conduction problem in a geometrical l-shaped domain, see Fig. 3a, which is divided into a finite element mesh of 360 triangular elements with 216 nodes. To start with, real climatic changes in temperature are imposed on the observed part of the boundary over several days. Measurements are assumed to be conducted by a thermal camera and/or by an array of discrete thermometers with appropriate interpolation providing continuous surface data. The observation period lasts 9 days and starts on Day Two with hourly intervals. This yields $m_t = 216$ time observations, see Fig. 4. Such time duration provides us with a sufficient amount of data for reconstructing thermal conductivity and the volumetric heat capacity fields, see Havelka et al. [9] as well as Figs. 5a and 5c for a comparison of a true fields of thermal conductivity and volumetric heat capacity, respectively, with the deterministic solution of the Calderón inverse problem. The boundary conditions are then defined as

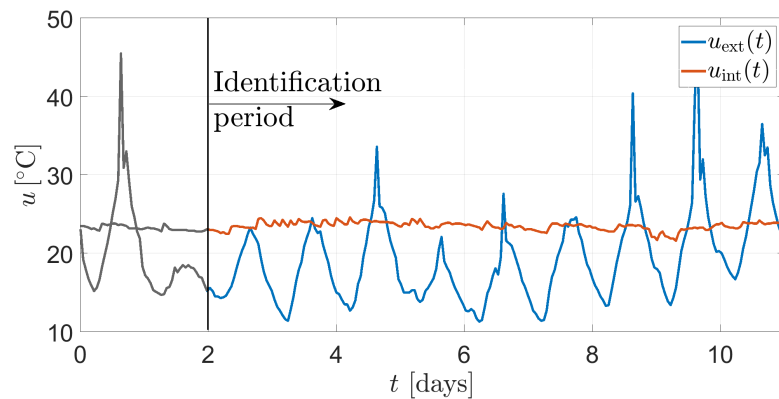


Figure 4: Ambient boundary conditions: Interior ($u_{\text{int}}(t)$) and exterior ($u_{\text{ext}}(t)$) temperatures; data included in the calculation ranges from days 2 to 11.

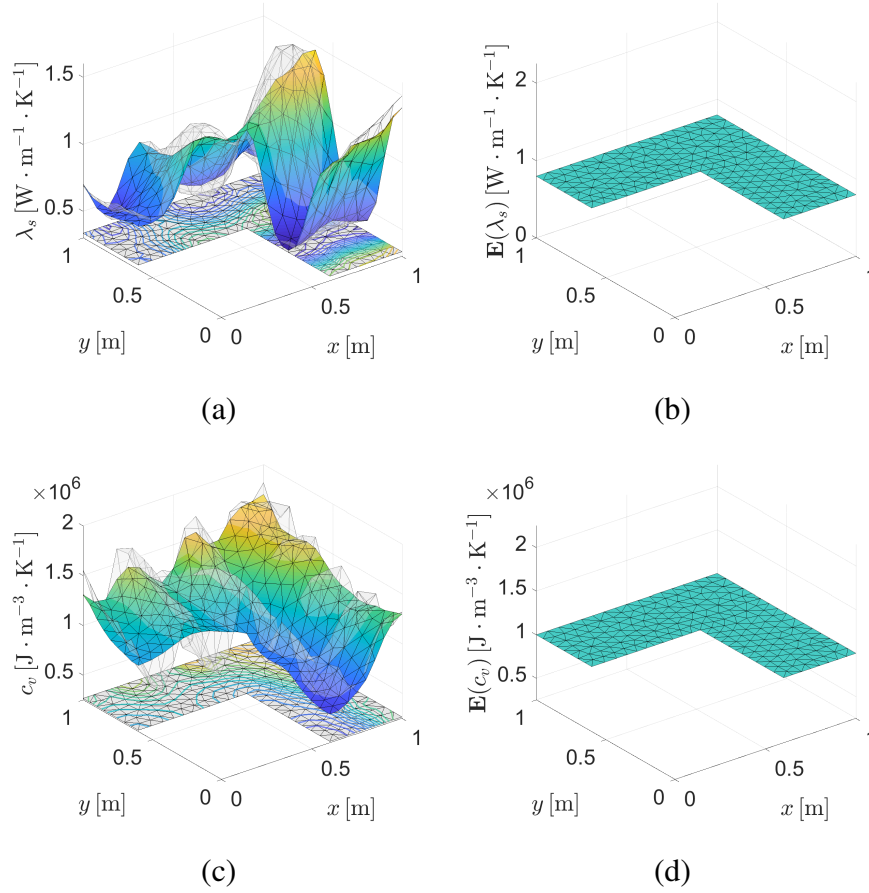


Figure 5: (a) Comparison of true thermal conductivity field with deterministic solution; (b) Mean of prior distribution of thermal conductivity; (c) Comparison of true volumetric heat capacity field with deterministic solution; (d) Mean of prior distribution of volumetric heat capacity.

$$\begin{aligned}
 \lambda_s \frac{\partial u}{\partial n}(\mathbf{x}, t)|_{\partial D_1} &= 10 \cdot (u(\mathbf{x}, t) - u_{\text{int}}(t)), \\
 \lambda_s \frac{\partial u}{\partial n}(\mathbf{x}, t)|_{\partial D_2} &= 10 \cdot (u(\mathbf{x}, t) - u_{\text{ext}}(t)), \\
 \lambda_s \frac{\partial u}{\partial n}(\mathbf{x}, t)|_{\partial D_3} &= 0,
 \end{aligned} \tag{26}$$

where the environmental temperatures $u_{\text{ext}}(t)$ and $u_{\text{int}}(t)$ are shown in Fig. 4 and where $\alpha = 10 \text{ Wm}^{-2}\text{K}^{-1}$. The observed part of the boundary coincides with ∂D_1 and ∂D_2 ($\partial D_T = \partial D_1 \cup \partial D_2$) and contains $m_n = 56$ nodes. The third condition in Eq. (26) represents the insulated part of the boundary, i.e. $\partial D_3 = \partial D \setminus \partial D_T$, which corresponds to the rest of the boundary in Fig. 3a.

The prior information about material parameters, both thermal conductivity λ_s and volumetric heat capacity c_v , are considered to be lognormally distributed with the mean and standard deviation given in Tab. 1. The mean values represent typical values for materials in civil engineering, with a standard deviation of 30% of the mean values. As the prior distribution of ξ_k in Eq. (24) is considered to be standard Gaussian with a zero mean, the mean of

prior fields \mathbf{q}_i is constant, see Fig. 5b and 5d.

	Thermal conductivity λ_s [Wm ⁻¹ K ⁻¹]	Volumetric heat capacity c_v [Jm ⁻³ K ⁻¹]
μ_q	0.8	$1.0 \cdot 10^6$
σ_q	0.24	$0.3 \cdot 10^6$

Table 1: Statistical moments of prior distributions.

To quantify the efficiency of the proposed algorithm, we define the true material fields $\mathbf{q}_i^{\text{true}}$ and simulate the corresponding response field \mathbf{u}^{true} . Due to unavailable real-world observations, we apply the algorithm to re-identify the material fields $\mathbf{q}_i^{\text{rec}}$ from these simulated data. As an advantage, this gives us the ability to properly evaluate the estimation accuracy in terms of both the response field as well as the material fields according to:

$$\varepsilon_p = \frac{\|\mathbf{p}^{\text{rec}} - \mathbf{p}^{\text{true}}\|_2}{\|\mathbf{p}^{\text{true}}\|_2}, \quad (27)$$

where \mathbf{p}^{rec} is the vector containing the identified quantity and \mathbf{p}^{true} is the vector containing the true values. The true thermal conductivity λ_s^{true} and volumetric heat capacity c_v^{true} fields are constructed for a two dimensional domain $\mathbf{x} = [x, y]$ using the following mathematical functions:

$$\lambda_s^{\text{true}}(x, y) = \frac{1}{15} \left(\text{abs}((5 + 3x^2 + 2y - yx - 5y \sin(x/0.075) + 10x \cos(10y))) + 5 \right), \quad (28)$$

and

$$c_v^{\text{true}}(x, y) = 850 \left(5(50x^3 + 100x^2 + 150y^2 - 100yx + 100y) + 500 + 300 \cos(10\pi xy) - 300 \sin(6\pi x) \right), \quad (29)$$

see Fig. 3b,c. Vectors $\mathbf{q}_i^{\text{true}}$ are then obtained by discretization of functions (28) and (29) in centroids of the same finite element mesh as the one used in the identification process. It is thus certain that the forward model is able to reproduce the observed data exactly when the full vectors \mathbf{q}_i are identified. The discrepancy between $\mathbf{q}_i^{\text{true}}$ and reidentified $\mathbf{q}_i^{\text{rec}}$ is thus caused by the approximation based on the truncated Karhunen-Loève expansion.

The Bayesian update was performed using the Metropolis algorithm (see Gelman et al. [7]) with Gaussian proposal distribution and a standard deviation $\sigma_0 = 0.0025$. Overall, 100,000 samples were generated in order to sample the posterior densities according to Eq. (16) combining Eqs. (13)-(15) with $\sigma_\varepsilon^2 = 0.09^\circ\text{C}$.

As outlined in Section 4, the spatial variability of each material field is approximated by a Karhunen-Loève expansion depending on a limited number m ($m < N_n$) of random variables to be identified. This is the principal difference between our proposed approach and the classical Calderón inverse problem where the material field is modeled using the N_n random variables defined in all nodes of finite element mesh. The resulting material fields are, of course, influenced also by parameters of chosen approximation, namely (i) m - number of eigenmodes and (ii) parameters of the covariance function (ρ, ν) entering the Karhunen-Loève expansion through eigenvalues and eigenmodes. The selection of appropriate values

for these parameters is, however, a non-trivial task. Since ν is the smoothness parameter, its impact on the shape of the random field is rather low. In the following numerical study, its value is fixed to $\nu = 5$. The effect of correlation length ρ is, on the contrary, significant. From the definition of the Karhunen-Loève expansion, see Eq. (24), it can be seen that the correlation length does not enter the expansion directly but rather through the spectral decomposition of the covariance matrix, see Eq. (22). Its estimation is thus a very complex task. Therefore, a numerical study was performed for a number of eigenmodes $m = [1, \dots, 50]$ and covariance lengths $\rho = [0.1, 0.25, 0.5, 1.0, 2.5, 5.0, 7.5, 10.0]$ to demonstrate the significance and role of these parameters. The methodology for estimation of correlation length from the experimental data is out of the scope of this paper, but an interested reader is referred to Lombardo et al. [18], which discusses its estimation using image analysis.

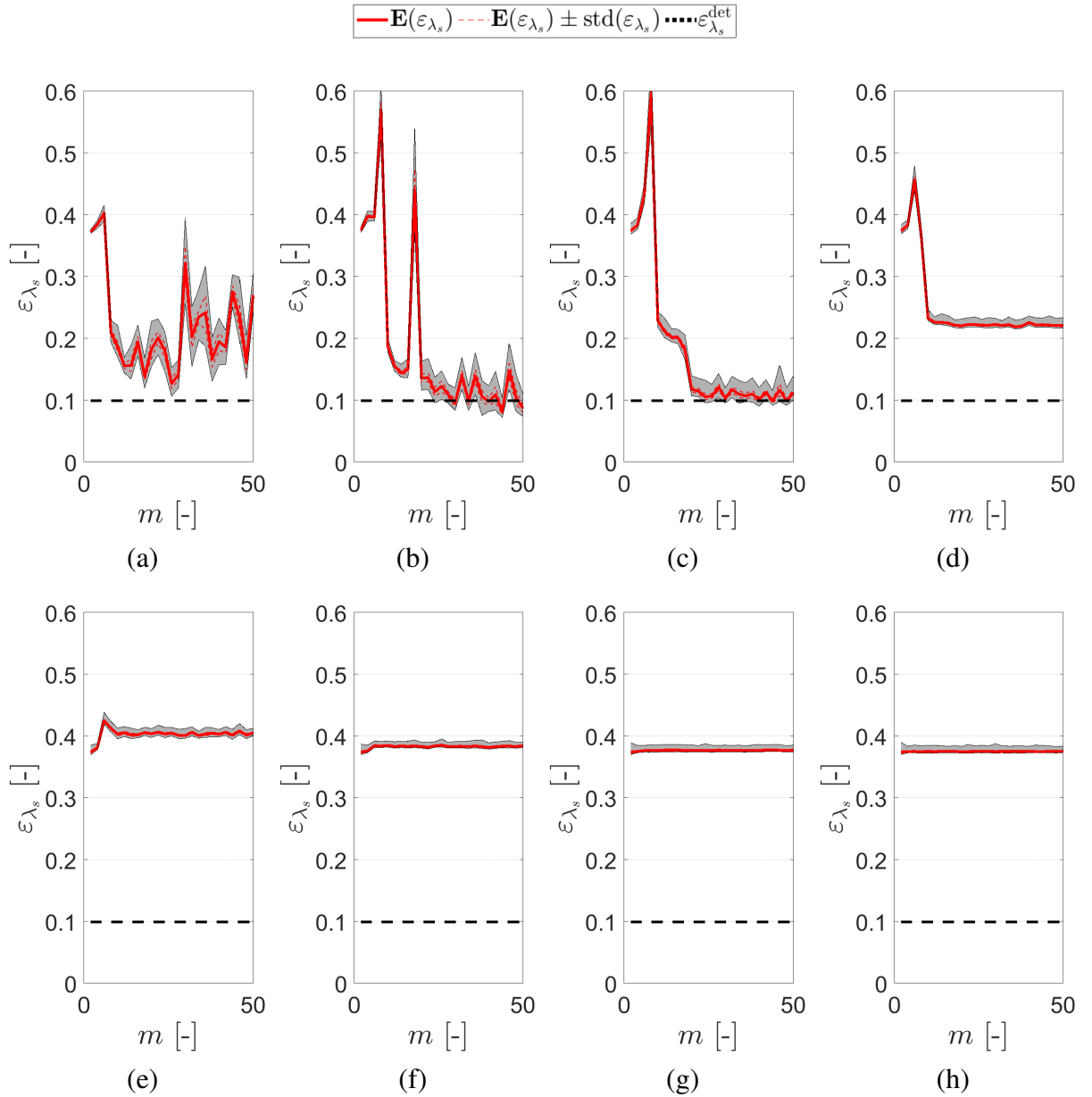


Figure 6: Resulting errors of thermal conductivity ε_{λ_s} as a function of the number of eigenmodes m ; study performed for following correlation lengths: (a) $\rho = 0.10$; (b) $\rho = 0.25$; (c) $\rho = 0.50$; (d) $\rho = 1.00$; (e) $\rho = 2.50$; (f) $\rho = 5.00$; (g) $\rho = 7.50$; (h) $\rho = 10.00$.

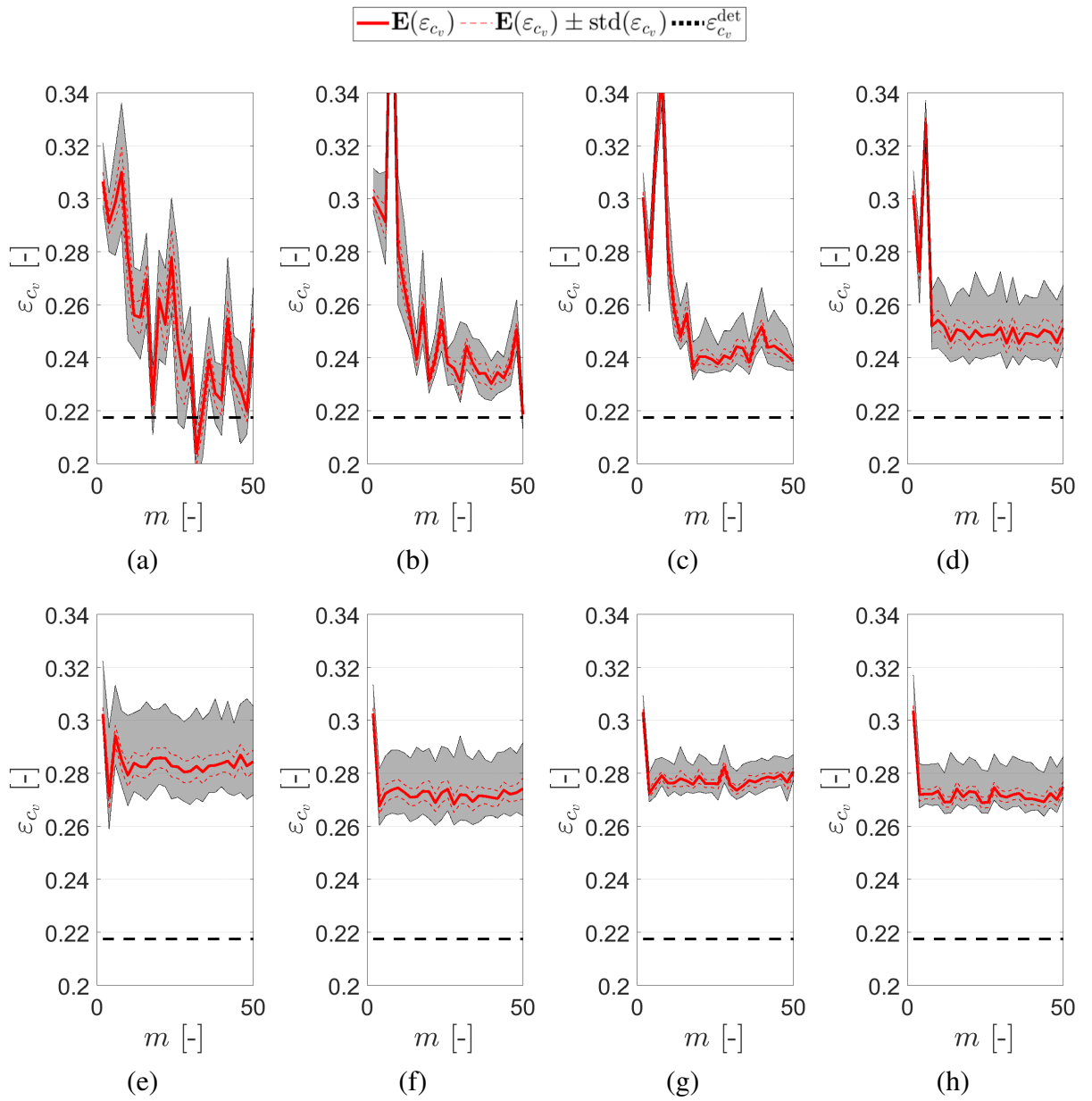


Figure 7: Resulting errors of volumetric heat capacity ε_{c_v} as a function of the number of eigenmodes m ; study performed for following correlation lengths: (a) $\rho = 0.10$; (b) $\rho = 0.25$; (c) $\rho = 0.50$; (d) $\rho = 1.00$; (e) $\rho = 2.50$; (f) $\rho = 5.00$; (g) $\rho = 7.50$; (h) $\rho = 10.00$.

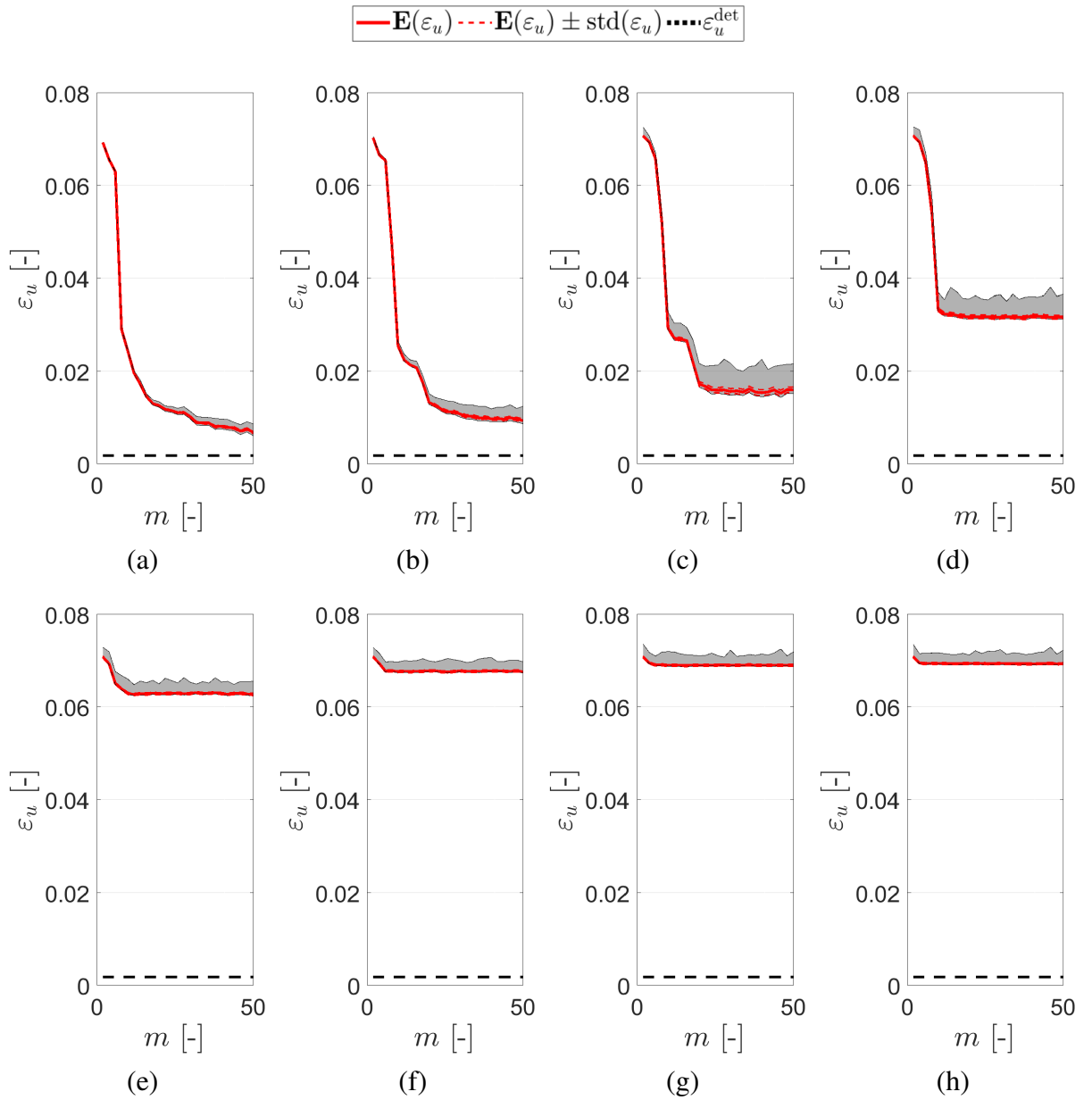


Figure 8: Resulting errors of temperature ε_u as a function of the number of eigenmodes m ; study performed for following correlation lengths: (a) $\rho = 0.10$; (b) $\rho = 0.25$; (c) $\rho = 0.50$; (d) $\rho = 1.00$; (e) $\rho = 2.50$; (f) $\rho = 5.00$; (g) $\rho = 7.50$; (h) $\rho = 10.00$.

The resulting errors of thermal conductivity ε_{λ_s} , volumetric heat capacity ε_{c_v} , and temperature ε_u as a function of the number of Karhunen-Loève eigenmodes m are depicted in Figs. 6-8. The grey surface on these figures represents the errors calculated for all posterior samples. The bold red line is the mean value and the standard deviation is represented by a red dashed line. Moreover, the black dashed line represents the values of errors obtained by the deterministic identification scheme without considering random fields in calculations, see our previous work Havelka et al. [9]. To be more specific, the desired parameter fields are recovered using a Calderón problem which is numerically solved by means of a regularized Gauss-Newton method. The achieved values were: (i) $\varepsilon_{\lambda_s}^{\text{det}} = 0.0950$, (ii) $\varepsilon_{c_v}^{\text{det}} = 0.2175$, and (iii) $\varepsilon_u^{\text{det}} = 0.0018$. Comparison with these errors derived from deterministic solutions gives us the opportunity to see the performance of our technique based on the dimensionality reduction.

Very good results are achieved for values with correlation length $\rho < 1.0$, where the amount of error still decreases with an increasing number of eigenmodes in the description of random fields. The mean of corresponding posterior fields for $m = 50$ eigenmodes is depicted in Fig. 9. It is interesting that while the amount of error in temperature fields in Fig. 8 decreases relatively smoothly with increasing number of eigenmodes, the errors in the parameter fields oscillate significantly, see Figs. 6 and 7. This means that a better description of the measured temperature field can be obtained for parameter fields which differ more

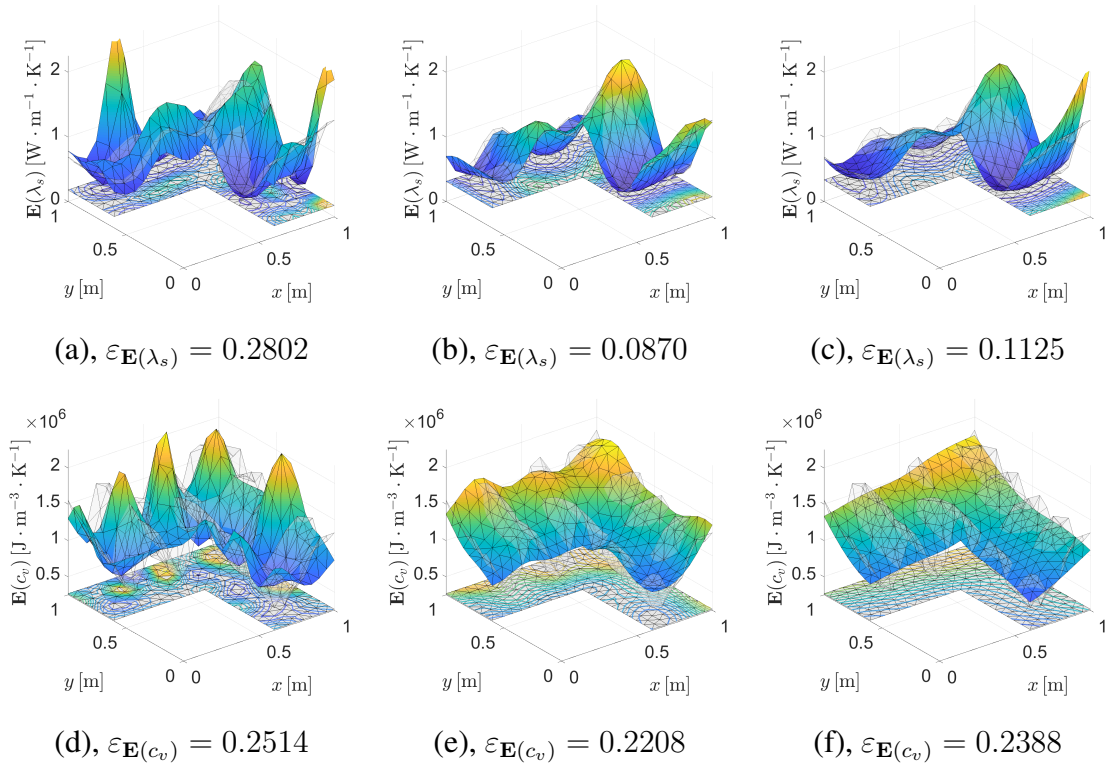


Figure 9: Comparison of true fields with mean of posterior fields constructed using the 50 eigenmodes: (a) Thermal conductivity, $\rho = 0.10$; (b) Thermal conductivity, $\rho = 0.25$; (c) Thermal conductivity, $\rho = 0.50$; (d) Volumetric heat capacity, $\rho = 0.10$; (e) Volumetric heat capacity, $\rho = 0.25$; (f) Volumetric heat capacity, $\rho = 0.50$.

from the true ones. This is visible also in Fig. 9, while the smallest amount of error in the temperature field is achieved for correlation length $\rho = 0.10$ and the smallest amount of error in the conductivity and capacity fields is obtained for $\rho = 0.25$. It is not very surprising that the inaccuracy in approximation with a limited number of eigenmodes may cause convergence of the identification process to an incorrect solution. More interesting is that including an additional eigenmode into the approximation, i.e. one additional degree of freedom, allows for improvement of the temperature field but may lead to significantly worse representation of the parameter fields. This is probably caused by the fact that particular eigenmodes were not constructed from the correct covariance kernel corresponding to the true fields and thus, such eigenmodes do not ensure smooth convergence. Moreover, the plots in Figs. 6 and 7, namely Fig. 6a, suggest that the amount of error is not converging towards the error of a deterministic solution at all – not even including all eigenmodes will allow for achieving the amount of error of a deterministic solution. On the other hand, a covariance kernel with correlation lengths $\rho = 0.25$ or $\rho = 0.50$, see Figs. 6b and 6c, seems to better represent the covariance structure of the true conductivity field indicated by more smooth convergence of the error values as well as by its proximity to the deterministic errors.

Regarding higher values of ρ ($\rho \geq 1.0$), the convergence graphs of error values in the parameters fields are already also relatively smooth, especially in case of thermal conductivity, see Figs. 6d – 6h. These graphs also clearly show that the error values quickly start to stagnate, and inclusion of additional eigenmodes does not bring any improvement. Moreover, the stagnation appears not only in the convergence graph of error in thermal conductivity or volumetric heat capacity fields, but also in the temperature fields, see Figs. 8d – 8h. This can be explained by the fact that high correlation lengths in the covariance kernel do not allow for description of higher frequencies in eigenmodes. This is connected to a ill-conditioned covariance matrix, which can be almost singular up to some numerical error amounts, and solution of the eigenvalue problem results in a very fast decay in eigenvalues suggests that only a few eigenvalues explain almost whole the variance of a random field, see Fig. 11. The remaining eigenvalues are nearly zero and thus the addition of corresponding eigenvectors to the Karhunen-Loève expansion brings no improvement to the quality of the random field approximation.

6. Conclusion

This paper presents a novel strategy for recovering spatially distributed thermal properties (thermal conductivity and volumetric capacity) based on the random field theory. To limit the number of variables describing the heterogeneity of material fields, a Karhunen-Loève expansion is introduced as an efficient tool for describing spatial variability with a relatively small number of eigenmodes. The results reported here indicate that the proposed algorithm is capable of identifying a heterogeneous material field from boundary measurements utilizing only a few eigenmodes. Moreover, the obtained results were compared with those provided by a standard deterministic identification approach used in thermal tomography. To summarize the results, Fig. 10 displays the comparisons of average errors in both the parameter fields as well as in the temperature fields for all the studied correlation lengths. It is thus clearly visible that all graphs start from an almost identical value of error, i.e. the error of the first mode, that is very similar for all correlation lengths. Furthermore, some graphs start to differ significantly with an increasing number included eigenmodes. With no doubt,

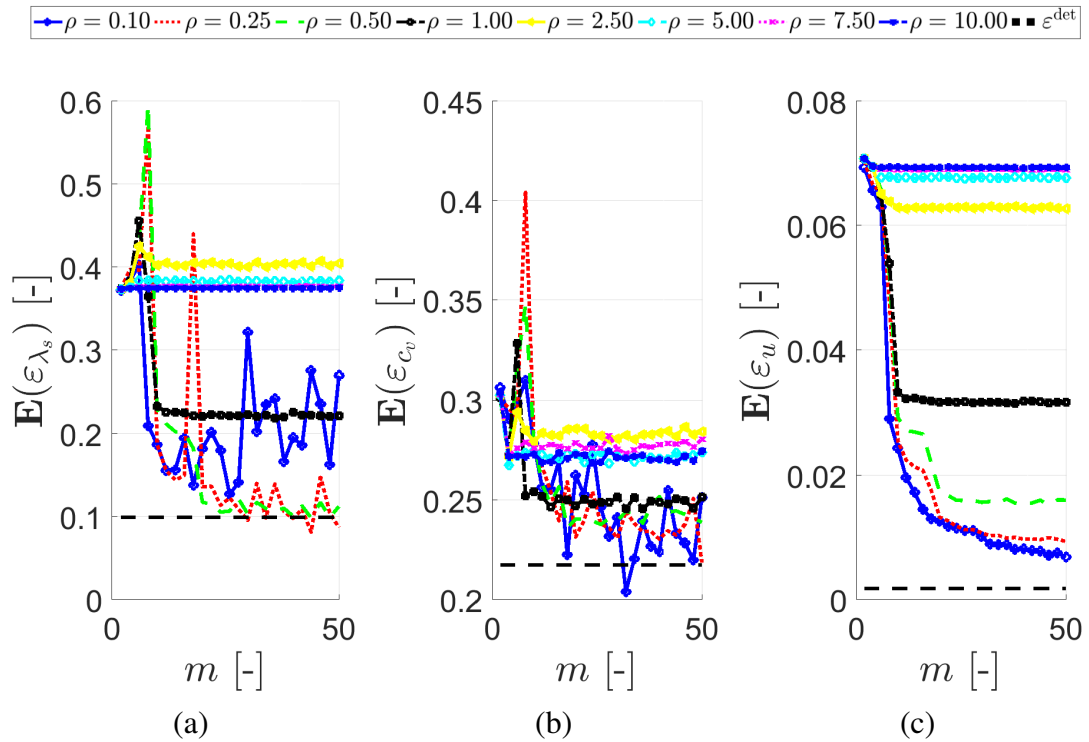


Figure 10: Final comparison: (a) Averaged of thermal conductivity ε_{λ_s} errors as a function of the number of eigenmodes m and ρ ; (b) Averaged of volumetric heat capacity ε_{c_v} errors as a function of the number of eigenmodes m and ρ ; (c) Averaged of temperature ε_u errors as a function of the number of eigenmodes m and ρ .

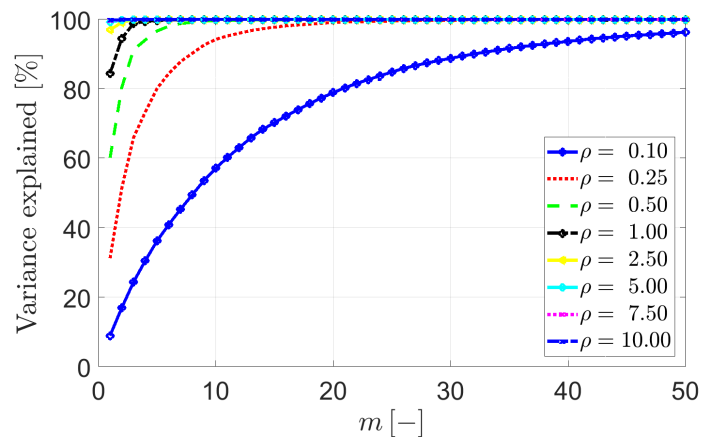


Figure 11: Decay of eigenvalues with different prior correlation lengths. Vertical axis shows the fraction of the prior variance explained by m eigenmodes.

for some specific correlation lengths, namely $\rho = 0.25$ and $\rho = 0.50$, the amount of error in parameter fields converges quickly towards the amount of error for a deterministic solution. This confirms that the proposed methodology has the potential for an efficient reduction in dimensionality in the solution of the Calderón problem. However, the results also reveal the

enormous significance in the appropriate choice of correlation lengths in material properties. The wrong correlation length choice may completely block the ability of a Karhunen-Loève expansion to converge towards a deterministic solution. Moreover, the effect of the shape of a covariance function was neglected in this study as being significantly less important than correlation length. Therefore, future research needs to be focused on a more detailed elaboration of the effects of covariance function on a Karhunen-Loève approximation and namely on the development of techniques allowing for its adequate estimation.

Acknowledgements

The authors are thankful for financial support from the Czech Science Foundation, project No. GA18-04262S and from the Center of Advanced Applied Sciences, the European Regional Development Fund No. CZ.02.1.01/0.0/0.0/16_019/0000778. The authors would also like to thank Prof. Dr. Hermann G. Matthies at the Technische Universität Braunschweig, Germany, for bringing our attention to the Calderón's inverse problem.

- [1] Adler, R. J. and Taylor, J. E. (2009). *Random fields and geometry*. Springer Science & Business Media.
- [2] Bakirov, V., Kline, R., and Winfree, W. (2004a). Discrete variable thermal tomography. In *AIP Conference Proceedings*, volume 700, pages 469–476. AIP.
- [3] Bakirov, V., Kline, R., and Winfree, W. (2004b). Multiparameter thermal tomography. In *AIP Conference Proceedings*, volume 700, pages 461–468. AIP.
- [4] Calderón, A. P. (2006). On an inverse boundary value problem. *Computational & Applied Mathematics*, 25:133 – 138.
- [5] Campana, S. and Piro, S. (2008). *Seeing the Unseen Geophysics and Landscape Archaeology*. Taylor & Francis.
- [6] Cheng, K. S., Isaacson, D., Newell, J. C., and Gisser, D. G. (1989). Electrode models for electric current computed tomography. *IEEE Transactions on Biomedical Engineering*, 36(9):918–924.
- [7] Gelman, A., Carlin, J., Stern, H. S., Dunson, D., Vehtari, A., and Rubin, D. (2013). *Bayesian data analysis*. Chapman and Hall/CRC.
- [8] Ghanem, R. G. and Spanos, P. D. (1991). Stochastic finite element method: Response statistics. In *Stochastic Finite Elements: A Spectral Approach*, pages 101–119. Springer.
- [9] Havelka, J. and Sýkora, J. (2018). Application of Calderón's inverse problem in civil engineering. *Applications of Mathematics*, 63(6):687–712.
- [10] Holder, D. S. (2004). *Electrical Impedance Tomography: Methods, History and Applications (Series in Medical Physics and Biomedical Engineering)*. Series in Medical Physics and Biomedical Engineering. Taylor & Francis, 1st edition.
- [11] Huang, C.-H. and Chin, S.-C. (2000). A two-dimensional inverse problem in imaging the thermal conductivity of a non-homogeneous medium. *International Journal of Heat and Mass Transfer*, 43(22):4061–4071.

- [12] Jones, M., Tezuka, A., and Yamada, Y. (1995). Thermal tomographic detection of inhomogeneities. *Journal of heat transfer*, 117(4):969–975.
- [13] Kolehmainen, V., Kaipio, J., and Orlande, H. (2007). Reconstruction of thermal conductivity and heat capacity using a tomographic approach. *International Journal of Heat and Mass Transfer*, 50(25-26):5150–5160.
- [14] Kučerová, A., Sýkora, J., Rosić, B., and Matthies, H. G. (2012). Acceleration of uncertainty updating in the description of transport processes in heterogeneous materials. *Journal of Computational and Applied Mathematics*, 236(18):4862–4872.
- [15] Kučerová, A. and Sýkora, J. (2011). Uncertainty updating in the description of coupled heat and moisture transport in heterogeneous materials. *Applied Mathematics and Computation*, 219(13):7252–7261.
- [16] Ladyzhenskaia, O. A., Solonnikov, V. A., and Ural'ceva, N. N. (1968). *Linear and quasi-linear equations of parabolic type*, volume 23. American Mathematical Society.
- [17] Langer, R. E. (1933). An inverse problem in differential equations. *Bulletin of the American Mathematical Society*, 39(10):814–820.
- [18] Lombardo, M., Zeman, J., Šejnoha, M., and Falsone, G. (2009). Stochastic modeling of chaotic masonry via mesostructural characterization. *International Journal for Multiscale Computational Engineering*, 7(2):171–185.
- [19] Marzouk, Y. M. and Najm, H. N. (2009). Dimensionality reduction and polynomial chaos acceleration of bayesian inference in inverse problems. *Journal of Computational Physics*, 228(6):1862–1902.
- [20] Matthies, H. G. (2007). *Encyclopedia of Computational Mechanics*, chapter Uncertainty Quantification with Stochastic Finite Elements. John Wiley & Sons, Ltd.
- [21] Matthies, H. G. and Keese, A. (2005). Galerkin methods for linear and nonlinear elliptic stochastic partial differential equations. *Computer Methods in Applied Mechanics and Engineering*, 194(12-16):1295–1331.
- [22] Minasny, B. and McBratney, A. B. (2005). The matérn function as a general model for soil variograms. *Geoderma*, 128(3):192–207.
- [23] Mueller, J. L. and Siltanen, S. (2003). Direct reconstructions of conductivities from boundary measurements. *SIAM Journal on Scientific Computing*, 24(4):1232–1266.
- [24] Rosić, B. and Matthies, H. G. (2008). Computational approaches to inelastic media with uncertain parameters. *Journal of the Serbian Society for Computational Mechanics*, 2(1):28–43.
- [25] Rosić, B. V., Kučerová, A., Sýkora, J., Pajonk, O., Litvinenko, A., and Matthies, H. G. (2013). Parameter identification in a probabilistic setting. *Engineering Structures*, 50:179–196.

-
- [26] Tarantola, A. (2005). *Inverse Problem Theory and Methods for Model Parameter Estimation*. Society for Industrial and Applied Mathematics.
- [27] Toivanen, J., Kolehmainen, V., Tarvainen, T., Orlande, H., and Kaipio, J. (2012). Simultaneous estimation of spatially distributed thermal conductivity, heat capacity and surface heat transfer coefficient in thermal tomography. *International Journal of Heat and Mass Transfer*, 55(25-26):7958–7968.
- [28] Toivanen, J., Tarvainen, T., Huttunen, J., Savolainen, T., Orlande, H., Kaipio, J., and Kolehmainen, V. (2014). 3D thermal tomography with experimental measurement data. *International Journal of Heat and Mass Transfer*, 78:1126–1134.
- [29] Vanmarcke, E. (2010). *Random fields: analysis and synthesis*. World Scientific.
- [30] Xiu, D. (2010). *Numerical methods for stochastic computations: a spectral method approach*. Princeton University Press.

LIST OF AUTHOR'S PUBLICATIONS

WOS journal papers

- Havelka, J., Kučerová, A., and Sýkora, J. (2019). Dimensionality reduction in thermal tomography. *Computers & Mathematics with Applications*, 78(9):3077–3089.
- Šejnoha, M., Sýkora, J., Vorel, J., Kucíková, L., Antoš, J., Pokorný, J., and Pavlík, Z. (2019). Moisture induced strains in spruce from homogenization and transient moisture transport analysis. *Computers & Structures*, 220:114–130.
- Havelka, J. and Sýkora, J. (2018). Application of Calderón's inverse problem in civil engineering. *Applications of Mathematics*, 63(6):687–712.
- Janouchová, E., Sýkora, J., and Kučerová, A. (2018). Polynomial chaos in evaluating failure probability: A comparative study. *Applications of Mathematics*, 63(6):713–737.
- Sýkora, J., Jarušková, D., Šejnoha, M., and Šejnoha, J. (2018). Fire risk analysis focused on damage of the tunnel lining. *Fire Safety Journal*, 95:51–65.
- Havelka, J., Kučerová, A., and Sýkora, J. (2016). Compression and reconstruction of random microstructures using accelerated lineal path function. *Computational Materials Science*, 122:102–117.
- Sýkora, J. (2014). Modeling of degradation processes in historical mortars. *Advances in Engineering Software*, 72:203–212.
- Rosić, B. V., Kučerová, A., Sýkora, J., Pajonk, O., Litvinenko, A., and Matthies, H. G. (2013). Parameter identification in a probabilistic setting. *Engineering Structures*, 50:179–196.
- Kučerová, A. and Sýkora, J. (2013). Uncertainty updating in the description of coupled heat and moisture transport in heterogeneous materials. *Applied Mathematics and Computation*, 219(13):7252–7261.
- Sýkora, J., Šejnoha, M., and Šejnoha, J. (2013). Homogenization of coupled heat and moisture transport in masonry structures including interfaces. *Applied Mathematics and Computation*, 219(13):7275—7285.
- Kučerová, A., Sýkora, J., Rosić, B., and Matthies, H. G. (2012). Acceleration of uncertainty updating in the description of transport processes in heterogeneous materials. *Journal of Computational and Applied Mathematics*, 236(18):4862–4872.
- Sýkora, J., Krejčí, T., Kruis, J., and Šejnoha, M. (2012). Computational homogenization of non-stationary transport processes in masonry structures. *Journal of Computational and Applied Mathematics*, 18:4745—4755.

Sýkora, J., Vorel, J., Krejčí, T., Šejnoha, M., and Šejnoha, J. (2009). Analysis of coupled heat and moisture transfer in masonry structures. *Materials and Structures*, 42(8):1153–1167.

Šejnoha, J., Šejnoha, M., Zeman, J., Sýkora, J., and Vorel, J. (2008). Mesoscopic study on historic masonry. *Structural Engineering and Mechanics*, 30(1):99–117.

Non-WOS journal papers

Šejnoha, M., Kucíková, L., Vorel, J., Sýkora, J., and De Wilde, W. (2019). Effective material properties of wood based on homogenization. *International Journal of Computational Methods and Experimental Measurements*, 7(2):167–180.

Šejnoha, J., Sýkora, J., Jarušková, D., Novotná, E., and Šejnoha, M. (2015). Analýza rizika požáru v silničních tunelech. *BETON-technologie*, 15(6):68–72.

Sýkora, J., Zeman, J., and Šejnoha, M. (2012). Selected topics in homogenization of transport processes in historical masonry structures. *The Open Civil Engineering Journal*, 6:148–159.

Sýkora, J., Vorel, J., and Šejnoha, M. (2008). Evaluation of effective conductivities for masonry with interfaces. *Bulletin of Applied Mechanics*, 4(13):18–23.

Vorel, J., Sýkora, J., and Šejnoha, M. (2008). Two step homogenization of effective thermal conductivity for macroscopically orthotropic c/c composites. *Bulletin of Applied Mechanics*, (14):4.

Book chapters

Rosić, B., Sýkora, J., Pajonk, O., Kučerová, A., and Matthies, H. G. (2016). Comparison of numerical approaches to bayesian updating. In *Computational Methods for Solids and Fluids*, pages 427–461. Springer.

Šejnoha, M. and Sýkora, J. (2012). Hierarchical modeling of transport processes in heterogeneous materials. application to historical masonry structures. In *Selected Chapters of Mechanics of Composite Materials II*, pages 1–48. Czech Technical University in Prague.